

Development of High Functional Tapping Tool Coated with Abrasive Particles

著者	Saito Yasuyoshi
学位授与機関	Tohoku University
学位授与番号	11301甲第17531号
URL	http://hdl.handle.net/10097/00121525

TOHOKU UNIVERSITY
Graduate School of Engineering

Development of High Functional Tapping Tool Coated with Abrasive Particles
(硬質粒子被膜を有する高機能タップ工具の開発)

A dissertation submitted for the degree of Doctor of Philosophy (Engineering)

Department of Mechanical Systems and Design

by

Yasuyoshi SAITO

January 10, 2017

Development of High Functional Tapping Tool Coated with Abrasive Particles

Yasuyoshi Saito

Abstract

This thesis, which describes the systematic study on development of high functional tapping tool coated with Ni-P/abrasive particle composite film, consists of seven chapters. The principal results in these chapters are summarized as follows:

The first chapter describes the background and purposes of the thesis.

The second chapter explains the development and the tribological properties of Ni-P/abrasive particles composite film. Ni-P/abrasive particle composite films were deposited on an HSS disk specimen using cBN particulates with a mean diameter of 10 μm or SiC particulates with mean diameters of 5.0 μm or 1.0 μm . The hardness and adhesion strength of the composite films and the friction coefficient under lubrication by emulsion cutting were investigated. The analysis clarified that the hardness of the Ni-P film was about 9 GPa and higher than the steam treatment (conventional treatment), and the composite film had excellent peeling resistance, which no film separation was observed. The friction coefficient for the composite films was greater than 0.15 and sliding velocities under emulsion-oil lubrication (0.05-0.25 m/s) that were higher than those for the other specimens by the abrasive particles in the film.

The third chapter demonstrated the development of tapping tools coated with the Ni-P/abrasive particle composite film and the cutting performance, such as the cutting resistance and the quality of the thread hole, of the tapping tool. A spiral-cut tapping tool (M6 \times 1) was coated with the Ni-P/abrasive particle composite films. The tapping test was conducted using a vertical machining center. The workpiece material was rolled structural steel (JIS SS400). The cutting speed was 10, 30, or 50 m/min. The cutting torque and thrust force were measured using a dynamometer. In addition, to evaluate the quality of thread hole, the surface of thread hole was observed using SEM and the shapes of thread hole were tested using screw thread-limiting gauge. The results showed that the tapping tool coated with the Ni-P/abrasive particle composite films satisfied the standard for thread gauge at high cutting speed condition. However, the Ni-P/cBN film caused the severe adhesion with plastic flow at the surface of thread hole at all cutting speed. Furthermore, the cutting torque produced by the tapping tool coated with the Ni-P/cBN film ($\bar{d} = 10 \mu\text{m}$) was the highest value in comparison with the other tapping tools. In contrast, the thrust force of the tapping tool coated with the Ni-P/abrasive particle composite films were lower than that of the others. Thus, these results suggested the optimal size of the SiC particles used in the composite film was less than 5.0 μm , as an excessively rough tool surface may cause damage and decrease the dimensional accuracy of the thread hole.

The fourth chapter suggested whether the tapping tool coated with Ni-P/abrasive particle composite film was able to prevent the chip snarling at high cutting speeds and increase the tool service life. The tapping tests for

SS400 were conducted at high cutting speeds. Furthermore, the mean friction coefficient was estimated from the measured cutting torque and thrust force. The results demonstrated that the chip snarling rate of the tapping tool coated with Ni-P/abrasive particle composite film was lower than that of the other tapping tools. The chip snarling rate increased as the chip curl diameter increased. The rate of chip snarling exceeded 40% at a dimensionless chip curl diameter of approximately 1.0. The chip curl diameter decreased with increasing of the mean friction coefficient. The mean friction coefficient of the tapping tool coated with Ni-P/abrasive particle composite film was higher than that of other tapping tools. Additionally, the tool service life of tapping tool coated with Ni-P/SiC film ($\bar{d} = 1 \mu\text{m}$) was 1.6 times greater than that of conventional tapping tool at 50 m/min.

The fifth chapter discussed the effect of the local friction coefficient at the sliding zone on chip curl diameter and the secondary shear zone thickness on the chip curl diameter. The local friction coefficient at the sliding zone and the secondary shear zone thickness were estimated using the sticking-sliding friction model. The results indicated that the chip curl diameter decreased as the local friction coefficient at the sliding zone increased. The local friction coefficient at the sliding zone of the tapping tool coated with the Ni-P/abrasive particle composite films was over 1.58 and higher than that of the other tapping tools. The secondary shear zone was affected by the local friction coefficient at the sliding zone; the secondary shear zone thickness increased with increase of the local friction coefficient.

The sixth chapter clarified the effect of workpiece materials on chip snarling for tapping tool coated with Ni-P/abrasive particle composite film. The tapping test was conducted on the workpiece material made from chrome molybdenum steel (JIS SCM440) and carbon steel (JIS S25C and S45C). The temperature at the primary shear zone was estimated to investigate the thermal effect on the chip curl diameter. The results indicated that the dimensionless chip curl diameter of the tapping tool coated with Ni-P/SiC film ($\bar{d} = 1 \mu\text{m}$) was less than 0.9 for all workpiece material and the rate of chip snarling of the tapping tool coated with Ni-P/SiC film was less than 10%. Additionally, the chip curl diameter was affected by the cutting speed, i.e. temperature at the primary shear zone, and decreased as the temperature decreased. The dimensionless chip curl diameter was less than 0.6 when the secondary shear zone thickness was as least 23 μm and the temperature at the primary shear zone was lower than 495 K.

The seventh chapter summarized the results of the thesis and main conclusions are presented. As the results of the study, the tapping tool coated with Ni-P/SiC film ($\bar{d} = 1 \mu\text{m}$) prevented the chip snarling on the tapping tool at high cutting speed and increased the tool service life at 50 m/min.

Table of contents

Chapter 1

Introduction

1.1	Background	1
1.2	Previous studies	5
1.2.1	Tapping process	5
1.2.2	Chip discharge in turning and drilling processes	8
1.2.3	Surface treatment of the tapping tool	12
1.2.4	Electrodeposited plating	16
1.3	Purpose of study	18
1.4	Structure of thesis	19
	References	21

Chapter 2

Tribological properties of Ni-P/abrasive particle composite film

2.1	Introduction	31
2.2	Preparation of an electroless plating composite film	32
2.3	Experimental methods	35
2.3.1	Disk specimens	35
2.3.2	Nanoindentation testing	38
2.3.3	Scratch testing	41
2.3.4	Friction testing	43
2.4	Experimental results	45
2.4.1	Vickers hardness and Young's modulus of the composite films	45
2.4.2	Adhesion strength of the composite films	47
2.4.3	Friction coefficient of the composite films	51
2.5	Discussion	54
2.6	Conclusions	58
	References	59

Chapter 3

Development of tapping tool coated with Ni-P/Abrasive particle composite film

3.1	Introduction	61
3.2	Development of a tapping tool coated with Ni-P/abrasive particle composite	62
3.3	Experimental methods	73

3.3.1 Experimental apparatus	73
3.3.2 Experimental conditions	74
3.3.3 Evaluation of the dimensional accuracy of thread hole	75
3.3.4 Evaluation method for cutting resistance	76
3.4 Results and discussion	77
3.4.1 Evaluation of the dimensional accuracy of thread holes	77
3.4.2 Cutting torque and thrust force	81
3.5 Effect of the diameter of codepositing particle on chip snarling	85
3.6 Conclusions	86
References	87

Chapter 4

Chip snarling prevention and tapping tool service life extension by coating with Ni-P/abrasive particle composite film

4.1 Introduction	89
4.2 Experimental methods	90
4.2.1 Tapping test	90
4.2.2 Estimation of friction coefficient at the rake face of the tool-workpiece interface	90
4.2.3 Durability testing	94
4.3 Results and discussion	95
4.3.1 Chip snarling and chip curl diameter	95
4.3.1.1 Rate of chip snarling	95
4.3.1.2 Chip curl geometry	97
4.3.1.3 Effect of chip curl diameter on chip snarling	101
4.3.2 Effect of the friction coefficient on chip curl diameter	106
4.3.2.1 Cutting torque and thrust force	106
4.3.2.2 Estimated friction coefficient	108
4.3.2.3 Effect of friction coefficient on chip curl diameter at the tool-chip interface	112
4.3.3 Tool service life	113
4.4 Conclusions	118
References	119

Chapter 5

Effect of the friction coefficient at the sliding zone of the chip-tool interface on chip curl diameter during the tapping process

5.1 Introduction	121
------------------	-----

5.2 Methods -----	122
5.2.1 Estimation of local friction coefficient at the sliding zone of the tool-chip interface -----	122
5.2.2 Observation of the secondary shear zone at the chip surface -----	129
5.3 Results and discussion -----	130
5.3.1 Relation between chip curl diameter and local friction coefficient at the sliding zone -----	130
5.3.2 Effect of local friction coefficient at the sliding zone on secondary shear zone thickness -----	132
5.3.3 Observation of the metal structure of cutting chips -----	134
5.3.4 Effect of stress field in the shear plane on secondary shear zone thickness --	137
5.4 Conclusions -----	141
References -----	142

Chapter 6

Effect of workpiece material on chip snarling for tapping tool coated with Ni-P/Abrasive Particles Composite Film

6.1 Introduction -----	144
6.2 Methods -----	145
6.2.1 Tapping tests -----	145
6.2.2 Workpiece materials -----	145
6.3 Results and discussion -----	147
6.3.1 Chip snarling and chip curl diameter -----	147
6.3.1.1 Rate of chip snarling -----	147
6.3.1.2 Chip curl diameter -----	149
6.3.1.3 Effect of dimensionless chip curl diameter on the rate of chip snarling -----	152
6.3.2 Effect of friction coefficient at the sliding zone on chip curl diameter -----	153
6.3.2.1 Cutting torque and thrust force -----	153
6.3.2.2 Local friction coefficient at the sliding zone -----	157
6.3.2.3 Relation between secondary shear zone thickness and local friction coefficient at the sliding zone -----	160
6.3.2.4 Relation between dimensionless chip curl diameter and secondary shear zone thickness -----	161
6.3.2.5 Effect of secondary shear zone thickness and temperature at the primary shear zone on dimensionless chip curl diameter -----	163
6.4 Conclusions -----	166
References -----	167

Chapter 7

Conclusions ----- 169

Appendix----- 179

Acknowledgements ----- 181

Nomenclature

A_{all}	resultant cutting area of all cutting edges [mm ²]	Δh_c	measured indentation depth [mm]
A_{nth}	cutting area of nth cutting edge [mm ²]	h_r	intersection point between indentation-depth axis and tangential line [mm]
A_s	area of primary shear plane [mm ²]	H_{IT}	indentation hardness [Pa]
A_{stick}	contact area at sticking zone [mm ²]	H_{max_a}	maximum height of flank face of advancing side [μm]
α_e	effective rake angle [degree]	H_v	Vickers hardness [Pa]
α_n	rake angle [deg]	η	chip flow angle [degree]
b	mean width of the cut chip [mm]	k	heat transfer coefficient [W/(m·K)]
b_b	width of the chip near rake face [mm]	k_{chip}	shear stress in chip at sticking zone [Pa]
b_t	width of the free surface of the chip [mm]	λ	thermal conductivity [kw/m/K]
β	chamfer angle [degree]	L	sliding zone [mm]
c	specific heat capacity [J/(kg·K)]	L_c	chip contact length [mm]
δ	secondary shear zone thickness [mm]	L_{slid}	chip contact length at sliding zone [mm]
d	tapping tool diameter [mm]	L_{stick}	chip contact length at sticking zone [mm]
\bar{d}	mean particle diameter [mm]	$\bar{\mu}$	mean (global) friction coefficient
D_c	chip curl diameter [mm]	μ_{slid}	local friction coefficient at sliding zone
D_d	dimensionless chip curl diameter	μ_0	initial local friction coefficient
E_i	Young's modulus of indenter [Pa]	ν	Poisson's rate
E_{IT}	Young's modulus [N/mm ²]	ν_i	Poisson's ratio of specimen
F	resultant friction force of all cutting edges [N]	ν_s	Poisson's ratio of indenter
F_n	resultant normal force of all cutting edges [N]	$\overline{\text{OB}}$	length of front cutting edge [mm]
F_{nth}	friction force of nth cutting edge [N]	P	pitch of thread hole [mm]
$F_{n_{\text{nth}}}$	normal force of nth cutting edge [N]	q	total hear quantity per unit time and unit area [J/(mm ² ·s)]
$F_{n_{\text{slid}}}$	normal force at sliding zone [N]	θ	torsion angle [degree]
$F_{n_{\text{stick}}}$	normal force at sticking zone [N]	θ'	half angle of thread of screw [degree]
F_M	circumferential force [N]	r	cutting ratio
F_{max}	maximum load [N]	R	cutting resistance [N]
F_{slid}	friction force at sliding zone [N]	R_c	rate of chip snarling [%]
F_{stick}	friction force at sticking zone [N]	R_{nth}	cutting resistance of nth cutting edge [N]
F_T	axial force [N]	R_h	heat volume ratio [%]
F_x	cutting force in x direction on rake face [N]	ρ	density [kg/mm ³]
F_y	cutting force in y direction on rake face [N]	σ_c	normal stress on rake face [Pa]
F_z	cutting force in z direction on rake face [N]	σ_s	normal stress in shear plane [Pa]
F_{z^*}	radial force [N]	σ_0	normal stress in tool tip [Pa]
ϕ	shear angle [degree]	t_1	uncut chip thickness [mm]
γ	lead angle [degree]		
γ_s	shear strain in primary shear plane [1/s]		
h_c	measured indentation depth [mm]		

t_2	chip thickness [mm]
τ_c	shear stress at the sticking zone [Pa]
τ_s	shear stress in primary shear zone [Pa]
T_{shear}	temperature at primary shear zone [K]
V	sliding velocity [m/s]
V_r	cutting speed [m/min]
V_c	chip flow velocity [m/min]
w	width of cutting edge [mm]
w_1	front cutting edge width [mm]
w_2	side cutting edge width [mm]
W_{ad}	adhesion strength [N]
W_{min}	minimum normal load [N]
W_{max}	maximum normal load [N]
W_t	width of helical flute width [mm]
ξ	characteristic value of pressure distribution
z	distance from the tool cutting tip [mm]

Chapter 1

Introduction

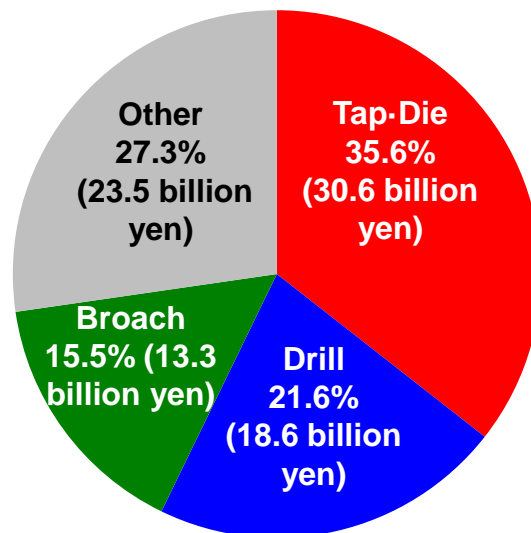
1.1 Background

Joining processes are an essential component of manufacturing and assembly operations. Joining processes fall into three groups: welding, adhesive bonding, and mechanical fastening [1]. Mechanical fastening includes traditional joining or fastening methods that use bolts, nuts, screws, pins, and a variety of other fasteners. Such methods are advantageous over others due to the ease of manufacturing, ease of assembly and transportation, ease of disassembly, maintenance, and parts replacement, and the lower cost of manufacturing the product [1]. Screws are one of the most commonly used threaded fasteners, and there are numerous related standards and specifications. Threaded holes are machined using the tapping process. The tapping process influences the quality of the threaded holes; poor quality can lead to the loosening of bolted joints [2, 3]. Figure 1.1 shows tool production in Japan in 2014 [4], and it can be seen that the production of tap and die tools was the largest among special steel tool manufacturing. This is because these tools are frequently replaced due to breakage.

To produce a threaded hole, machining using a tapping tool is the most common method [5]. Tapping tools generally fall into two types: a cut tapping tool and a roll tapping tool, as shown in Table 1.1. Each cut tapping tool usually has three or four chip evacuation flutes. Cut tapping tools are classified according to the geometry of their flutes. Hand taps, which are used to cut brittle materials, have straight flutes. Spiral pointed taps, often called gun taps, have a negative rake angle. Because of this unique flute shape, spiral pointed taps are able to discharge chips from the bottom of the threaded hole. Therefore, chip clogging, an issue resulting in the breakage of taps, is largely mitigated with this type of tapping tool. However, the use of spiral pointed taps and hand taps is limited because these taps require a through or blind hole with sufficient chip room for the prepared hole [5]. On the other

hand, spiral taps, which have spiral flutes, can be applied to each type of hole (i.e., through holes and blind holes) because the chips are discharged upward to the top of the threaded hole. In contrast, roll taps machine threaded holes by plastic deformation; thus, roll taps avoid chip issues [6]. However, roll taps often cause large tapping torques and require a high degree of accuracy of the prepared hole.





In order to meet the need for a tapping process suitable for high machining efficiency, improvements in tapping tools are required to allow for their functioning at high cutting velocities and to extend tool service life. However, at high cutting velocities, conventional cut tapping tools cause a decrease in the chip discharge ability, which results in chip snarling [7, 8] and chip clogging [9, 10]. These chip discharge problems cause both damage to the workpiece materials and chip packing, resulting in tool breakage [11, 12], as shown in Fig. 1.2. Since snarled and clogging chips must be removed manually, machining efficiency is reduced. Thus, chip snarling must be prevented to increase cutting velocity as well as to extend tool service life.



Total production: 86.1 billion yen

Fig. 1.1 Production of tools in Japan in 2014 [4]

Table 1.1 Tapping tools

Kind of tapping tool		Use	Disadvantage
Cut tapping tool	Hand tap 	- High hardness material should be used.	- Sufficient chip room is required.
	Spiral pointed tap 	- Long chips are discharged. - Less chip trouble.	- Needs through hole. (not applicable to a blind hole)
Roll tapping tool	Spiral tap 	- Tapping process is possible in blind hole or through hole.	- Chip trouble often occurs.
		- No chip trouble.	- Needs high accuracy of prepared hole.

*These pictures were provided by MIYAGITANOI MFG. CO., LTD

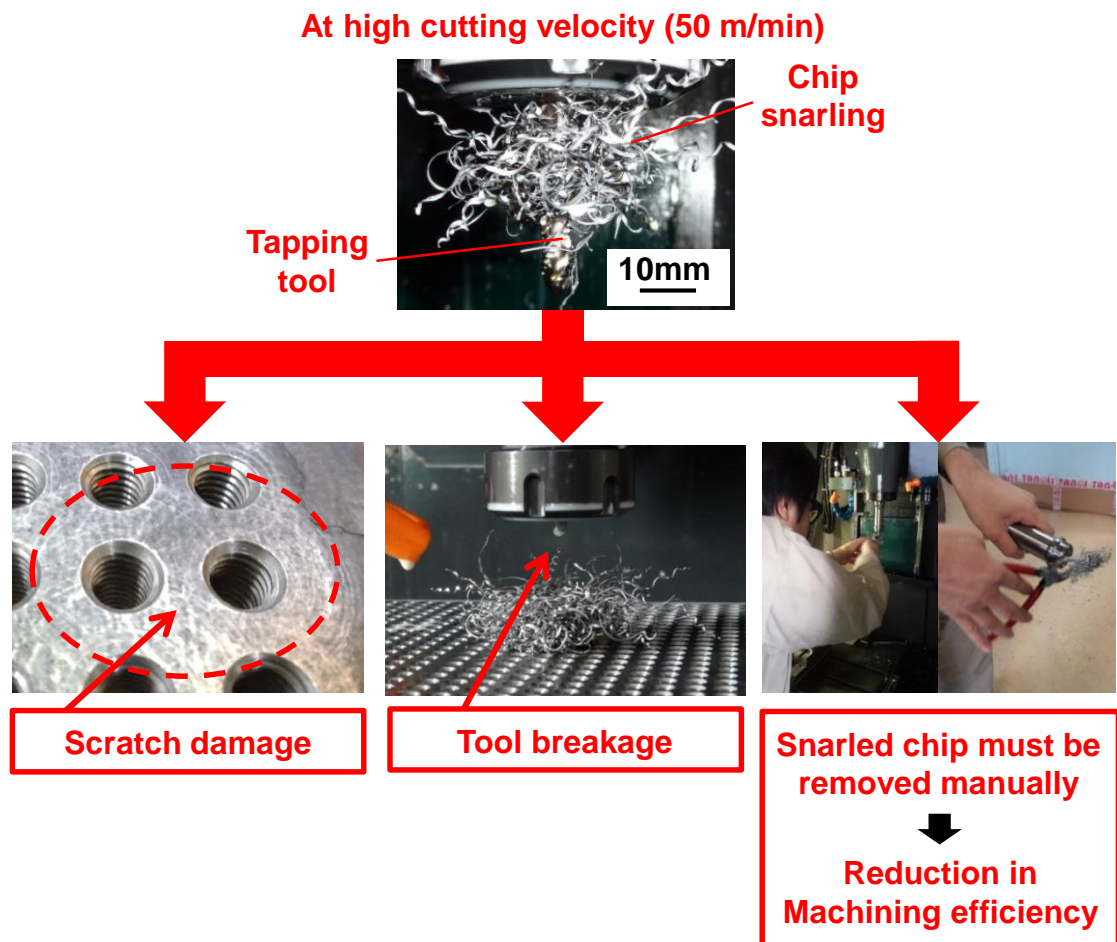


Fig. 1.2 Problems caused by chip snarling during the tapping process

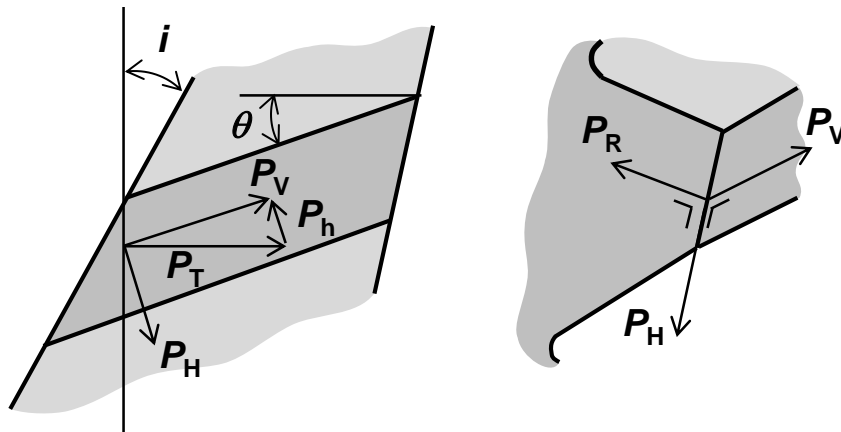
1.2 Previous studies

1.2.1 Tapping process

Many studies of tapping processes have been performed with the aim of improving thread quality and machining efficiency [13-27]. Previous studies on tapping processes are summarized in Table 1.2. In most of these studies, the thrust forces and cutting torques measured during the tapping process are used for analysis because a real cutting point is not accessible and direct observation is difficult. Thrust force is used to evaluate how much the tapping tool is fed into the workpiece [14, 15]. A high thrust force often causes an over-sized or defective thread shape. Cutting torque is the cutting moment in the radial direction. The torque during the tapping process is mainly used to estimate the cutting performance or tool wear [21-23, 26]. Yamaoka et al. [21] suggested that the cutting torque is suitable for abnormality detection during tapping because the change in cutting torque is larger than the thrust force when abnormalities such as chip packing occur during tapping. In fact, the amount of literature on cutting torque is greater than that on thrust force [21, 26]. Lorenz [28] investigated the effect of cutting condition and tool geometry on the cutting torque of hand taps. He showed that the cutting torque is significantly affected by the interaction between the cutting speed and the chamfer relief angle. An oblique cutting test is used to observe the cutting force components on the rake face of the tapping tool [29, 30]. Watanabe [29] conducted oblique cutting tests with a cutting tool and developed a model of the edge of the tapping tool. Then, the cutting forces on the rake face of the tapping tool were estimated, as shown in Fig. 1.3. This study attempted to produce a design guideline for tapping tools on the basis of the relation between chip geometry and the calculated cutting force components.

Table 1.2 Previous studies of tapping processes [13], [15], [17], [18], [26], [27]

Researchers, (year)	Tapping tool	Surface treatment	Workpiece material	Cutting velocity	Object	Reference number
Komura, A., Yamamoto, M. and Ikawa, N. (2001)	Hand tap (M42 X 4.5)	Without coating (High speed steel)	Carbon steel (JIS:S45C)	1.3 m/min	Thread quality	13
Doyle, D. E. and Dean, K. S. (1973)	Hand tap (M22 X 1.0)	Without coating (High speed steel)	Carbon steel (JIS:S20C)	5.4 m/min	Thrust force	15
Tanaka, R. et al. (2012)	Spiral tap (M10 X 1.5)	With TiN coating (High speed steel)	Carbon steel (JIS:S45C) Stainless steel (JIS:SUS303, SuS304)	20 m/min, 25 m/min, 30 m/min	Temperature at cutting edge	17
Lu, H., Zhang, D. and Liu, Y. (2011)	Hand tap (M3)	Without coating (High speed steel)	Metal matrix composites Al ₂ O ₃ /Al, SiC _p /Al	3.8 m/min~ 5.7 m/min	Vibration tapping	18
Gil Del Val, A. et al. (2013)	Hand tap (M10 X 1.5)	With TiN coating (High speed steel)	Nodular cast iron GGG50	65 m/min	Thread quality	26
Yamaoka, Y. et al. (2000)	Spiral tap (M3~M10)	Without coating (High speed steel)	Carbon steel (JIS:S45C), Cast iron (JIS: FC250), Aluminum alloy (JIS: A5052)	~ 43 m/min	Automation of tapping process	27



P_R, P_V, P_H : 3 components of cutting force
 i : Helix angle
 θ : Lead angle

Fig. 1.3 Three-dimensional cutting forces of a tapping tool [29]

Furthermore, some researchers have attempted to apply the cutting force model for other cutting processes, such as turning and drilling [31], to the tapping process [32, 33]. Armarego and Chen [32] numerically analyzed the relation between tapping tool geometry and cutting velocity in order to construct a predictive tapping model. With this predictive model, the cutting torque, thrust force, and unbalanced side force can be calculated for a tapping tool with a straight flute. In contrast, Kumabe and Daimon [34, 35] demonstrated that the specific cutting resistance values differ among each cutting edge of the tapping tool. As shown in Fig. 1.4, the specific cutting resistance values were markedly different for the different cutting edge positions.

As mentioned above, there have been many studies regarding tapping processes; however, chip snarling on the tapping tool has not been well investigated to date.

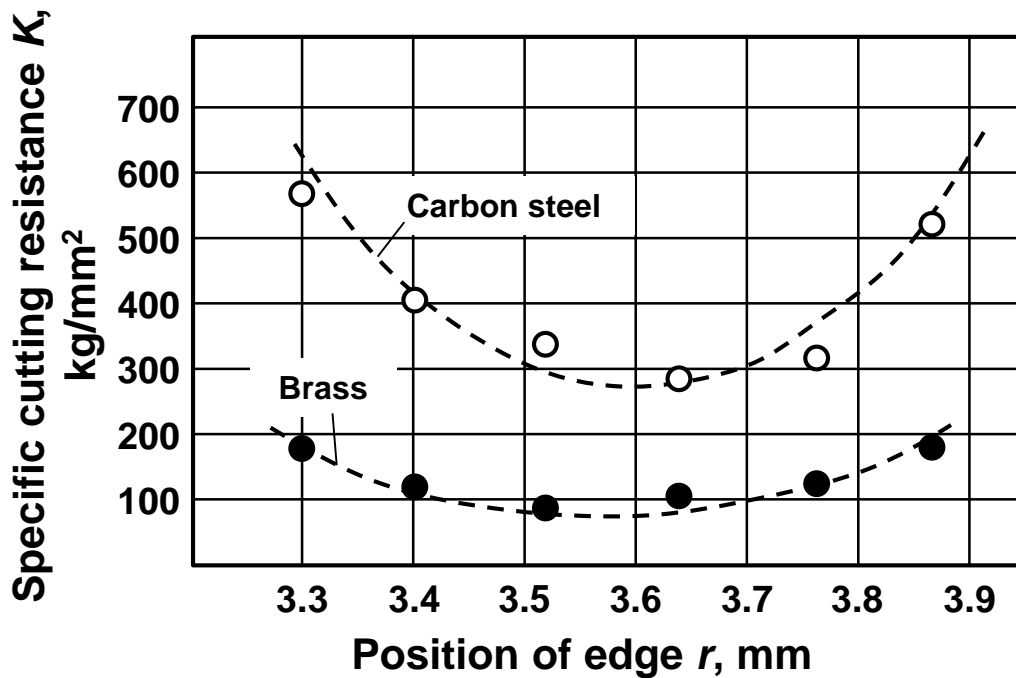


Fig. 1.4 Relation between cutting resistance and edge position of a tapping tool [34]

1.2.2 Chip discharge in turning and drilling processes

Chip discharge is an important factor in the tapping process and is related to chip clogging and chip snarling, which result in tool breakage. In a spiral tap, cutting chips are disposed at the top of the threaded hole via spiral flutes on the tapping tool. Therefore, the chip discharge property is affected by the relation between chip geometry and the flutes [5]. However, since the depth of the flutes on the tapping tool is designed to provide tool strength, controlling chip geometry is an important consideration in improving cutting chip disposability because it is difficult to enlarge flute size only for chip discharge.

Chip geometries are classified into several types based on the curl type formed during the cutting process, as shown in Fig. 1.5 [36]. During the tapping process, it is known that the up-curling tubular chip is mainly generated [37]. There is much research on chip deformation and chip geometry [38-55]. A cutting process removes extra portions of a workpiece using a cutting tool. During the removal process, the cutting chip is deformed by the force in the shear domain [38, 39, 44, 45] and the rake

face of the tool [40-43]. Generally, chip geometry, i.e., the diameter of the spiral shape, pitch, and inclining angle of the central axis, is uniquely determined by the combination of up-curl, side-curl, and chip flow direction, as shown in Fig. 1.6 [40, 46, 47].

Nakayama et al. [41] proposed two mechanisms for the generation of chip up-curl in metal cutting. One is deformation by the bending moment caused by a chip breaker or build-up-edge. The other is deformation by secondary flow, which corresponds to plastic deformation in the region of the chip adjacent to the tool surface. As a mechanism for the enhancement of up-curl, Takeshima et al. [44] proposed the expansion of the chip surface due to frictional heat. They carried out orthogonal cutting tests over a wide range of cutting velocity conditions and chip flow was observed. It was shown that up-curl diameter decreased with an increase in cutting velocity because the chip surface expands with frictional heat between the chip surface and tool rake face.

In addition, some literature has shown that chip up-curl is generated by the velocity gradient on the boundary-line of the shear domain [38, 39, 44, 45]. Okushima and Hitomi [45] investigated the shear domain distribution and velocity distribution in the domain and indicated that the end of the boundary-line of the shear domain was upward convex.

As listed above, there are many studies on the chip curl mechanism, such as in-situ observation of the chip-tool interface during orthogonal cutting or machining simulations [48-50]. However, it is impossible to dissociate these mechanisms in order to explain the chip curl because the chip curl is an instability phenomenon occurring at high temperature, high pressure, and a high strain rate [51, 52].

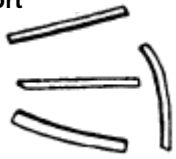
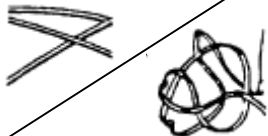



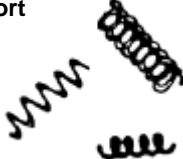


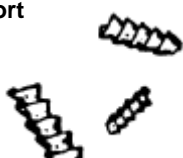


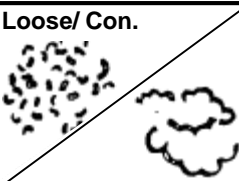

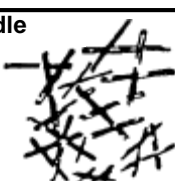
Curling	Nomenclature	Favorable	Unfavorable	
Straight	Ribbon Chips	Short 		Long/Snarled 
		Mainly Up-Curling	Tubular Chips Short 	Long 
	Spiral Chips		Flat/ Conical 	
Mainly Side-Curling	Washer type Chips	Short 	Long 	Snarled 
Up- and Side-Curling	Conical Helical Chips	Short 	Long 	Snarled 
	Arc Chips	Loose/ Con. 		
No Cutting	Natural Broken Chips	Elemental 		Needle 

Fig. 1.5 Classification of chip curl [36]

Chip discharge has been investigated in turning and drilling processes. [52]. In turning processes, cutting chips are easily observed because the periphery of the cylindrical workpiece is cut and the cutting chip is immediately evacuated outside the workpiece–tool interface. The effects of tool geometry and cutting conditions on chip curl phenomena have also been investigated [52-54]. Since

tool geometry and cutting conditions of the cutting tool are not strictly restricted in the turning process, chip discharge can be easily controlled by machining conditions such as feed rate, cutting velocity, and uncut chip thickness [52, 55, 56]. In drilling processes, the tool cuts inside the prepared hole and the remaining chips, which are not evacuated outside the hole, cause chip clogging and chip packing; however, it is difficult to directly observe whether a cutting chip is evacuated through the flute of the tool or remains inside the hole. Therefore, the chip flow direction at the edge of the drilling tool [57-63] and the binding force applied on the chip in the helical flute [64, 65] have been investigated. Hanasaki [65] observed chip deformation in a helical flute and revealed that a bending moment was applied to the chips at the machined hole surface. Furthermore, the control of chip geometry, rather than the control of flute geometry, edge geometry of the drilling tool, and cutting conditions (cutting velocity, lubrication, etc.) [66-68], was verified as effective in preventing chip issues (chip clogging, chip packing, etc.).

As mentioned above, much research on chip curl and chip evacuation during the turning and drilling processes has been conducted. However, there are few studies on chip curl and chip evacuation during tapping processes [21, 37, 69]; thus, it remains unclear how to prevent chip snarling on the tapping tool during tapping.

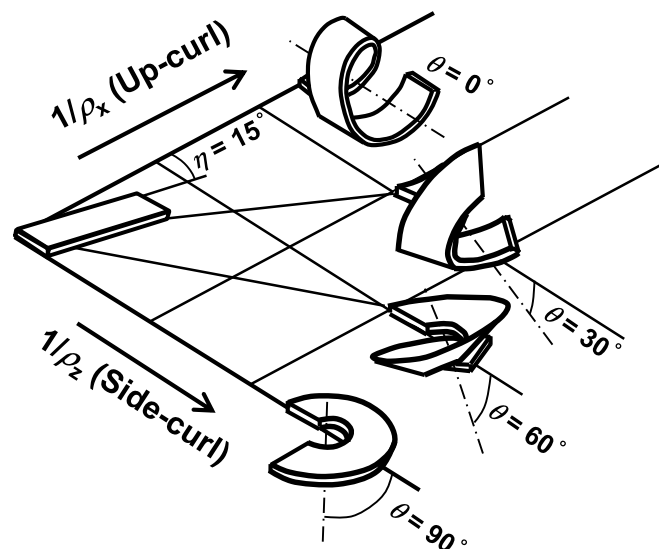


Fig. 1.6 Chip formation: up-curl, side-curl, and flow direction [41]

1.2.3 Surface treatment of the tapping tool

The demands of a cutting tool are to produce a superior cutting performance and provide a long service life. However, it is very difficult to simultaneously realize these demands because tool edge strength decreases as the tool edge is sharpened. One approach to solve this problem is a coating film for the cutting tool [70-74]. As shown in Fig. 1.7, several coating films have been developed since 1970. Each coating film provides excellent mechanical properties, such as low friction and high resistance to wear, adhesion, oxidation, and corrosion resistance, to the cutting tool [70, 75, 76]. Recently, the use of a combination of different layers, each with excellent mechanical properties, has been developed. As such, coating film technology has made remarkable advances and these films are essential for high-speed and high-efficiency machining.

Coating films are also used for tapping tools and there are many studies on hard coating and lubricant films (or their composite films) [77-83]. Reiter et al. [78] conducted tapping tests in austenitic stainless steel using a high-speed steel (HSS) tap coated with various hard coating films or lubricant films and investigated the wear resistance of the coating film and the cutting performance. In order to investigate the wear resistance, a ball-crater test was conducted. The abrasive wear rates for each coating film are shown in Fig. 1.8. TiCN, AlCrN (70/30), and diamond like carbon (DLC) films exhibited good wear resistance. The tapping test was conducted using a tapping tool coated with these films. The results showed that wear resistance and tool service life exhibit a positive correlation. This result indicates that a coating film with excellent wear resistance increases tool service life because damage to the tool edge is prevented. Furthermore, a combination film of a hard TiCN coating film base layer overlaid by a low-friction DLC layer was produced and a tapping tool coated with this film was developed. A coating film with excellent adhesion resistance has also been developed in order to conduct the tapping test on a workpiece; this film easily adheres to tool surfaces [81-83].

Recently, a dry tapping process has been investigated with the aim of preventing environmental pollution by lubricant oil. However, this approach has a disadvantage in that the cooling properties are

considerably poorer than those of the wet approach. In order to solve this problem, Bhowmick [82] investigated the tapping process of Al-Si alloys using a tapping tool coated with DLC film, which has excellent adhesion resistance. A dry tapping test was conducted and machining performance was investigated. Figure 1.9 shows the change in the cutting torque during the tapping process with respect to the number of tapping holes. The cutting resistance of the DLC coated tool was lower than that of the HSS tapping tool without coating under both dry and minimum quantity lubricant (MQL) conditions. This tapping test indicated that a tapping tool coated with a DLC coating film is effective in cutting a workpiece under dry conditions.

Jin et al. [83] developed a tapping tool coated with cubic boron nitride (cBN), which has good wear resistance. The tool was developed for cutting a beta-type titanium alloy, which is known as a hard-to-cut material. In order to investigate the adhesion resistance, a ball-on-disk friction test was conducted. Figure 1.10 shows the sliding time until adhesion occurred. This result indicates that the cBN coating film has a higher adhesion resistance than other coating films. As a result, the tool service life for the tapping tool coated with cBN coating film was three times that of a tapping tool with a conventional surface treatment.

Coating films contribute to the improvement of various cutting tool mechanical properties. However, chip clogging and chip snarling issues on the tapping tool [7] are inevitable for conventional coating films and surface treatments. Therefore, it is necessary to develop a new tapping tool coating film that will provide both a long service life of the tool and good chip discharge ability.

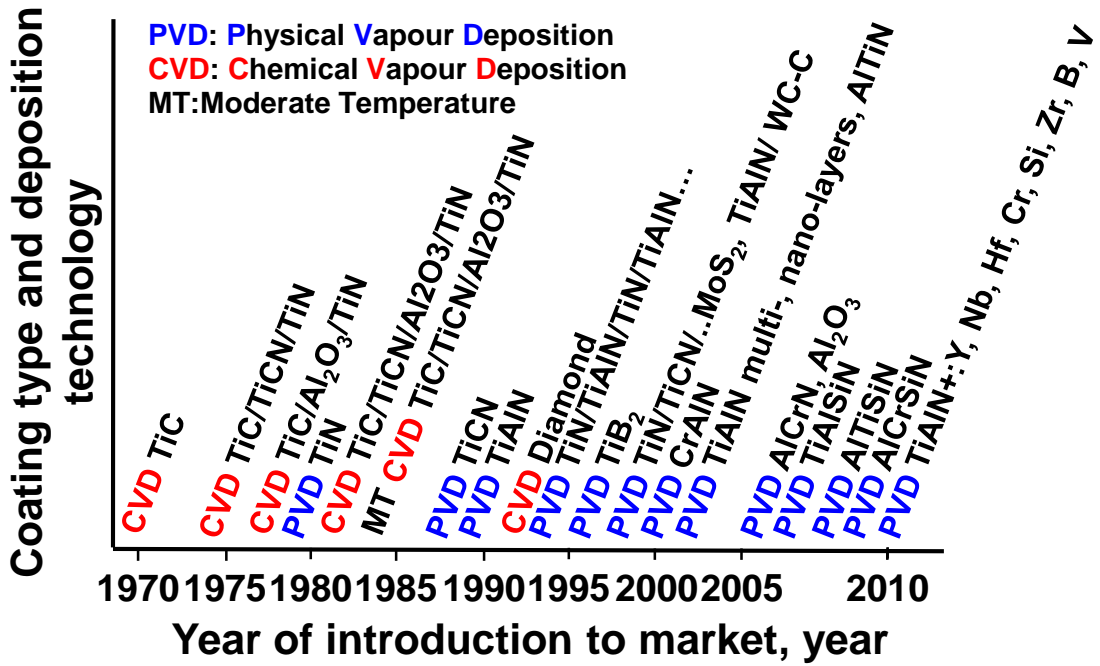


Fig. 1.7 History of coating films [70]

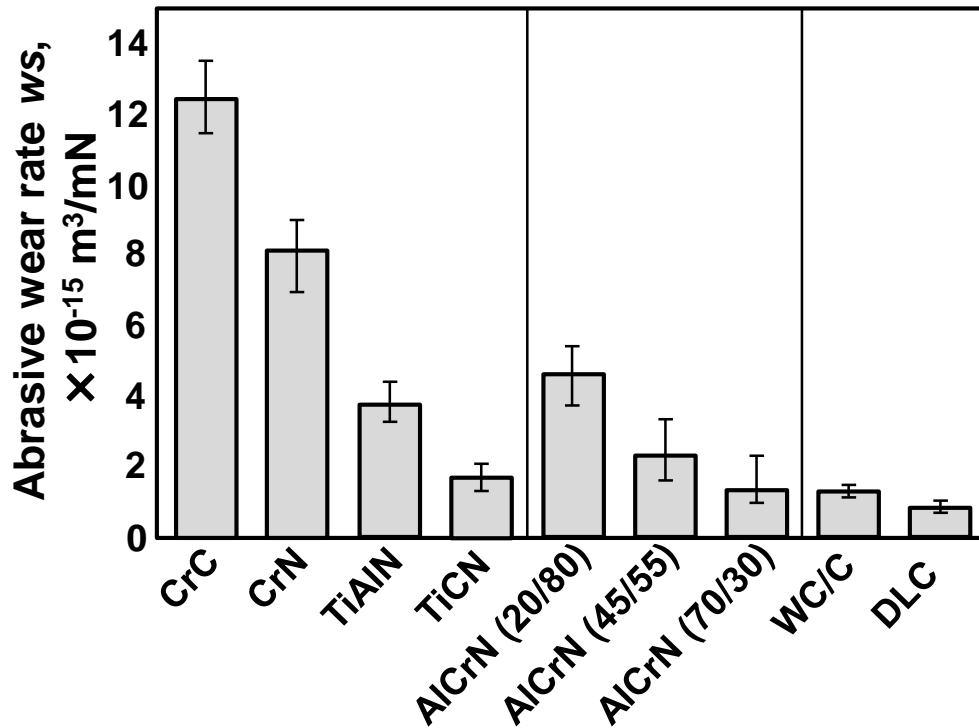


Fig. 1.8 Abrasive wear rate of the investigated coatings [81]

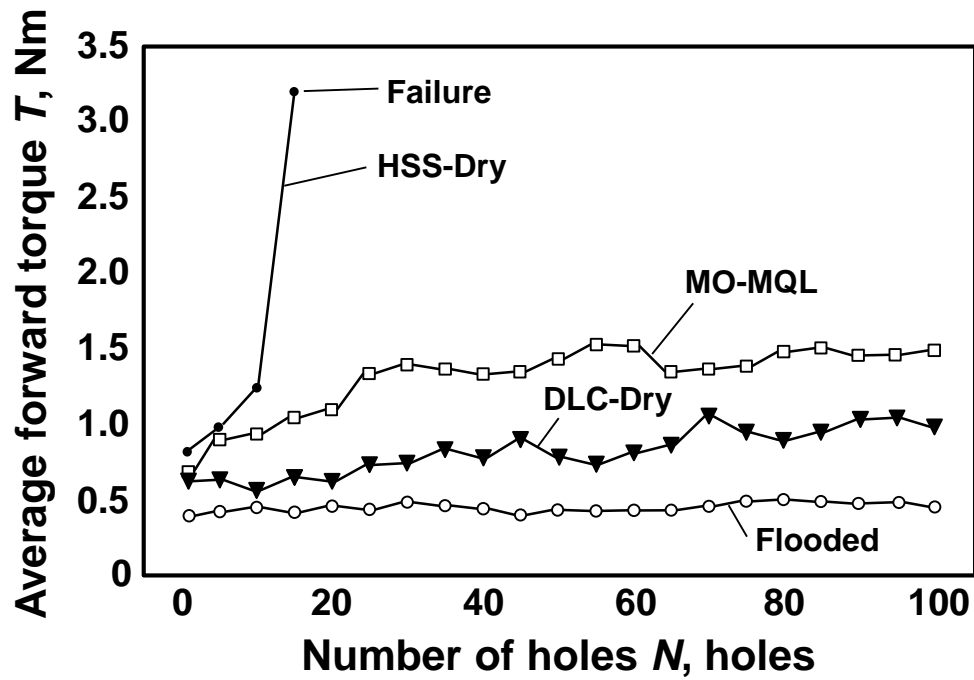


Fig. 1.9 Average forward torques for each tapping test [82]

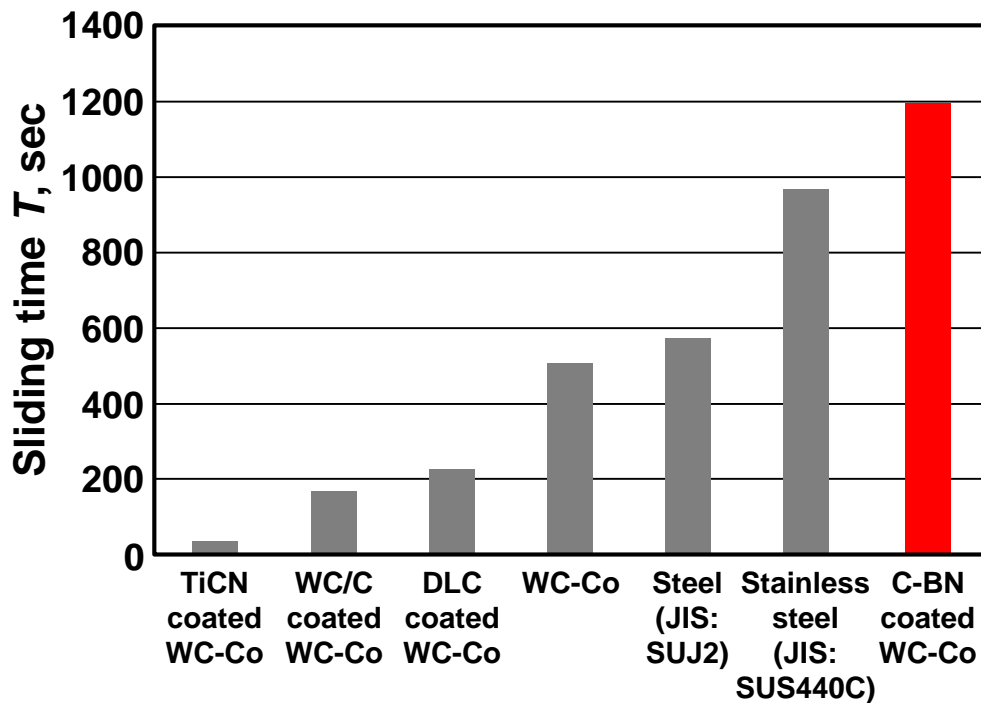


Fig. 1.10 Sliding times of test disk adherence to the ball surface [83]

1.2.4 Electrodeposited plating

A composite film of nickel-phosphorus (Ni-P)/abrasive particles is a plating film containing abrasive particles, such as diamond, cBN, or silicon carbide (SiC), which are deposited by electroplating methods or electroless plating methods [84]. In general, because a tool coated with a composite film can be reused after re-plating, the tool cost is low and the tool can be used for the precision grinding of brittle materials such as ceramic or glass [85-90]. Good mechanical properties such as wear resistance, corrosion resistance, and self-lubrication of the Ni-P/abrasive particle composite film can be obtained by changing the plating particle, particle size, or plating solution [84], [91-95]. Balaraju et al. [84] developed composite plating films with different particles and indicated that the structure of the base film material can be varied by co-depositing particles. For titanium carbide (TiC), silicon nitride (Si_3N_4), cerium oxide (CeO_2), and titanium oxide (TiO_2), structural change of the base material (i.e., Ni) was not observed. On the other hand, in the case of boron carbide (B_4C) particles, the orientation of the Ni structure was changed, and the structural stability of the composite film increased when using SiC particles. Furthermore, with heat treatment, the Ni-P phase of the Ni-P/SiC composite film changes from an amorphous to a crystalline structure, which significantly increases the hardness of the composite film (i.e., 1.6 times that of the composite film without heat treatment). In the case of a Ni-P/hard particle composite film, the hard particles plow the counterpart materials, resulting in a high degree of friction. In the case of a Ni-P/soft particle composite film, since the soft particles adhere to the counterpart material and the shear stress at the interface decreases, the friction coefficient decreases. The wear rate of electroless Ni-P/particle composite films versus carbon steel is shown in Fig. 1.11. This result indicates that the wear resistance of the Ni-P/hard particle composite film is almost equivalent to that of a hard chromium plating film.

In coming years, Ni-P/abrasive particle composite films are expected to be of use in the precision processing of metal materials [88, 89]. Ko et al. [90] developed a milling tool covered with diamond particles using electrodeposition, as shown in Fig. 1.12. They conducted a cutting test on zirconia

ceramics using this milling tool. The results indicated that the milling tool cut with a flow-type continuous chip shape. Furthermore, since the composite film had good wear resistance, wear of the tool edge was extremely low.

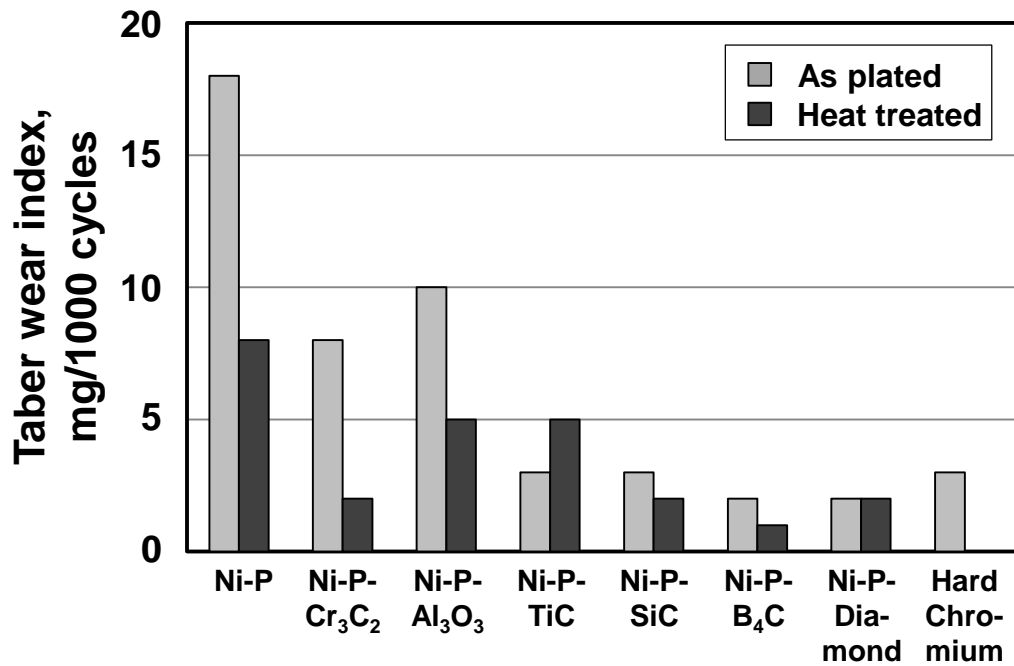
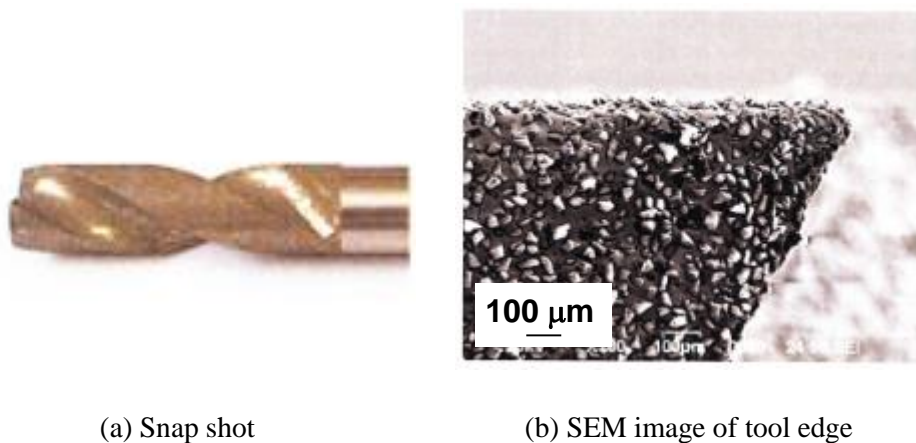


Fig. 1.11 Abrasive wear index of electroless Ni-P/particle composite films [84]



(a) Snap shot

(b) SEM image of tool edge

Fig. 1.12 Milling tool covered with diamond particles [90]

A chip trouble during tapping process was caused by a low friction at chip-tool such as hard coating [7]. However, in order to improve tool service life, the tool surface needs to be coated with a high wear resistance film. Therefore, a Ni-P/abrasive particle composite film was focused. The abrasive particles in the composite film should abrade the chip surface such that the abraded chips are easily broken. Thus, it is expected that the composite film prevents chip snarling on the tapping tool and extends tool service life at high cutting velocities.

1.3 Purpose of study

On the basis of the background mentioned above, the purpose of this thesis is to develop a tapping tool coated with a composite film composed of Ni-P/abrasive particles and investigate whether the tapping tool prevents chip snarling and increases tool service life even at high cutting velocity conditions.

1.4 Structure of thesis

The structure of the thesis is described as follows (Fig. 1.13):

Chapter 1 presents the introduction.

Chapter 2 describes the mechanical properties and tribological properties of Ni-P/abrasive particle composite films.

Chapter 3 describes the development of a tapping tool coated with the Ni-P/abrasive particle composite films and assesses cutting performance.

Chapter 4 describes the prevention of chip snarling and extension of tool service life for the developed tapping tool.

Chapter 5 describes the effect of friction coefficient at the sliding zone of chip-tool interface on chip curl diameter during the tapping process.

Chapter 6 describes the effect of workpiece materials on chip snarling for tapping tool coated with Ni-P/abrasive particle composite film.

Chapter 7 outlines the conclusions of this study.

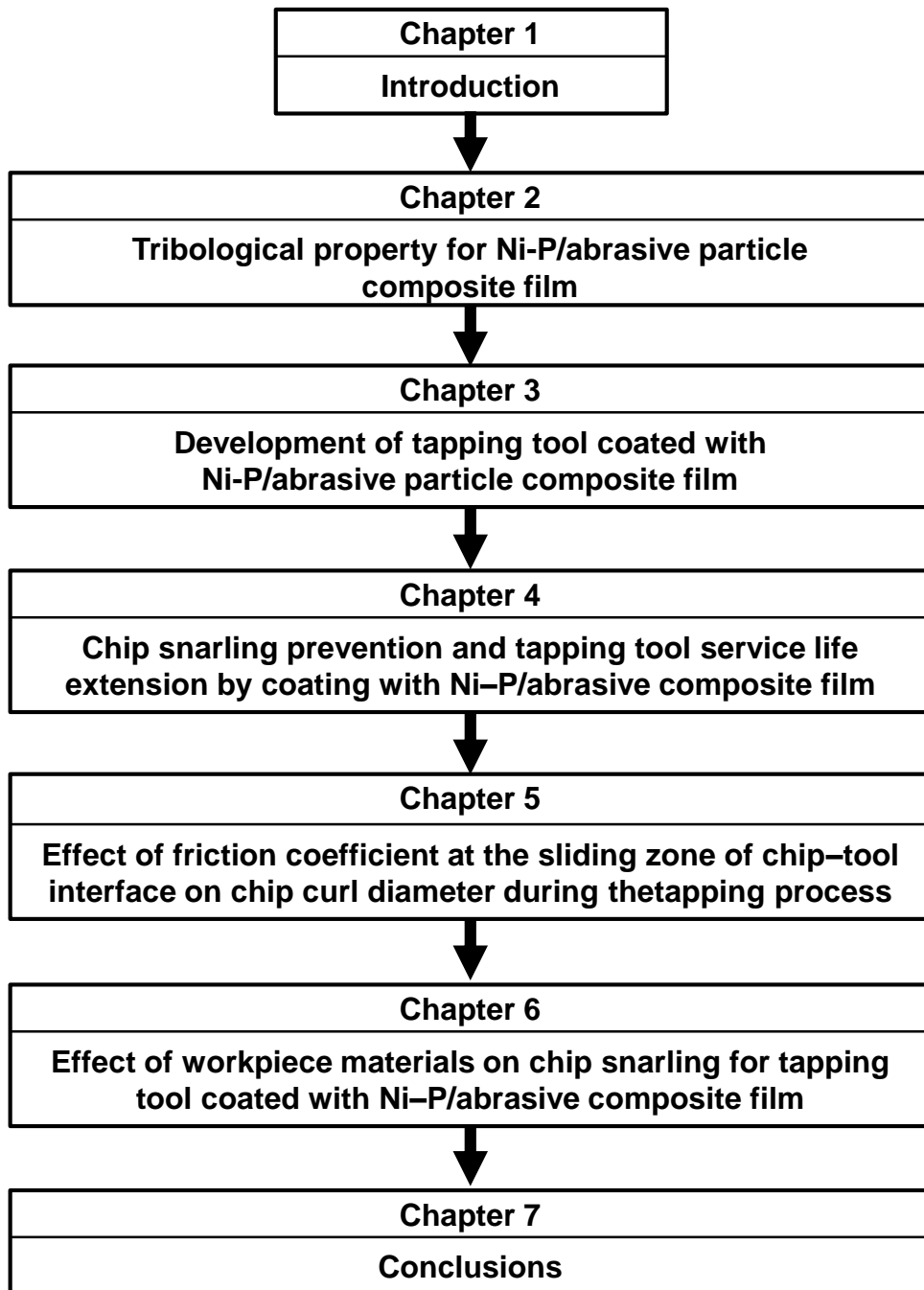


Fig. 1.13 Outline of this study

References

- [1] Kalpakjian, S. and Schmid, R. S., “Manufacturing Engineering and Technology, Seventh Edition,” Pearson, 2009, 16.
- [2] Ishimura, M., Yamanaka, H., Syoji, Y., Kobayashi, T. and Sawa, T., “Loosening of Bolted Joints Under Transverse Repeated Displacements,” The Japan Society of Mechanical Engineers, **77**, 781, 2011, 1444-1452 (in Japanese).
- [3] Sato, S., Tumura, T. and Otiai, K., “Studies on Loosing Mechanism of Bolt Nut Units (1st Report)–On the Friction Torque–,” The Japan Society for Precision Engineering, 44, 518, 1978, 161-166 (in Japanese).
- [4] The Japan Solid Cutting Tool’s Association, “Production transition table of special steel,” http://www.kouguko.com/pdf/new_seisansuii.pdf (accessed 2016-4-23) (in Japanese).
- [5] Kibbe, R. R., Neely, E. J., White, T. W. and Meyer, O. M., “Machine Tool Practices (9th Edition),” Prentice Hall, 2009, 67-71.
- [6] Li, Y. and Zhao, S., “The Key Technology in Extrusion Tapping of Internal Thread,” Advanced Materials Research, 295-297, 2011, 2636-2641.
- [7] Wood, S., “Tapping for Oil,” Cutting Tool Engineering, 62, 8, 2010, 52-57.
- [8] Cheng, K., “Machining Dynamics Fundamentals, Applications and Practices,” Springer Series in Advanced Manufacturing, 2009, 129-133.
- [9] Araujo, C. A., Silveira, L. J., Jun, G. B. M., Kapoor, G. S. and DeVor, R., “A Model for Thread Milling Cutting Forces,” International Journal of Machine Tools and Manufacture, 46, 2006, 2057-2065.
- [10] Cao, T. and Sutherland, W. J., “Investigation of Thread Tapping Load Characteristics Through Mechanistic Modeling and Experimentation,” International Journal of Machine Tools and Manufacture, 42, 14, 2002, 1527-1538.

- [11] Troubleshooting application problems with new taps,
<http://www.guhring.com/documents/Tech/Troubleshoot/Tap.pdf> (accessed 2016-4-23).
- [12] Mezentsev, A. O., Zhu, R., DeVor, E. R., Kapoor G. S. and Kline, A. W., “Use of Radial Forces for Fault Detection in Tapping,” *International Journal of Machine Tools and Manufacture*, 42, 4, 2002, 479-488.
- [13] Komura, A., Yamamoto, M. and Ikawa, N., “Study of a Tapping Method for Large Size Threads (3rd Report)—Consideration for Roughness of Thread Surface by Tapping—,” *The Japan Society for Precision Engineering*, 57, 11, 1991, 2001-2006 (in Japanese).
- [14] Johnson, E., “Some Experiments on Tapping,” *Proceeding of the Institution of Mechanical Engineers*, 164, 1, 1951, 46-51.
- [15] Doyle, D. E. and Dean, K. S., “Effect of Axial Forces on Dimensional Accuracy During Tapping,” *International Journal of Machine Tool Design and Research*, 14, 1974, 325-333.
- [16] Dov, A., “As the Tap Turns,” *Cutting Tool Engineering*, 62, 12, 2010, 38-42.
- [17] Tanaka, R., Yamazaki, S., Hosokawa, A., Furumoto, T., Ueda, T. and Okada, M., “Analysis of Cutting Behavior during Tapping and Measurement of Tool Edge Temperature Measured by a Two-Color Pyrometer,” *Journal of Advanced Mechanical Design, Systems, and Manufacturing*, 7, 2, 2013, 115-123.
- [18] Lu, H., Zhang, D. and Liu, Y., “Research on the Vibration Tapping Performance of Particle Reinforced Aluminum Matrix Composites,” *Advanced Materials Research*, 189-193, 2011, 3198-3207.
- [19] Zhang, D. and Chen, D., “Relief-Face Friction in Vibration Tapping,” *International Journal of Mechanical Sciences*, 40, 12, 1998, 1209-1222.
- [20] Uzun, G. and Korkut, İ., “The Effect of Cryogenic Treatment on Tapping,” *The International Journal of Advanced Manufacturing Technology*, 67, 1, 2013, 857-864.
- [21] Yamaoka, Y., Kakino, Y., Suzuki, Y., Nagae, A. and Muraki, T., “High Speed, High Productive

- Tapping by Intelligent Machine Tools (1st report)—Automatic Detection of Tool Failure and Chip Jamming—,” The Japan Society for Precision Engineering, 66, 12, 2000, 1922-1926 (in Japanese).
- [22] Yamaoka, Y., Kakino, Y., Sato, T. and Suzuki, Y., “High Speed, High Productive Tapping by Intelligent Machine Tools (2nd report)—Prevention of Tap Tool breakage and Improvement of Productivity by Adaptive Control—,” The Japan Society for Precision Engineering, 67, 8, 2001, 1338-1342 (in Japanese).
- [23] Yamaoka, Y., Kakino, Y. and Sato, T., “High Speed, High Productive Tapping by Intelligent Machine Tools (3rd report)—Prevention of Tap Breakage and Monitoring of Tool Failure for Difficult-to-Machine Materials by Real-Time Adaptive Control—,” The Japan Society for Precision Engineering, 68, 9, 2002, 1226-1230 (in Japanese).
- [24] Cao, T., Batzer, A. S. and Sutherland, A. J., “Experimental Investigation of Tapped Thread Surface Roughness for Cast Aluminum Alloys,” *Manufacturing Science and Technology*, 1, 1997, 189-195.
- [25] Mezentsev, A. O., DeVor E. R. and Kapoor, G. S., “Prediction of Thread Quality by Detection and Estimation of Tapping Faults,” *Journal of Manufacturing Science and Engineering*, 124, 3, 2002, 643-650.
- [26] Val Del Gil. A., Fernandez, J., del Castillo, E., Arizmendi, M. and Veige, F., “Monitoring of Thread Quality When Tapping Nodular Cast Iron with TiN-Coated HSS Cutting Taps,” *The International Journal of Advanced Manufacturing Technology*, 69, 2013, 1273-1282.
- [27] Patel, J. H., Patel, P. M. and Patel, M. S., “A Review on Thread Tapping Operation and Parametric Study,” *International Journal of Engineering Research and Applications*, 2, 3, 2012, 109-113.
- [28] Lorenz, G., “On Tapping Torque and Tap Geometry,” *Annals of the CIRP*, 29, 1, 1980, 1-4.
- [29] Watanabe, Z., “Research on the Spiral Fluted Tap by Three Dimensional Turning,” *Transactions of the Japan Society of Mechanical Engineering*, 118, 22, 1956, 378-383 (in Japanese).

- [30] Komura, A., Yamamoto, M. and Okusima, K., “Study of a Tapping Method for Large Size Threads (1st report)–Consideration for the Initial Thrust Force and Tapping–,” The Japan Society for Precision Engineering, 55, 7, 1989, 1313-1318 (in Japanese).
- [31] Kaymakci, M., Kilic, M. Z. and Altintas, Y., “Unified cutting force model for turning, boring, drilling and milling operations,” International Journal of Machine Tools and Manufacture, 54-55, 2012, 34-45.
- [32] Armarego, A. J. E. and Chen, P. N. M., “Predictive Cutting Models for the Forces and Torque in Machine Tapping with Straight Flute Taps,” CIRP Annals–Manufacturing Technology, 51, 1, 2002, 75-78.
- [33] Dogra, S. P. A., Kapoor, G. S. and Devor, E. R., “Mechanistic Model for Tapping Process with Emphasis on Process Faults and Hole Geometry,” 124, 2002, 18-25.
- [34] Kumabe, J. and Daimon, M., “Study on Tapping Torque (1st Report),” The Japan Society for Precision Engineering, 35, 7, 1969, 464-470 (in Japanese).
- [35] Kumabe, J. and Daimon, M., “Study on Tapping Torque (2nd Report),” The Japan Society for Precision Engineering, 35, 9, 1969, 464-470 (in Japanese).
- [36] Show, C. M., “Metal Cutting Principles,” Oxford Series on Advanced Manufacturing, 2005, 495.
- [37] Chen, M., Liu, G. and Zhang, X., “Optimization studies on Hole-Making Tools for High-Performance Cutting Austenitic Stainless Steel,” Machining Science and Technology, 11, 2, 2007, 183-200.
- [38] Piispanen, V., “Theory of Formation of Metal Chips,” Journal of Applied Physics, 19, 876, 1948, 876-881.
- [39] Merchant, E. M., “Mechanics of the Metal cutting Process. II. Plasticity Conditions in Orthogonal Cutting,” Journal of Applied Physics, 16, 318, 1945, 318-324.
- [40] Nakayama, K., “Chip Form Geometry–Study on the Form of Chip in Metal Cutting (Part 1)–,” The Japan Society for Precision Engineering, 38, 450, 1972, 592-598 (in Japanese).

- [41] Nakayama, K., Uenoyama, M. and Tamura, K., “Chip Curl in Metal Cutting,” The Japan Society for Precision Engineering, 27, 321, 1961, 681-688 (in Japanese).
- [42] Nakayama, K., “A Study on Chip-Breaker,” Bulletin of JSME, 27, 178, 1961, 833-843 (in Japanese).
- [43] Zhang, Z. Y., “Chip Curl, Chip Breaking and Chip Control of the Difficult-to-Cut Materials,” CIRP Annals–Manufacturing Technology, 29, 1980, 79-83.
- [44] Takeshima, T., Morita, N., Yamada, S., Takano, N. and Oyama, T., “The Study of the Cutting Phenomenon by Visualization of Orthogonal Cutting Behavior,” Journal of the Japan Society for Abrasive Technology, 49, 1, 2005, 24-29 (in Japanese).
- [45] Okushima, K. and Hitomi, K., “The Mechanism of Chip Curl in Orthogonal Cutting,” The Japan Society for Precision Engineering, 25, 293, 1959, 320-327 (in Japanese).
- [46] Masuda, M., Chujo, Y., Hara, T. and Qiao, S. H., “Studies on the Chip Control in Metal Cutting (2nd Report)–Estimation of the Chip Curl Based on the Side Flow–,” The Japan Society for Precision Engineering, 53, 4, 1987, 558-564 (in Japanese).
- [47] Arai, M., “Study on Chip Control in Metal Cutting–On the Sideward Curl of Chip–,” The Japan Society for Precision Engineering, 67, 7, 2001, 1164-1168 (in Japanese).
- [48] Sutter, G., “Chip Geometries During High-Speed Machining for Orthogonal Cutting Conditions,” Machine Tools and Manufacture, 45, 2005, 719-726.
- [49] Sutter, G. and Ranc, N., “Temperature Fields in a Chip During High-Speed Orthogonal Cutting–An Experimental Investigation,” International Journal of Machine Tools and Manufacture, 47, 10, 2007, 1507-1517.
- [50] List, G., Sutter, G. and Bouthiche, A., “Cutting Temperature Prediction in High Speed Machining by Numerical Modeling of Chip Formation and its Dependence with Crater Wear,” International Journal of Machine Tools and Manufacture, 54-55, 2012, 1-9.
- [51] Nasu, Y., “Study on the Phenomenon of Instability in Metal Cutting (1st Report)–On the

- Possibility and the Types of Chip,” The Japan Society for Precision Engineering, 35, 2, 1969, 116-121 (in Japanese).
- [52] Jawahir, S. I. and van Luttervelt, A. C., “Recent Developments in Chip Control Research and Applications,” CIRP Annals Manufacturing Technology, 42, 2, 1993, 659-693.
- [53] Okushima, K. and Minato, K., “On the Behavior of Chip at Steel Cutting,” Journal of Japan Society of Mechanical Engineers, 25, 158, 1959, 333-339 (in Japanese).
- [54] Schulz, H., Abele, E. and Sahm, A., “Material Aspects of Chip Formation in HSC Machining,” CIRP Annals-Manufacturing Technology, 50, 1, 2001, 45-48.
- [55] Kim, D. J. and Kweun, B. O., “A Chip-Breaking System for Mild Steel in Turning,” International Journal of Machine Tools and Manufacture, 37, 5, 1997, 607-617.
- [56] Bhuiyan, H. S. M., Choudhury, A. I. and Nukman, Y., “An Innovative Approach to Monitor the Chip Formation Effect on Tool State Using Acoustic Emission in Turning,” International journal of Machine Tools and Manufacture, 58, 2012, 19-28.
- [57] Dasch, M. J., Ang, C. C., Wong, A. C., Cheng, T. Y., Weiner, M. A., Lev, C. L. and Konca, E., “A Comparison of Five Categories of Carbon-Based Tool Coatings for Dry Drilling of Aluminum,” Surface and Coating Technology, 200, 9, 2006, 2970-2977.
- [58] Mellinger, C. J., Ozdoganlar, B. O., DeVor, E. R. and Kapoor, G. S., “Modeling Chip-Evacuation Forces and Prediction of Chip-Clogging in Drilling,” Journal of Manufacturing Science and Engineering, 124, 3, 2002, 605-614.
- [59] Kasahara, K. and Hirota, A., “Drilling with Flat Rake Face Drills and Analysis of Long-Pitch Helical Chip Formation Process,” Journal of Japan Society of Mechanical Engineers, 56, 6, 1990, 1075-1081 (in Japanese).
- [60] Ke, F., Ni, J. and Stephenson, A. D., “Continuous Chip Formation in Drilling,” International Journal of Machine Tools and Manufacture, 45, 2005, 1652-1658.
- [61] Hirota, A. and Kasahara, K., “Analytical Prediction of Chip Formation and Cutting Forces in

- Drilling Operation (1st Report)–Cutting Model, Energy Method and Preliminary Results–,” The Japan Society for Precision Engineering, 47, 8, 1981, 987-993 (in Japanese).
- [62] Wang, Y., Yan, X., Li, B. and Tu, G., “The Study on the Chip Formation and Wear Behavior for Drilling Forged Steel S48CS1V with TiALN-Coated Gun Drill,” International Journal of Refractory Metals and Hard Materials, 30, 1, 2012, 200-207.
- [63] Kubota, H. and Tabei, H., “Drilling of a Small and Deep Hole Using a Twist Drill,” Transactions of the JSME, 62, 601, 1996, 3691-3697 (in Japanese).
- [64] Hanasaki, S., Hosoi, R., Hosoi, T., Nagamachi, T. and Hasegawa, Y., “Chip Exhaust Mechanism of Twist Drill Drillable Deep Hole Under Continuously High Feed Rate,” Transactions of the JSME, 65, 631, 1999, 1229-1234 (in Japanese).
- [65] Hanasaki, S., Hosoi, R., Hosoi, T. and Nishimura, S., “Twist Drill Drillable Deep Hole Under Continuous High Feed Rate (Mechanism of Particular Type Chip Formation of 0-Degree Rake Angle Twist Drill),” Transactions of the JSME, 70, 692, 2004, 1229-1234 (in Japanese).
- [66] Ogawa, M. and Nayama, K., “Effects of Chip Splitting Nicks in Drilling,” Annals of the CIRP, 34, 1985, 101-104.
- [67] Zabel, A. and Heilmann, M., “Deep Hole Drilling Using Tools with Small Diameters–Process Analysis and Process Design,” CIRP Annals-Manufacturing Technology, 61, 2012, 111-114.
- [68] Sakurai, K., Adachi, K. and Hanasaki, S., “Breaking Mechanism of Chips in Intermittently Decelerated Feed Drilling of Aluminum Alloys,” Journal of Japan Institute of Light Metals, 48, 4, 1998, 195-198 (in Japanese).
- [69] Yamauchi, M., Horiuchi, O., Murakami, Y., Sugano, H. and Shibutani, H., “Development of a Chip-Breaking Tool for Tapping (1st Report)–Prototype of the Tool and its Effectiveness–,” The Japan Society for Precision Engineering, 70, 12, 2004, 1565-1569 (in Japanese).
- [70] Bouzakis, D. K., Michailidis, N., Skordaris, G., Bouzakis, E., Biermann, D. and M’Saoubi, R., “Cutting with Coated Tools: Coating technologies, Characterization Methods and Performance

- Optimization,” *CIRP Annals–Manufacturing Technology*, 61, 2, 2012, 703-723.
- [71] Setoyama, M., Fukui, H. and Moriguchi, H., “Recent PVD Coating Films for Cutting Tool,” *Journal of High Temperature Society*, 33, 2, 2007, 90-94 (in Japanese).
- [72] Buhl, R., Pulker, K. H. and Moll, E., “TiN Coating on Steel,” *Thin Solid Films*, 80, 1981, 265-270.
- [73] Okada, M., Hosokawa, A., Tanaka, R. and Ueda, T., “Cutting Characteristics of Coated Carbide Tools in Hardmilling–Influence of Coating Film and Base Material of Coated Carbide Tool–,” *The Japan Society for Precision Engineering*, 75, 8, 2009, 979-983 (in Japanese).
- [74] Yang, L., Okazaki, S., Hashimoto, M. and Yamamoto, Y., “Influence of Atmosphere and Combination of Materials on Friction and Wear Characteristics of SiC, TiN and TiC,” *Transactions of the JSME*, 627, 64, 1998, 300-307 (in Japanese).
- [75] Byrne, G., Dornfeld D. and Denkena, B., “Advancing Cutting Technology,” *CIRP Annals Manufacturing Technology*, 52, 2, 2003, 483-507.
- [76] Podgornik, B., Hogmark, S. and Sandberg, O., “Influence of Surface Roughness and Coating Type on the Galling Properties of Coated Forming Tool Steel,” *Surface and Coating Technology*, 184, 2004, 338-348.
- [77] da Mota, R. P., Reis, M. A., da Silva, B. M. and Goncalves, A. R., “Tapping Operation at High Cutting Speed,” *International Congress of Mechanical Engineering*, 1, 2005, 1-6.
- [78] Reiter, E. A., Brunner, B., Ante, M. and Rechberger, J., “Investigation of Several PVD Coatings for Blind Hole Tapping in Austenitic Stainless Steel,” *Surface and Coating Technology*, 200, 2006, 5532-5541.
- [79] Derflinger, V., Brändle, H. and Zimmermann, H., “New Hard/Lubricant Coating for Dry Machining,” *Surface and Coating Technology*, 113, 1999, 286-292.
- [80] Henderer, W. and Xu, F., “Hybrid TiSiN, CrC/C PVD Coatings Applied to Cutting Tools,” *Surface and Coatings Technology*, 215, 2013, 381-385.

- [81] Steininger, A., Siller, A. and Bleicher, F., "Investigations Regarding Process Stability Aspects in Thread Tapping Al-Si Alloys," 25th DAAAM International Symposium on Intelligent Manufacturing and Automation, DAAAM 2014, 100, 2015, 1124-1132.
- [82] Bhowmick, S., Lukitsch, J. M. and Alpas, T. A., "Tapping of Al-Si Alloys with Diamond-Like Carbon Coated Tools and Minimum Quantity Lubrication," *Journal of Materials Processing Technology*, 210, 2010, 2142-2153.
- [83] Jin, M., Watanabe, S., Miyake S. and Murakawa, M., "Trial Fabrication and Cutting Performance of c-BN-Coated Taps," *Surface and Coating Technology*, 133-134, 2000, 443-447.
- [84] Balaraju, N. J., Narayanan, S. N. S. T. and Seshadri, K. S., "Electroless Ni-P Composite Coatings," *Journal of applied Electrochemistry*, 33, 2003, 807-816.
- [85] Brinksmeier, E., Riemer, O. and Twardy, S., "Tribological Behavior of Micro Structured Surfaces for Micro Forming Tools," *International Journal of Machine Tools and Manufacture*, 50, 2010, 425-430.
- [86] Park, K. H., Onikura, H., Ohnishi, O. and Sharifuddin, A., "Development of Micro-Diamond Tools Through Electroless Composite Plating and Investigation into Micro-Machining Characteristics," *Precision Engineering*, 34, 2010, 376-386.
- [87] Horne, F. D. and Loh, E., "Milling Optical glass with Electroplated Diamond Tools," *International Journal of Optics*, 23, 9, 1976, 709-722.
- [88] Mizobuchi, A., Ogawa, H. and Sasaoka, T., "Grinding Force and Crack size on Through-Hole Drilling of Glass Plate Used Electroplated Diamond Tool in Helical Drilling," *Journal of the Japan Society for Abrasive Technology*, 54, 12, 2010, 731-736 (in Japanese).
- [89] Hara, K., Isobe, H., Yoshihara, H., Kyusojin, A. and Yanagi, K., "Ultrasonically Assisted Machining for Mirror Finishing of Die (1st report)–Face Grinding of Die Steel Using Electroplated Diamond tool–," *The Japan Society for Precision Engineering*, 72, 9, 2006, 1134-1138 (in Japanese).

- [90] Ko, J. T. and Yoon, J. I., "Mill-Grinding with Electroplated Diamond Abrasive for Ceramic Cutting," *International Journal of Precision Engineering and Manufacturing*, 13, 1, 2012, 5-10.
- [91] Gyftou, P., Stroumbouli, M., Pavlatou, A. E., Asimidis, P. and Spyrellis, N., "Tribological Study of Ni Matrix Composite Coatings Containing Nano and Micro SiC Particles," *Electrochimica Acta*, 50, 2005, 4544-4550.
- [92] Bozzini, B., Martini, C., Cavallotti, L. P. and Lanzoni, E., "Relationships Among Crystallographic Structure, Mechanical Properties and Tribological Behavior of Electroless Ni-P (9%)/B4C Films," *Wear*, 225-229, 1999, 806-813.
- [93] Straffelini, G., Colombo, D. and Molinari, A., "Surface durability of electroless Ni-P composite deposits," *Wear*, 236, 1999, 179-188.
- [94] Hojo, J., Takamatsu, A. and Kato, A., "Influence of Size and Dispersion of SiC Particles in the Preparation of Ni-P-SiC Composite Plating," *Journal of the Ceramic Society of Japan*, 98, 1990, 22-28 (in Japanese).
- [95] Furukawa, N., "Properties of Dispersion Coatings," *Jitsumu hyoumen gijutsu*, 33, 1, 1986, 16-19 (in Japanese).

Chapter 2

Tribological properties of Ni–P/abrasive particle composite film

2.1 Introduction

To improve the service life of tapping tools, hard coating films and lubricant films, which have excellent wear resistance and lubricity, are often used on the cutting surface. However, coating a tapping tool with these films causes chip snarling and chip packing because the low friction that these coating films induce leads to a long chip being produced [1]. To address this problem, a coating film that has excellent wear resistance but does not cause chip snarling must be developed. In this study, the development of a nickel-phosphorus (Ni–P)/abrasive particle composite film, which is also known as an electroless plating film, was focused. This composite film generates high friction because of the increase in plowing friction caused by the abrasive particles [2-4]. In addition, its mechanical properties can be controlled by varying the particle size and type of the material used [2]. Therefore, using this composite film offers an approach for improving the service life of a tool while preventing chip snarling during tapping.

In this chapter, the formation of electroless composite films on a high-speed steel (HSS) plate using cubic boron nitride (cBN) and silicon carbide (SiC) as the abrasive particles is reported. The hardness and adhesion strength of the composites and the friction coefficient under lubrication by emulsion cutting oil are investigated.

2.2 Preparation of an electroless plating composite film

There are two types of plating: electro plating and electroless plating. In the electro plating process, a metal film is formed by passing a positively charged electrical current through a solution containing metal ions dissolved from the anode and a negatively charged electrical current through the part to be plated (the cathode). In the electroless plating process, a metal film is formed on the substrate without using an external electrical charge. Electroless plating is particularly appropriate when working with nonconductive materials because no energization is needed [5]. Furthermore, electroless plating produces a completely uniform deposit even on workpieces with a complex shape. Therefore, in this study, electroless plating was used to apply the composite film to the tapping tool surface.

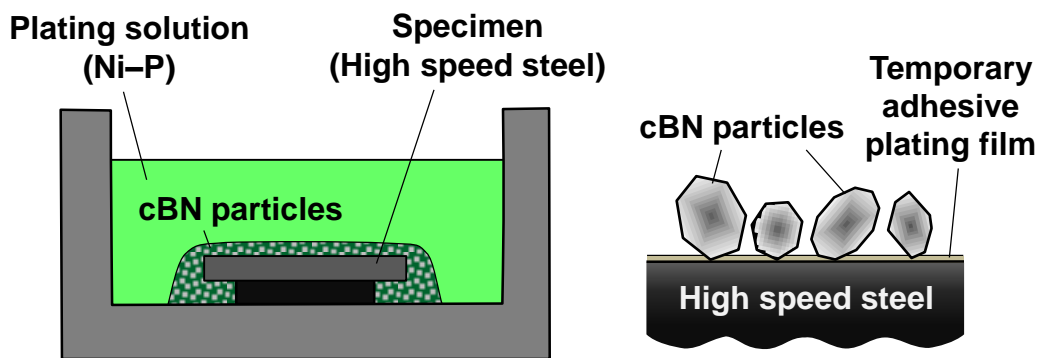
Table 2.1 shows the mechanical properties of the abrasives that are commonly used as codepositing particles in electroless plating [6-9]. As can be seen, diamond and cBN particles have the highest hardness and thermal conductivity. In particular, cBN particles exhibit high heat resistance, thermal conductivity, and chemical stability [6]. In this study, cBN was used for codepositing because diamond is incompatible with steel materials at high temperatures [10]. SiC particles exhibit superior characteristics than the particles of other materials such as Al_2O_3 and Si_3N_4 . The Ni-P/SiC particle composite film is also known to possess excellent mechanical properties [2]. Therefore, in this study, SiC particles were also used as codepositing particles.

Figures 2.1 and 2.2 show the schematics of the deposition processes for the Ni-P/cBN and Ni-P/SiC films, respectively. These composite films were deposited onto an HSS disk specimen with a Vickers hardness of 7.4 GPa, Young's modulus of 220 GPa, and surface roughness of approximately 0.1 μm . In the case of the Ni-P/cBN film, a two-step deposition process was employed. First, the HSS disk specimen was buried in cBN particles within the Ni-P plating solution, as shown in Fig 2.1 (a). In this process, the cBN particles adhered to the specimen surface, creating a Ni-P plating film with a thickness of 3–4 μm . Then, as shown in Fig. 2.1(b), the Ni-P plating film was grown until the film thickness was 60% of the mean diameter of the cBN particles. In the case of the Ni-P/SiC film, the

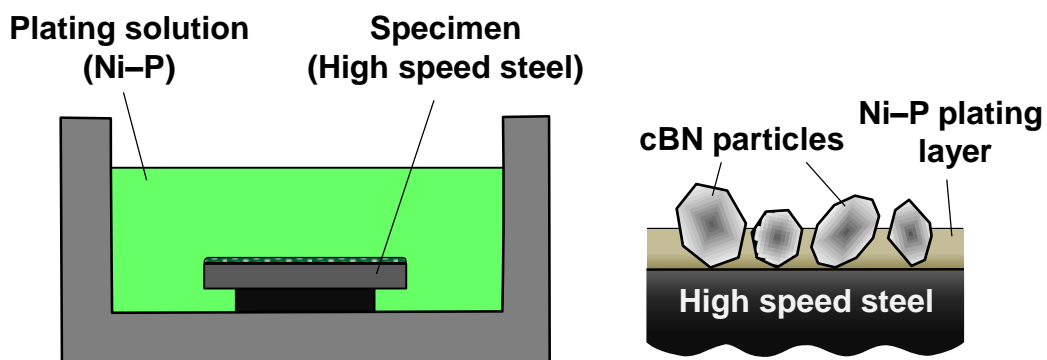
composite film was deposited onto the HSS disk in a Ni–P plating solution containing SiC particles, as shown in Fig. 2.2. The cBN particles had a mean diameter \bar{d} of 10 μm , whereas SiC particles of two different diameters, 5.0 μm and 1.0 μm , were used. After heat-treatment at 300 °C, the hardness of the Ni–P layer approximately doubled [2].

Table 2.1 Mechanical properties of abrasive particles [6-9]

	Vickers hardness H_v , GPa	Young's modulus E , GPa	Poisson's rate ν	Thermal conductivity λ , kw/m·K
Diamond	56-102	1050	0.04-0.11	0.17-0.19
cBN	35-40	587-680	0.15-0.22	0.044-0.1
SiC	29.4-34.3	43.9	0.18-0.19	0.006
Al₂O₃	25.5-26.7	50-59.3	0.21-0.27	0.013
Si₃N₄	8.0-19.0	14.5-47.1	0.24	0.033-0.034



(a) First step (cBN particles adhere to the substrate)



(b) Second step (growth of the Ni-P plating layer)

Fig. 2.1 Electroless plating process for the Ni-P/cBN particle composite film

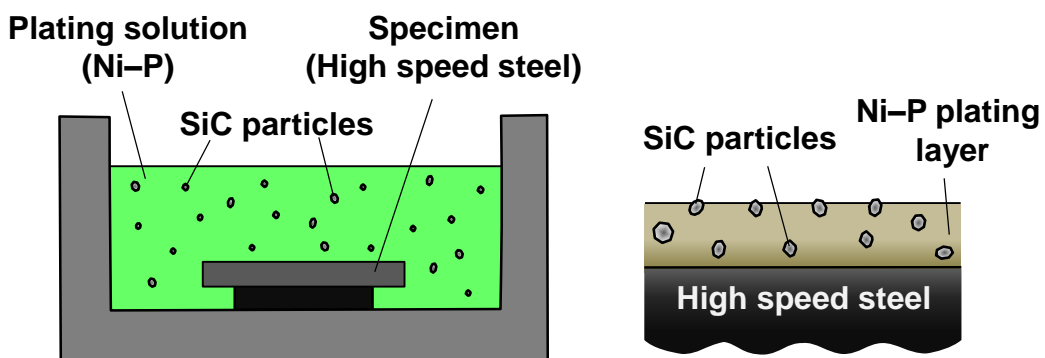


Fig. 2.2 Electroless plating process for the Ni-P/SiC particle composite film

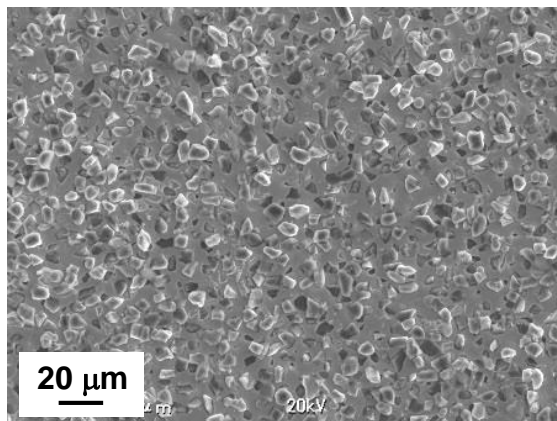
2.3 Experimental methods

2.3.1 Disk specimens

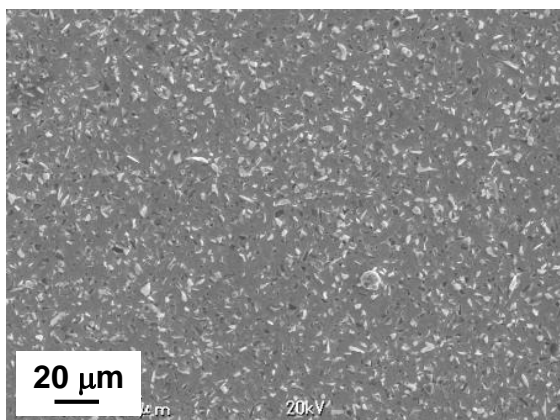
The test specimens were disks with a diameter of 42.5 mm and thickness of 5.4 mm. Steam treatment was used to create an iron oxide (Fe_3O_4) layer on the HSS disk surface [11]. Other specimens were coated with a titanium carbo-nitride (TiCN) film. Figure 2.3 shows the scanning electron microscope (SEM) images of each specimen's disk surface. The thickness of the Ni-P/cBN film ($\bar{d} = 10 \mu\text{m}$) was $20 \mu\text{m}$; moreover, the thickness of both the Ni-P/SiC film ($\bar{d} = 5 \mu\text{m}$) and the Ni-P/SiC film ($\bar{d} = 1 \mu\text{m}$) was $5 \mu\text{m}$ and that of the other specimens was approximately $1 \mu\text{m}$. In the composite films, the abrasive particles appeared on the surface of the plating layer. Conversely, several small pits were observed on the surfaces of the disk specimens that were steam-treated. The TiCN coating film had a smooth surface. Table 2.2 lists the surface roughnesses of the specimens. The surface roughness of the composite films was higher than that of the steam treated and TiCN coated specimens. The surface roughness of the composite films increased with the diameter of the codepositing particles. Figures 2.4-2.6 show the profile curve and protrusion height for each Ni-P/abrasive particle composite film. The protrusion height for the Ni-P/cBN film ($\bar{d} = 10 \mu\text{m}$), Ni-P/SiC film ($\bar{d} = 5 \mu\text{m}$), or Ni-P/SiC film ($\bar{d} = 1 \mu\text{m}$) was $3.9 \pm 0.7 \mu\text{m}$, $1.5 \pm 0.4 \mu\text{m}$, or $0.4 \pm 0.1 \mu\text{m}$, respectively. Thus, the ratio of protrusion height to the mean diameter of codepositing particle R_p was approximately 40 %.

Table 2.2 Average roughnesses of the disk specimens

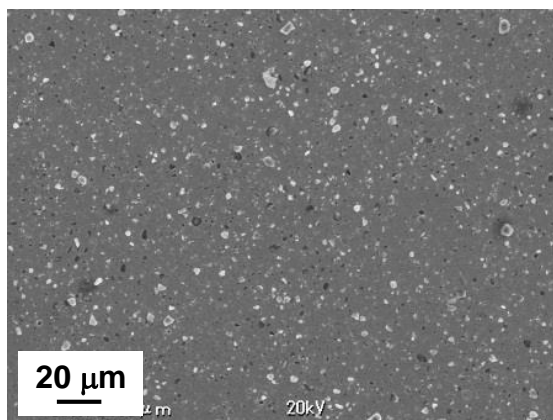
Ni-P/cBN film ($\bar{d} = 10 \mu\text{m}$)	Ni-P/SiC film ($\bar{d} = 5 \mu\text{m}$)	Ni-P/SiC film ($\bar{d} = 1 \mu\text{m}$)	Steam treatment	TiCN film
1.128 $\pm 0.034 \mu\text{m}$	0.413 $\pm 0.028 \mu\text{m}$	0.273 $\pm 0.025 \mu\text{m}$	0.09 $\pm 0.018 \mu\text{m}$	0.075 $\pm 0.028 \mu\text{m}$



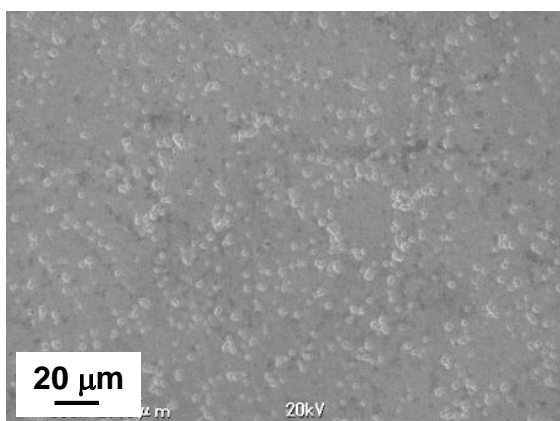
(a) Ni-P/cBN particle composite film
(Mean particle diameter: 10 μm)



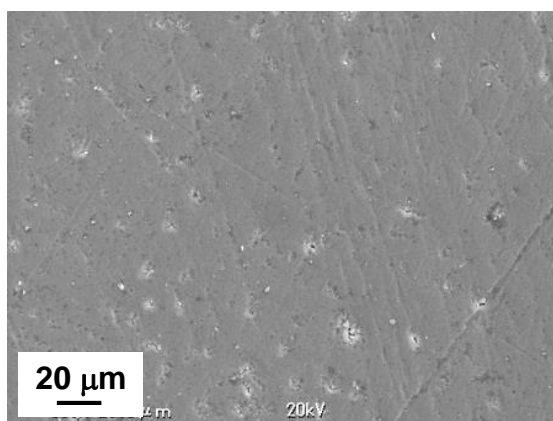
(b) Ni-P/SiC particle composite film
(Mean particle diameter: 5 μm)



(c) Ni-P/SiC particle composite film
(Mean particle diameter: 1 μm)

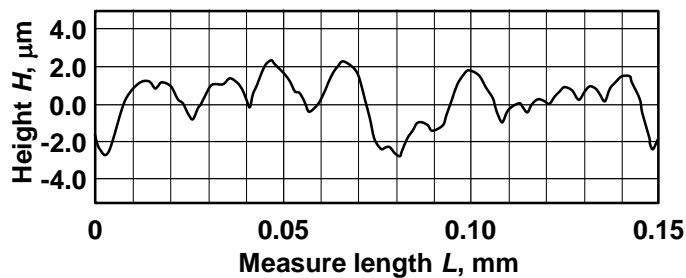


(d) Steam treatment

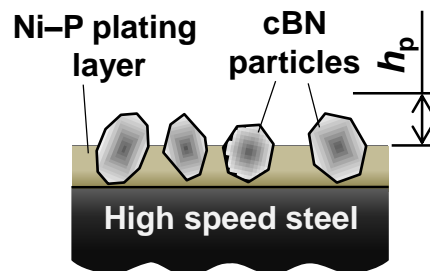


(e) TiCN film

Fig. 2.3 Scanning electron microscopy (SEM) images of the surfaces of the disk specimens



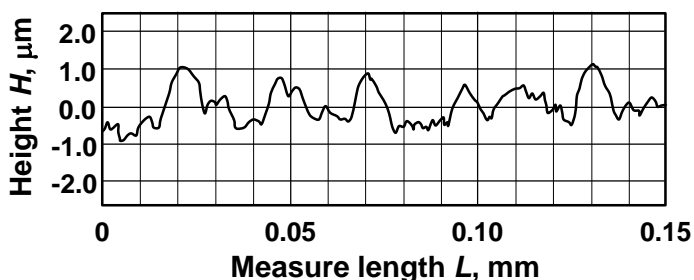
(a) Profile curve



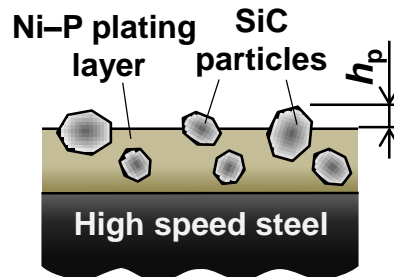
Protrusion height
 $h_p = 3.9 \pm 0.7 \mu\text{m}$

(b) Protrusion height

Fig. 2.4 Profile curve and protrusion height for Ni-P/cBN particle composite film
 (Mean particle diameter: 10 μm)



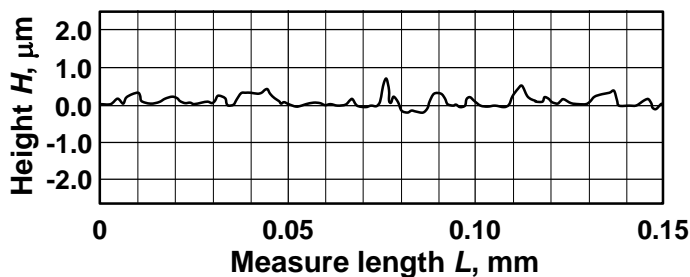
(a) Profile curve



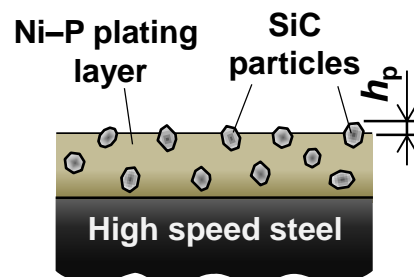
Protrusion height
 $h_p = 1.5 \pm 0.4 \mu\text{m}$

(b) Protrusion height

Fig. 2.5 Profile curve and protrusion height for Ni-P/SiC particle composite film
 (Mean particle diameter: 5 μm)



(a) Profile curve



Protrusion height
 $h_p = 0.4 \pm 0.1 \mu\text{m}$

(b) Protrusion height

Fig. 2.6 Profile curve and protrusion height for Ni-P/SiC particle composite film
 (Mean particle diameter: 1 μm)

2.3.2 Nanoindentation testing

A nanohardness tester (ENT-2100, ELIONIX INC.) was used to measure the hardness and Young's modulus of each coating film and treatment surface, as shown in Fig. 2.7. A schematic of the nanoindentation test is shown in Fig. 2.8. The mechanical properties were measured according to the following procedure [12]:

- ① Increasing the test load ($0 \leq F \leq F_{\max}$)
- ② Maintaining the test load ($F = F_{\max}$)
- ③ Decreasing the test load ($F_{\max} > F \geq 0$)

The indentation hardness was used as the Vickers hardness in this study. It and the Young's modulus of the coating film were obtained via Eqs. (2.1) and (2.3), respectively, using the depth of plastic deformation and the relationship between the load and the indentation depth, respectively.

(1) Vickers hardness

The indentation hardness was calculated as follows:

$$H_{IT} = \frac{F_{\max}}{23.96 \times (h_c + \Delta h_c)^2} \quad (2.1)$$

$$h_c = h_{\max} - 0.75 \times (h_{\max} - h_r) \quad (2.2)$$

where F_{\max} is the maximum load [N], h_c is the measured indentation depth [mm], Δh_c is the correction depth [mm], and h_r is the intersection point between the indentation-depth axis and a tangential line [mm]. The indentation hardness [N/mm^2] was converted into Vickers hardness [kgf/mm^2] using the following transformation [13]:

$$H_V = 0.0924 \times H_{IT} \quad (2.3).$$

(2) Young's modulus

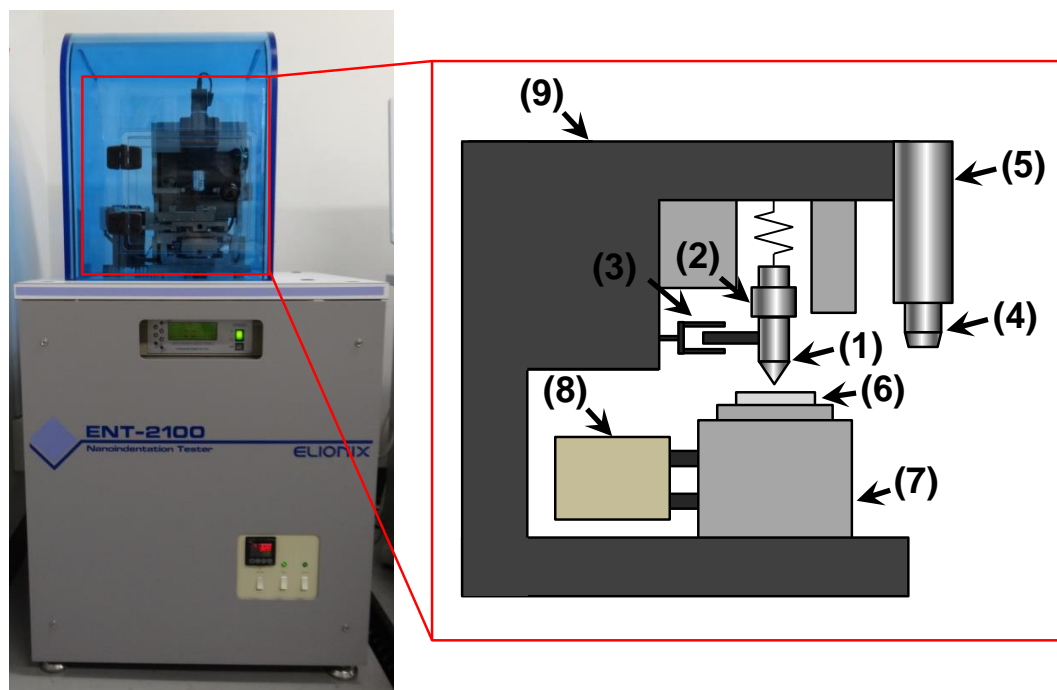
The Young's modulus E_{IT} was obtained using the following equations:

$$E_{IT} = \frac{1 - \nu_s^2}{\frac{1}{E_r} - \frac{1 - \nu_i^2}{E_i}} \quad (2.4)$$

$$E_r = \frac{\sqrt{\pi}}{2 \times (C - C_f) \times \sqrt{23.96 \times (h_c + \Delta h_c)^2}} \quad (2.5)$$

$$C = \left(\frac{0.181}{E_r} \right) \left(\frac{1}{h_c} \right) + C_f \quad (2.6)$$

where ν_s is the Poisson's ratio of the indenter, ν_i is the Poisson's ratio of the specimen, E_i is the Young's modulus of the indenter, C is the compliance, and C_f is the flame compliance.



- | | | |
|-----------------|--------------------------|-----------------------|
| (1) Indenter | (2) Load generation part | (3) Displacement gage |
| (4) Object lens | (5) CMOS camera | (6) Sample stage |
| (7) XYZ stage | (8) Moter | (9) Frame |

Fig. 2.7 Nanoindentation tester used in this study

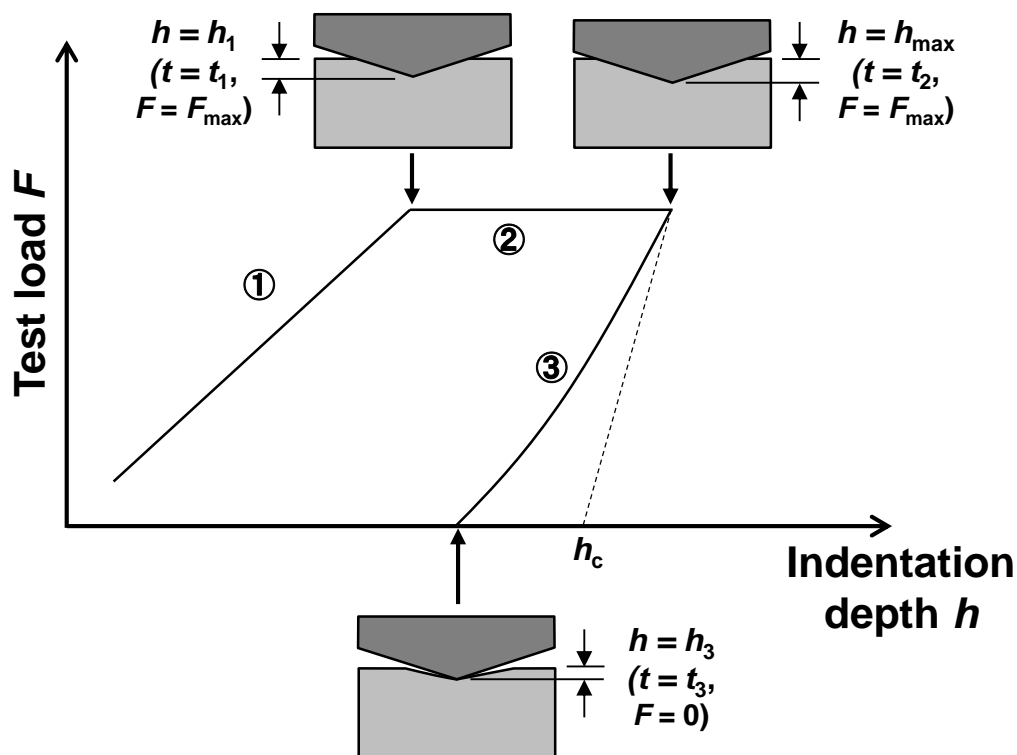


Fig. 2.8 Schematic of nanoindentation process

The experimental conditions for the nanoindentation test are shown in Table 2.3. A disk specimen coated with a Ni-P plating film was used instead of the Ni-P/abrasive particle composite films developed herein because the abrasive particles might have obstructed the hardness measurement. A Berkovich indenter was used. The maximum test load at which the plastic-deformation depth reached 10% of the film thickness was used. There were 500 partitions at a step interval of 20 ms. The holding time was 1000 ms. Each test was repeated five times under the same conditions.

Table 2.3 Experimental conditions for the nanoindentation test

Disk specimen	Ni–P plating film
	Steam treatment
	TiCN film
Indenter	Berkovich indenter
Maximum test load F_{\max} , mN	30, 100
Number of partition N_p , times	500
Step interval, ms	20
Holding time T_{hold}, ms	1000
Number of tests under the same condition N, times	5

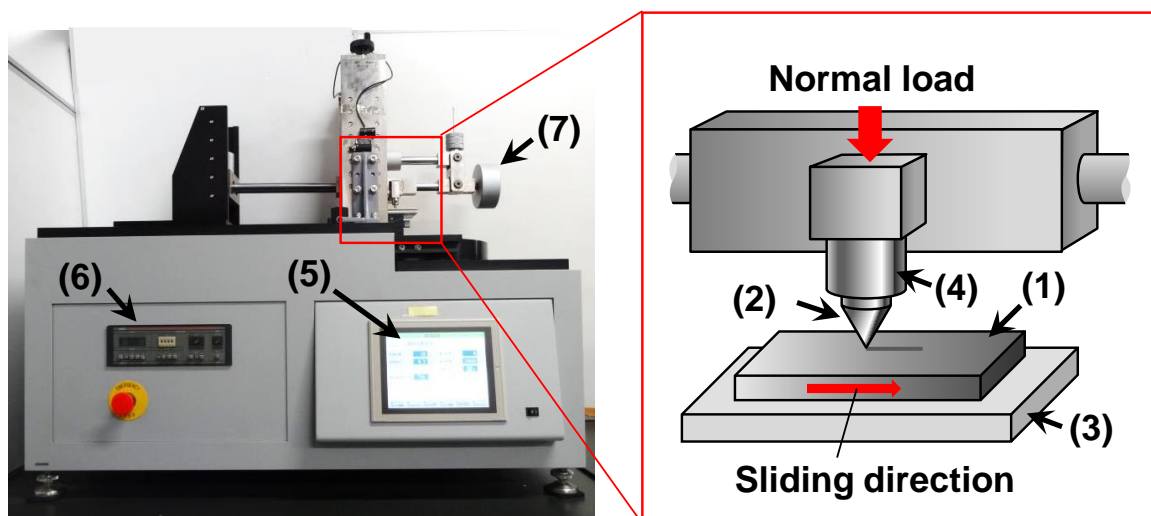
2.3.3 Scratch testing

The adhesion strength of the composite films was measured via a scratch test using a load-fluctuation friction-abrasion tester (HHS-3000, SHINTO Scientific Co., Ltd.), as shown in Fig. 2.9. The normal load was increased in a linear manner with respect to the sliding distance. The sliding distance $L_{\text{separation}}$ for film separation was measured, and the value of the normal load when the film separation occurred was used to evaluate the adhesion strength W_{ad} via the following equation:

$$W_{\text{ad}} = W_{\text{max}} \times \frac{L_{\text{separation}}}{L} \quad (2.7)$$

where W_{max} is the maximum normal load and L is the sliding distance.

The experimental conditions used in the scratch test are shown in Table 2.4. A diamond-pin specimen with a point angle of 60° and tip radius of 0.2 mm was used. The normal load W was increased in a linear manner from 0 N to 98.1 N ($=W_{\text{max}}$), with an associated increase in the sliding distance L from 0 mm to 10 mm. The sliding velocity was 0.2 mm/s. The scratched surface was observed using a digital microscope (DSX510, Olympus Corporation). The separation point was determined by the exposure of the HHS substrate. The friction test was repeated three times under the same conditions.



- (1) Disk specimen (2) Pin specimen (3) Linear stage
 (4) Pin holder (5) Control monitor (6) Amplifier
 (7) Balance regulating weight

Fig. 2.9 Schematic of the load-fluctuation friction-abrasion tester

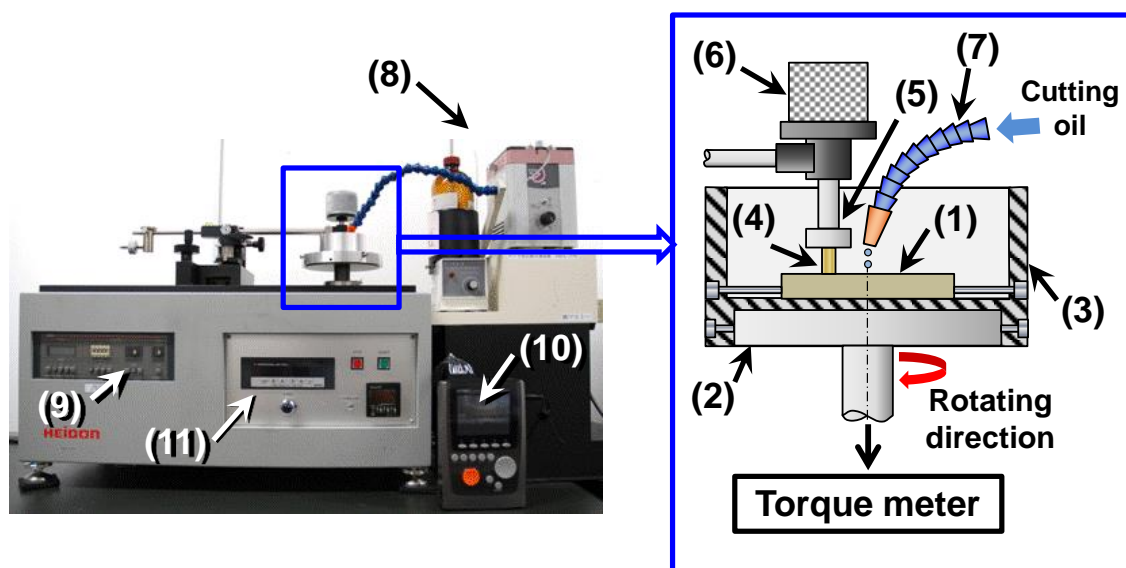
Table 2.4 Experimental conditions for the adhesion strength test

Disk specimen	Ni-P/cBN film ($\bar{d} = 10 \mu\text{m}$)
	Ni-P/SiC film ($\bar{d} = 5 \mu\text{m}$)
	Ni-P/SiC film ($\bar{d} = 1 \mu\text{m}$)
	Steam treatment
	TiCN film
Indenter	Diamond pin
Minimum indentation load W_{\min} , N	0
Maximum indentation load W_{\max} , N	98.1
Sliding velocity V, mm/s	0.2
Sliding distance L, mm	10
Number of tests under the same condition N_t, times	3

2.3.4 Friction testing

A pin-on-disk friction test (HEIDON Type20, SHINTO Scientific Co., Ltd.) was conducted to measure the friction coefficients of each disk specimen. A schematic of the test apparatus is shown in Fig. 2.10. The disk specimen was fixed onto a disk holder placed on a stage, and a diamond-pin specimen was fixed onto an upper arm using a pin holder. A normal load was applied using a weight, and the stage was rotated at a constant speed. Cutting oil was supplied through an automatic dropper to allow the friction test to be conducted under lubrication. The friction coefficient was calculated using the rotational radius, normal load, and friction torque measured using a torque meter mounted on the rotation shaft.

The experimental conditions are given in Table 2.5. The diamond-pin specimen ($\phi = 1\text{mm}$) was manufactured using rolled structural steel (JIS: SS400), and it had a surface roughness of $R_a = 0.7 \pm 0.1 \mu\text{m}$. The normal load was 0.49 N, and the sliding velocities were 0.05 m/s, 0.15 m/s, or 0.25 m/s corresponding to 3.0 m/min, 9.0 m/min, or 15.0 m/min, respectively. This was done to simulate the friction coefficient between the chip and the surface of the tapping tool. The sliding distance was 10 m. Emulsion cutting oil was supplied at a rate of 2.25 ml/min. The friction test was conducted only once.



- | | | |
|-------------------|-------------------------------------|-----------------|
| (1) Disk specimen | (2) Stage | (3) Disk holder |
| (4) Pin specimen | (5) Pin holder | (6) Weight |
| (7) Nozzle | (8) Automatic-dropping-water device | |
| (9) Amplifier | (10) Recorder | (11) Controller |

Fig. 2.10 Schematic of the pin-on-disk friction apparatus

Table 2.5 Experimental conditions for the friction test

Pin specimen	Rolled-structure steel (JIS: SS400)
Disk specimen	Ni-P/cBN film ($\bar{d} = 10 \mu\text{m}$)
	Ni-P/SiC film ($\bar{d} = 5 \mu\text{m}$)
	Ni-P/SiC film ($\bar{d} = 1 \mu\text{m}$)
	Steam treatment
	TiCN film
Normal load W , N	0.49
Sliding velocity V , m/s	0.05, 0.15, 0.25
Sliding distance L , mm	10
Lubricant	Emulsion cutting oil ($\nu = 1.20 \text{ mPa}\cdot\text{s}$ at 21.6°C)

2.4 Experimental results

2.4.1 Vickers hardness and Young's modulus of the composite films

Figure 2.11 shows the Vickers hardness for each coating film and surface treatment. The TiCN-coated film had the highest hardness (>36 GPa). The steam-treated and Ni-P films had hardnesses of approximately 11 and 6.3 GPa, respectively. The hardness of the composite film was not measured, but the hardness of the Ni-P layer of the Ni-P/abrasive-particle composite films was assumed to be equivalent to or higher than that of the Ni-P film [2]. These results suggest that composite films can be used as coating materials for tapping tools because the hardness of the Ni-P layer is higher than that of the conventional coating materials used for tapping tools; thus, the life of the tools should also increase.

Figure 2.12 shows the Young's modulus for each coating film and surface treatment. The Young's modulus of the TiCN-coated film specimen was the highest (~ 470 GPa). The Young's modulus of the steam-treated and Ni-P film specimens were approximately 230 GPa and 180 GPa, respectively.

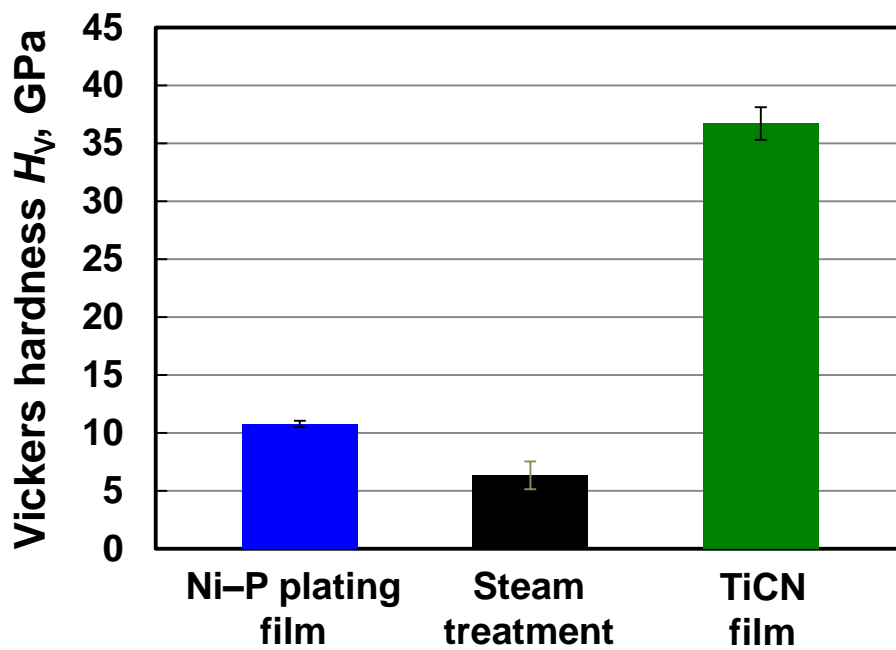


Fig. 2.11 Mean values of the Vickers hardness for each coating film. error bars represent standard deviations.

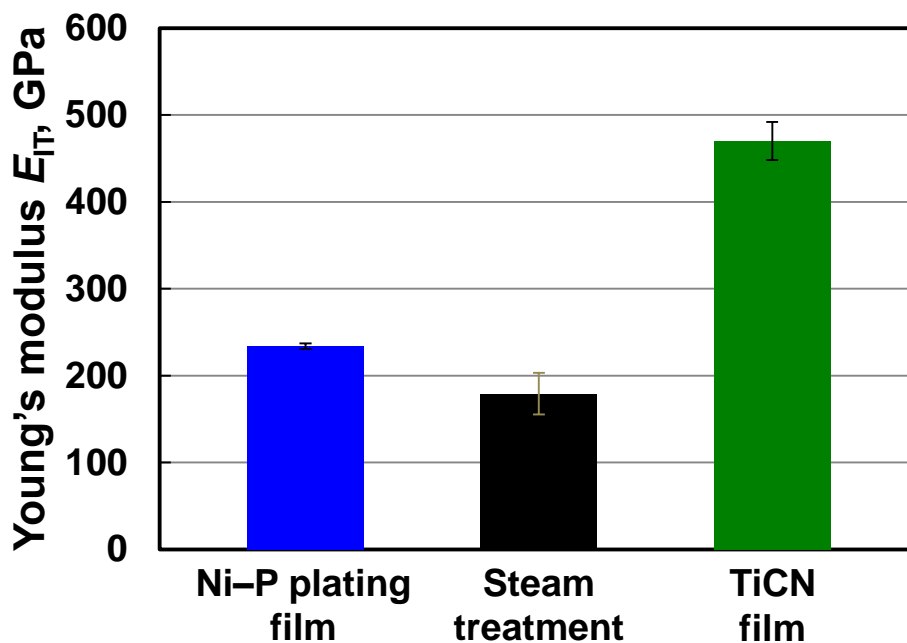


Fig. 2.12 Mean values of the Young's modulus for each coating film. Error bars represent standard deviations.

2.4.2 Adhesion strength of the composite films

Figure 2.13 shows the variation in the friction coefficient over time in the scratch tests. The separation point could not be determined from these variations because the coefficient for the composite films in the scratch test was unstable. This was because of the collisions between the diamond pin and abrasive particles in the composite film.

Figures 2.14 and 2.15 show the optical microscope images and energy-dispersive X-ray spectroscopy (EDX) line scan images of the scratched surfaces of the disk specimens, respectively. The EDX line scan images correspond to the part of the surface labeled as “A” in Fig. 2.14. As shown in Fig. 2.15, in the composite films, the Ni film remains on the substrate; this suggests that no separation occurred. Conversely, the steam-treated and TiCN-coated disk specimens show film separation at 0.4 and 4.6 mm, respectively, because of the reduction in the amount of oxygen (in the oxide layer) and Ti (in the TiCN film) at the scratched point. Based on these results, the adhesion strength of each disk specimen is shown in Fig. 2.16. The composite films showed excellent peeling resistance, with values greater than 98.1 N. These values were higher than those exhibited by the steam-treated (4.2 N) and TiCN-coated (42.9 N) specimens. The steam-treated specimen exhibited the lowest adhesion strength among the five coating films because of its brittle iron oxide layer.

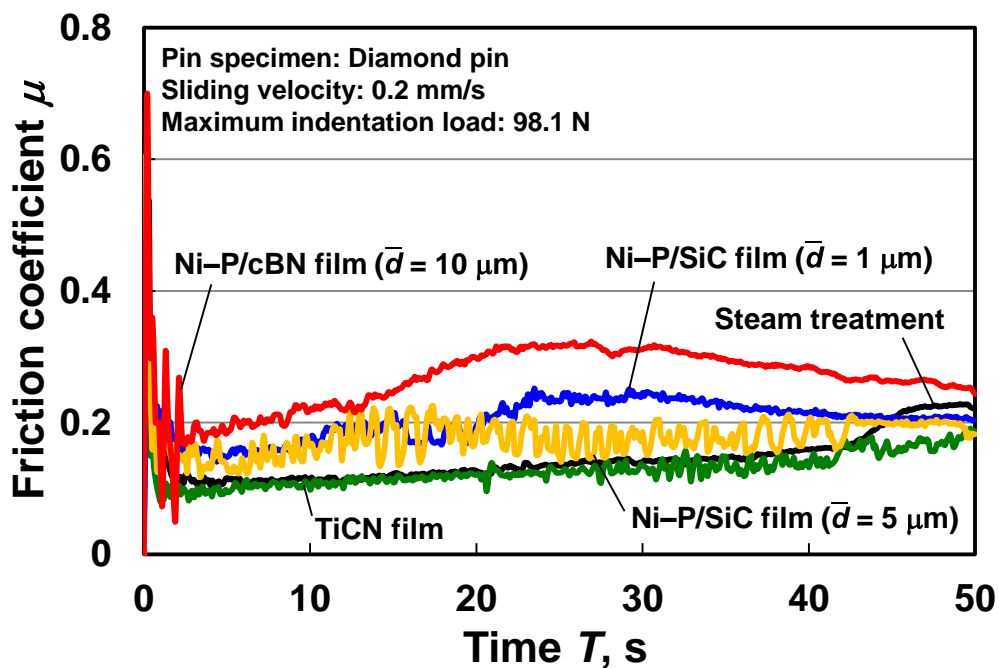


Fig. 2.13 Relation between the friction coefficient and time in the scratch test



(a) Ni-P/cBN particle composite film (mean particle diameter: 10 μm)

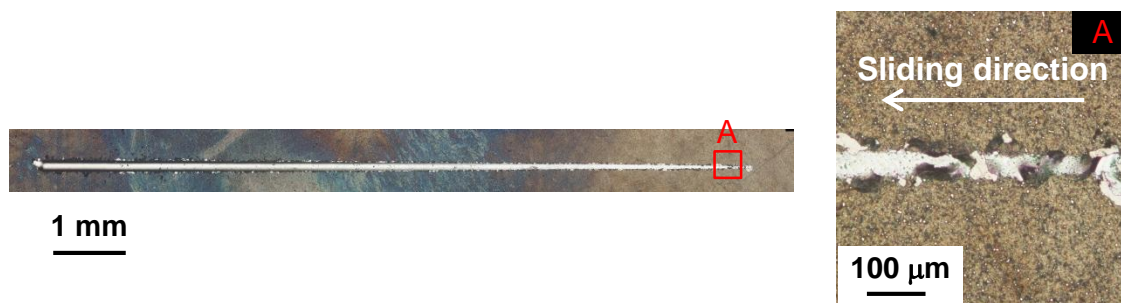


(b) Ni-P/SiC particle composite film (mean particle diameter: 5 μm)

Fig. 2.14 Optical microscope images of the disk surfaces



(c) Ni-P/SiC particle composite film (mean particle diameter: 1 μm)

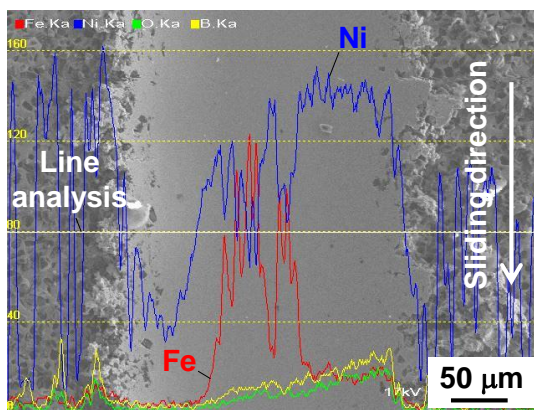


(d) Steam treatment

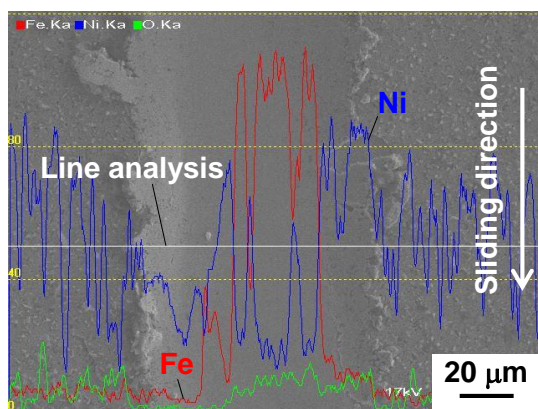


(e) TiCN film

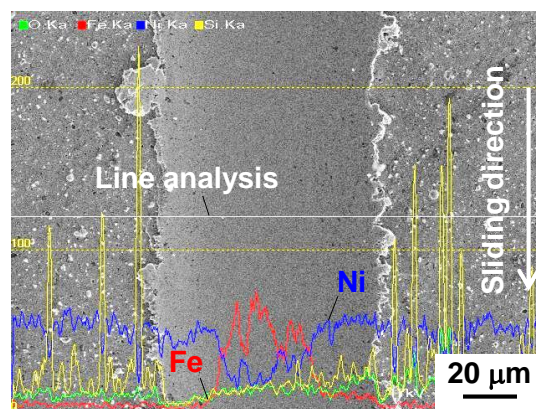
Fig. 2.14 Optical microscope images of the disk surfaces



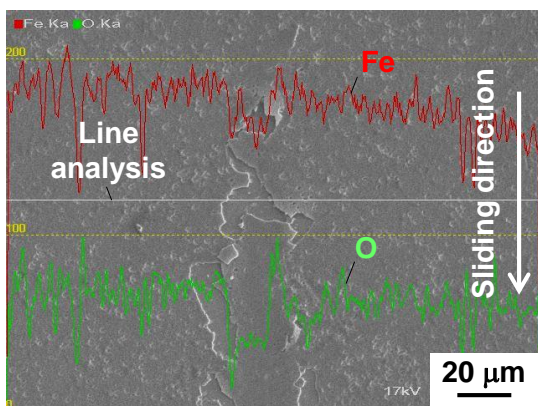
(a) Ni-P/cBN particle composite film
(mean particle diameter: 10 μm)



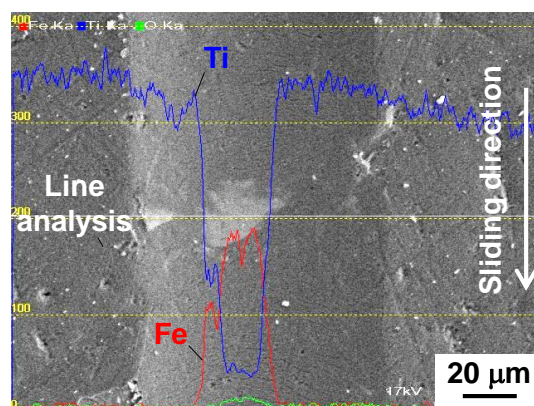
(b) Ni-P/SiC particle composite film
(mean particle diameter: 5 μm)



(c) Ni-P/SiC particle composite film
(mean particle diameter: 1 μm)



(d) Steam treatment



(e) TiCN film

Fig. 2.15 SEM and EDX line scan images of the scratched surface

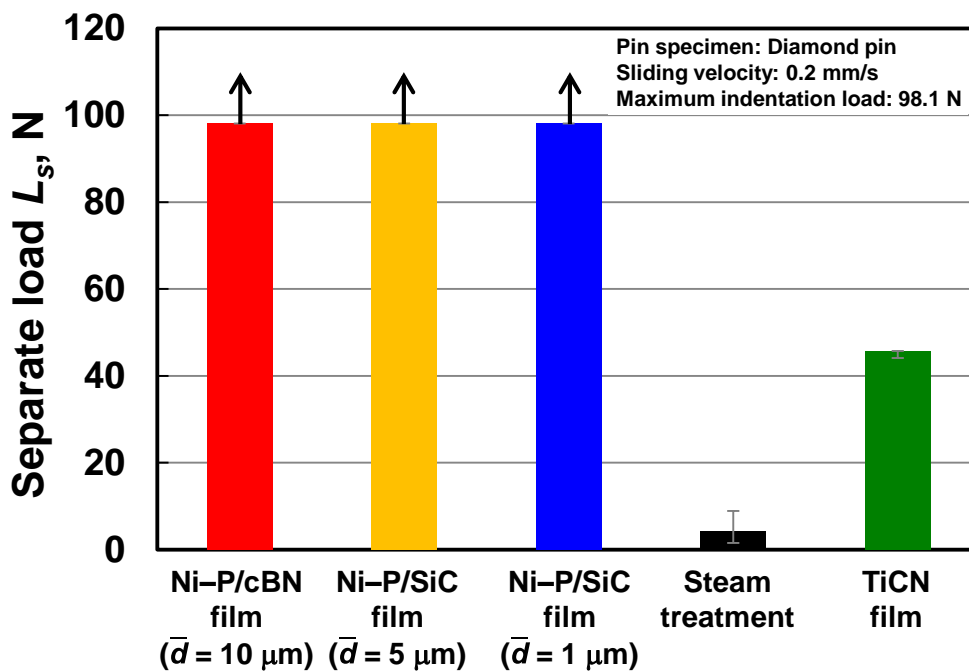


Fig. 2.16 Separation load of the Ni-P/abrasive particle composite film

2.4.3 Friction coefficient of the composite films

Figure 2.17 shows the relationship between the friction coefficient for each surface-treated disk specimen and the sliding distance in the friction tests. As can be seen, the friction coefficient for all the specimens is high during the initial stages and then decreases before eventually becoming constant.

The mean friction coefficient at 8.0–10.0 m for each disk specimen is shown in Fig. 2.18. The mean friction coefficient for the composite films developed herein was greater than 0.15, higher than those of the steam-treated and TiCN-coated specimens at every sliding velocity. The Ni-P/cBN film ($\bar{d} = 10 \mu\text{m}$) had the highest friction coefficient among the composite films.

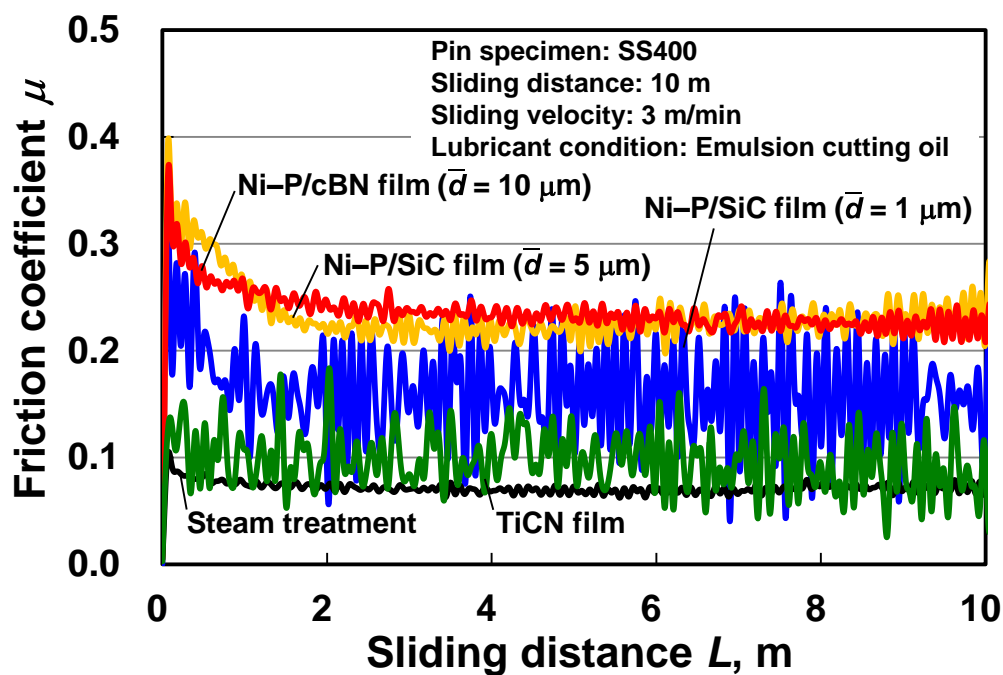
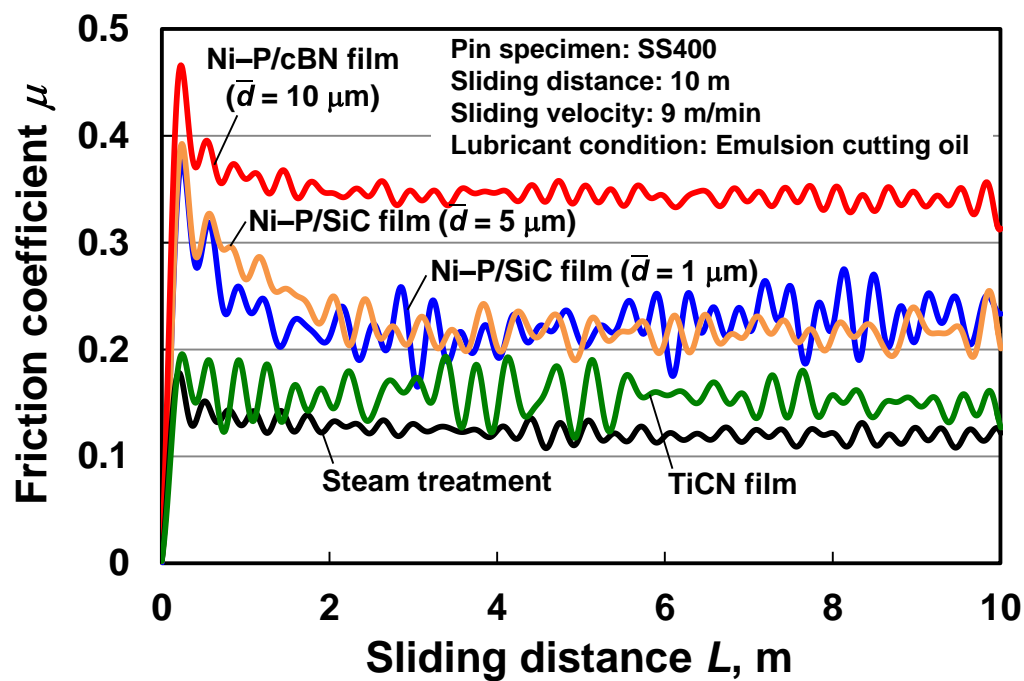
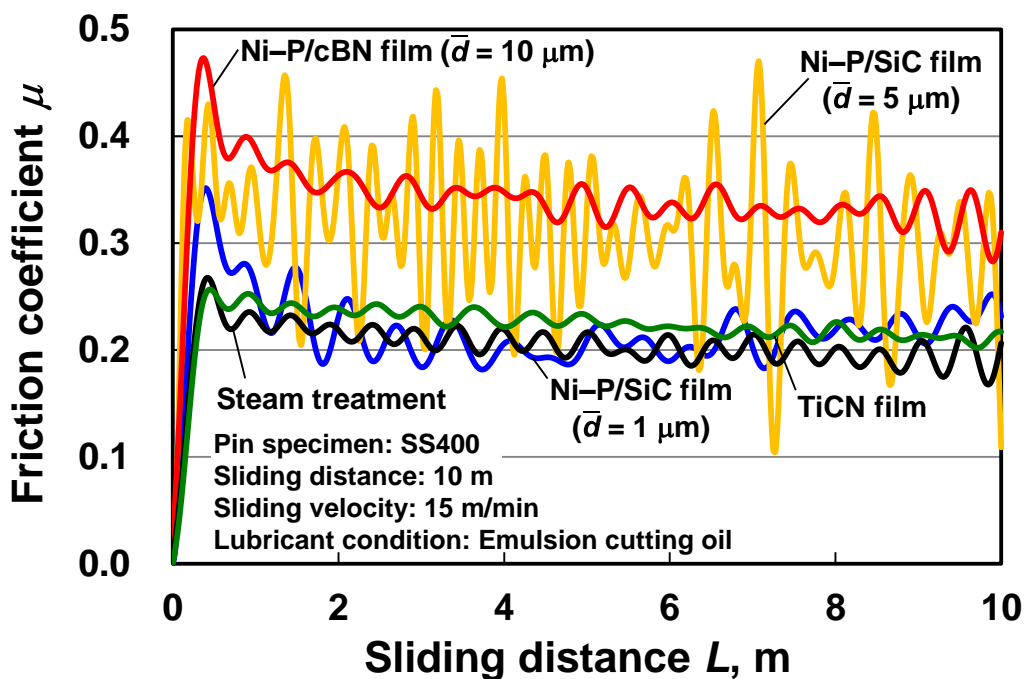
(a) $V = 3 \text{ m/min}$ (b) $V = 9 \text{ m/min}$

Fig. 2.17 Relation between the friction coefficient and sliding distance



(c) $V = 15 \text{ m/min}$

Fig. 2.17 Relation between the friction coefficient and sliding distance

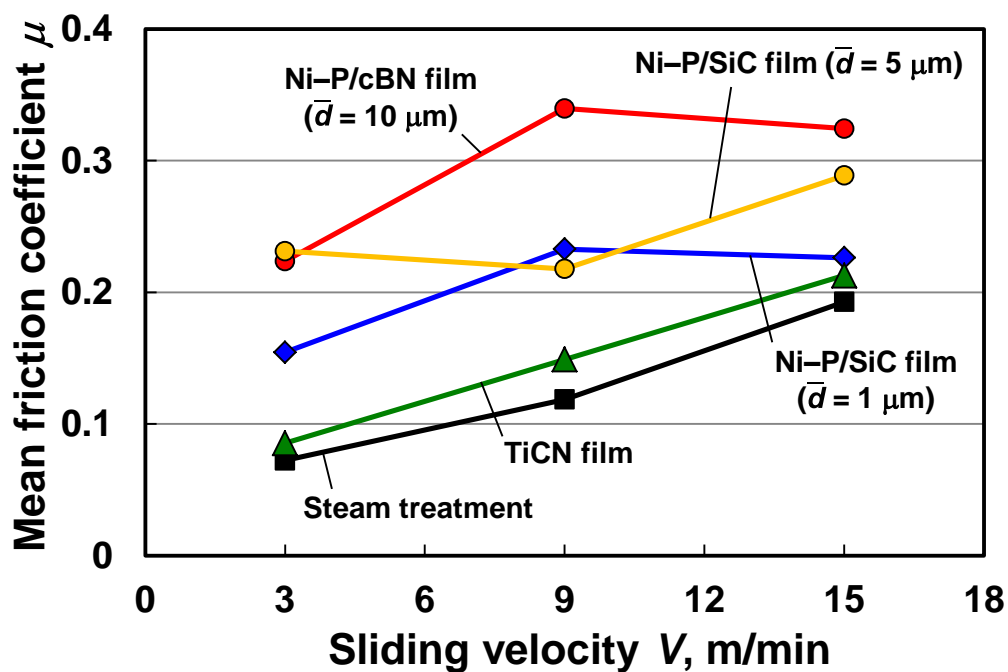


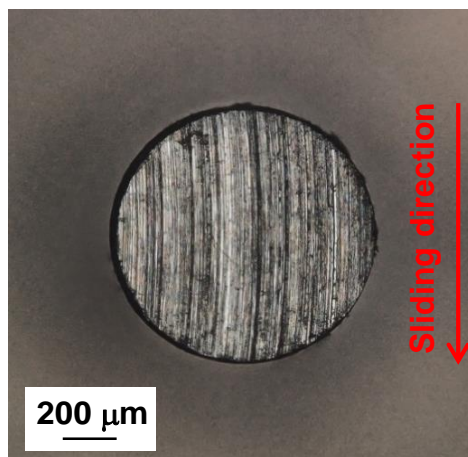
Fig. 2.18 Relation between the friction coefficient and sliding velocity

2.5 Discussion

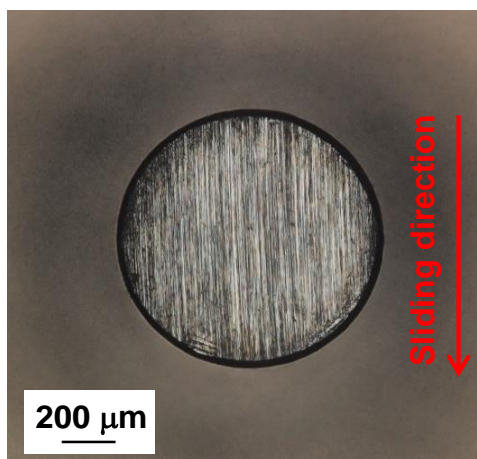
According to the results, the composite film developed herein using Ni-P/abrasive particle showed excellent adhesion strength. This may be because of the composite film had a Young's modulus (230 GPa) similar to that of the HSS substrate (220 GPa); this may have produced an equivalent strain when the contacting load was applied during scratch testing. No delamination or peeling was observed in the composite film.

The composite film had a higher friction coefficient than the steam-treated or TiCN-coated films under emulsion oil lubrication. Because the composite film included abrasive particles, the plowing effect may have increased the friction coefficient even if the adhesion friction would have been reduced by oil lubrication. To confirm this, the surface of each rolled-steel pin specimen was observed. Figure 2.19 shows the optical microscope images of each specimen surface after the friction test. In the case of the composite films, the surface was plowed by the abrasive particles in the film, as indicated by the scratch marks on the surface. However, as can be seen in Fig. 2.19 (d) and (e), the pin specimens for the steam-treated and TiCN-coated films show partial contact with the disk specimens because the initial abrasion mark was observed. Because of this small contact area, these films exhibited a lower friction coefficient than the composite films. These results also demonstrate that the composite films cause heavier abrasive wear in their counterparts rolled-steel pins, which would result in breaking of the chip into small pieces if the composite film is used as the coating film for a tapping tool.

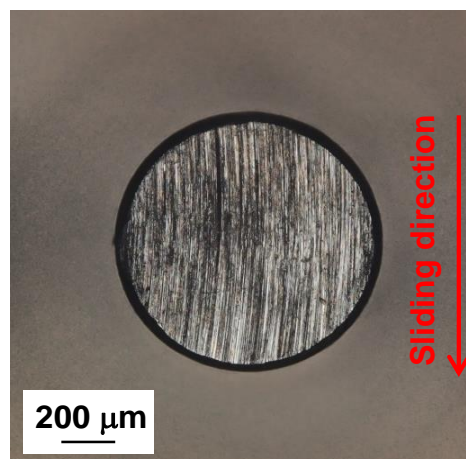
The Ni-P/abrasive particle composite films showed high hardness and excellent wear resistance. This could extend the service life of a tool.



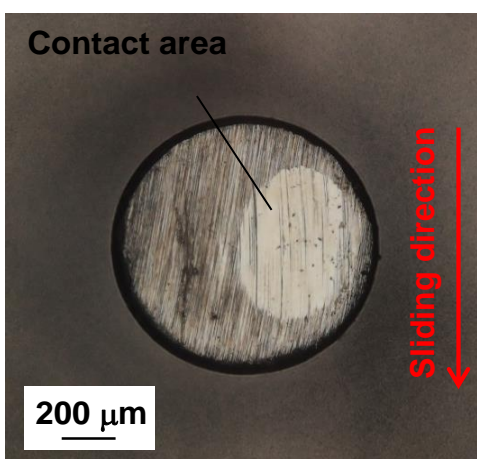
(a) Ni-P/cBN particle composite film
(mean particle diameter: 10 μm)



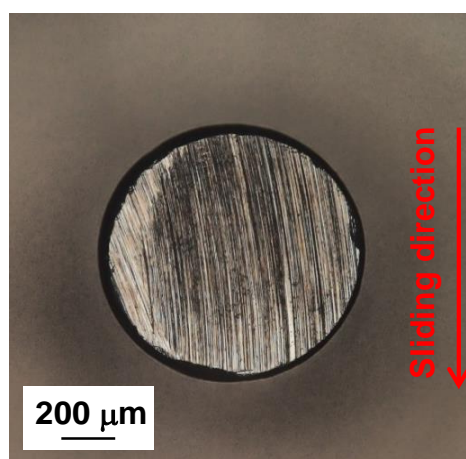
(b) Ni-P/SiC particle composite film
(mean particle diameter: 5 μm)



(c) Ni-P/SiC particle composite film
(mean particle diameter: 1 μm)



(d) Steam treatment



(e) TiCN film

Fig. 2.19 Optical microscope images of the rolled-steel pin specimen surfaces after the friction test

A pin-on-disk friction test was conducted to investigate the effect of the ratio of the protrusion height to the diameter of codepositing particles R_p on the friction coefficient. In this test, the cBN particles with mean diameter of 10 μm were used for the codepositing particles. The HSS disk specimen coated with the Ni-P/cBN film with different R_p values (0%, 20%, and 40%) were prepared. The pin specimen ($\phi = 1\text{mm}$) was manufactured using carbon steel (JIS: S45C), and it had a surface roughness of $R_a = 0.5 \pm 0.1 \mu\text{m}$. The normal load was 19.8 N, and the sliding velocity was 0.5 m/s. The sliding distance was 10 m. Emulsion cutting oil was supplied at a rate of 2.25 ml/min.

Figure 2.20 show the effect of R_p values on the maximum friction coefficient. The maximum friction coefficient increased with increase of the R_p values. The results could be due to an increase of penetration of the abrasive particles onto the mating steel surface, which results in the increase of ploughing friction. These results indicated that the ratio of the protrusion height to the diameter of codepositing particles R_p should be 40 % in terms of high friction.

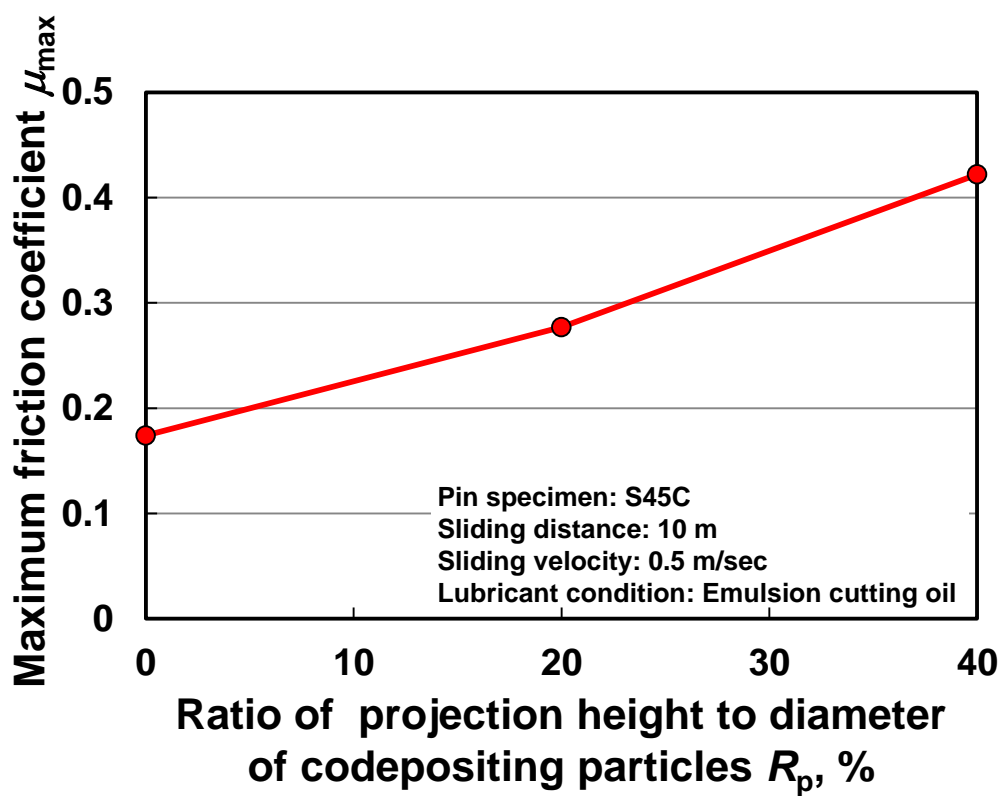


Fig. 2.20 Effect of R_p values on the mean friction coefficient

2.6 Conclusions

Herein, Ni–P/abrasive particle composite films were formed on HSS disks using electroless plating. The hardness, adhesion strength, and friction coefficients of the composite-film coated, stream-treated, and TiCN-coated disk specimens were compared. The conclusions of this study are as follows:

- (1) Ni–P/abrasive particle composite films were deposited on an HSS disk specimen using cBN particulates with a mean diameter of 10 μm or SiC particulates with mean diameters of 5.0 μm or 1.0 μm . The surface roughness of the composite films was higher than that of the other specimens.
- (2) The hardness of the Ni–P plating film was ~ 11 GPa, which suggests that the composite film, which included the hard particles, was harder than the Ni–P plated film.
- (3) No film separation was observed in the composite films in the scratch tests, which exhibited a peeling resistance greater than that of the other surface-treated specimens.
- (4) The composite films showed friction coefficients greater than 0.15 at sliding velocities under emulsion-oil lubrication (0.05–0.25 m/s), which were higher than those of the other specimens.

As noted above, the Ni–P/abrasive particle composite films exhibited excellent adhesion strength, wear resistance, and high friction coefficients under emulsion oil lubrication. This suggests that such composite films can be used as coating materials for tapping tools and may increase their service life without inducing chip snarling.

References

- [1] Cheng, K., "Machining Dynamics Fundamentals," Applications and Practices, Springer Series in Advanced Manufacturing, 2009, 129-133.
- [2] Balaraju, N. J., Narayanan, S. N. N. T. and Seshadri, K. S., "Electroless Ni-P Composite Coatings," Journal of applied Electrochemistry, 33, 2003, 807-816.
- [3] Straffelini, G., Colombo, D. and Molinari, A., "Surface Durability of Electroless Ni-P Composite Deposites," Wear, 236, 1999, 179-188.
- [4] Brinksmeier, E., Riemer, O. and Twardy, S., "Tribological Behavior of Micro Structured Surfaces for Micro Forming Tools," International Journal of Machine Tools and Manufacture, 50, 2010, 425-430.
- [5] Hojo, J., Takamatsu, A. and Kato, A., "Influence of Size and Dispersion of SiC Particles in the Preparation of Ni-P-SiC Composite Plating," Journal of the Ceramic Society of Japan, 98, 1990, 22-28 (in Japanese).
- [6] Shackelford, J. F. and Alexander, W., "Materials Science and Engineering Handbook," CRC press, 2001.
- [7] Savvides, N. and Bell, J. T., "Hardness and Elastic Modulus of Diamond and Diamond-like Carbon Films," Thin Solid Films, 228, 1993, 289-292.
- [8] Klein, A. C. and Cardinale, F. G., "Young's Modulus and Poisson's Ratio of CVD Diamond," Diamond and Related Materials, 2, 1993, 918-923.
- [9] Slack, A. G., "Thermal Conductivity of Pure and Impure Silicon, Silicon Carbide, and Diamond," J. Appl. Phys., 35, 3460, 1964, 3460-3466.
- [10] Wakatsuki, M., "New Materials Based on the B-C-N Compositions and Synthesis Processes at High Pressure", The Review of High Pressure Science and Technology, 4, 1995, 280-286 (in Japanese).

- [11] Upadhyaya, S. G., "Powder Metallurgy Technology," Cambridge Intl. Science Pub., Cambridge, 1998, 123.
- [12] Katayama, S., "The Hardness Evaluation Testing Technology for Plating and that Application," J. Surf. Finish. Soc. Jpn., 58 , 2007, 206-212 (in Japanese).
- [13] Hashimoto, M., Iijima, M., Kaga, M. and Endo, K., "Mineralization by Acrylic Resin Containing Portland Cement Powder for Long-term Water Storage Analyzed by SEM, XPS and XRD," Nano Biomedicine, 4, 1, 2012, 1-10.

Chapter 3

Development of tapping tool coated with Ni-P/abrasive particle composite film

3.1 Introduction

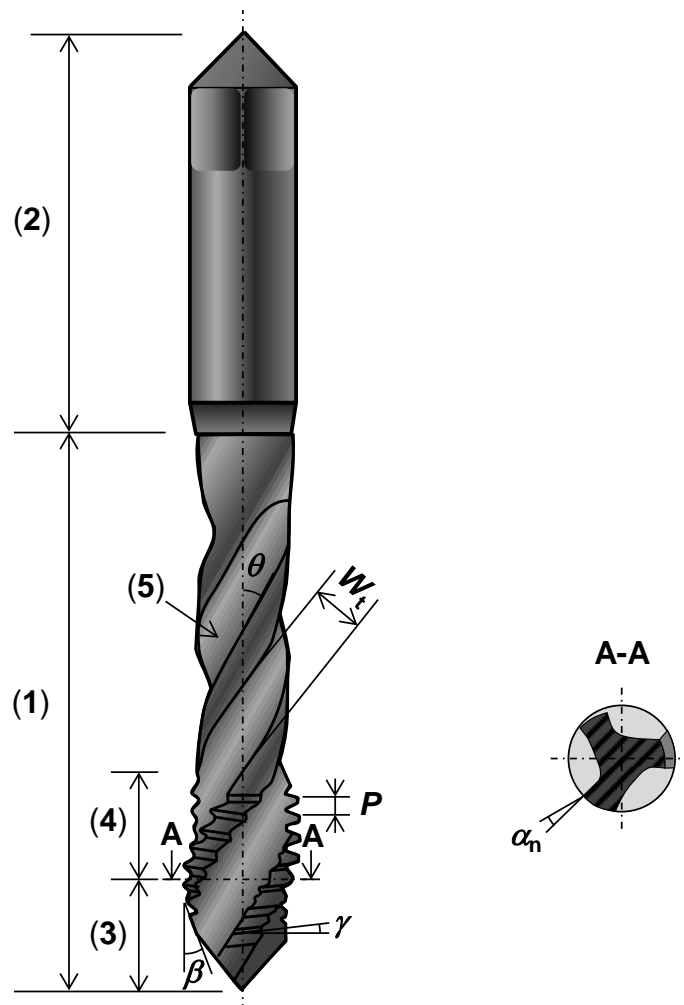
It has been shown that the Ni-P/abrasive particle composite film is high in hardness, has a high friction coefficient, and has excellent adhesion strength. This gives Ni-P/abrasive particle composite films excellent wear resistance. Composite films can also prevent chip snarling on the tapping tool because the polished chip surface produced by the abrasive particles causes the chip to break up.

Maintaining the quality of the thread hole is as important as the prevention of chip snarling [1-3]. This is challenging to ensure when using a tapping tool coated with the Ni-P/abrasive particle composite film because the rough surface creates strong friction. This may increase the surface roughness and reduce the dimensional accuracy of the hole. In general, the quality of a thread hole is assessed from its appearance and size-tolerance [4]. The visual inspection of the thread surface is a qualitative assessment, whereas the size-tolerance examination provides a quantitative assessment of the thread geometry using screw thread-limiting gauges. Defects in thread holes may be caused by inappropriate selection of tools or the cutting conditions, such as the rotation speed or feed rate of the tapping tool. These must be controlled on the basis of the lead geometry of the thread hole. The driving force generated by the reaction force at the surface of the thread hole increases with the cutting speed so that the tapping tool may be excessively driven [5], [6].

In this chapter, the development of a tapping tool coated with the Ni-P/abrasive particle composite film and discuss the cutting performance of the tool and the quality of the thread hole produced are described.

3.2 Development of a tapping tool coated with Ni-P/abrasive particle composite film

Figure 3.1 shows a schematic of the spiral-cut tapping tool developed in this study. It is evident from the figure that the tool comprised a body and shank. The body had a chamfer part and a complete thread part. The cutting edges, which had an angled chamfer, were located in the chamfer section. The tool had three helical flutes to eject the chips from the hole.



- | | | |
|--------------------------|-------------------|------------------|
| (1) Body | (2) Shank | (3) Chamfer part |
| (4) Complete thread part | (5) Helical flute | |

P : Pitch

W_t : Width of helical flute

γ : Lead angle

β : Chamfer angle

θ : Torsion angle

α_n : Rake angle

Fig. 3.1 Schematic of spiral-cut tapping tool

Table 3.1 summarizes the specifications of the tap. It comprised three helical flutes and eight cutting edges. Figure 3.2 shows the geometry and position of each edge. As shown in Fig. 3.2(a), the uncut chip thickness of the second, third, fourth, fifth, sixth, and seventh cutting edges was 75 μm in each case. Compared with the uncut chip thicknesses of other cutting edges, the uncut chip thickness of the first and eighth cutting edges were smaller, i.e., 29 and 12 μm , respectively. The cutting widths increased as follows: eighth (64 μm), first (114 μm), seventh (224 μm), sixth (317 μm), second (411 μm), fifth (449 μm), fourth (562 μm), and third (620 μm). On the edge face of each helical flute, cutting edges are formed (Figs. 3.2(b)–3.2(d)). The edge faces of Flute 1 formed the first, fourth, and seventh cutting edges, that of Flute 2 formed the second, fifth, and eighth cutting edges, and that of Flute 3 formed the third and sixth cutting edges. The number of cutting chips evacuated from each helical flute matched the number of cutting edges.

Table 3.1 Specification of spiral-cut tap

Nominal size	M6 × 1
Pitch P, mm	1
Number of helical flutes N_f, flutes	3
Width of helical flute W_t, mm	3.2
Lead angle γ, deg	3.03
Chamfer angle β, deg	15.4
Torsion angle θ, deg	43.4
Rake angle α_n, deg	5.5

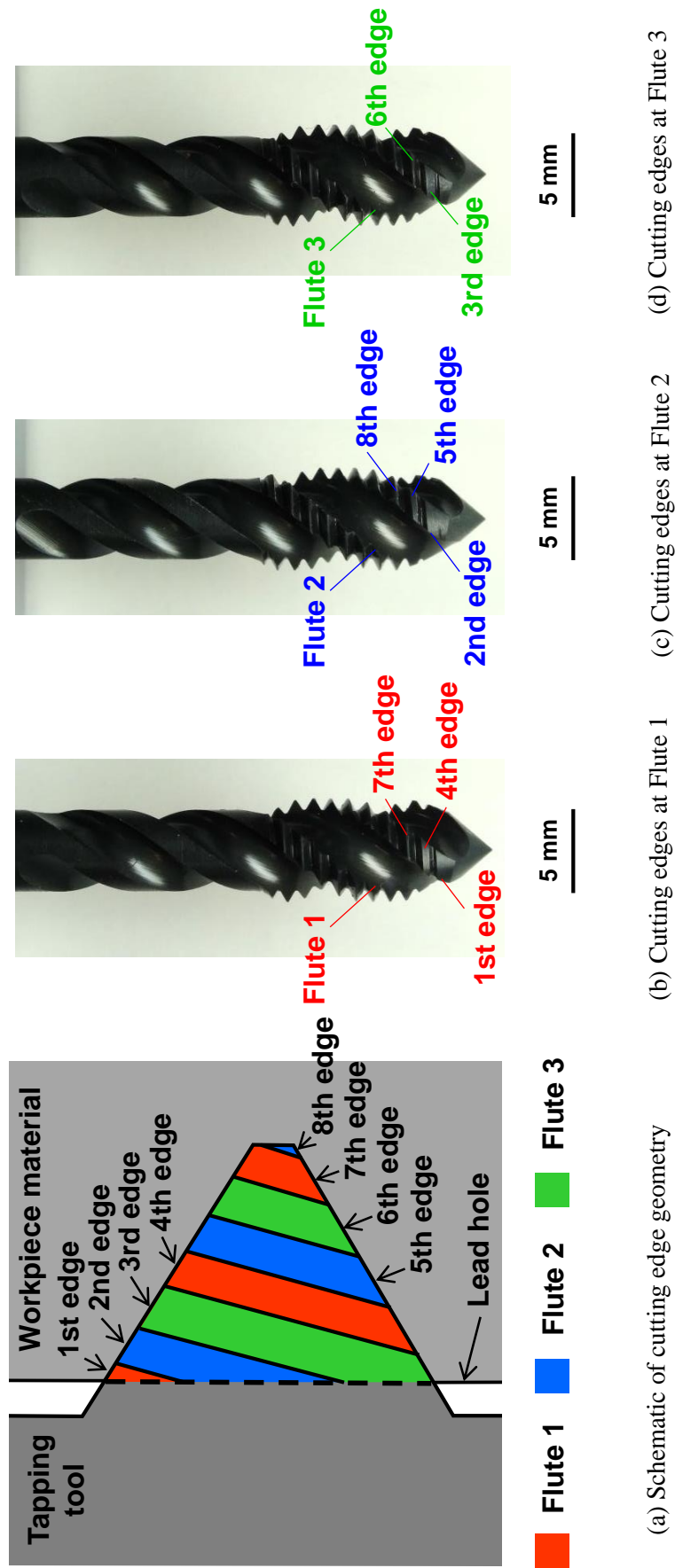
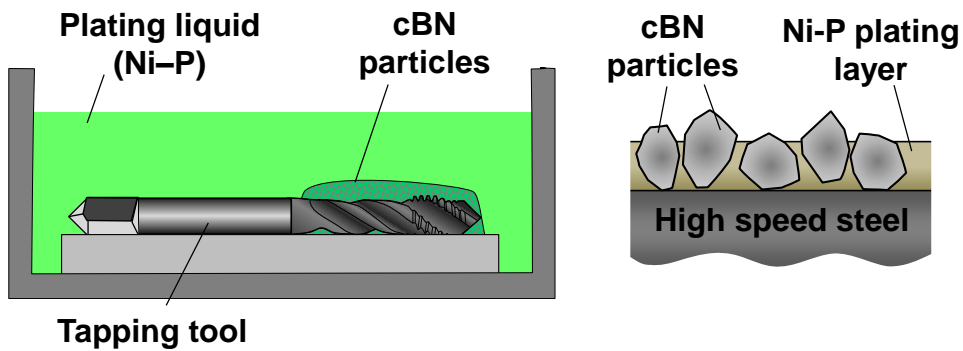
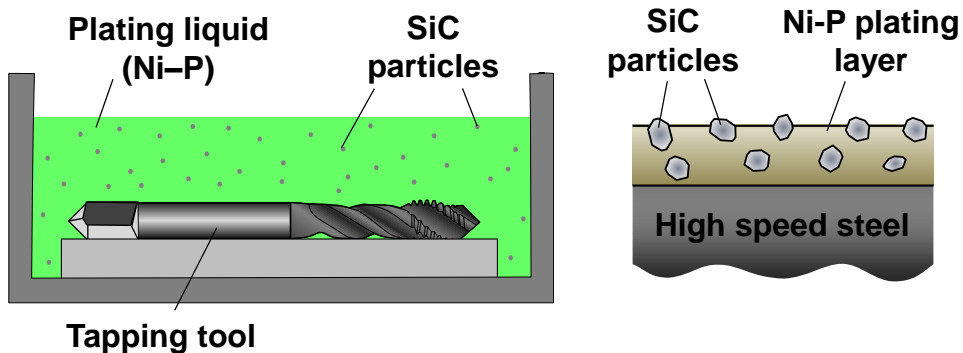


Fig. 3.2 Geometry and position of cutting edge

The tapping tool was coated with the Ni-P/abrasive particle composite film using the electroless plating process shown in Fig. 3.3 [7]. The plating methods for the Ni-P/cBN and Ni-P/SiC films were the same as those used for the disk specimens discussed in Section 2.2.



(a) Ni-P/cBN particle composite film



(b) Ni-P/SiC particle composite film

Fig. 3.3 Schematic of the electroless plating method for coating tapping tool with composite film

The tools coated with the Ni–P/abrasive particle composite film are shown in Figs. 3.4(a)–3.4(c). A tapping tool produced using steam treatment (Fig. 3.4(d)) and that coated with the TiCN coating film were prepared in order to compare the effect of tapping tool. Figures 3.5–3.9 show scanning electron microscopy (SEM) images of the rake face of the cutting edges of the tapping tools: the images of the tool coated with the Ni–P/cBN film ($\bar{d} = 10 \mu\text{m}$) are shown in Fig. 3.5, those coated with the Ni–P/SiC film ($\bar{d} = 5 \mu\text{m}$) are shown in Fig. 3.6, and those coated with the Ni–P/SiC film ($\bar{d} = 1 \mu\text{m}$) are shown in Fig. 3.7, those with steam treatment are shown in Fig. 3.8, those coated with the TiCN film are shown in Fig. 3.9. It is evident from these figures that the abrasive particles were uniformly distributed on the rake face and edge part of the tools coated with the Ni–P/abrasive particle composite film. In contrast, the tapping tool produced using steam treatment and those coated with the TiCN film had a smoother rake face, as shown in Figs. 3.8 and 3.9.

5 mm
—



(a) Ni-P/cBN film ($\bar{d} = 10 \mu\text{m}$)

5 mm
—



(b) Ni-P/SiC film ($\bar{d} = 5 \mu\text{m}$)

5 mm
—



(c) Ni-P/SiC film ($\bar{d} = 1 \mu\text{m}$)

5 mm
—



(d) Steam treatment

5 mm
—



(e) TiCN coating

Fig. 3.4 Tapping tools used in tapping test

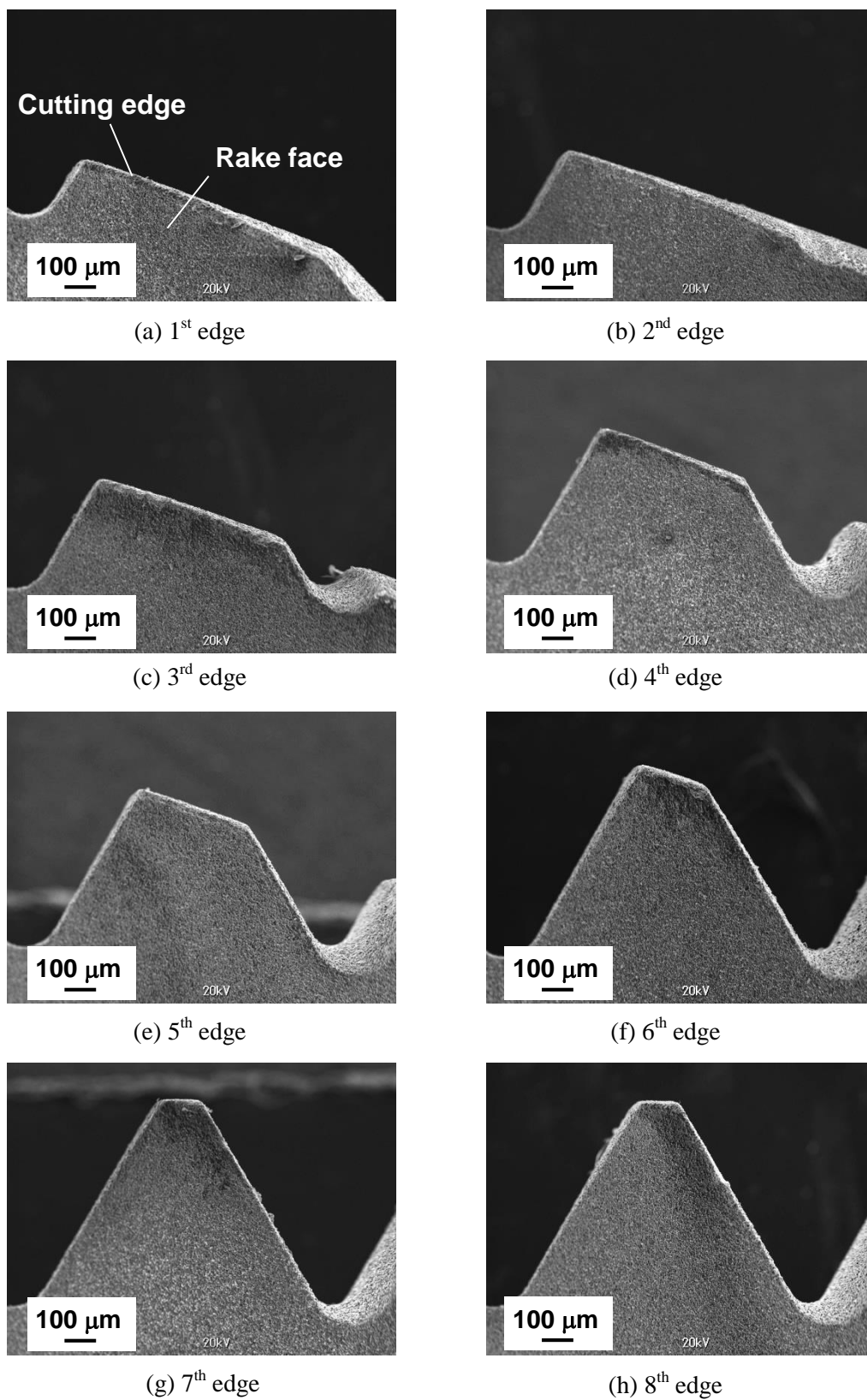


Fig. 3.5 SEM images of cutting edges of tool coated with Ni-P/cBN film ($\bar{d} = 10 \mu\text{m}$)

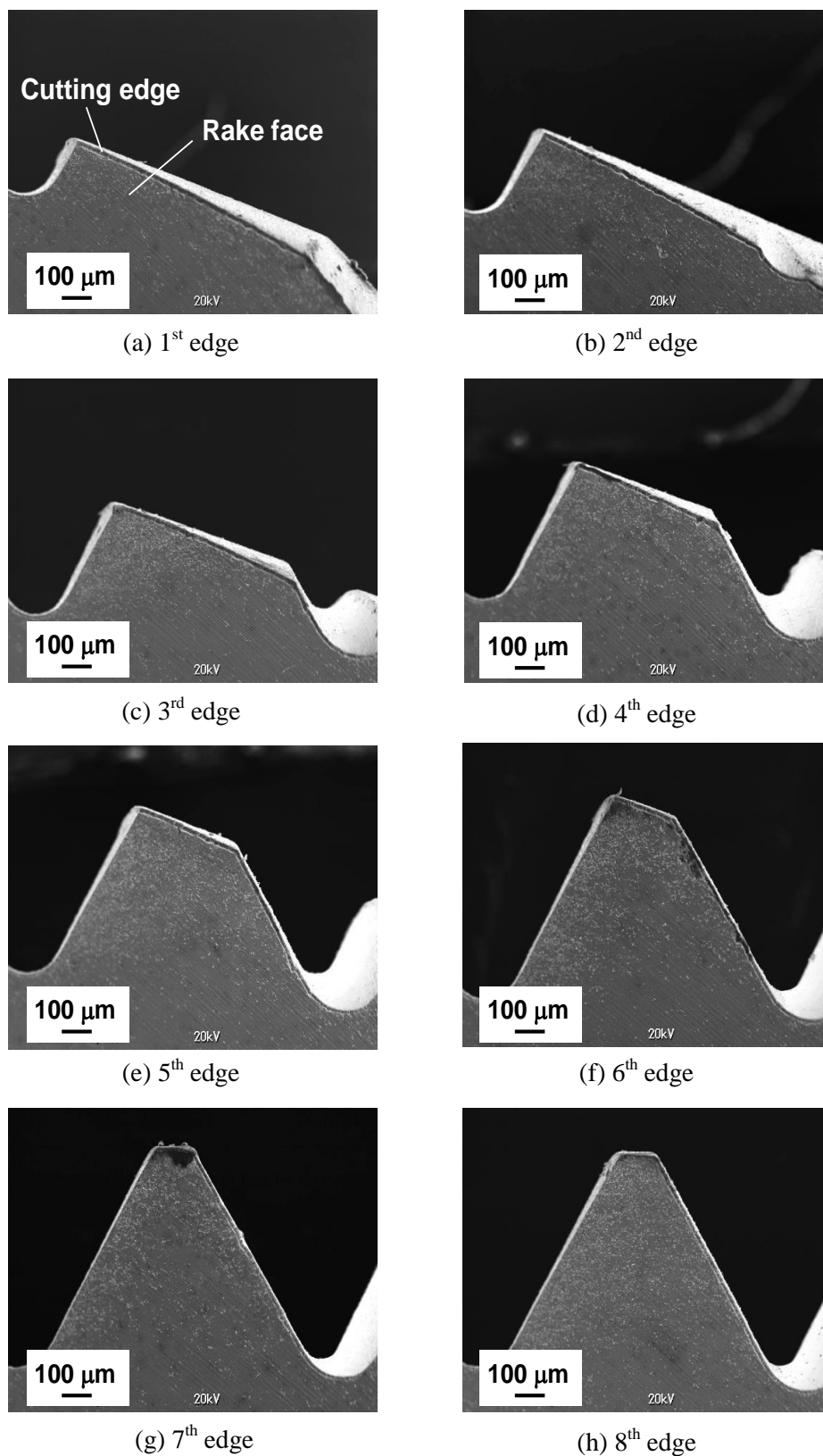


Fig. 3.6 SEM images of cutting edges of tool coated with Ni-P/SiC film ($\bar{d} = 5 \mu\text{m}$)

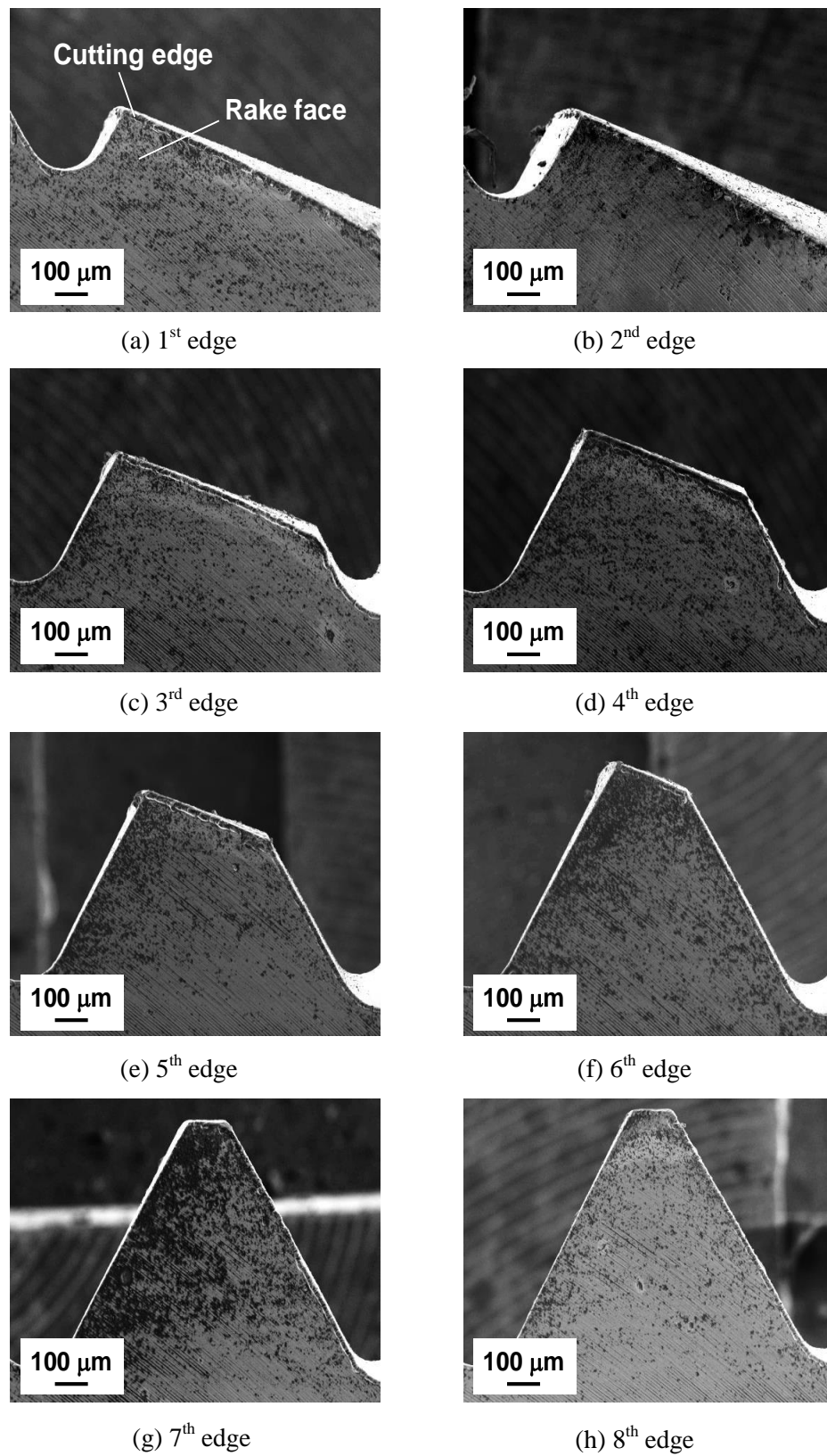


Fig. 3.7 SEM images of cutting edges of tool coated with Ni-P/SiC film ($\bar{d} = 1 \mu\text{m}$)

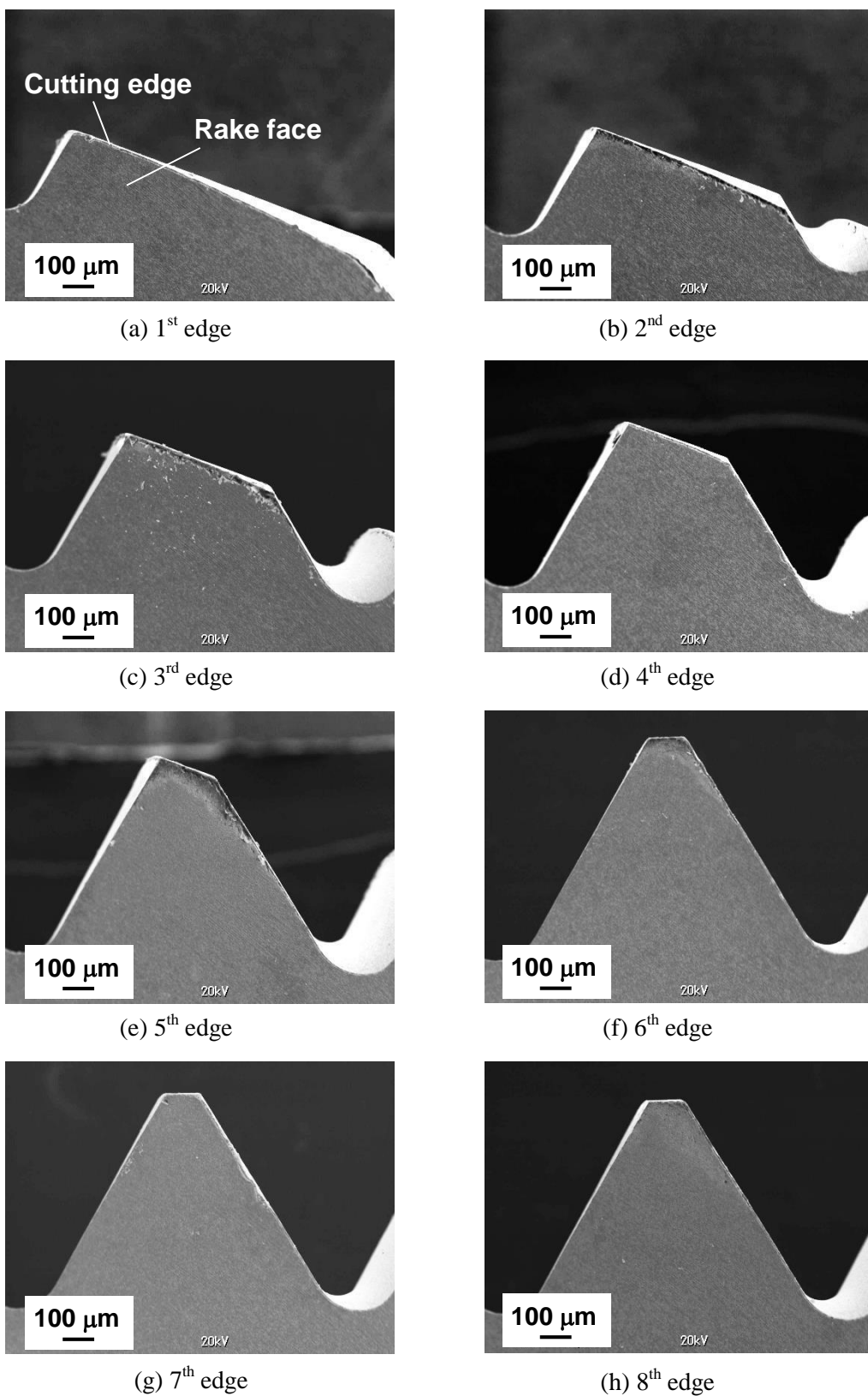


Fig. 3.8 SEM images of cutting edges of tool with steam treatment

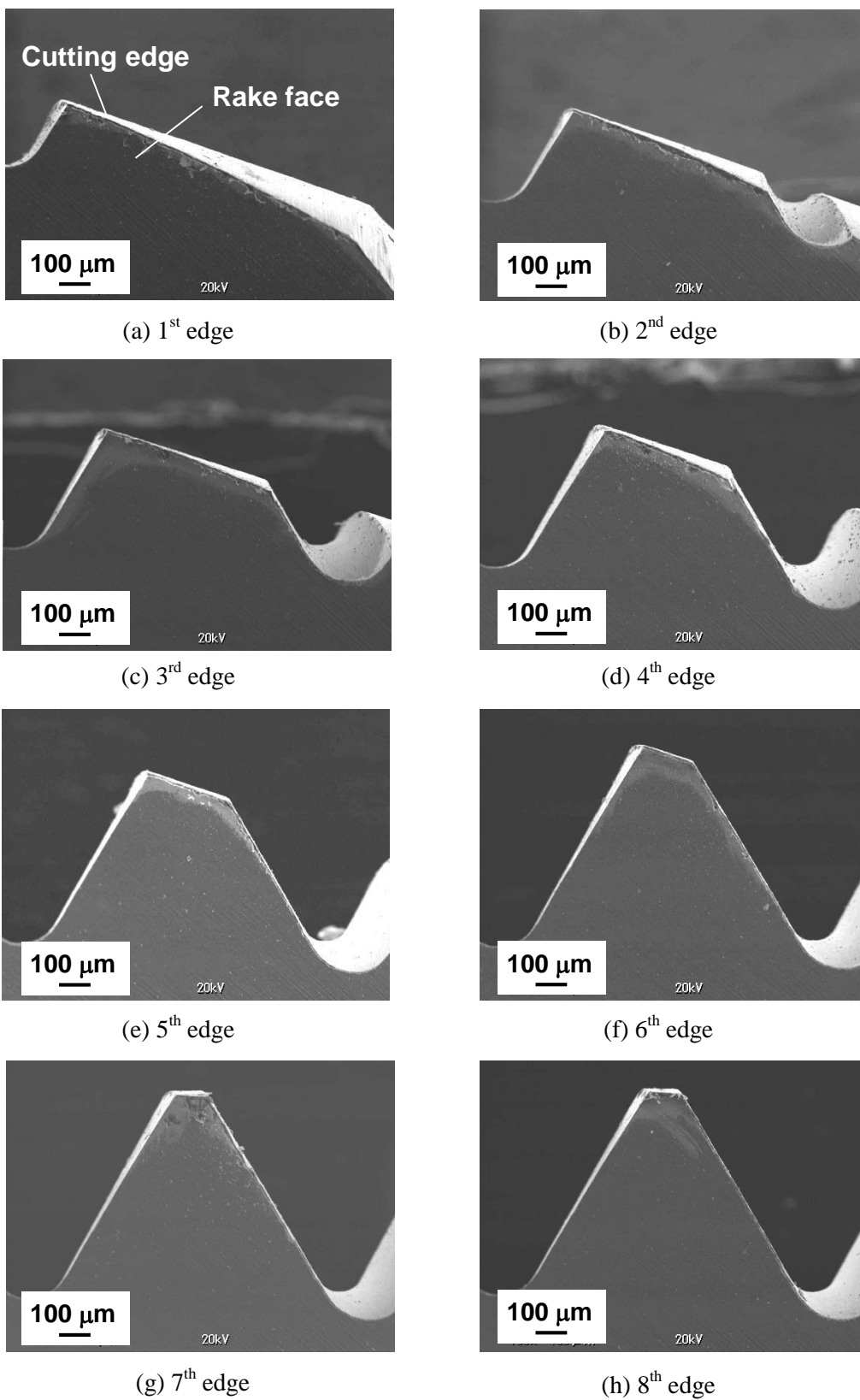
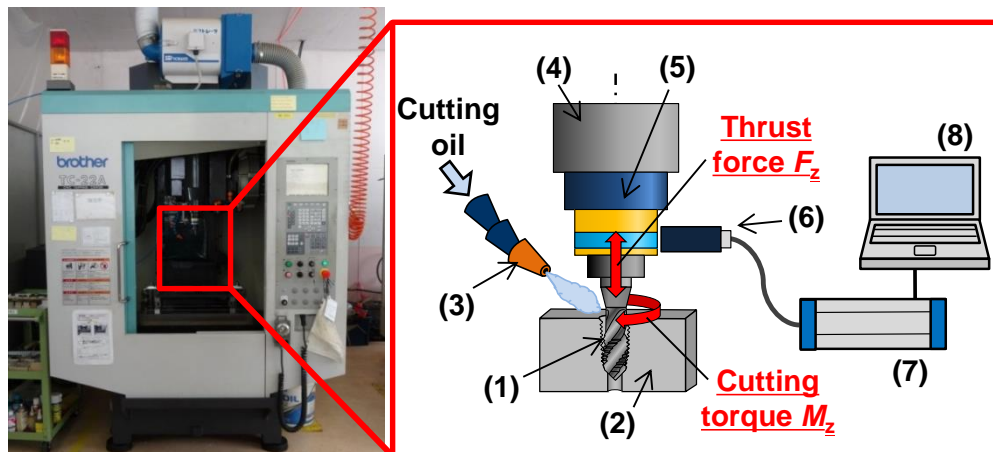


Fig. 3.9 SEM images of cutting edges of tool coated with TiCN coating

3.3 Experimental methods

3.3.1 Experimental apparatus

Tapping tests were conducted using a vertical machining center (TC-22A, Brother Industries, Ltd.) shown in Fig. 3.10. A synchronized feed control was used for tapping. Emulsion cutting oil was used to cool the tapping tool and workpiece. The cutting torque and thrust force were measured using a dynamometer (9125A, Kistler Japan Co., Ltd.) with a measurement range of thrust force of -3000 – 3000 N and a measurement range of cutting torque of -50 – 50 Nm. Data were recorded by a computer via the amplifier.



- (1) Tapping tool (2) Workpiece material (3) Nozzle
 (4) Spindle (5) Dynamo meter (6) Non-contact sensor
 (7) Amplifier (8) PC

Fig. 3.10 Vertical machining center

3.3.2 Experimental conditions

Table 3.2 lists the experimental conditions for evaluate a thread hole accuracy. The tested tools had a spiral tap (HSS, M6 × 1) with eight cutting edges. The workpiece was a rectangular block of rolled structural steel (JIS: SS400) with dimensions of 14.0 × 310.0 × 450.0 mm³. Through holes with a hole pitch of 10 mm were drilled into the workpiece. To maintain a thread engagement of 91%, the diameter of each hole drilled by the tapping tool coated with the Ni-P/cBN film ($\bar{d} = 10 \mu\text{m}$) was 5.15 mm, while all other holes had a diameter of 5.10 mm. Cutting speeds of 10 (the conventional cutting speed), 30, and 50 m/min were used. Lubrication was provided by an emulsion cutting oil (YUSHIROKEN FGE360, Yushiro Chemical industry Co., Ltd.) with a viscosity of 1.20 mPa·s at 21.6°C. Each test was conducted once.

Table 3.2 Cutting conditions

Type of tapping tool	Spiral-tap (HSS, M6 × 1)
Surfacae treatment	Ni-P/cBN film ($\bar{d} = 10 \mu\text{m}$)
	Ni-P/SiC film ($\bar{d} = 5 \mu\text{m}$)
	Ni-P/SiC film ($\bar{d} = 1 \mu\text{m}$)
	Steam treatment
	TiCN film
Workpiece material	Rolled-structure steel (JIS: SS400)
Cutting speed V_r, m/min	10, 30, 50
Lubricant	Emulsion cutting oil ($\nu = 1.20 \text{ mPa}\cdot\text{s}$ at 21.6°C)
Number of cutting process N, hole	1

3.3.3 Evaluation of the dimensional accuracy of thread hole

To evaluate the geometry of the thread holes, the flank face at the advancing side (Fig. 3.11) was observed using SEM and the maximum height of flank face of advancing side H_{\max_a} proposed by Kadota et al. [8] was measured. Additionally, the shapes of the holes were tested using screw thread-limiting gauges (M6 × 1), which is standardized in JIS B 3102 (Fig. 3.12). The thread-limiting gauge had go and no-go thread plug gauges. A go thread plug checks the screwing performance, whereas a no-go thread plug checks whether the effective diameter of the thread hole exceeds the standard diameter (5.35–5.5 mm). If, the go thread plug fails to pass through the thread hole or the no-go thread plug passes through the hole in more than two revolutions, the hole is judged to be non-standard.

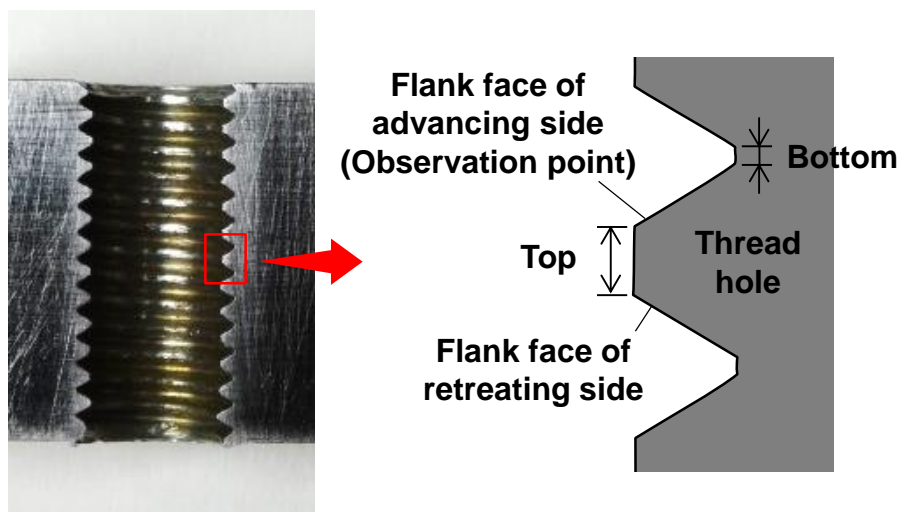


Fig. 3.11 Observation point of thread hole



Fig. 3.12 Screw thread-limiting gauge

3.3.4 Evaluation method for cutting resistance

Figure 3.13 shows the change in the thrust force and cutting torque with respect to the cutting time. The points A, B, C, and D show the points at which the first cutting edge contacts the workpiece, the eighth cutting edge begins to cut, the first cutting edge finishes cutting, and the eighth cutting edge is extracted from the hole, respectively [9]. The cutting resistance of each tapping tool was evaluated from the mean cutting torques and thrust forces between points B and C, which represent the resultant cutting torques and thrust forces for the eight cutting edges. When evaluating the cutting torque, a positive value and a negative value represent the torque in the counterclockwise and clockwise directions, respectively. In the case of the thrust force, a positive value and a negative value represent the compression and tensile forces, respectively. The sampling frequency for cutting torque and thrust force was 2000 Hz, and low-pass filtering was performed with cut-off frequencies of 60 Hz at 10 m/min, 100 Hz at 20 m/min, and 150 Hz at 30 m/min.

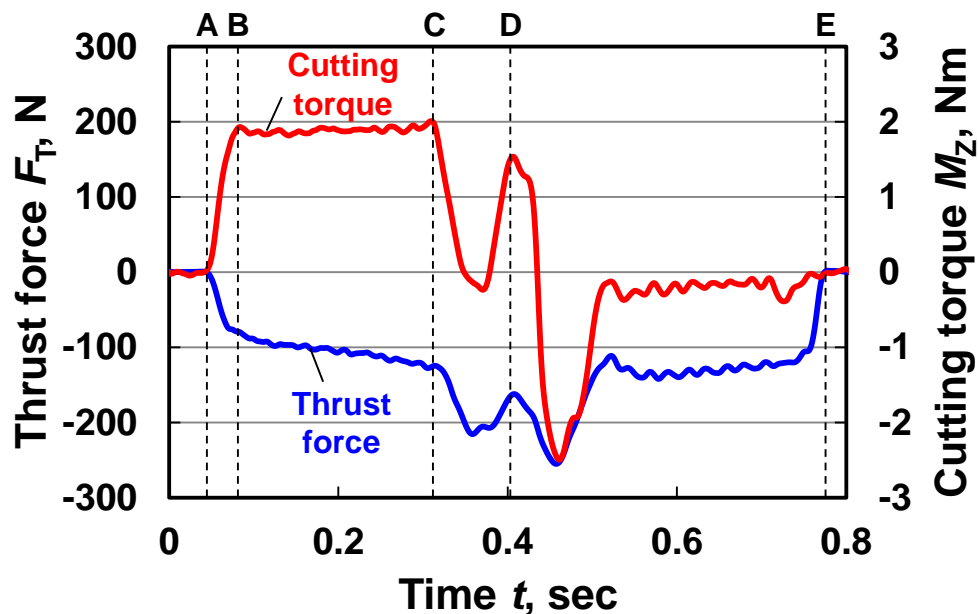


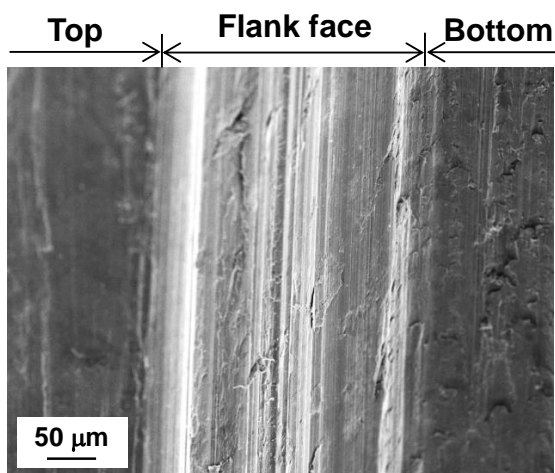
Fig. 3.13 Cutting torque and thrust force during the machining of a single hole (for TiCN);
 $V_f = 50$ m/min

3.4 Results and discussion

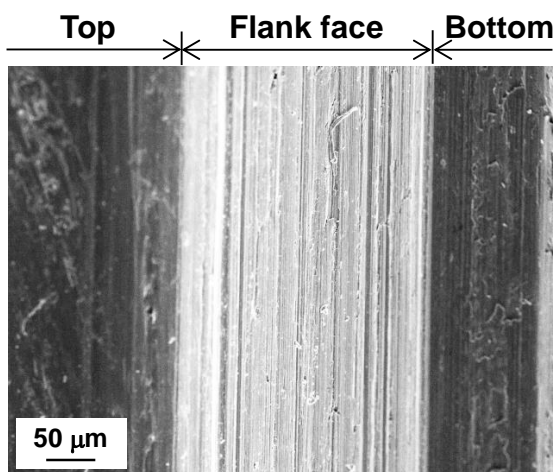
3.4.1 Evaluation of the dimensional accuracy of thread holes

Each thread hole was evaluated using the thread gauges. Consequently, all thread holes met the appropriate standard, demonstrating that the tapping tool coated with the Ni-P/abrasive particle composite film produced thread holes of satisfactory dimensions and precision.

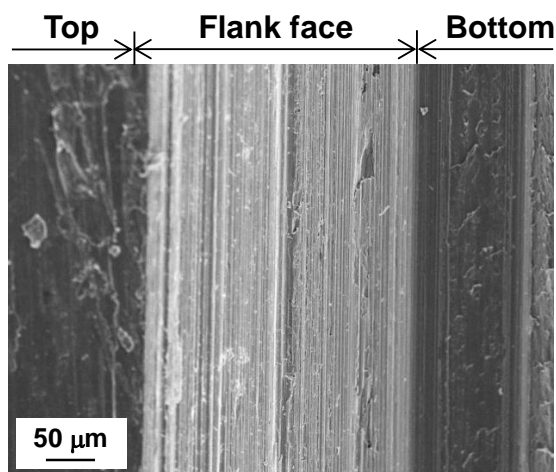
Figures 3.14, 3.15, and 3.16 show SEM images of the flank face of a thread hole machined with each tapping tool. It is evident from these figures that the tapping tool coated with the Ni-P/cBN particle composite film ($\bar{d} = 10 \mu\text{m}$) produced severe adhesion with plastic flow at the surface of the thread hole; therefore, as shown in Figure 3.17, the maximum height of flank face of advancing side for the tapping tool coated with the Ni-P/cBN particle composite film ($\bar{d} = 10 \mu\text{m}$) was larger than that for the other tapping tool at all cutting speed conditions. This suggested that the Ni-P/cBN particle composite film ($\bar{d} = 10 \mu\text{m}$) had excessive surface roughness or that the size of cBN particle used in this study was considerably large for the surface treatment of the tapping tool [10].



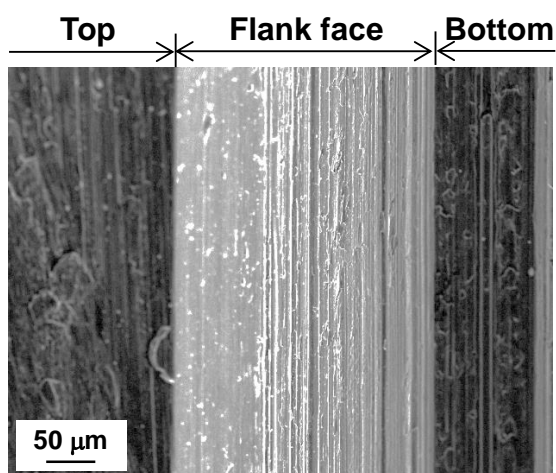
(a) Ni-P/cBN film ($\bar{d} = 10 \mu\text{m}$)



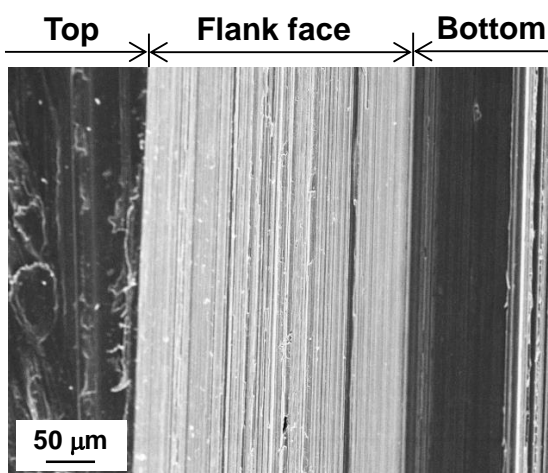
(b) Ni-P/SiC film ($\bar{d} = 5 \mu\text{m}$)



(c) Ni-P/SiC film ($\bar{d} = 1 \mu\text{m}$)

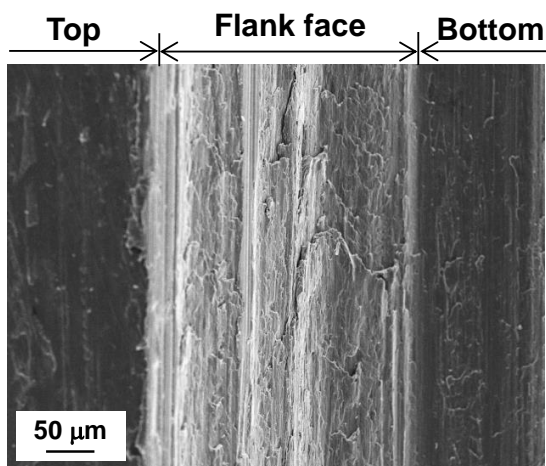


(d) Steam treatment

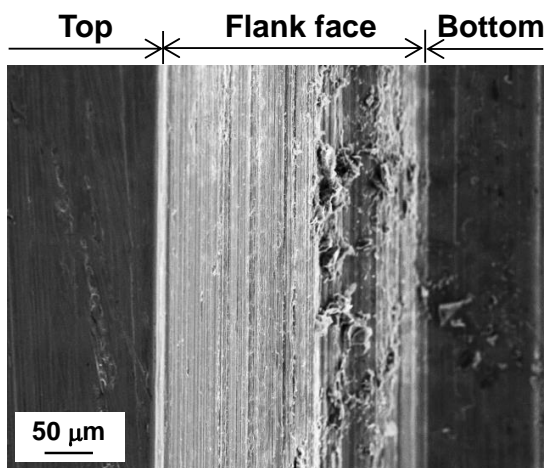


(e) TiCN film

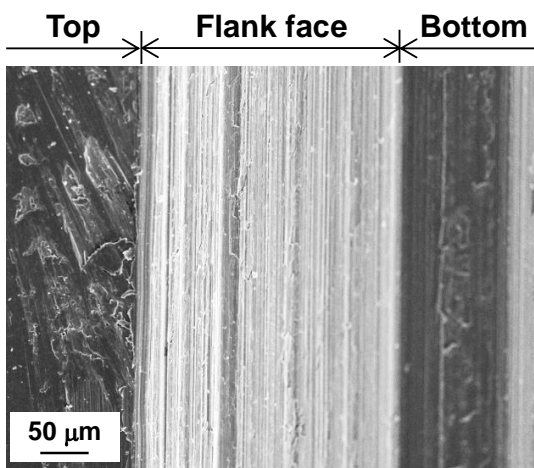
Fig. 3.14 SEM images of flank face of thread hole ($V_r = 10 \text{ m/min}$)



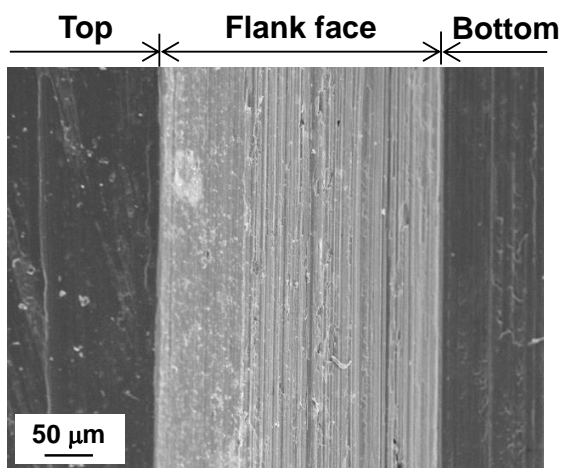
(a) Ni-P/cBN film ($\bar{d} = 10 \mu\text{m}$)



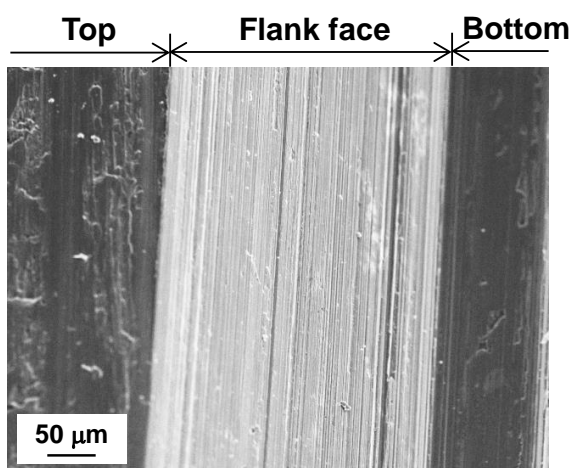
(b) Ni-P/SiC film ($\bar{d} = 5 \mu\text{m}$)



(c) Ni-P/SiC film ($\bar{d} = 1 \mu\text{m}$)



(d) Steam treatment



(e) TiCN film

Fig. 3.15 SEM images of flank face of thread hole ($V_r = 30 \text{ m/min}$)

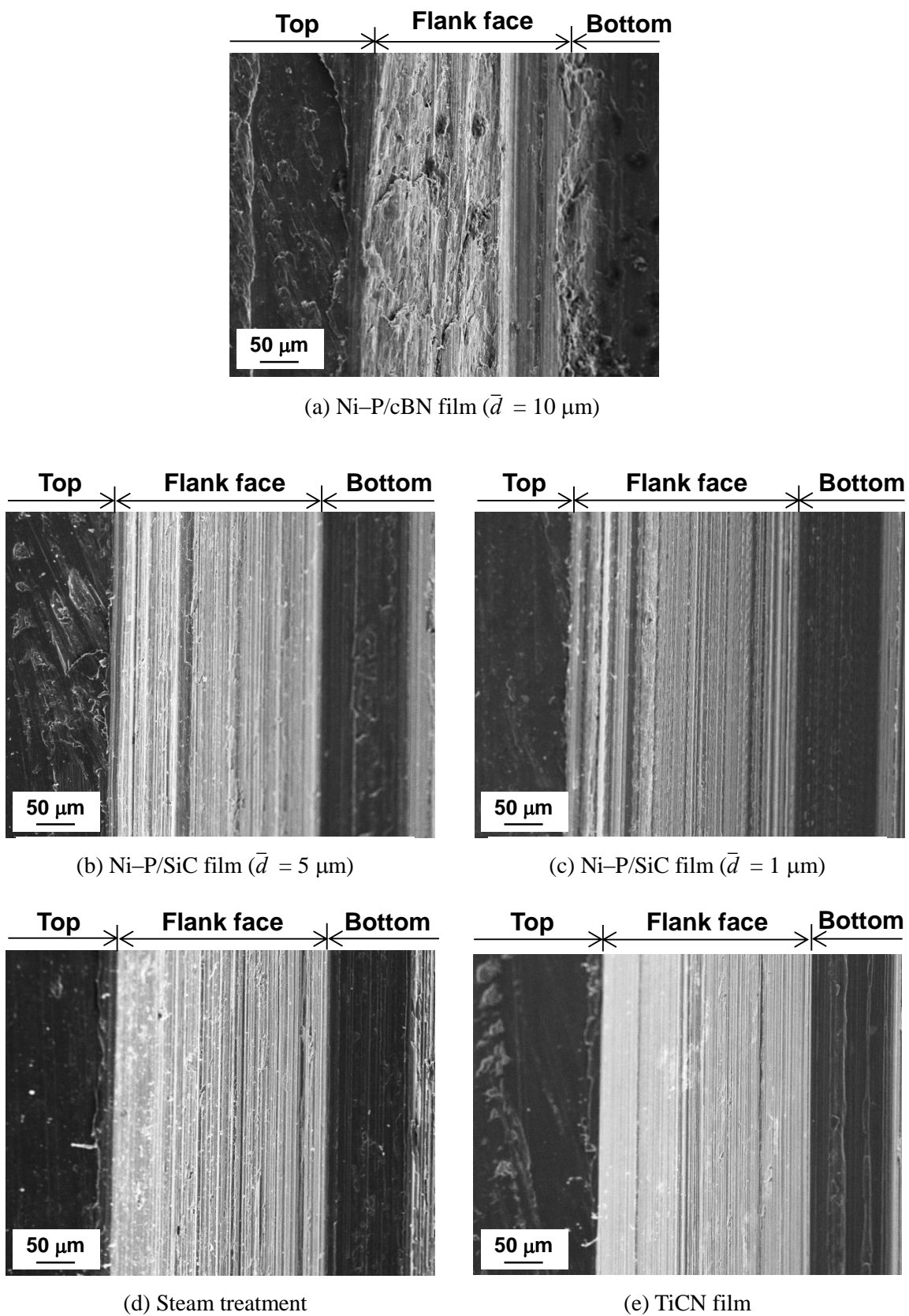


Fig. 3.16 SEM images of flank face of thread hole ($V_r = 50 \text{ m/min}$)

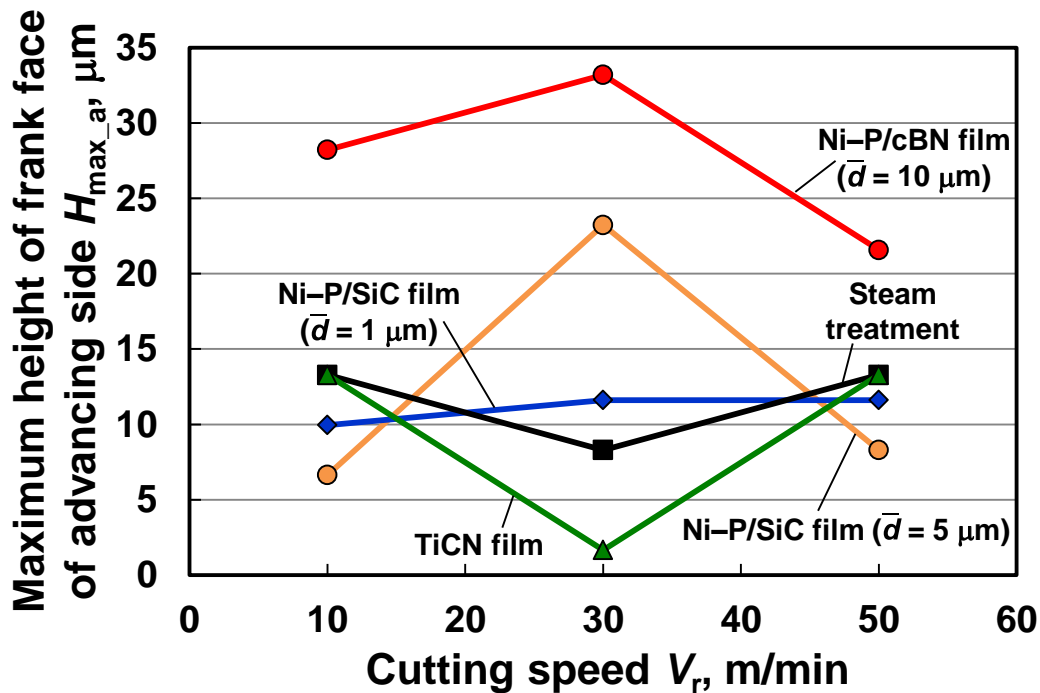


Fig. 3.17 Maximum height of frank face of advancing side

3.4.2 Cutting torque and thrust force

Figures 3.18 and 3.19 show the variation in cutting torque and thrust force over time, respectively. It is evident from Fig. 3.18 that the cutting torque of the Ni-P/cBN film was unstable for high values at 10 m/min and 50 m/min, whereas the other tools had relatively stable torque. As shown in Fig. 3.19, the thrust force of the TiCN coating film acts as the high tensile force produced between points B and C as shown in Fig. 3.13 in the cutting process at all cutting speeds. The absolute value of the thrust force of the composite films was smaller than that of the TiCN coating film, decreasing almost to zero or becoming positive (compression force) at low cutting speeds.

Figure 3.20 shows the relation between the mean cutting torque and cutting speed. It is evident from the figure that the tapping tool coated with the Ni-P/cBN particle composite film ($\bar{d} = 10 \mu\text{m}$) produced the highest cutting torque at all cutting speeds (2.5–3.7 Nm). We assume that this was because the friction coefficient of the Ni-P/cBN particle composite film was the highest of the all

surface treatments, as discussed in Section 2.4.3. This high friction caused damage and increased the roughness of the surface of the thread hole, as shown in Figs. 3.14–3.16. A large particle size creates a plowing effect, as demonstrated in Section 2.4.3. In contrast, the cutting torque of the other tapping tools was relatively constant at 1.8–2.3 Nm.

Figure 3.21 shows the relation between the thrust force and cutting speed. It is evident from the figure that the tapping tool coated with the TiCN film produced the highest tensile force, while that of the other tools was less than 100 N. The tensile force also increased in line with the cutting speed. This is undesirable because the application of a large tensile force to the tapping tool increases the diameter of the thread hole [11]. In contrast, the tapping tools coated with the Ni–P/abrasive particle composite film exhibited lower thrust forces. Especially, the tensile force by the composite films was less than 50 N at 50m/min. Because the thrust tensile force of the tool coated with the Ni–P/abrasive particle composite film was lower than that of the conventional tools, the drawing force on the thread hole was also lower. This suggested that the Ni–P/abrasive particle composite film can be used in the surface treatment of tapping tools working at high cutting speeds.

The optimal size of the SiC particles used in the composite film was less than 5.0 μm , as an excessively rough tool surface may cause damage and decrease the dimensional accuracy of the thread hole. Note again that the dimensions and precision of the thread holes machined with the tapping tool coated with the Ni–P/cBN particle composite film ($\bar{d} = 10 \mu\text{m}$) were within the relevant standards of the thread gauge.

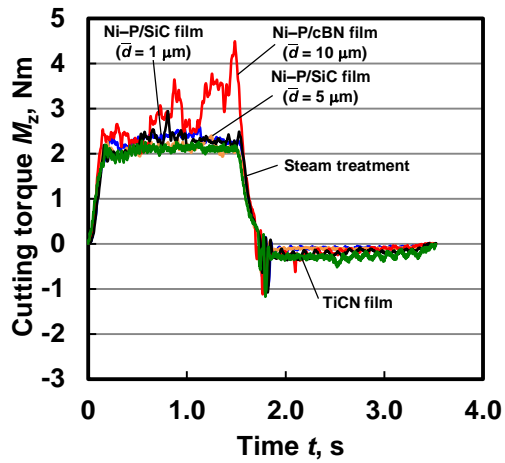
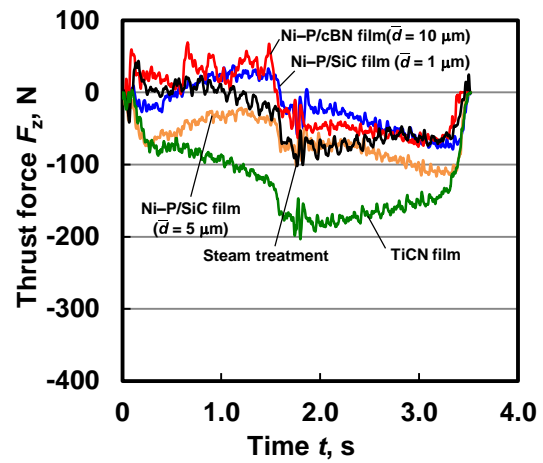
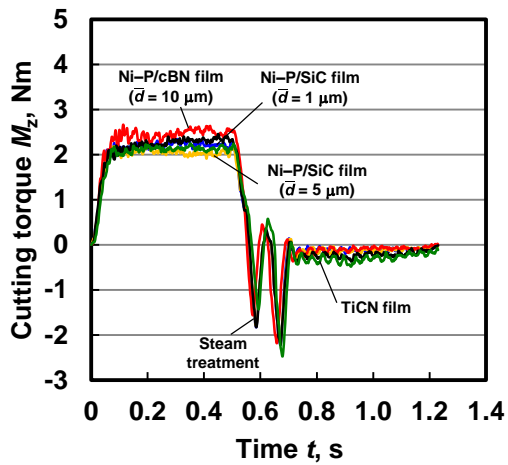
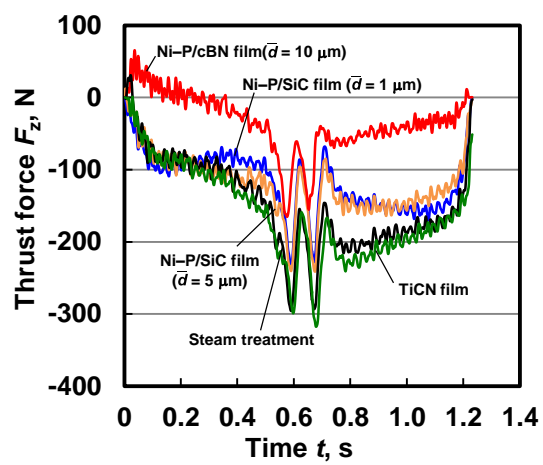
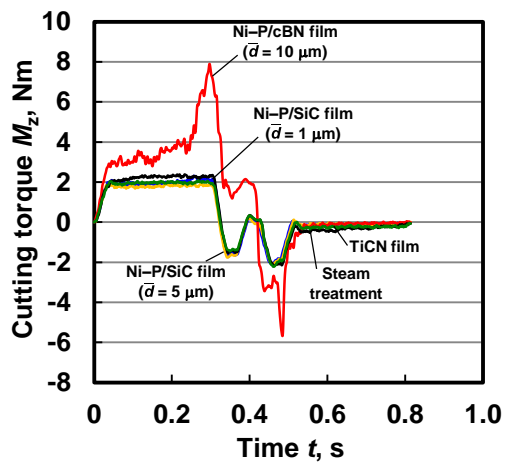
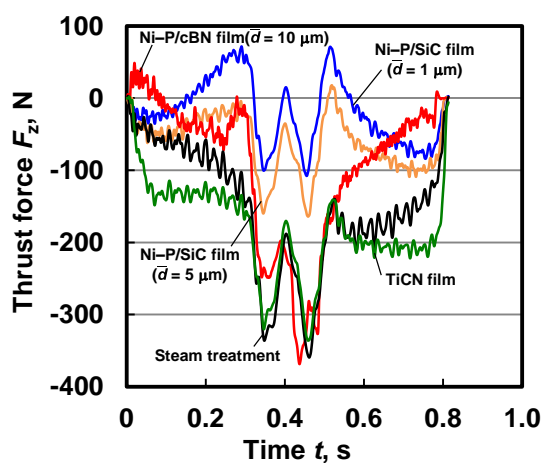
(a) $V_r = 10$ m/min(a) $V_r = 10$ m/min(b) $V_r = 30$ m/min(b) $V_r = 30$ m/min(c) $V_r = 50$ m/min(c) $V_r = 50$ m/min

Fig. 3.18 Relation between cutting torque and time

Fig. 3.19 Relation between thrust force and time

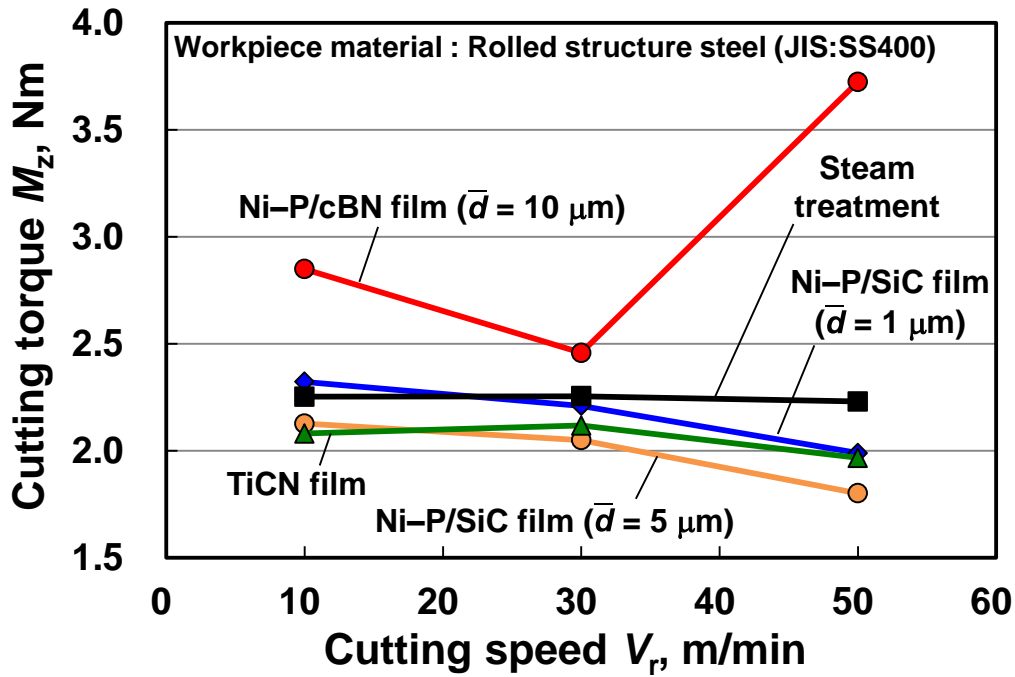


Fig. 3.20 Relation between cutting torque and cutting speed

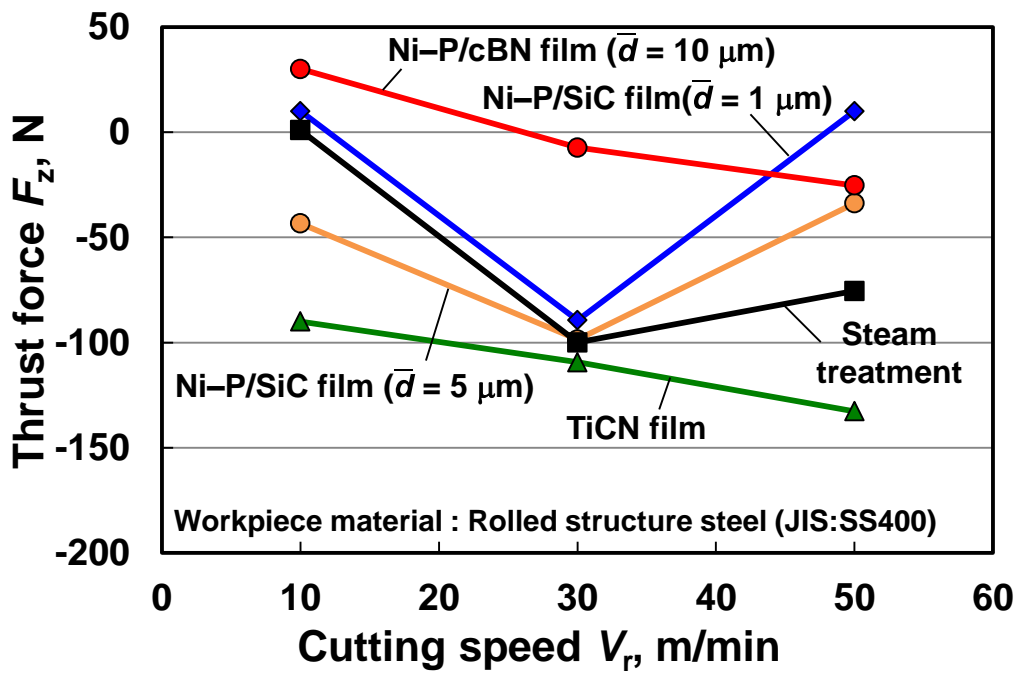


Fig. 3.21 Relation between thrust force and cutting speed

3.5 Effect of the diameter of codepositing particle on chip snarling

In order to investigate the effect of the diameter of codepositing particle on chip snarling, the tapping tool coated with Ni-P/SiC particle composite film using a smaller diameter of SiC particles ($\bar{d} = 0.3 \mu\text{m}$) was prepared. The tapping test was conducted using the tapping tool coated with Ni-P/SiC film ($\bar{d} = 1 \mu\text{m}$) or Ni-P/SiC film ($\bar{d} = 0.3 \mu\text{m}$). The workpiece was a carbon steel (JIS: S45C). Cutting speeds was 50 m/min, and lubrication was provided by an emulsion cutting oil (YUSHIROKEN FGE360, Yushiro Chemical industry Co., Ltd.) with a viscosity of 1.20 mPa·s at 21.6 °C. The number of cutting process was 25 holes.

Figure 3.22 show the snapshot of tapping tool after cutting 25 holes. The tapping tool coated with Ni-P/SiC film ($\bar{d} = 1 \mu\text{m}$) obviously prevented the chip snarling. In contrast, the tapping tool coated with Ni-P/SiC film ($\bar{d} = 0.3 \mu\text{m}$) caused the chip snarling on the tapping tool. This result indicated that the mean diameter of the codepositing SiC particles, which was effective in preventing the chip snarling, was over $1 \mu\text{m}$.

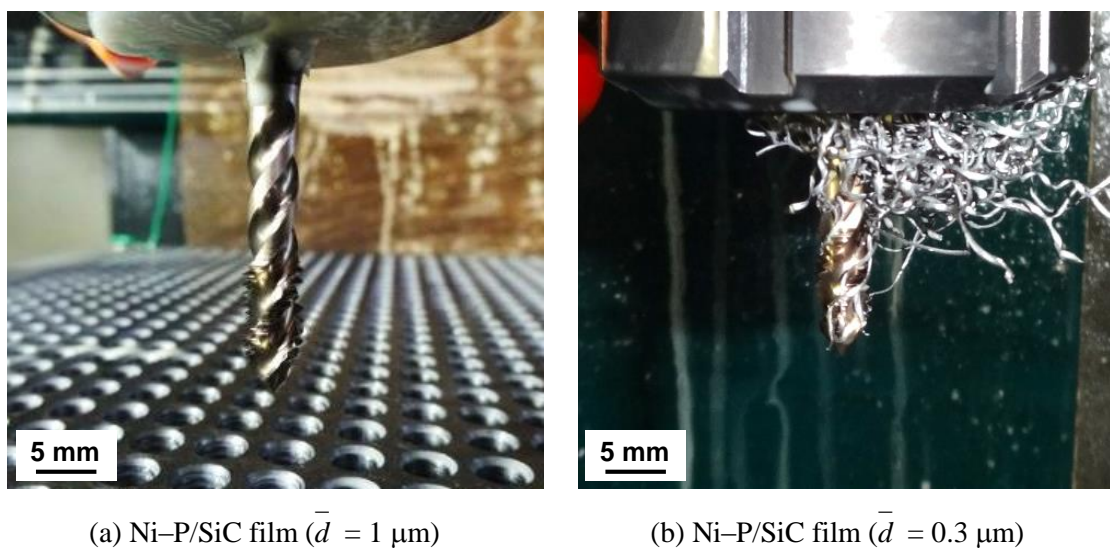


Fig. 3.22 Snapshot of tapping tool after tapping test

3.6 Conclusions

A tapping tool coated with the Ni-P/abrasive particle composite film was developed. The dimensional accuracy of the thread holes and the cutting resistance (i.e., cutting torque and thrust force) were experimentally investigated via tapping tests. The conclusions of this chapter are as follows:

- (1) Tapping tools coated with the Ni-P/cBN ($\bar{d} = 10 \mu\text{m}$), Ni-P/SiC ($\bar{d} = 5 \mu\text{m}$), and Ni-P/SiC ($\bar{d} = 1 \mu\text{m}$) films were developed.
- (2) The thread holes produced by the tools coated with the Ni-P/cBN ($\bar{d} = 10 \mu\text{m}$), Ni-P/SiC ($\bar{d} = 5 \mu\text{m}$), and Ni-P/SiC ($\bar{d} = 1 \mu\text{m}$) films satisfied the relevant standard for thread gauge. However, the surface of the thread holes machined by the tapping tool coated with the Ni-P/cBN particle composite film ($\bar{d} = 10 \mu\text{m}$) was rougher at all cutting speeds.
- (3) The tapping tool coated with the Ni-P/cBN particle composite film ($\bar{d} = 10 \mu\text{m}$) produced the highest cutting torque and thrust force.
- (4) The tensile force produced by the tool coated with the Ni-P/abrasive particle composite film was less than 50 N at 50 m/min.

References

- [1] Ivanina, V. I., “Influence of Parameters of the Cutting Part of Taps on Threading Accuracy,” *Measurement Techniques*, 48, 10, 2005, 990-994.
- [2] Ishimura, M., Yamanaka, H., Syoji, Y., Kobayashi, T. and Sawa, T., “Loosening of Bolted Joints Under Transverse Repeated Displacements,” *The Japan Society of Mechanical Engineers*, 77, 781, 2011, 1444-1452 (in Japanese).
- [3] Troubleshooting application problems with new taps,
<http://www.guhring.com/documents/Tech/Troubleshoot/Tap.pdf> (accessed 2016-4-23).
- [4] The Kinzoku Sangyo Simbunsha Press, http://www.neji-bane.jp/feature/testing_mcn.html#d
(accessed 2016-11-01).
- [5] Johnson, E., “Some Experiments on tapping,” *Proceeding of the Institution of Mechanical Engineers*, 164, 1, 1951, 46-51.
- [6] Doyle, D. E. and Dean, K. S., “Effect of Axial Forces on Dimensional Accuracy During Tapping,” *International Journal of Machine Tool Design and Research*, 14, 4, 1974, 325-333.
- [7] Saito, Y., Yamaguchi, T., Shibata, K., Kadota, Y., Kubo, T., Watanabe, W. and Hokkirigawa, K., “Development of a New Tapping Tool Covered with Nickel/Abrasive Particles Composite Film for Preventing Chip Snarling Chip Snarling and Tool Service Life Extension,” *Tribology Online*, 11, 2, 2016, 81-87.
- [8] Kadota, Y., Saito, Y., Yamaguchi, T., Shibata, K., Kubo, T., Wataru, W. and Hokkirigawa, K., “Evaluation of Threaded Hole Surface Machined with Tapping Tool Covered with Nickel/Abrasive Particles Composite Film,” *Proceeding of Tribology conference 2014 Autumn Morioka*, (2014), in USB memory (in Japanese).
- [9] Tanaka, R., Yamazaki, S., Hosokawa, A., Furumoto, T., Ueda, T. and Okada, M., “Analysis of Cutting Behavior During Tapping and Measurement of Tool Edge Temperature Measured by a

Two-Color Pyrometer,” *Journal of Advanced Mechanical Design, Systems, and Manufacturing*, **7**, 2, 2013, 115-123.

[10] Fukumoto, I. and Heshiki, K., “Multi-Regression Analysis of the Grinding Surface Roughness in Steel,” *Transactions of the Japan Society of Mechanical Engineers*, 53, 491, 1987, 1577-1580 (in Japanese).

[11] Araujo, C. A., Silveira, L. J., Jun, B. M., Kapoor, G. S. and Vor, D. R., “A Model for Thread Milling Cutting Forces,” *International Journal of Machine Tools and Manufacture*, 46, 2006, 2057-2065.

Chapter 4

Chip snarling prevention and tapping tool service life extension by coating with Ni–P/abrasive particle composite film

4.1 Introduction

A common cause of problems in the tapping process is the failure to dispose the chip effectively [1-4]. Snarled chips on the tapping tool cause damage to the cutting edge or breakage of the tool. Because tapping is the final stage in the production process, defects arising during tapping are costly. In general, tapping is performed at speeds less than 10 m/min, as chip snarling often occurs at higher cutting speeds. When snarled on the tapping tool, chips must be manually removed. Therefore, to increase the efficiency of the tapping process, improving chip disposal at high cutting speeds is necessary. To improve wear resistance and lubrication, hard coatings or lubricant coating films have been developed for tapping tools [5-8]. However, it has been reported that coated tapping tools produce chips of greater length and with greater curl, exacerbating the snarling problem [9-10]. Hence, tapping tools that prevent chip snarling at high cutting speeds and increase the tool service life must be developed.

In this chapter, tapping tests were performed to investigate whether a tapping tool coated with Ni–P/abrasive particle composite film, described in Chapter 2, was able to prevent chip snarling at high cutting speeds and increase the tool service life. A cutting model for the rake face of the tapping tool was also proposed, and the friction coefficient of the rake face at the tool–workpiece interface was calculated from the measured thrust force and cutting torque. The effect of this estimated friction coefficient on chip snarling was analyzed.

4.2 Experimental methods

4.2.1 Tapping test

Table 4.1 shows the tapping test conditions. The tapping tools, workpiece, lubricant, and experimental apparatus were same as those used in the tests presented in Chapter 3. The cutting speeds were 10 (the conventional cutting speed), 30, and 50 m/min. Twenty-five holes were cut. The evacuated chips and the snarled chips were collected after each thread hole had been cut.

Table 4.1 Experimental conditions

Type of tapping tool	Spiral-tap (HSS, M6 × 1)
Surface treatment	Ni–P/cBN film ($\bar{d} = 10 \mu\text{m}$)
	Ni–P/SiC film ($\bar{d} = 5 \mu\text{m}$)
	Ni–P/SiC film ($\bar{d} = 1 \mu\text{m}$)
	Steam treatment
	TiCN film
Workpiece material	Rolled-structure steel (JIS: SS400)
Cutting speed V_r, m/min	10, 30, 50
Lubricant	Emulsion cutting oil ($\nu = 1.20 \text{ mPa}\cdot\text{s}$ at 21.6°C)

4.2.2 Estimation of friction coefficient at the rake face of the tool–workpiece interface

The friction coefficient between the rake face of the tapping tool and the chip was estimated from the measured thrust force and cutting torque. The cutting resistance at point B in Fig. 3.10 was used to estimate the resultant cutting resistances at each cutting edge, as the cutting resistance between points B and C was affected by the friction between the flank face of the tool and thread hole [11]. The positive and negative cutting torques represent the counterclockwise and clockwise directions, respectively. For thrust force, a positive value represents compression force, whereas a negative value represents tensile force.

To estimate the friction coefficient, it was assumed that the measured torque and thrust force were generated by the resultant cutting resistances from the eight cutting edges. Figure 4.1 shows the global coordinate system (X - Y - Z) [8] wherein X is the axis in the direction of circumferential force, Y is the axis in the direction of axial force, and Z is the axis in the direction of radial force. Figure 4.2 shows the schematics of the relations between the global coordinate system (X - Y - Z) and the local coordinate system (x - y - z), where x is the axis in the direction of normal force on the rake face, y is the axis in a direction parallel to the front cutting edge, and z is the axis in the direction vertical to the rake face. Here, β is the chamfer angle [degree], θ is the torsion angle [degree], and α_n is the rake angle [degree].

The transformation matrix M for the rotating coordinate conversion is given by the angles β , θ , and α_n as follows:

$$\begin{aligned} M &= \begin{pmatrix} \sin \alpha_n & 0 & \cos \alpha_n \\ 0 & 1 & 0 \\ -\cos \alpha_n & 0 & \sin \alpha_n \end{pmatrix} \begin{pmatrix} \cos \theta & -\sin \theta & 0 \\ \sin \theta & \cos \theta & 0 \\ 0 & 0 & 1 \end{pmatrix} \begin{pmatrix} 1 & 0 & 0 \\ 0 & \cos \beta & -\sin \beta \\ 0 & \sin \beta & \cos \beta \end{pmatrix} \\ &= \begin{pmatrix} \sin \alpha_n \cos \theta & -\sin \alpha_n \sin \theta \cos \beta + \cos \alpha_n \sin \beta & \sin \alpha_n \sin \theta \sin \beta + \cos \alpha_n \cos \beta \\ \sin \theta & \cos \theta \cos \beta & -\cos \theta \sin \beta \\ -\cos \alpha_n \cos \theta & \cos \alpha_n \sin \theta \cos \beta + \sin \alpha_n \sin \beta & -\cos \alpha_n \sin \theta \sin \beta + \sin \alpha_n \cos \beta \end{pmatrix} \quad (4.1). \end{aligned}$$

Thus, the measured force components (F_M , F_T , F_Z) in the global coordinate system (X - Y - Z) are transformed into the cutting force components (F_x , F_y , F_z) in the local coordinate system (x - y - z) as follows:

$$\begin{pmatrix} F_x \\ F_y \\ F_z \end{pmatrix} = M \begin{pmatrix} F_M \\ F_T \\ F_{Z^*} \end{pmatrix} \quad (4.2)$$

where F_M is the circumferential force [N], which is the cutting torque divided by the radius of the tapping tool, F_T is the axial force [N], which is the thrust force measured by the dynamometer, and F_{Z^*} is the radial force [N]. F_{Z^*} cannot be measured by the dynamometer because it is the centripetal force in the radial direction of the tap. To estimate the radial force, two hypotheses were introduced. The first was that a chip flows along the surface of the screw thread, as shown in Fig. 4.3. Thus, the chip

flow angle η was determined from the tool geometry to be 15.37 degree. The second was that the chip flow direction is the same as the direction of friction force [12]. The chip flow angle η can also be expressed using F_y and F_z as follows:

$$\tan \eta = \frac{F_y}{F_z} \quad (4.3).$$

Combining Eqs. (4.1)–(4.3), F_{Z^*} can be expressed as follows:

$$F_{Z^*} = \frac{(\sin \theta - \sin \alpha_n \cos \theta \tan \eta) F_M + (\cos \theta \cos \beta + \sin \alpha_n \sin \theta \cos \beta \tan \eta - \cos \alpha_n \sin \beta \tan \eta) F_T}{\cos \alpha_n \cos \beta \tan \eta + \sin \alpha_n \sin \theta \sin \beta \tan \eta + \cos \theta \sin \beta} \quad (4.4).$$

The friction force F is calculated as follows:

$$F = \sqrt{F_z^2 + F_y^2} \quad (4.5).$$

Thus, the friction coefficient is given as follows:

$$\bar{\mu} = \frac{F}{F_x} \quad (4.6).$$

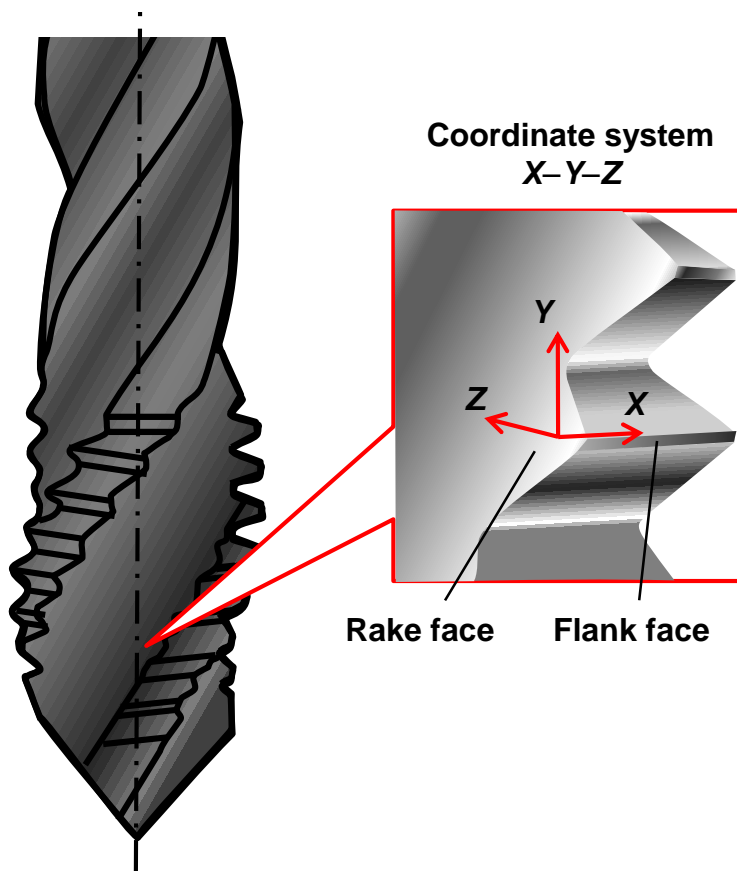


Fig. 4.1 The global coordinate system (X-Y-Z) on the cutting edge

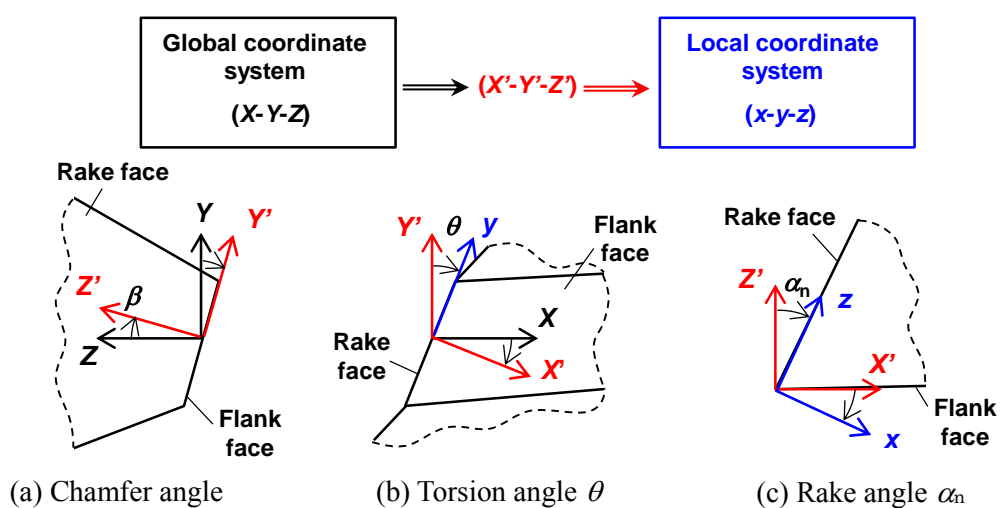


Fig. 4.2 Schematics of the rotation angles

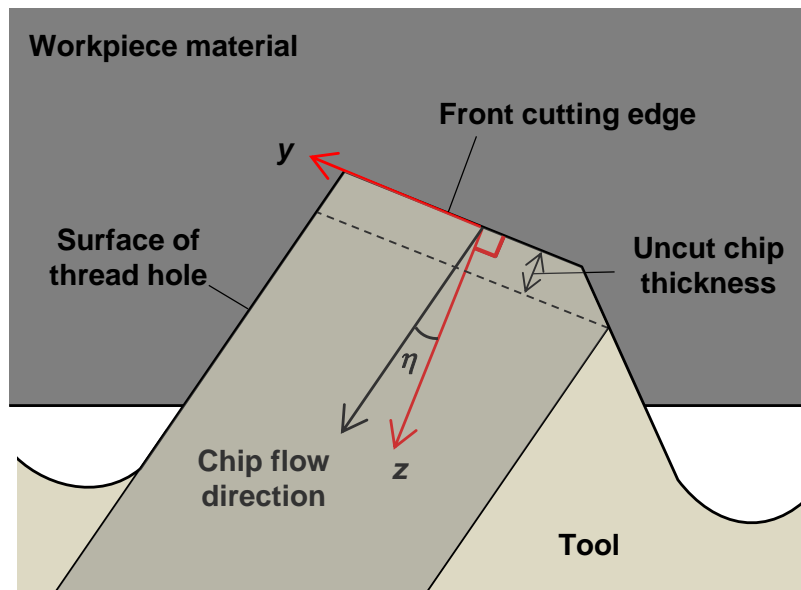


Fig. 4.3 Schematic of the chip flow angle

4.2.3 Durability testing

The durability testing of the tapping tools was conducted for evaluating the tool service life. The tapping tools, workpiece, experimental apparatus, and lubricant were the same as those used in the tapping test discussed in Chapter 2. The cutting speed was 50 m/min. The sound level was measured using a sound level meter (LA-5560, Ono Sokki Co., Ltd). The cutting test was conducted until the number of tapping processes reached the end of the tool service life. This was defined as either a tool breakage or an abrupt increase in the cutting torque, with noise exceeding 90 dB. In both cases, the quality of the thread hole was then evaluated using a screw thread gauge. Chip snarling was checked after every 200 holes, and the chips were not removed even though the chips snarled on the tapping tool.

4.3 Results and discussion

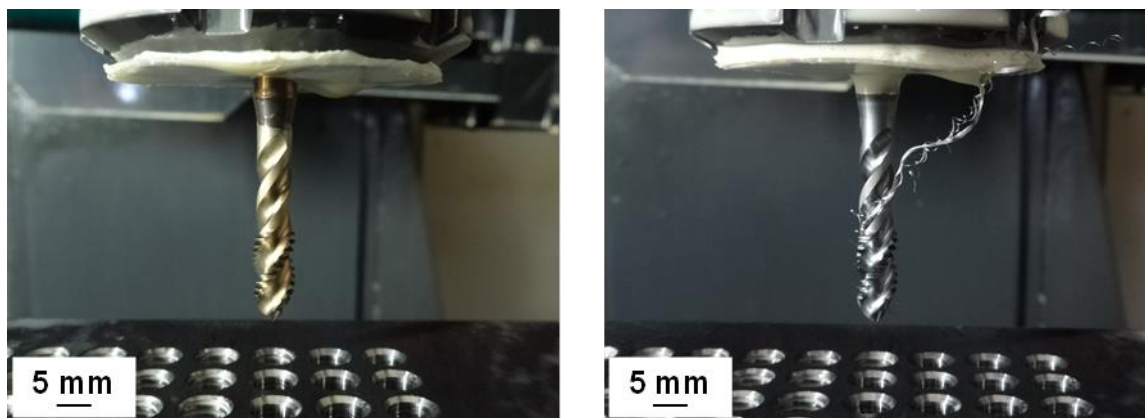
4.3.1 Chip snarling and chip curl diameter

4.3.1.1 Rate of chip snarling

Figure 4.4 shows a snapshot of the tapping tool after tapping at 10 m/min. It is evident from the figure that the chips were snarled on the tool coated with the TiCN coating film (Fig. 4.4(b)); however, they were not snarled on the tool coated with the Ni–P/SiC particle composite film ($\bar{d} = 1.0 \mu\text{m}$) (Fig. 4.4(a)). To evaluate the frequency of chip snarling, the rate of chip snarling R_c was introduced and is expressed as follows:

$$R_c = \frac{N_c}{N_{all}} \times 100 \quad (4.7)$$

where N_c is the number of trials with chip snarling [holes] and N_{all} is the number of tapping processes [holes] ($N_{all} = 25$ holes). Figure 4.5 shows the relation between the cutting speed and the rate of chip snarling. With the exception of the tool coated with the TiCN film, the rate of snarling increased as the cutting speed increased. In the case of the tapping tool coated with the TiCN film, the rate of chip snarling decreased as the cutting speed increased. The tapping tool coated with the Ni–P/SiC film ($\bar{d} = 1 \mu\text{m}$) had the smallest rate at nearly 0% at all cutting speeds. This clearly demonstrated the effectiveness of the composite film coating in reducing the frequency of chip snarling across a wide range of cutting speeds.



(a) No chip snarling (Tapping tool coated with Ni-P/SiC film ($\bar{d} = 1.0 \mu\text{m}$); $V_r = 10 \text{ m/min}$)

(b) Chip snarling (Tapping tool coated with TiCN film; $V_r = 10 \text{ m/min}$)

Fig. 4.4 Snapshot of tapping tool after tapping test

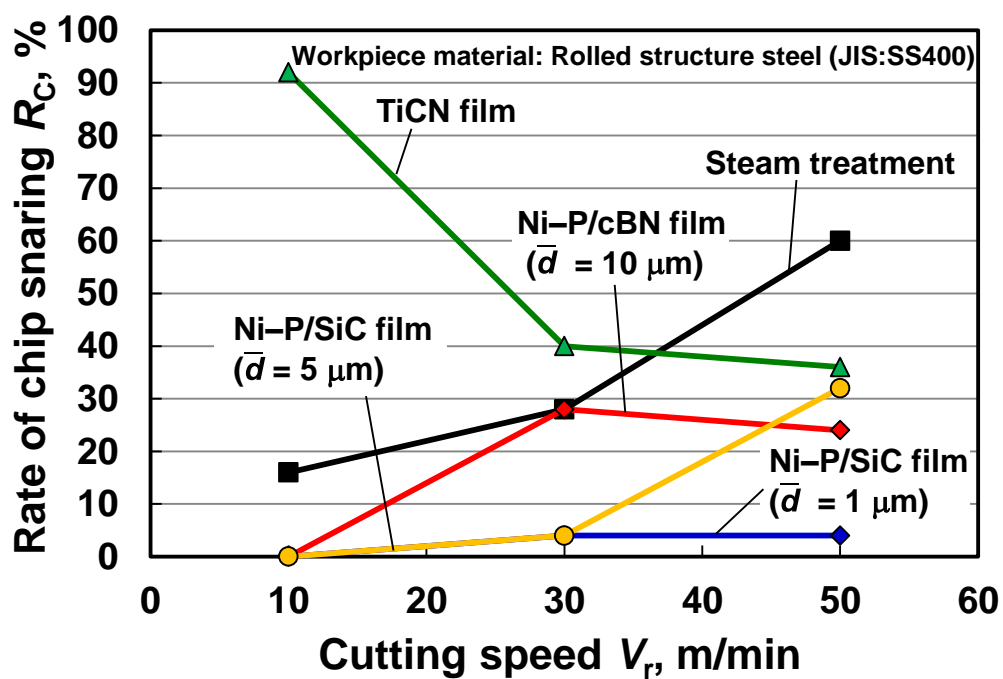


Fig. 4.5 Relation between the rate of chip snarling and cutting speed

4.3.1.2 Chip curl geometry

Figures 4.6–4.8 show the collected chips that were cut from the 4th cutting edge at 10, 30, and 50 m/min, respectively. From these figures, it was observed that the chip curl diameter was smaller for the tapping tools coated with the composite films than that for the steam treatment tool or the tool coated with the TiCN film at any cutting speed. Furthermore, the chip curl diameter increased in line with an increase in the cutting speed. This suggested a relation between the chip curl diameter and chip snarling. Next, the effect of the chip shape on the chip snarling was analyzed.

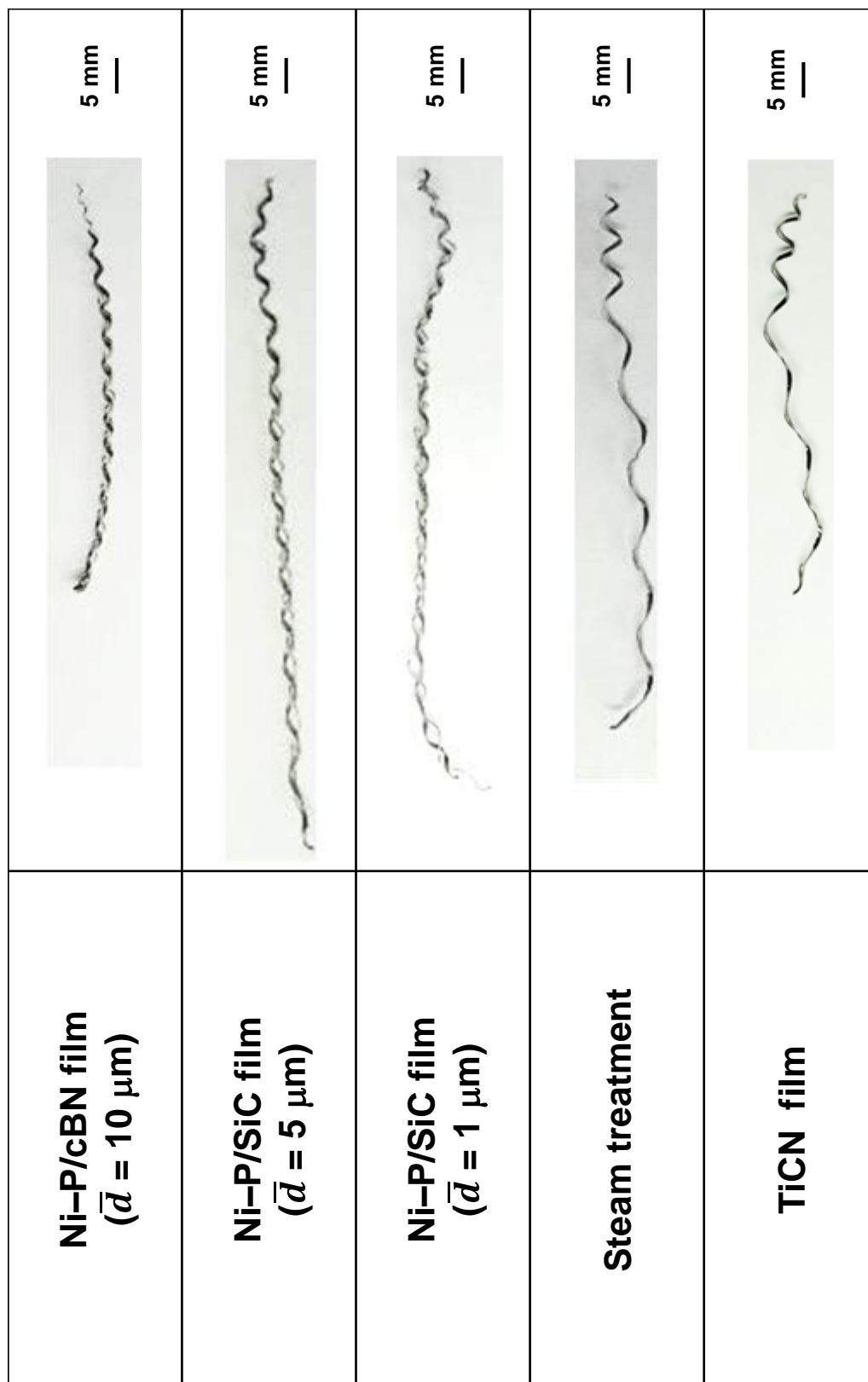


Fig. 4.6 Cutting chip for the 4th cutting edge at 10 m/min

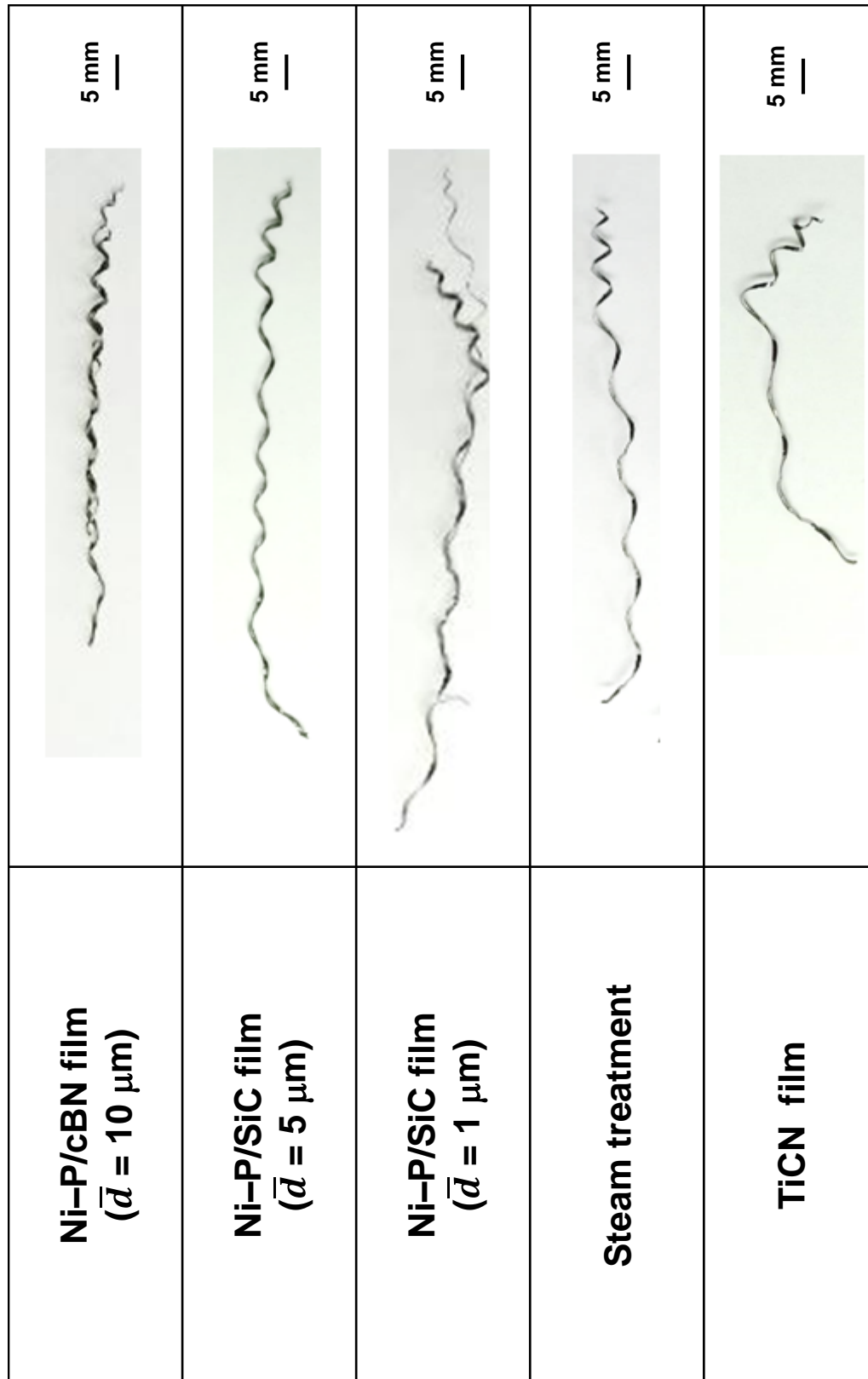


Fig. 4.7 Cutting chip for the 4th cutting edge at 30 m/min

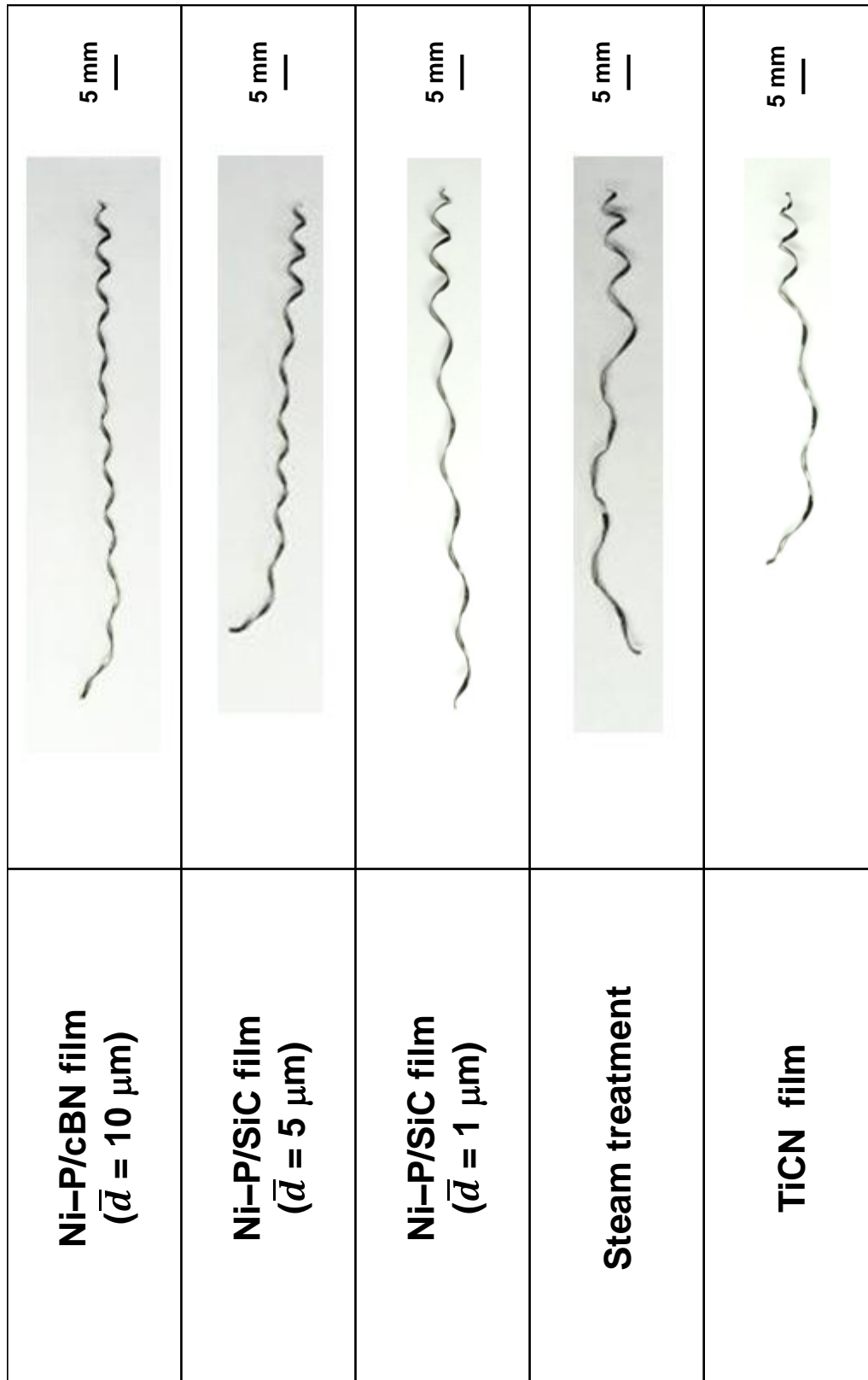


Fig. 4.8 Cutting chip for the 4th cutting edge at 50 m/min

4.3.1.3 Effect of chip curl diameter on chip snarling

To evaluate the geometry of chip curl, the diameter was measured as shown in Fig. 4.9. The chip was divided into three regions along the chip length: Region I, Region II, and Region III. In Region I, the chip curl diameter increased until the uncut chip thickness became constant. Assuming that the cutting distance is equal to the chip length, the chip length in Region I is the length L_1 , which can be expressed as follows:

$$L_1 = \frac{\pi d w}{P \cos \gamma} \quad (4.8)$$

where d is the tapping tool diameter [mm], w is the width of the cutting edge of the tapping tool [mm], p is the pitch of the thread hole [mm], and γ is the lead angle [degree]. Region II was defined as the region between the end of Region I and the point at which the chip rotates once along the helical flute after Region I. In this region, the shape of the curl is constant. Thus, the chip length in this stable region (L_S) is given by the following equation:

$$L_S = \pi W_t \quad (4.9)$$

where W_t is the width of the helical flute (Fig. 4.10). In this study, the length of Region II was 13.2–23.2 mm. Region III was defined as remainders are of the chip (Region II). In this study, the chip curl diameter in Region II was used to investigate the effect of the coating films on the chip curl diameter during tapping [13].

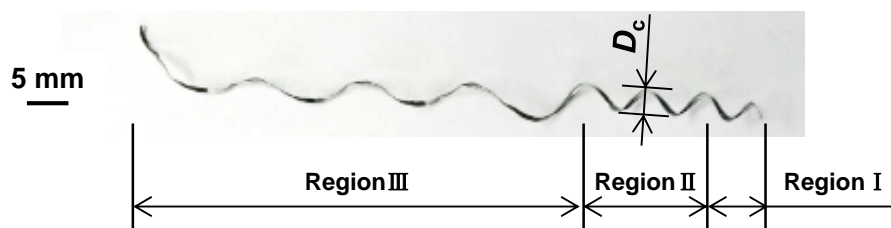


Fig. 4.9 Chip curl diameter in stable region



Fig. 4.10 Width of the helical flute

Figure 4.11 shows the relation between the chip curl diameter and cutting speed. It is evident from the figure that the chip curl diameters for the tools coated with composite films were smaller than those for the other tapping tools at all cutting speeds. With the exception of the tool coated with TiCN film, the chip curl diameter increased in line with an increase in the cutting speed. In contrast, the chip curl diameter for the tapping tool coated with TiCN film decreased as the cutting speed increased. Figure 4.12 shows the relation between the rate of chip snarling and the chip curl diameter. The rate of snarling increased in line with an increase in the chip curl diameter for chip curl diameters larger than 2.3 mm. In contrast, chip snarling did not occur (i.e., $R_c = 0\%$) at chip curl diameters less than 2.3 mm. This demonstrated that the tools coated with composite films prevented chip snarling by reducing the chip curl diameter. Further, the relation between the width of the helical flute (W_t), which the cutting chips pass through, and the chip curl diameter were investigated using the dimensionless chip curl diameter D_d defined as follows [11]:

$$D_d = \frac{D_c}{W_t} \quad (4.10).$$

When the D_d value reaches 1.0, the chip curl diameter is the same as the width of the helical flute. The relation between the dimensionless chip curl diameter and the rate of chip snarling is shown in Fig. 4.13. It is evident from the figure that when the dimensionless chip curl diameter was greater than 0.8, the rate of chip snarling increased in line with the dimensionless chip curl diameter, exceeding 40% of the rate of chip snarling at a diameter of approximately 1.0. Thus, chip snarling became more frequent when the chip curl diameter approached the width of the helical flute. Figures 4.14(a) and

4.14(b) show schematics of the tapping processes without and with chip snarling, respectively. When the chip curl diameter was shorter than the width of the helical flute, the chips were evacuated along the flute. In contrast, when the chip curl diameter approached the width of the helical flute, the chips followed the spiral flute of the tapping tool, producing chip snarling. Hanasaki et al. [14] noted that the chip curl of the drilling process was also affected by the geometry of the helical flute of the drilling tool because of the binding force from the wall of the flute.

These results suggested that the tool coated with the Ni-P/abrasive particle composite film prevented chip snarling by decreasing the chip curl diameter at both high and low cutting speeds.

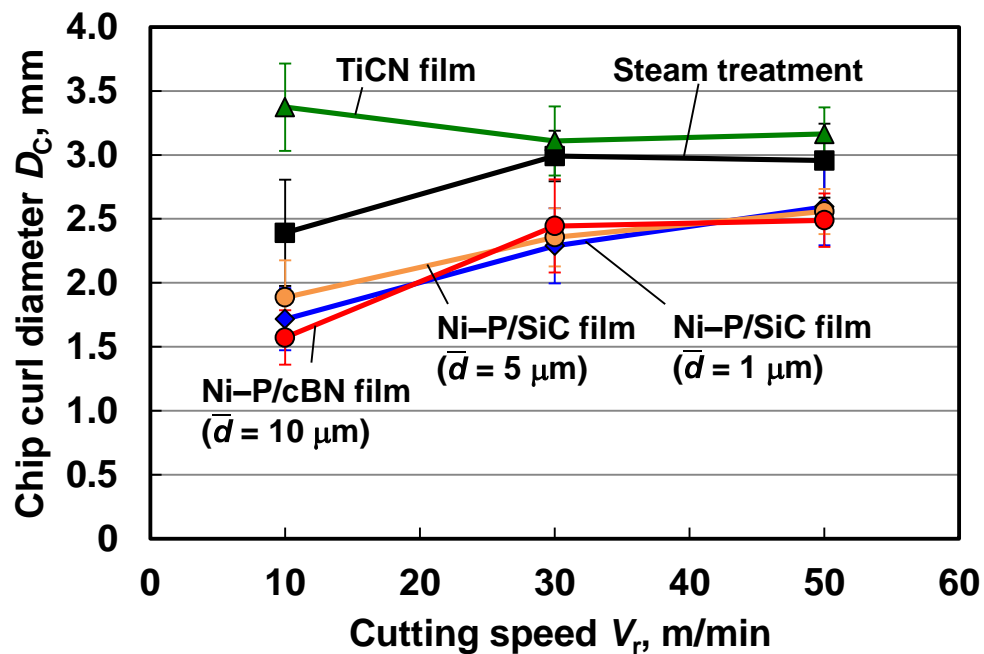


Fig. 4.11 Relation between the chip curl diameter and cutting speed

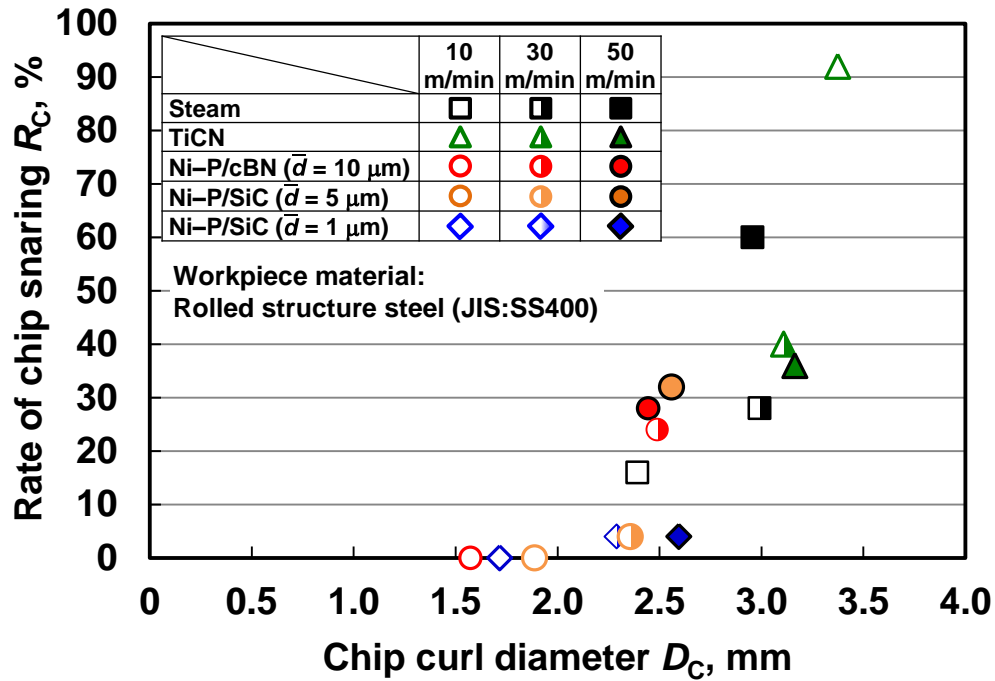


Fig. 4.12 Relation between the rate of chip snarling and chip curl diameter

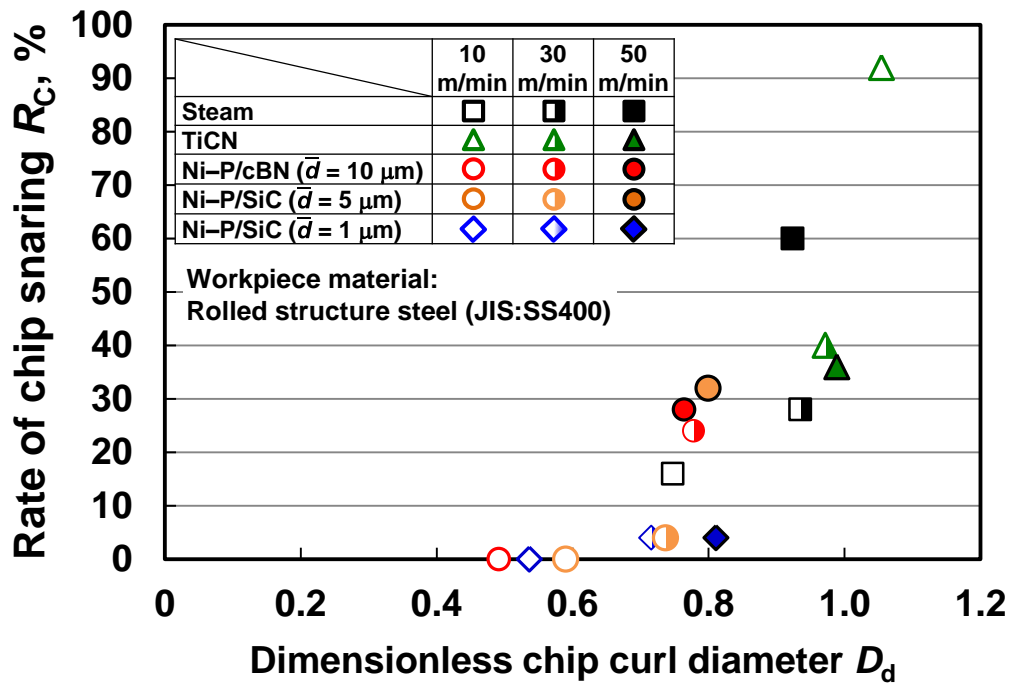


Fig. 4.13 Relation between the rate of chip snarling and dimensionless chip curl diameter

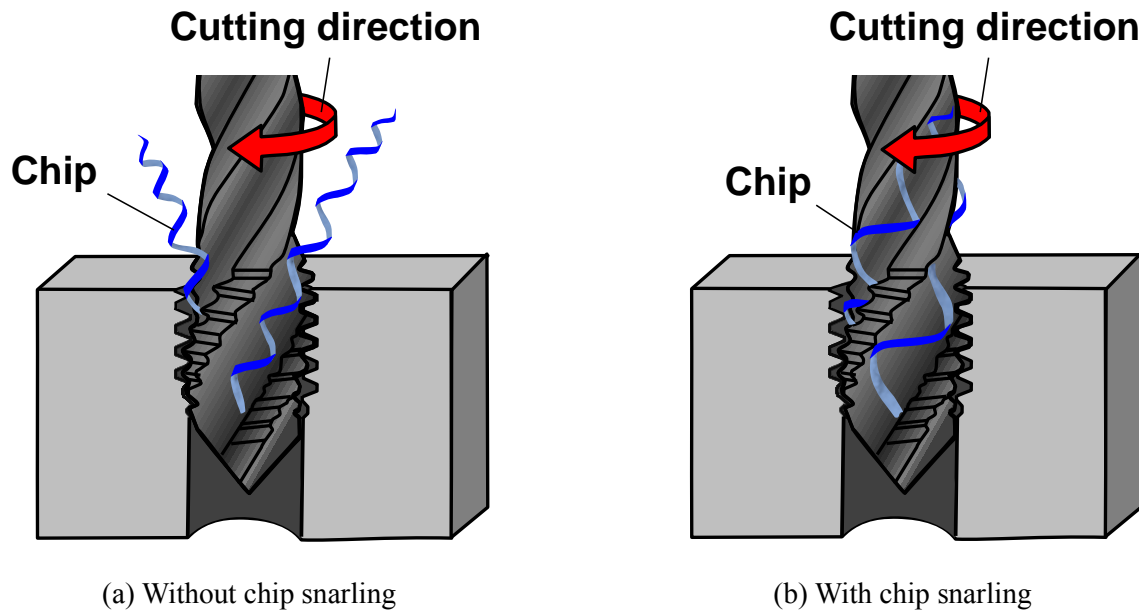


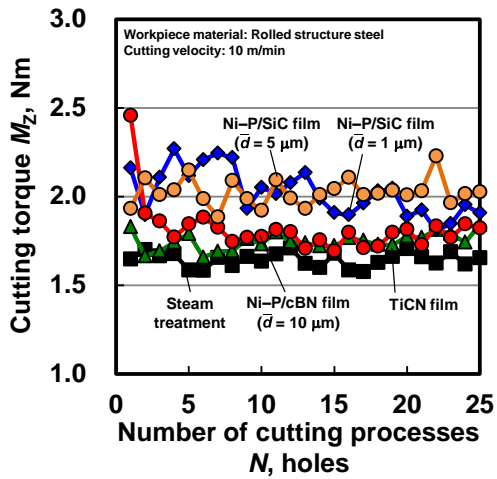
Fig. 4.14 Schematics of the tapping process

4.3.2 Effect of the friction coefficient on chip curl diameter

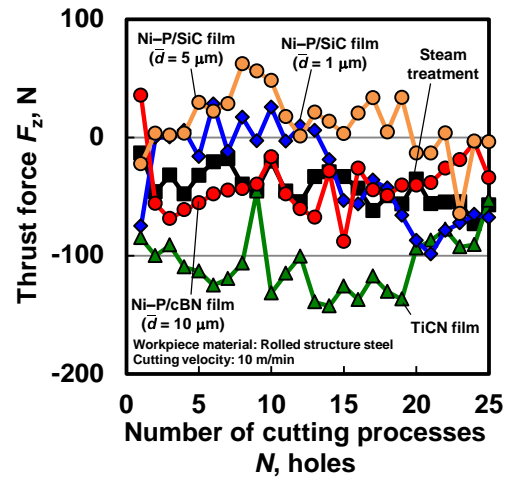
4.3.2.1 Cutting torque and thrust force

Figures 4.15(a)–4.15(c) show the change in the cutting torque with respect to the number of cutting processes at 10, 30, and 50 m/min, respectively. In Fig. 4.15(a), the cutting torque of the Ni–P/cBN film ($\bar{d} = 10 \mu\text{m}$) was higher than 2.4 Nm at the first hole, which then decreased to 1.8 Nm. The other tools showed almost constant values. The cutting torques of the Ni–P/SiC film ($\bar{d} = 5 \mu\text{m}$) and Ni–P/SiC film ($\bar{d} = 1 \mu\text{m}$) were both higher than 1.8 Nm. From Fig. 4.15(b), the cutting torque of the Ni–P/SiC film ($\bar{d} = 1 \mu\text{m}$) and steam treatment decreased as the number of cutting processes increased. The other tools showed almost constant values, with the cutting torque of the Ni–P/cBN film ($\bar{d} = 10 \mu\text{m}$) and Ni–P/SiC film ($\bar{d} = 5 \mu\text{m}$) being approximately 2.4 and 1.8 Nm, respectively. Figure 4.15(c) shows that the cutting torque of the Ni–P/cBN film ($\bar{d} = 10 \mu\text{m}$) was greater than 2.8 Nm at the first hole, which then decreased to 1.8–2.2 Nm. The cutting torque of the Ni–P/SiC film ($\bar{d} = 1 \mu\text{m}$) was nearly constant at approximately 1.9 Nm. Additionally, the values for the other tools were approximately constant at 1.6–1.8 Nm.

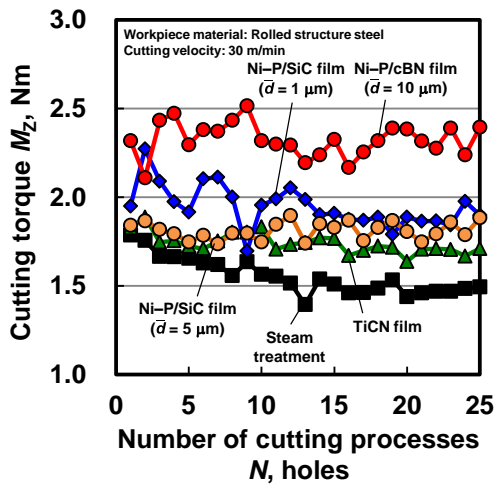
Figures 4.16(a)–4.16(c) show the change in the thrust force with respect to the number of cutting processes at 10, 30, and 50 m/min, respectively. As shown in Fig. 4.16(a), the magnitudes of the thrust forces for the tapping tool with steam treatment and the tools coated with the Ni–P/cBN ($\bar{d} = 10 \mu\text{m}$) and Ni–P/SiC ($\bar{d} = 1 \mu\text{m}$) films ranged between –100 and 0 N. The thrust force for the tool coated with Ni–P/SiC film ($\bar{d} = 5 \mu\text{m}$) was close to 0 N. The tool coated with the TiCN film exhibited the lowest force. Figure 4.16(b) shows that the thrust force of the tapping tools with steam treatment, that coated with the Ni–P/SiC film ($\bar{d} = 5 \mu\text{m}$), and that coated with the Ni–P/SiC film ($\bar{d} = 1 \mu\text{m}$) ranged between –100 and 0 N. The thrust force of the tools coated with the TiCN and Ni–P/cBN ($\bar{d} = 10 \mu\text{m}$) films were close to –100 N. Figure 4.16(c) shows that the thrust forces of the tools with the Ni–P/cBN film ($\bar{d} = 10 \mu\text{m}$) and steam treatment decreased as the number of cutting processes increased to approximately –100 N and –80N, respectively. Other tools exhibited almost constant values of –50 N.



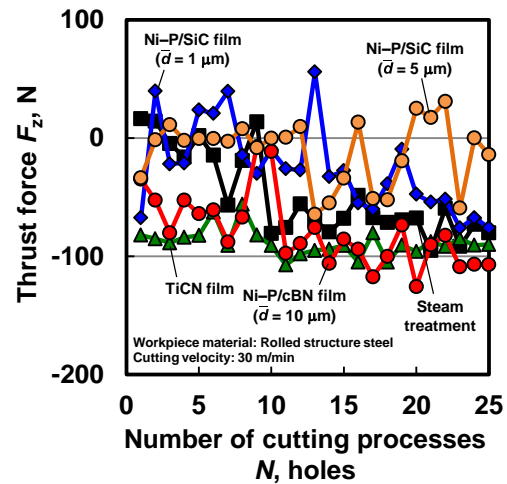
(a) $V_r = 10$ m/min



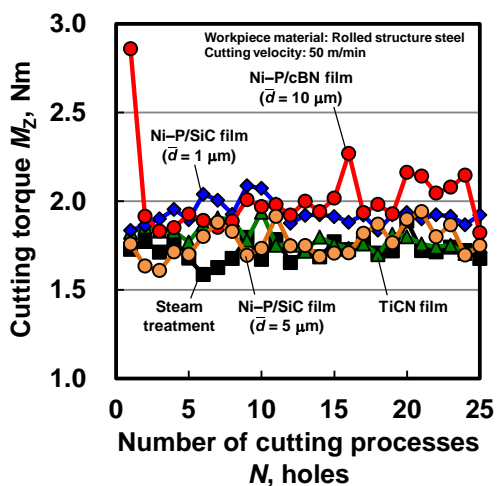
(a) $V_r = 10$ m/min



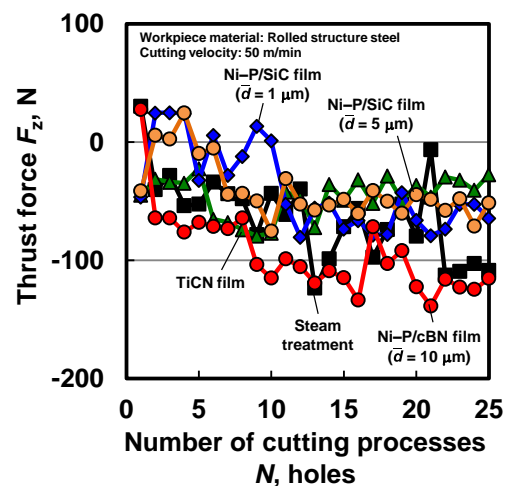
(b) $V_r = 30$ m/min



(b) $V_r = 30$ m/min



(c) $V_r = 50$ m/min



(c) $V_r = 50$ m/min

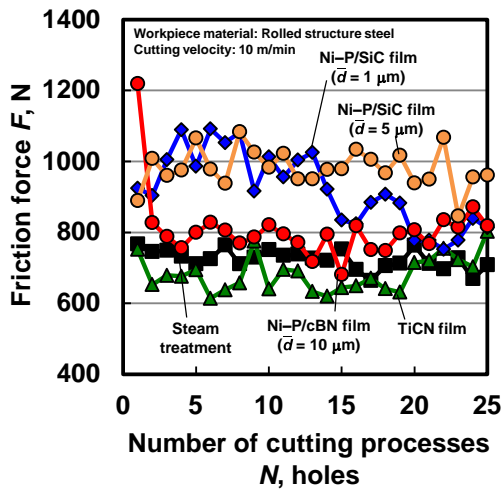
Fig. 4.15 Change in cutting torque with respect to the number of cutting process

Fig. 4.16 Change in thrust force with respect to the number of cutting process

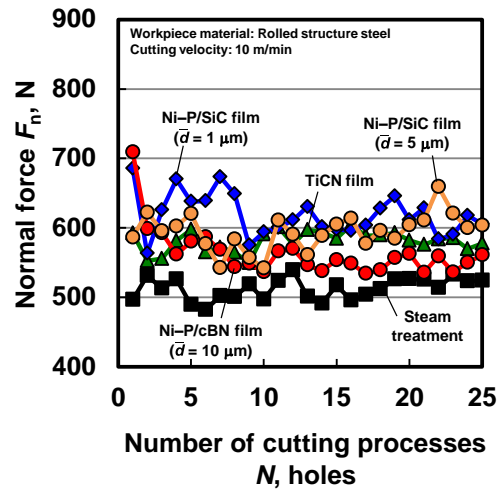
4.3.2.2 Estimated friction coefficient

Figures 4.17(a)–4.17(c) show the change in the friction force with respect to the number of cutting processes at 10, 30, and 50 m/min, respectively. From these figures, the friction forces for the novel tapping tools were greater than 800 N. The forces for the tapping tool coated with the Ni–P/cBN ($\bar{d} = 10.0 \mu\text{m}$) and Ni–P/SiC ($\bar{d} = 1.0 \mu\text{m}$) films decreased as the number of cutting processes increased under all conditions. This decrease could be due to tool wear. In contrast, the values for the other tools were nearly constant between 600 and 800 N.

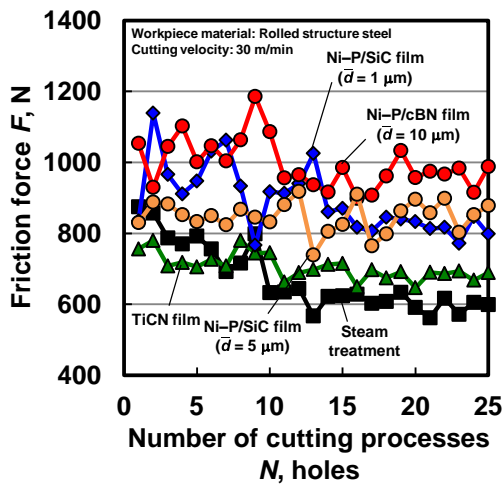
Figures 4.18(a)–4.18(c) show the change in the normal force with respect to the number of cutting processes at 10, 30, and 50 m/min, respectively. From these figures, the normal forces for the Ni–P/cBN film ($\bar{d} = 10.0 \mu\text{m}$) at 30 and 50 m/min were greater than 600 N. In contrast, the other tools showed almost constant values between 500 and 600 N under all cutting conditions.



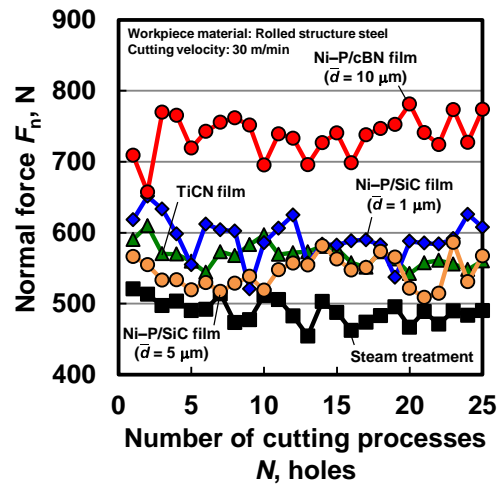
(a) $V_r = 10$ m/min



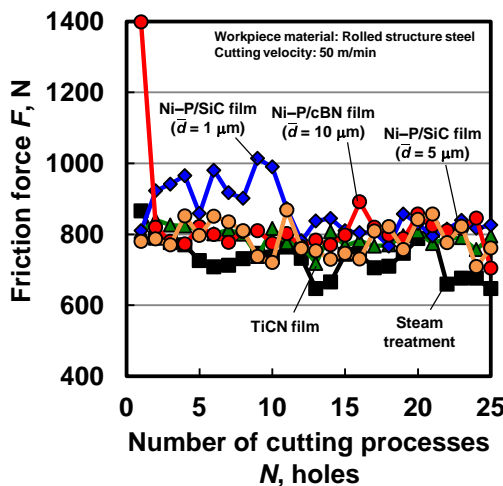
(a) $V_r = 10$ m/min



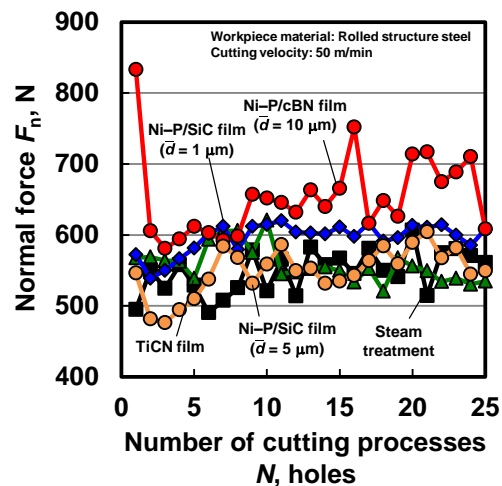
(b) $V_r = 30$ m/min



(b) $V_r = 30$ m/min



(c) $V_r = 50$ m/min

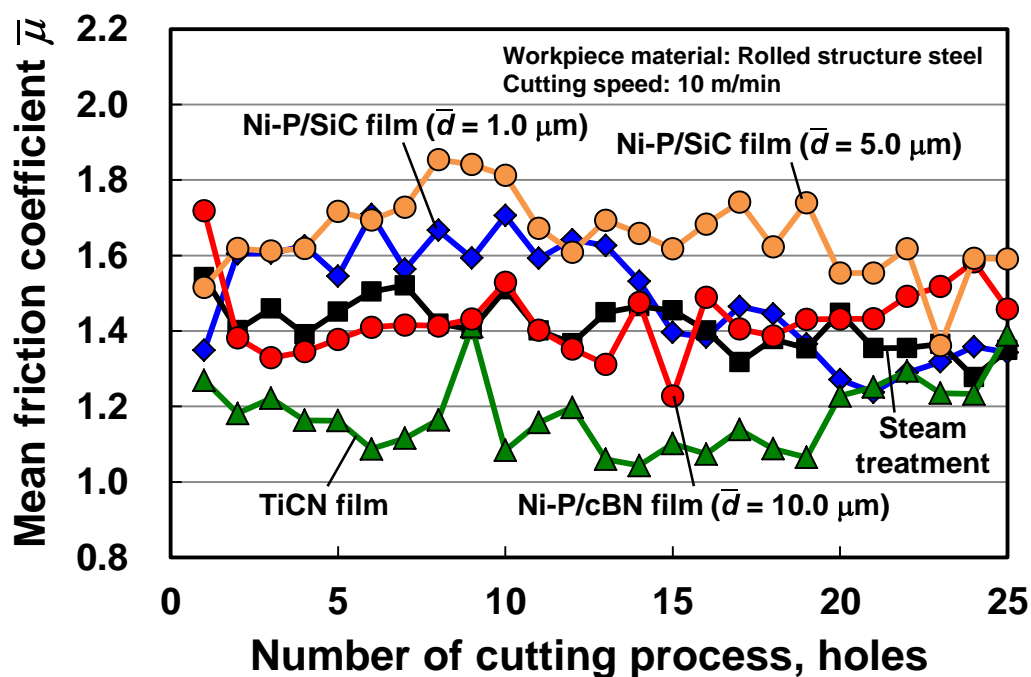


(c) $V_r = 50$ m/min

Fig. 4.17 Change in the frictional force with respect to the number of cutting processes

Fig. 4.18 Change in the normal force with respect to the number of cutting processes

Figures 4.19(a)–4.19(c) show the change in the mean friction coefficient with respect to the number of cutting processes at 10, 30, and 50 m/min, respectively. As shown in Fig. 4.19(a), the mean frictional coefficient for the tapping tool coated with TiCN film was the smallest, at 10 m/min. The mean friction coefficients for the tapping tools coated with composite film were higher than 1.35 at 10 m/min. As shown in Figs. 4.19(b) and 4.19(c), the mean friction coefficients for the tools coated with composite films were also higher than those for the other tools at the higher cutting speeds of 30 and 50 m/min, respectively.



(a) $V_r = 10 \text{ m/min}$

Fig. 4.19 Change in the mean frictional coefficient with respect to the number of cutting processes

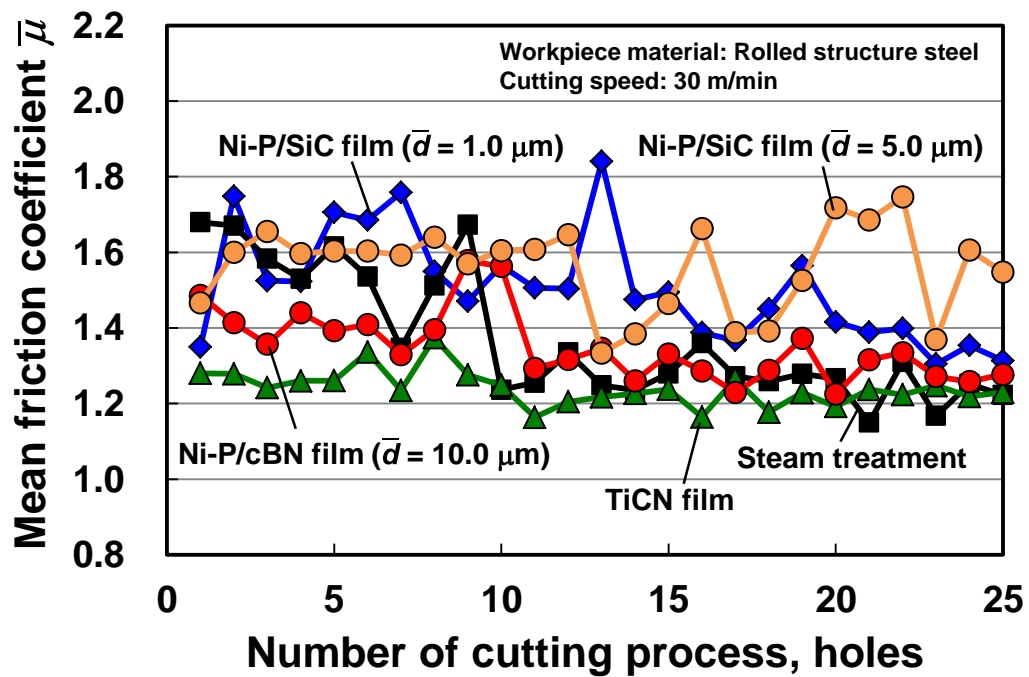
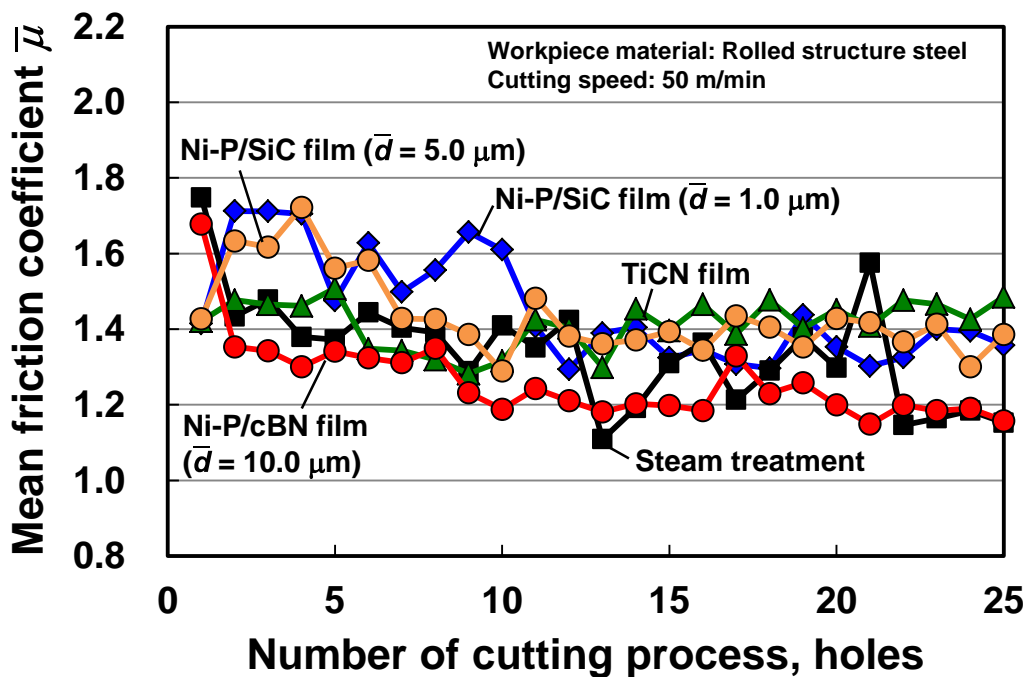
(b) $V_r = 30 \text{ m/min}$ (c) $V_r = 50 \text{ m/min}$

Fig. 4.19 Change in the mean frictional coefficient with respect to the number of cutting processes

4.3.2.3 Effect of friction coefficient on chip curl diameter at the tool–chip interface

Figure 4.20 shows the relation between the mean friction coefficient at the chip–tool rake face and chip curl diameter. As shown in the figure, the chip curl diameter decreased as the mean friction coefficient increased, suggesting that an increase in the friction coefficient at the chip–tool rake face effectively decreased the chip curl diameter.

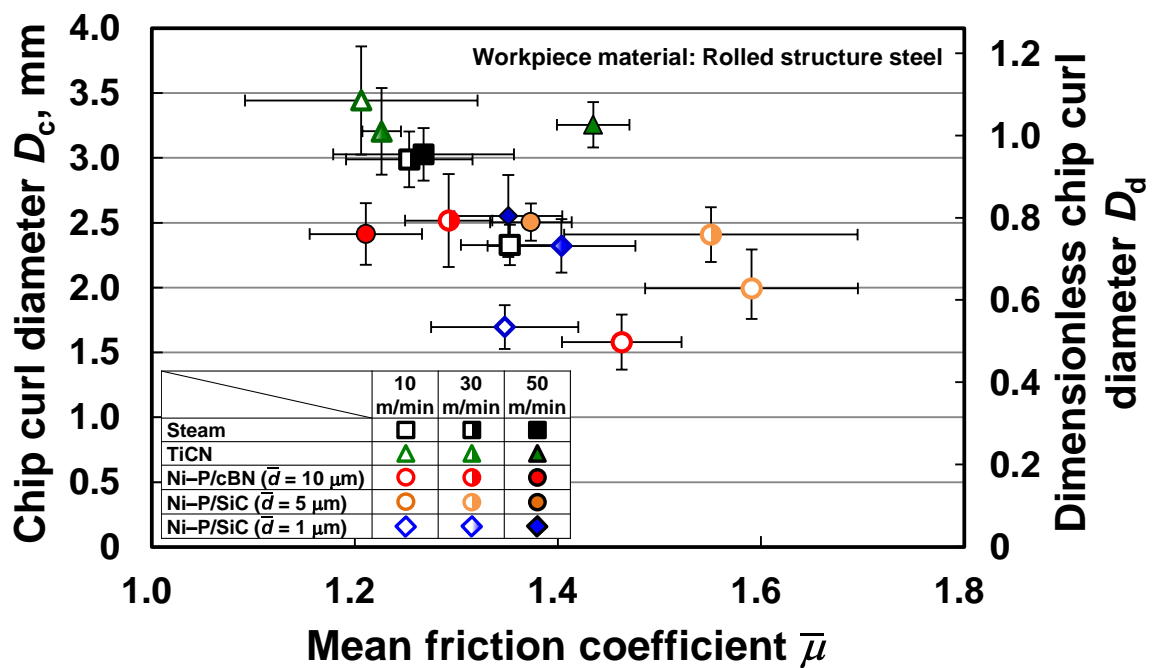


Fig. 4.20 Relation between the chip curl diameter and mean friction coefficient

4.3.3 Tool service life

Figure 4.21 shows the change in the cutting torque with respect to the number of cutting processes up to the end of the tool service life. The cutting torque of the tool coated with the Ni–P/cBN film ($\bar{d} = 10 \mu\text{m}$) film abruptly increased after approximately 80 holes, whereas the tool coated with the Ni–P/cBN film ($\bar{d} = 10 \mu\text{m}$) broke after 214 holes. The thread of the 201th hole of the tapping tool coated with Ni–P/cBN film ($\bar{d} = 10 \mu\text{m}$) was measured with the screw thread gauge and determined to be unsatisfactory. The cutting torque of the tools with steam treatment, that coated with the Ni–P/SiC film ($\bar{d} = 5 \mu\text{m}$), and that coated with the Ni–P/SiC film ($\bar{d} = 1 \mu\text{m}$) gradually increased in line with the number of cutting processes. The end of the service life of these tools was decided by an abrupt increase in the cutting torque that was indicated by a noise greater than 90 dB. The tapping tool coated with the TiCN film caused thread failure at the first hole so that its service life was zero.

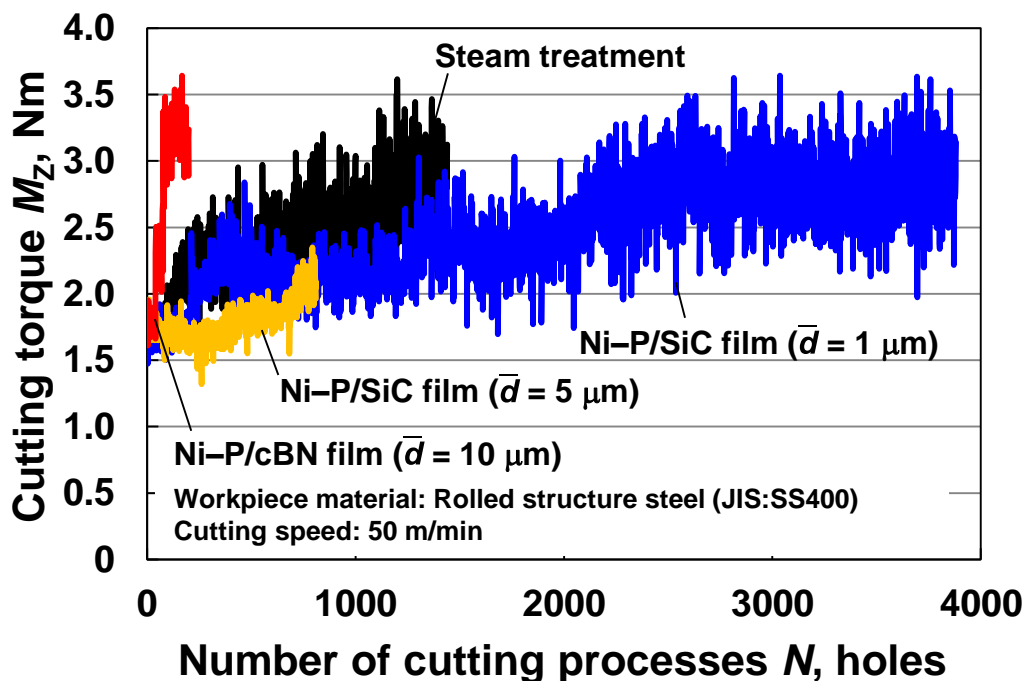


Fig. 4.21 Change in mean cutting torque with respect to the number of cutting processes

Figure 4.22 shows chip snarling with respect to the number of cutting processes within the service life of each tool. The blue circles indicate that chips were evacuated, whereas the red circles indicate that they snarled on the tapping tool across 200 tapping processes. Figure 4.23 shows the tapping tool after the test. As shown in the figure, the conventional tapping tool with steam treatment produced significant chip snarling. In contrast, the tools coated with the Ni-P/cBN ($\bar{d} = 10 \mu\text{m}$) and Ni-P/SiC ($\bar{d} = 1 \mu\text{m}$) films largely prevented significant chip snarling throughout their service lives. The tool coated with the Ni-P/SiC film ($\bar{d} = 5 \mu\text{m}$) prevented snarling up to the 600th hole; however, snarling was observed in the 601st–800th holes, demonstrating the inability of this film to prevent snarling.

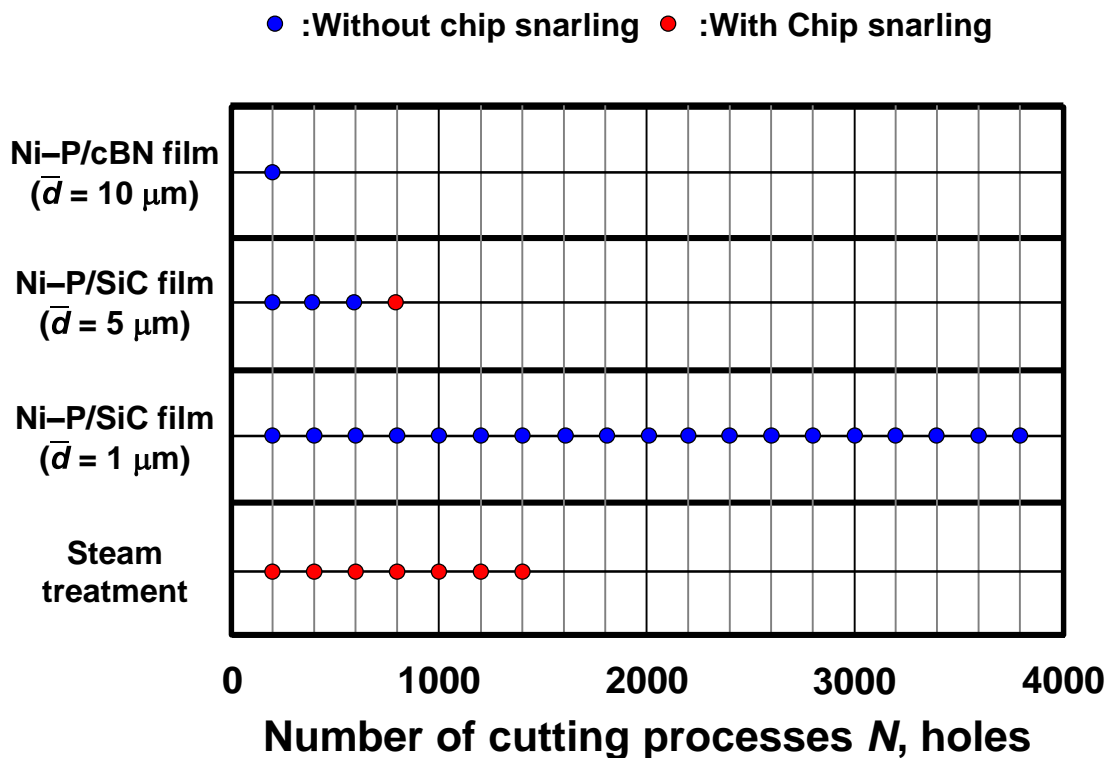


Fig. 4.22 Chip snarling with respect to the number of cutting processes

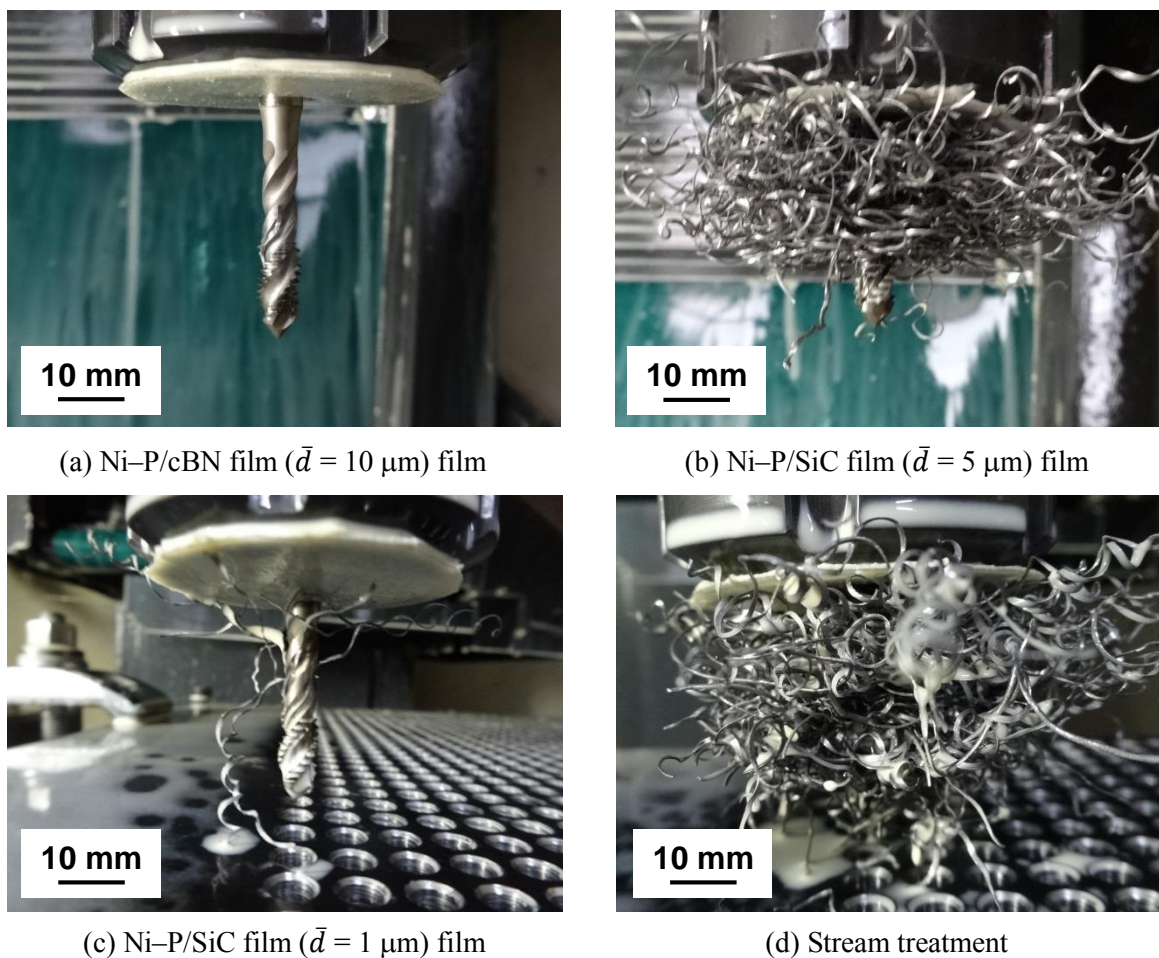


Fig. 4.23 Snapshot of tapping tool after tapping test

Figure 4.24 shows a plot of the number of cutting processes over the tool service life. As shown in the figure, the tool coated with the Ni-P/cBN film ($\bar{d} = 10 \mu\text{m}$) film had the shortest service life. SEM and energy-dispersive X-ray spectrometry (EDX) images of 4th cutting edge of each tapping tool are shown in Figs. 4.25–4.27. The broken tool is not shown. As shown in these figures, in each case, each surface treatment was worn away by the friction between the chip and the tool. However, the Ni-P/SiC ($\bar{d} = 5 \mu\text{m}$) and the Ni-P/SiC ($\bar{d} = 1 \mu\text{m}$) films survived in tool-chip interface. In the case of the tools with steam treatment and those coated with Ni-P/SiC film ($\bar{d} = 5 \mu\text{m}$), the edge tips were also worn away. The tool coated with the Ni-P/SiC film ($\bar{d} = 1 \mu\text{m}$) had the longest service life, completing 1.6 times the number of cutting processes of the tool with steam treatment. Because this tapping tool prevented chip snarling, wear due to the chipping of the cutting edge was also prevented, as shown in Fig. 4.25.

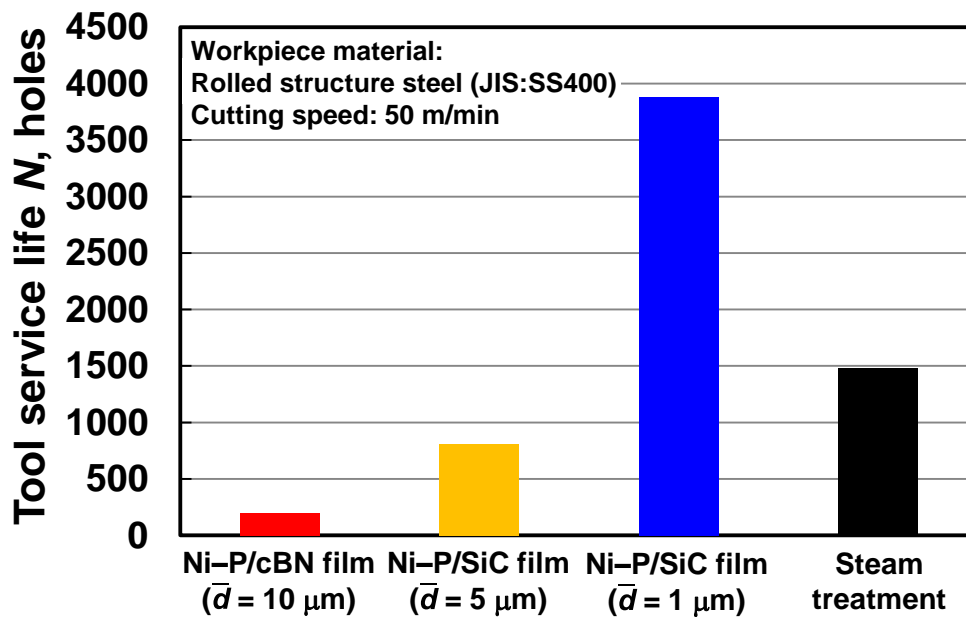
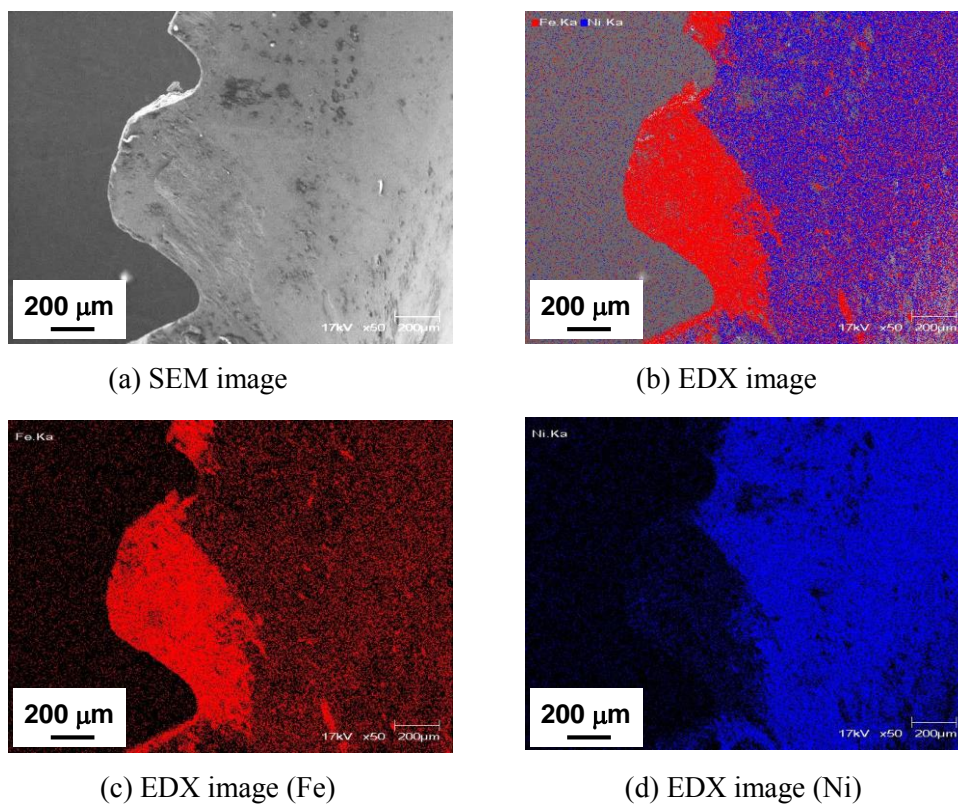


Fig. 4.24 Tool service life

Fig. 4.25 SEM and EDX images of the tapping tool coated with the Ni-P/SiC film ($\bar{d} = 5 \mu\text{m}$)

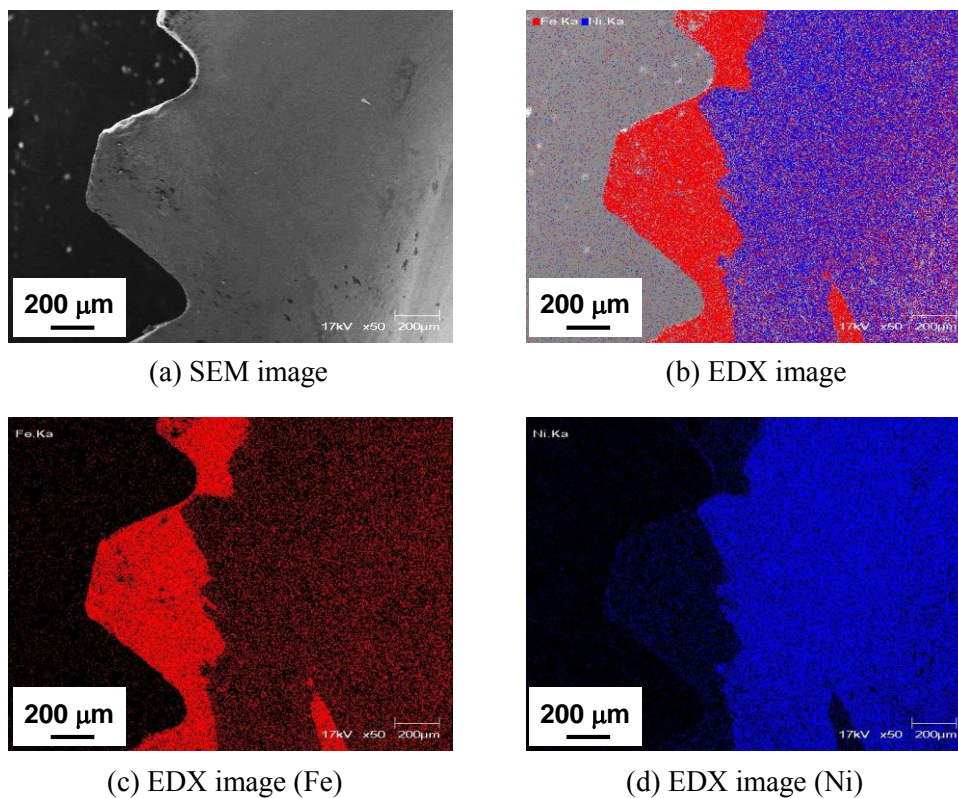


Fig. 4.26 SEM and EDX images of the tapping tool coated with the Ni-P/SiC film ($\bar{d} = 1 \mu\text{m}$)

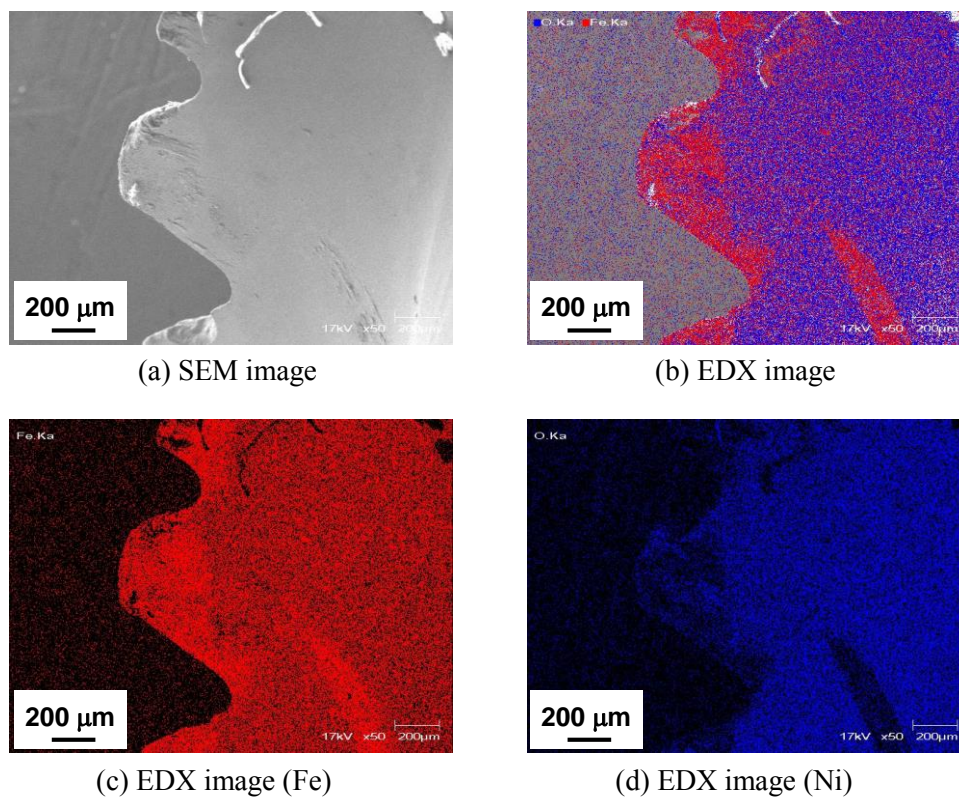


Fig. 4.27 SEM and EDX images of the tapping tool with steam treatment

4.4 Conclusions

Tapping tests were performed to investigate whether the tapping tools coated with the Ni–P/abrasive particle composite film were able to prevent chip snarling and increase the tool service life at high cutting speeds. The friction coefficient at the tool–workpiece rake face interface was estimated using the measured thrust force and cutting torque, and the effect of the friction coefficient on chip snarling was investigated. The conclusions are summarized as follows:

- (1) The tools coated with composite film had lower rates of chip snarling. This was particularly true for the Ni–P/SiC film ($\bar{d} = 1 \mu\text{m}$), which had a chip snarling rate of less than 5%.
- (2) The rate of chip snarling increased in line with the chip curl diameter. The tapping tools coated with composite film were able to prevent snarling by maintaining the chip curl diameter below the width of the helical flute of the tapping tool (3.2 mm) at high cutting speeds. The rate of chip snarling exceeded 40% at a dimensionless chip curl diameter of approximately 1.0.
- (3) The tapping tools coated with composite films had the highest cutting torque under all cutting conditions. The tools coated with the Ni–P/SiC film ($\bar{d} = 5.0 \text{ mm}$) and those coated with the Ni–P/SiC film ($\bar{d} = 1.0 \text{ mm}$) had thrust forces greater than 1.8 Nm, exceeding that of the conventional tapping tool at all cutting speeds. The tool with the Ni–P/cBN film ($\bar{d} = 10 \text{ mm}$) had a thrust force smaller than that of the conventional tool at 30 and 50 m/min.
- (4) The mean friction coefficient between the chip and tool rake face was derived from a coordinate transformation of the measured cutting torques and thrust forces. The mean friction coefficient of the tapping tools coated with the Ni–P/SiC ($\bar{d} = 5 \mu\text{m}$) and Ni–P/SiC ($\bar{d} = 1 \mu\text{m}$) films were higher than that of the conventional tapping tool at all cutting speeds. The chip curl diameter decreased as the mean friction coefficient increased.
- (5) At high cutting speeds ($V_r = 50 \text{ m/min}$), the service life of the tapping tool coated with the Ni–P/SiC film ($\bar{d} = 1 \mu\text{m}$) was 2.6 times as high as that of the conventional steam treatment tool.

References

- [1] Araujo, C. A., Silveira, L. J., Jun, B. M., Kapoor, G. S. and Vor, D. R., “A Model for Thread Milling Cutting Forces,” *International Journal of Machine Tools Manufacture*, 46, 2006, 2057-2065.
- [2] Cao, T. and Sutherland, W. J., “Investigation of Thread Tapping Load Characteristics Through Mechanistic Modeling and Experimentation,” *International Journal of Machine Tools Manufacture*, 42, 2002, 1527-1538.
- [3] Yamaoka, Y., Kakino, Y., Suzuki, Y., Nagae, A. and Muraki, T., “High Speed, High Productive Tapping by Intelligent Machine Tools (1st report)–Automatic Detection of Tool Failure and Chip Jamming–,” *The Japan Society for Precision Engineering*, 66, 2000, 1922-1926 (in Japanese).
- [4] Yamauchi, M., Horiuchi, O., Murakami, Y., Sugano, H. and Shibutani, H., “Development of a Chip-breaking Tool for Tapping (1st report),” *The Japan Society for Precision Engineering*, 70, 2004, 1565-1569 (in Japanese).
- [5] Jin, M., Watanabe, S., Miyake, S. and Murakawa, M., “Trial Fabrication and Cutting Performance of c-BN-coated taps,” *Surface and Coatings Technology*, 133-134, 2000, 443-447.
- [6] Reiter, E., Brunner, B., Ante, M. and Rechberger, J., “Investigation of Several PVD Coatings for Blind Hole Tapping in Austenitic Stainless Steel,” *Surface and Coatings Technology*, 200, 2006, 5532-5541.
- [7] Henderer, W. and Xu, F., “Hybrid TiSiN, CrC/C PVD Coatings Applied to Cutting Tools,” *Surface and Coatings Technology*, 215, 2012, 381-385.
- [8] Derflinger, V., Brändle, H. and Zimmermann, H., “New Hard/Lubricant Coating for Dry Machining,” *Surface and Coatings Technology*, 113, 1999, 286-292.
- [9] Cheng, K., “Machining Dynamics Fundamentals, Applications and practices,” *Springer Series in Advanced Manufacturing*, 2009, 129-133.
- [10] Wood, S., “Tapping for Oil,” *Cutting Tool Engineering*, 62, 2010, 52-57.

- [11] Saito, Y., Takiguchi, S., Yamaguchi, T., Shibata, K., Kubo, T., Watanabe, W., Oyama, S. and Hokkirigawa, K., “Effect of Friction at Chip-tool Interface on Chip Geometry and Chip Snarling in Tapping Process,” *International Journal of Machine Tools Manufacture*, 107, 2016, 60-65.
- [12] Hirota, A. and Mori, Y., “Prediction of Chip Formation and Cutting Forces in Oblique Cutting (2nd report)–Comparison of Predicted and Measured Results–,” *The Japan Society for Precision Engineering*, 54, 1988, 755-760 (in Japanese).
- [13] Saito, Y., Yamaguchi, T., Shibata, K., Kadota, Y., Kubo, T., Watanabe, W. and Hokkirigawa, K., “Development of a New Tapping Tool Covered with Nickel/Abrasive Particles Composite Film for Preventing Chip Snarling Chip Snarling and Tool Service Life Extension,” *Tribology Online*, 11, 2, 2016, 81-87.
- [14] Hanasaki, S., Hosoi, R., Hosoi, T. and Nishimura, S., “Twist Drill Drillable Deep Hole under Continuous High Feed Rate (Mechanism of Particular Type Chip Formation of 0-degree Rake Angle Twist Drill),” *Transactions of the JSME*, 70, 2004, 1229-1234 (in Japanese).

Chapter 5

Effect of the friction coefficient at the sliding zone of the chip–tool interface on chip curl diameter during the tapping process

5.1 Introduction

In Chapter 4, it was revealed that chip snarling on a tapping tool was prevented at a high cutting speed condition ($V_r = 50$ m/min) by coating the tapping tool with a Ni–P/abrasive particle composite film. The curl diameter of chips evacuated without chip snarling tended to be shorter than the width of the helical flute. Therefore, generating a shorter chip curl diameter is important in order to prevent chip snarling.

It is generally known that chip curl diameter is affected by the shear zone of the workpiece material [1–4]. In orthogonal cutting tests, the shear zone is influenced by the tool geometry, the built-up edge, and the secondary shear zone [5–7]. The geometry of each tapping tool used in the tapping test in Chapter 4 was the same and a built-up edge was not observed. Therefore, it is considered that the secondary shear zone caused decreasing chip curl diameter when using the tapping tool coated with a Ni–P/abrasive particle composite film. The secondary shear zone corresponds to the sticking zone where the chip contacts the tool rake face; it is created due to friction at the chip–tool interface [5]. In the secondary shear zone, plastic flow occurs and the shear velocity gradually increases up to the bulk chip speed. In orthogonal cutting, Nakayama et al. [5] demonstrated that chip curl diameter decreased with an increase in secondary shear zone thickness. As presented in Chapter 4, the increased friction coefficient at the tool (rake face)–chip interface decreased chip curl diameter; therefore, it is hypothesized that the friction coefficient increased the thickness of the secondary shear zone. However, there is no research investigating the relation between the friction coefficient at the

chip–tool interface and the secondary shear zone thickness during the tapping process or during orthogonal cutting. On the rake face, the chip–tool contact zone is divided into two regions: 1) the sticking zone, a plastic region characterized by a sticking friction with a plastic localization, where stresses reach a maximum level, as mentioned above; and 2) the sliding zone, an elastic region characterized by a sliding friction and a linear proportionality between the normal and shear stresses (Usui and Takeyama [8]). The friction coefficient at the sliding zone (i.e., local friction coefficient) could affect the secondary shear zone thickness, resulting in variation of the chip curl diameter.

In this chapter, the local friction coefficient at the sliding zone of the chip–tool interface and the secondary shear zone thickness were estimated using the sticking–sliding friction model [9] and the cutting torque and thrust force obtained in Chapter 4. Then, the effect of the local friction coefficient at the sliding zone on chip curl diameter and secondary shear zone thickness was investigated.

5.2 Methods

5.2.1 Estimation of local friction coefficient at the sliding zone of the tool-chip interface

The cutting resistance on the tool rake face, which was calculated in Chapter 4, is the resultant value for all cutting edges. Assuming that the specific cutting resistance, which is the cutting resistance per unit of contact area, for each cutting edge of the tapping tool is the same, the cutting resistance for the n th cutting edge R_{nth} is given by

$$R_{nth} = R \times \frac{A_{nth}}{A_{all}} \quad (5.1)$$

where R is the cutting resistance [N], which is calculated by $R = \sqrt{F^2 + F_x^2}$, F is the resultant friction force of all cutting edges [N], F_x is the cutting force in x direction on rake face [N], A_{nth} is the cutting area of the n th cutting edge [mm²], which is calculated from the uncut chip thickness and geometry of each cutting edge, and A_{all} is the resultant cutting area of all cutting edges [mm²].

In this study, the cutting model for the cutting edge of the tapping tool is represented as an

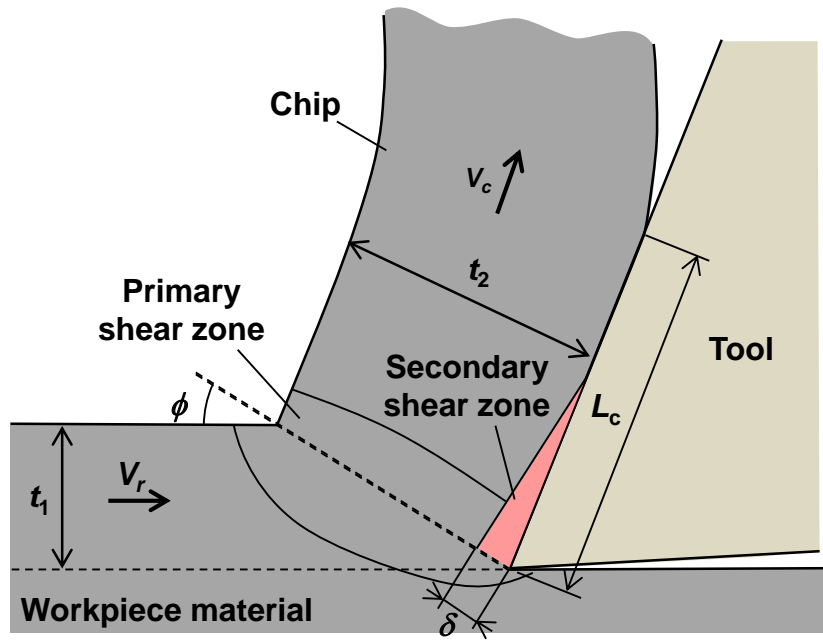


Fig. 5.1 Schematic image of orthogonal cutting model

orthogonal cutting model to estimate the friction coefficient at the sliding zone. Figure 5.1 shows the shear zone distribution in the orthogonal cutting model of this study. In this model it is assumed that the shear phenomenon occurs in the primary shear zone and that the secondary shear zone spreads over the rake face of the cutting edge [10]. The shear stress τ_s and normal stress σ_s in the primary shear plane are calculated by Eq. (5.2) and (5.3).

$$\tau_s = \frac{R_{nth} \times \cos(\phi + \tan^{-1} \bar{\mu} - \alpha_e)}{A_s} \quad (5.2)$$

$$\sigma_s = \frac{R_{nth} \times \sin(\phi + \tan^{-1} \bar{\mu} - \alpha_e)}{A_s} \quad (5.3)$$

where ϕ is the shear angle [degree], $\bar{\mu}$ is the mean friction coefficient, α_e is the effective rake angle [degree], and A_s is the area of the primary shear plane [mm^2]. The area of the primary shear plane A_s and the shear angle ϕ are calculated from the chip thickness and chip width as follows:

$$A_s = \frac{(b_t + b_b)}{2 \times \sin \phi} \times \frac{t_1}{\cos \eta} \quad (5.4)$$

$$\phi = \tan^{-1} \left(\frac{r \cos \alpha_e}{1 - r \sin \alpha_e} \right) \quad (5.5)$$

where b_t is the width of the free surface of the chip [mm], b_b is the width of the chip near rake face of the tool [mm], and r is the cutting ratio, which is calculated by $r = t_1/(\cos \eta \times t_2)$, where t_1 is the uncut chip thickness [mm], t_2 is the chip thickness [mm], and η is the chip flow angle [degree].

According to Moufki [11], the normal stress distribution on the rake face $\sigma_c(z)$ is given by Eq. (5.6).

$$\sigma_c(z) = \sigma_0 \left(1 - \frac{z}{L_c} \right)^\xi \quad (5.6)$$

where σ_0 is the normal stress at the tool tip [Pa], z is the distance from the tool cutting tip along the chip contact zone [mm], L_c is the chip contact length [mm], and ξ is the characteristic value of the pressure distribution. The normal stress in tool chip σ_0 and the chip contact length L_c are calculated by the following equations:

$$\sigma_0 = \frac{F_{n_nth}}{\int_0^{L_c} \left(1 - \frac{z}{L_c} \right)^\xi w(z) dz} \quad (5.7)$$

$$L_c = \frac{t_1}{\cos \eta} \times \frac{\xi + 2}{2} \times \frac{\sin(\phi + \tan^{-1} \bar{\mu} - \alpha_e)}{\sin \phi \times \cos(\tan^{-1} \bar{\mu})} \quad (5.8)$$

where $w(z)$ is the width of each cutting edge [mm].

Figure 5.2 shows the sticking–sliding friction model [9]. In this model, there are two contact conditions: one is the sticking zone where the material is deformed plastically by the large normal stress at the tool tip, and the other is the sliding zone where the chip slides on the rake face. In the sticking zone, where the normal stress is higher than the yield stress, the shear stress is constant because the plastic flow of the material is generated. In the sliding zone, the shear stress is proportional to the normal stress according to the coulomb friction law [9]. Assuming that the primary

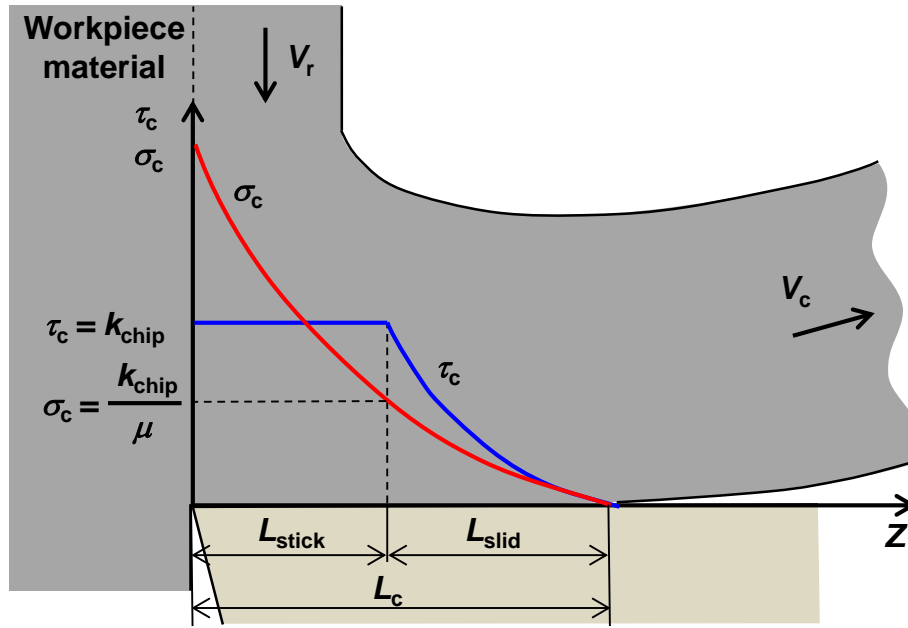


Fig. 5.2 Schematic image of the sticking–sliding friction model

shear zone spreads to the sticking zone [12], the shear stress at the sticking zone is equal to the yield shear stress in the primary shear plane as follows:

$$\tau_c(z) = k_{\text{chip}} = \tau_s \quad 0 \leq z < L_{\text{stick}} \quad (5.9)$$

where k_{chip} is the shear stress in chip at the sticking zone [Pa].

The shear stress in the sliding zone is calculated by Coulomb's law as follows:

$$\tau_c(z) = \mu_{\text{slid}} \times \sigma_c(z) \quad L_{\text{stick}} \leq z < L_c \quad (5.10).$$

The chip contact length L_c , friction force F_{nth} , and normal force $F_{\text{n,nth}}$ are given by the following equations:

$$L_{\text{stick}} + L_{\text{slid}} = L_c \quad (5.11)$$

$$F_{\text{stick}} + F_{\text{slid}} = F_{\text{nth}} \quad (5.12)$$

$$F_{\text{n,stick}} + F_{\text{n,slid}} = F_{\text{n,nth}} \quad (5.13)$$

where L_{stick} is the chip contact length at the sticking zone [mm], L_{slid} is the chip contact length at the

sliding zone [mm], F_{stick} is the friction force at the sticking zone [N], F_{slid} is the friction force at the sliding zone [N], F_{n_stick} is the normal force at the sticking zone [N], and F_{n_slid} is the normal force at the sliding zone [N].

The friction force at the sticking zone is obtained by the relation between the shear stress in the sticking zone and contact area A_{stick} [mm²] as follows:

$$F_{stick} = k_{chip} \times A_{stick} \quad (5.14).$$

The normal force at the sliding zone is given as follows:

$$F_{n_slid} = F_{n_nth} \times \frac{\int_{L_{stick}}^{L_c} \left(1 - \frac{z}{L_c}\right)^{\xi} w(z) dz}{\int_0^{L_c} \left(1 - \frac{z}{L_c}\right)^{\xi} w(z) dz} \quad (5.15).$$

Thus, the local friction coefficient at the sliding zone is calculated as follows:

$$\mu_{slid} = \frac{F_{slid}}{F_{n_slid}} \quad (5.16).$$

The flow chart for the calculation of the local friction coefficient at the sliding zone is shown in Fig. 5.3. In order to solve the simultaneous equations, the initial local friction coefficient at the sliding zone was temporarily set as 1.0. When the difference between the initial value of the local coefficient of friction at the sliding zone μ_0 and the calculated coefficient of friction at the sliding zone μ_{slid} was over 0.01, the value of μ_{slid} is substituted for the value of μ_0 and the calculation was continued. When the difference between the initial local friction coefficient and calculated local friction coefficient $|\mu_{slid} - \mu_0|$ was within 0.01, the calculation was terminated and the local friction coefficient at the sliding zone was determined.

The secondary shear zone thickness, which is the stagnation area of material flow in the absence of the built-up edge, is given as follows [13]:

$$\delta = L_{stick} \times \sin(\phi - \alpha_e) \quad (5.17).$$

Experimental data for the tapping test, such as cutting resistance, chip curl diameter, chip thickness, and chip width, which were used to calculate each variable in this chapter, were acquired as described in the previous chapter. The tapping tool was a spiral-tap (HSS, M6 × 1) and the surface treatments of the tapping tools were (i) steam treatment, (ii) TiCN film coating, (iii) Ni–P/cBN film ($\bar{d} = 10 \mu\text{m}$) coating, (iv) Ni–P/SiC film coating ($\bar{d} = 5 \mu\text{m}$), and (v) Ni–P/SiC film coating ($\bar{d} = 1 \mu\text{m}$). The workpiece material was rolled structure steel (JIS SS400) in the form of a rectangular block of 14 × 310 × 450 mm. The cutting velocities were 10 (normal cutting speed), 30, and 50 m/min. During the tapping process, an emulsion cutting oil was used. The number of cutting processes (holes) undertaken was 25. The cutting torque and thrust force were measured using a dynamometer. The measured forces were transformed to the resultant cutting resistance of all cutting edges R using the proposed coordinate transformation in Chapter 4 [5]. The cutting chips were collected after cutting each hole, and the chip curl diameter, chip thickness, and chip width were measured. The mean value of the local friction coefficient at the sliding zone for 16–25 holes was used for analysis.

Table 5.1 shows the parameters used in the calculation of friction coefficient. The effective rake angle, uncut chip thickness, and resultant cutting area of all cutting edges are given by the tool geometry. According to Childs et al. [14], the characteristic pressure stress value for carbon steel ξ is 2.34. In this study, the calculated local friction coefficient at the sliding zone of the fourth cutting edge was considered to be representative of all cutting edges.

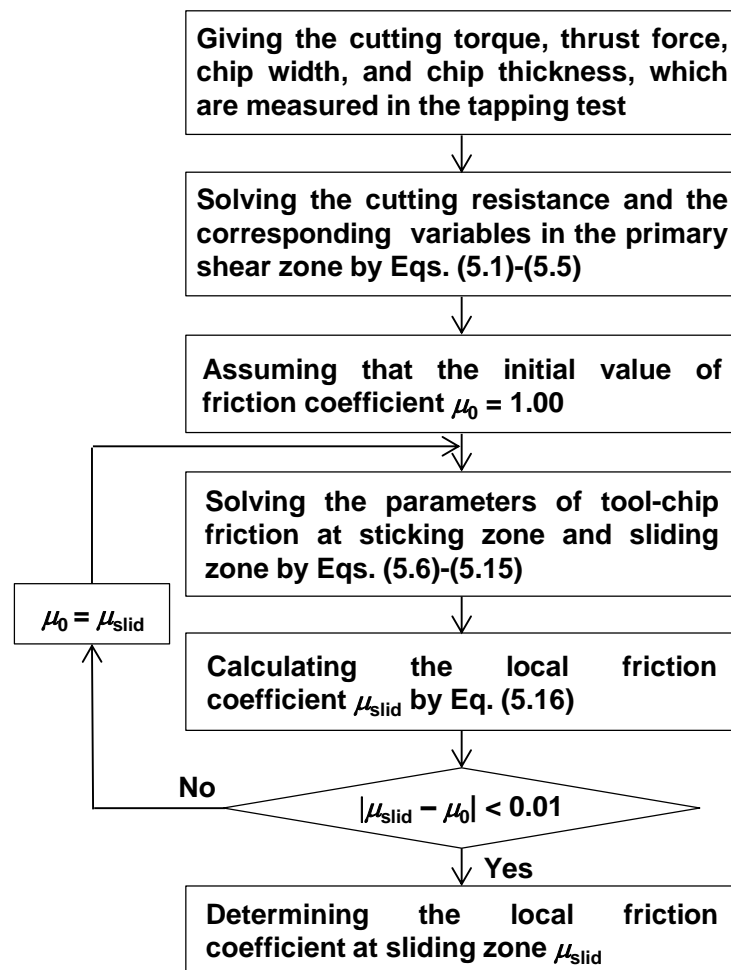


Fig. 5.3 Flow chart for the calculation of local friction coefficient at the sliding zone

Table 5.1 Parameters used in the calculation of friction coefficient

Effective rake angle α_e , degree	14.3
Uncut chip thickness t_1 , mm	0.075
Characteristic value of pressure stress ξ [14]	2.34
Resultant cutting area of all edges A_{all} , mm ²	0.1925

5.2.2 Observation of the secondary shear zone at the chip surface

To confirm the existence of the secondary shear zone, the chip was padded with methyl methacrylate and cut as shown in Fig. 5.4. The cross section was subjected to mirror polishing using abrasive paper and buff polishing using alumina abrasive grains and colloidal silica. The metal structure of the polished chip cross section was observed using a reflection electron microscope (JSM-7800F, JEOL Ltd.) to investigate the existence and thickness of the secondary shear zone.

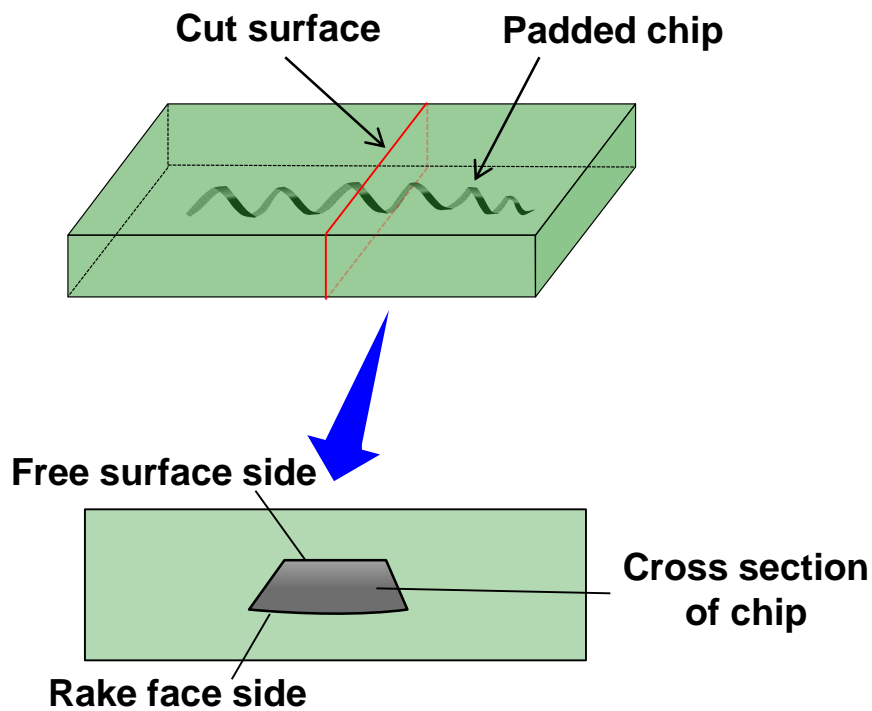


Fig. 5.4 Sample preparation for observation of the cross section of a chip

5.3 Results and discussion

5.3.1 Relation between chip curl diameter and local friction coefficient at the sliding zone

Figure 5.5 shows the relation between the local friction coefficient at the sliding zone and the cutting speed. For the tapping tool coated with Ni-P/SiC film coating ($\bar{d} = 1 \mu\text{m}$), the local friction coefficient at the sliding zone was not significantly affected by the cutting speed, ranging from 1.7 to 1.8. For the tapping tool treated with steam, that coated with a Ni-P/cBN film ($\bar{d} = 10 \mu\text{m}$), and that coated with a Ni-P/SiC film ($\bar{d} = 5 \mu\text{m}$), the local friction coefficient at the sliding zone tended to decrease as the cutting speed increased. In contrast, for the tapping tool coated with TiCN film, the local friction coefficient at the sliding zone increased as the cutting speed increased.

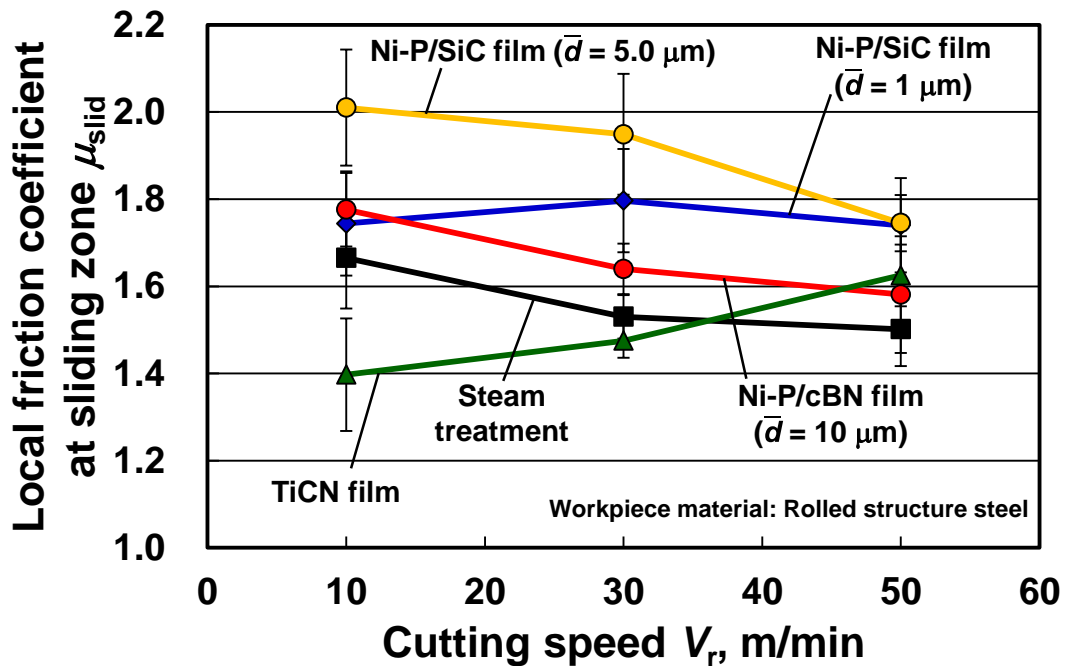


Fig. 5.5 Relation between the local friction coefficient at the sliding zone and cutting speed

Figure 5.6 shows the relation between chip curl diameter and the local friction coefficient at the sliding zone. As shown in this figure, chip curl diameter decreased with an increase in the local friction coefficient at the sliding zone. The local friction coefficient at the sliding zone was higher than 1.4 for all cutting conditions. For the developed tapping tool, the local friction coefficient at the sliding zone was higher than 1.58. Furthermore, except for the tapping tool coated with TiCN film, the friction coefficient at the sliding zone decreased with an increase in cutting speed. In contrast, the local friction coefficient for the tapping tool coated with TiCN film increased with an increase in cutting speed.

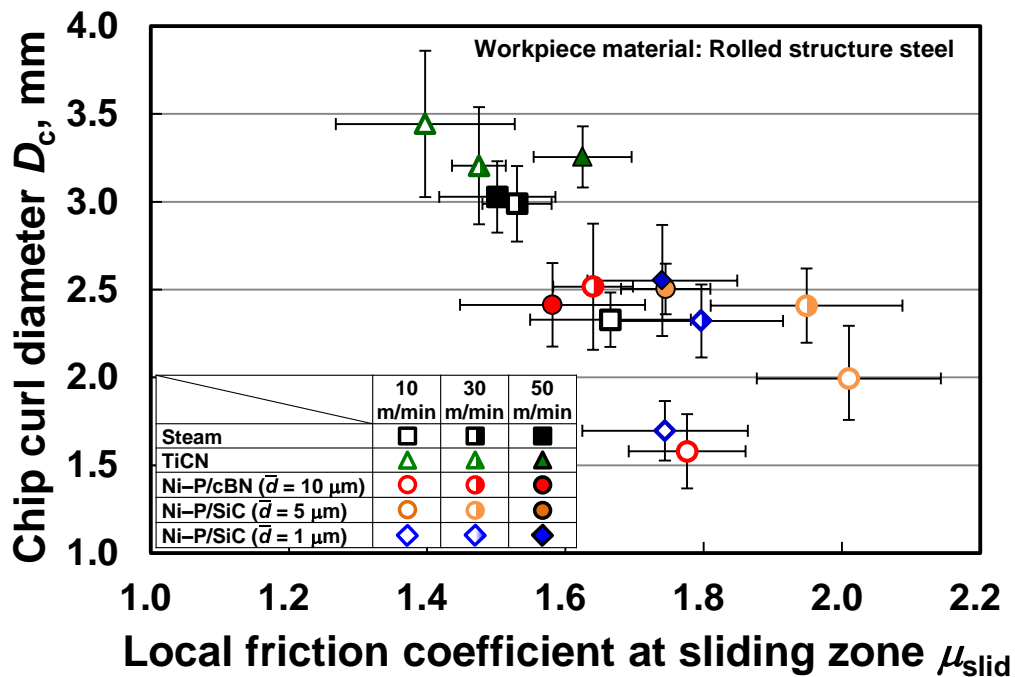


Fig. 5.6 Relation between chip curl diameter and local friction coefficient at the sliding zone

5.3.2 Effect of local friction coefficient at the sliding zone on secondary shear zone thickness

Figure 5.7 shows the relation between the secondary shear zone thickness and the local friction coefficient at the sliding zone. The secondary shear zone thickness increased with an increase in the local friction coefficient at the sliding zone. The secondary shear zone thickness of the developed tapping tool was higher than 0.017 mm for all conditions. This indicates that the high local friction coefficient tends to enhance secondary flow. Figure 5.8 shows the relation between the chip curl diameter and the secondary shear zone thickness. This figure indicates that the chip curl diameter decreased with an increase in the thickness of the secondary shear zone. Consequently, these results demonstrate that chip curl was enhanced by an increase in the size of the secondary shear zone at the chip–tool interface during tapping. According to Nakayama et al. [5], the curvature of a chip curl increases with an increase in the secondary shear zone thickness because the chip curl is deformed along the secondary shear zone in orthogonal cutting.

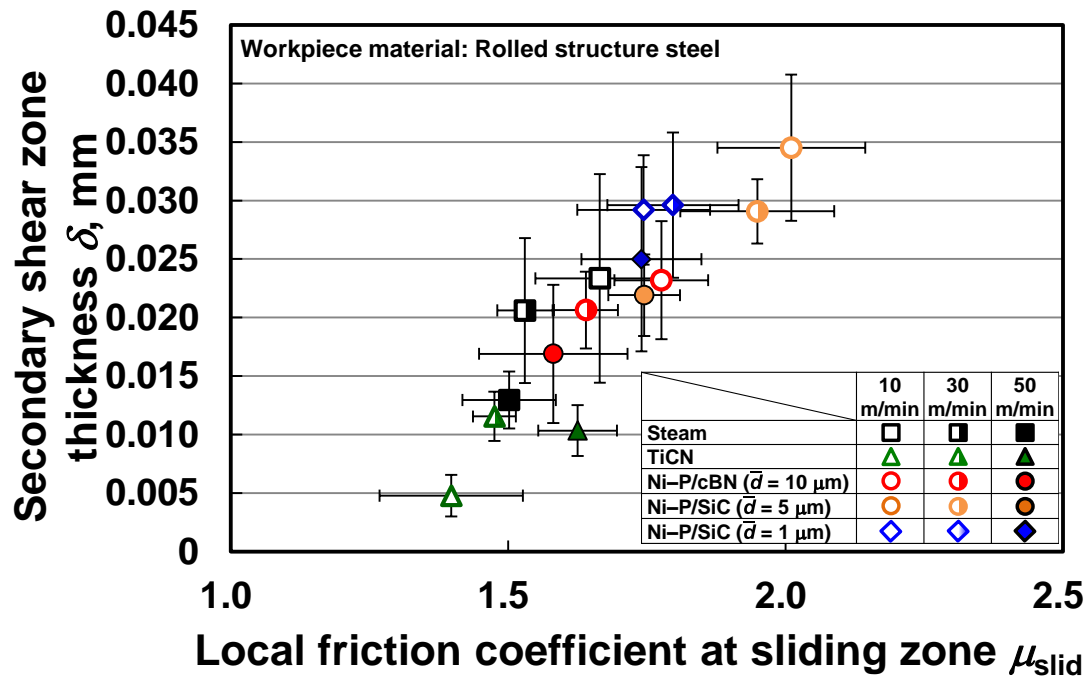


Fig. 5.7 Relation between secondary shear zone thickness and friction coefficient at the sliding zone

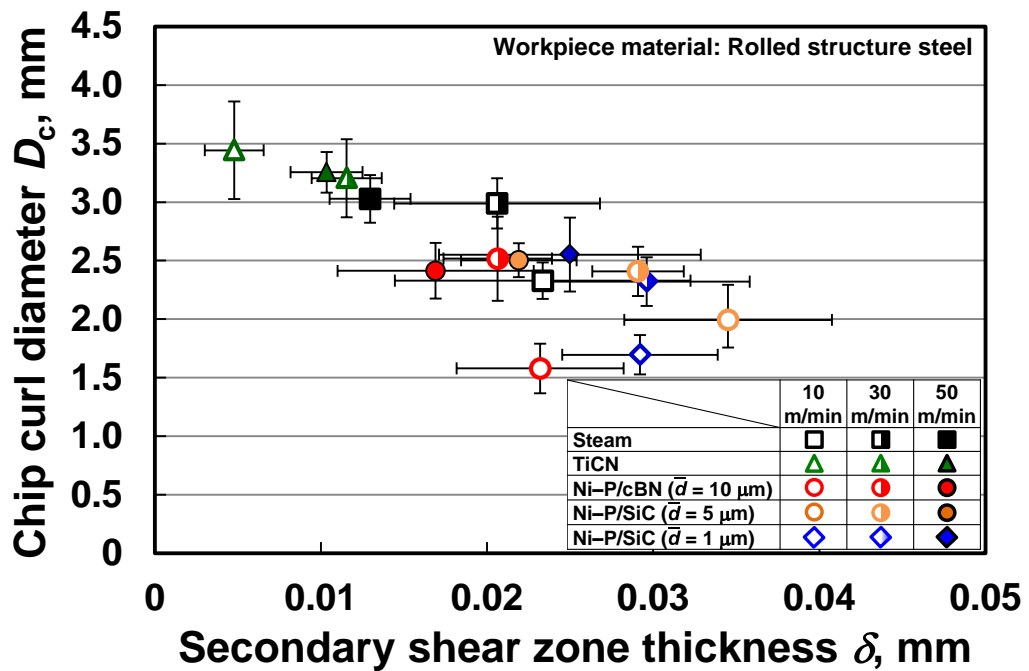
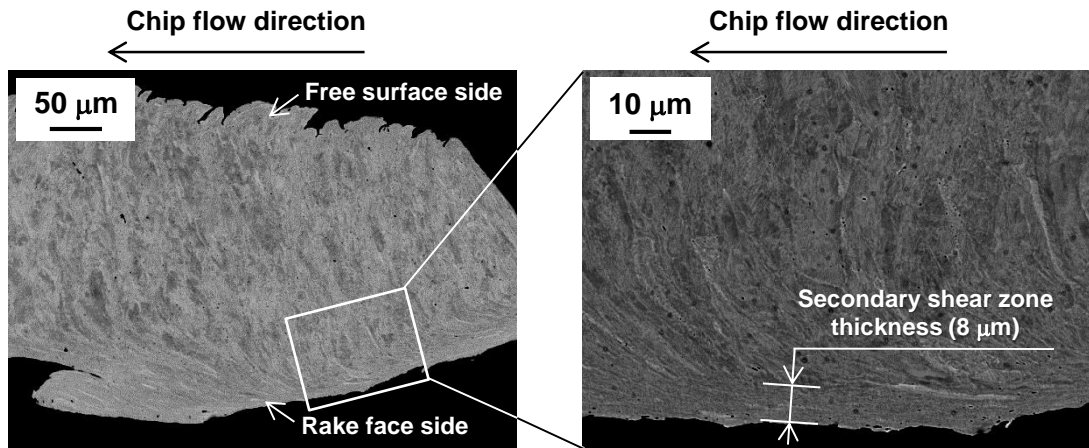


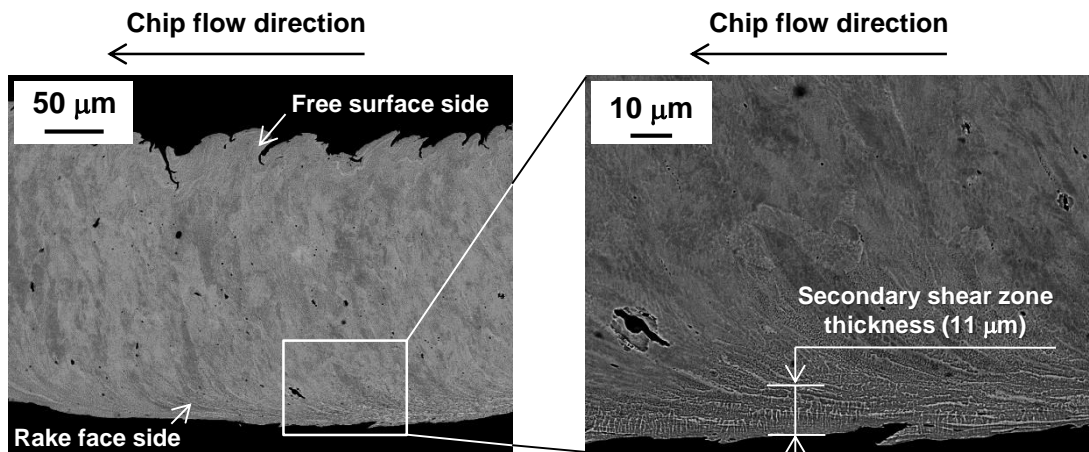
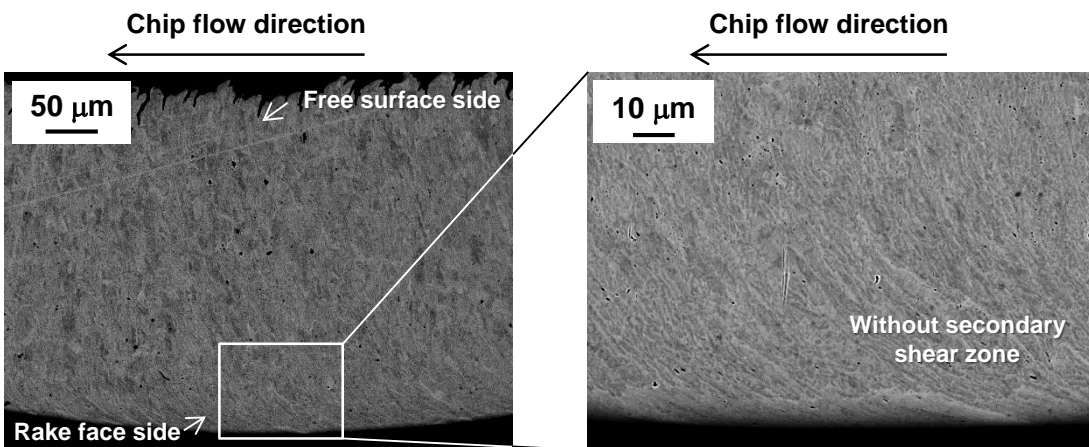
Fig. 5.8 Relation between chip curl diameter and secondary shear zone thickness

5.3.3 Observation of the metal structure of cutting chips

Figures 5.9 and 5.10 show the reflected electron images of cutting chips collected after cutting by the tapping tool treated with steam, the tapping tool coated with TiCN film, and the tapping tool coated with the Ni–P/SiC film ($\bar{d} = 1 \mu\text{m}$) at 10 and 50 m/min, respectively. The bottom surface of the chips shown in the figures was in contact with (and slid against) the rake face of each tapping tool. Horizontal flow marks of the crystal grain of the chip of the rake face side can be observed for the cutting performed with the steam treated tapping tool (Fig. 5.8(a) and Fig. 5.9(a)) and the tapping tool coated with Ni–P/SiC film ($\bar{d} = 1 \mu\text{m}$) (Fig. 5.8(b) and Fig. 5.9(b)) at 10 m/min and 50 m/min. These horizontal flow mark areas may correspond to the secondary shear zone (sticking zone). The thickness of the zone is about 11–12 μm for the tapping tool coated with Ni–P/SiC film ($\bar{d} = 1 \mu\text{m}$) and 8–9 μm for that treated with steam. The secondary shear zone thickness estimated from the images is almost equivalent to the calculated values (25–30 μm for the tapping tool coated with Ni–P/SiC film ($\bar{d} = 1 \mu\text{m}$); 13–23 μm for that with steam treatment). In contrast, the extent of deformation of the crystal grain of the cutting chip produced by the tapping tool coated with TiCN film at 10 m/min was lower than that for cutting chips produced by the other tapping tools. Deformation of the cutting chip at the chip–tool interface for the tapping tool coated with TiCN film at 50 m/min was also observed; however, the thickness of the secondary shear zone was much less than that for the other tapping tools.

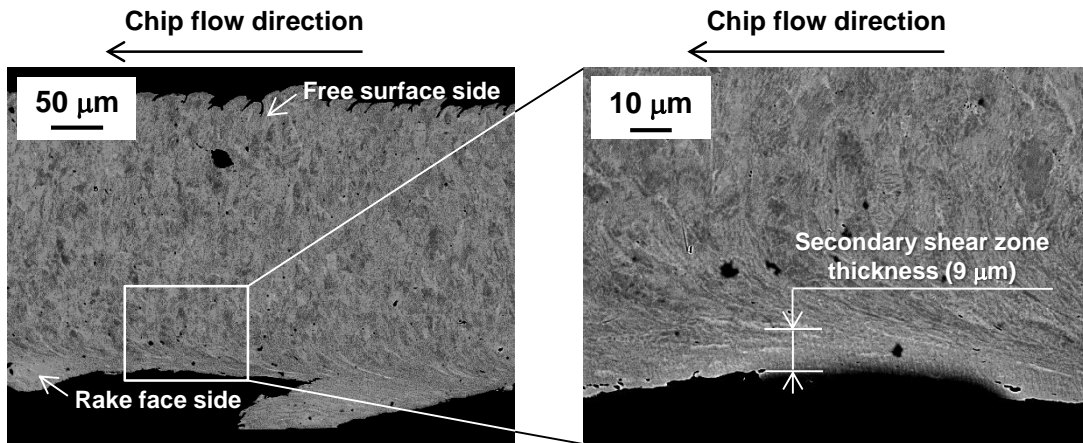


(a) Tapping tool with steam treatment

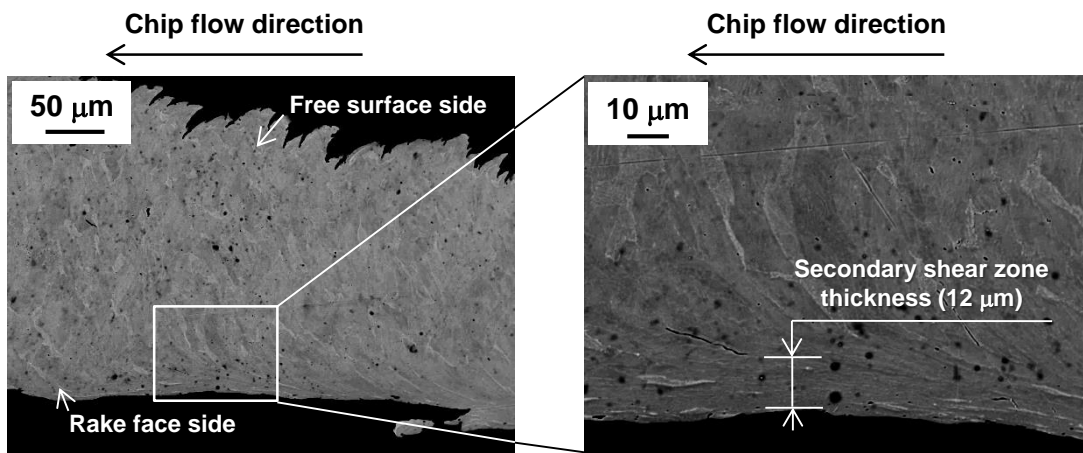
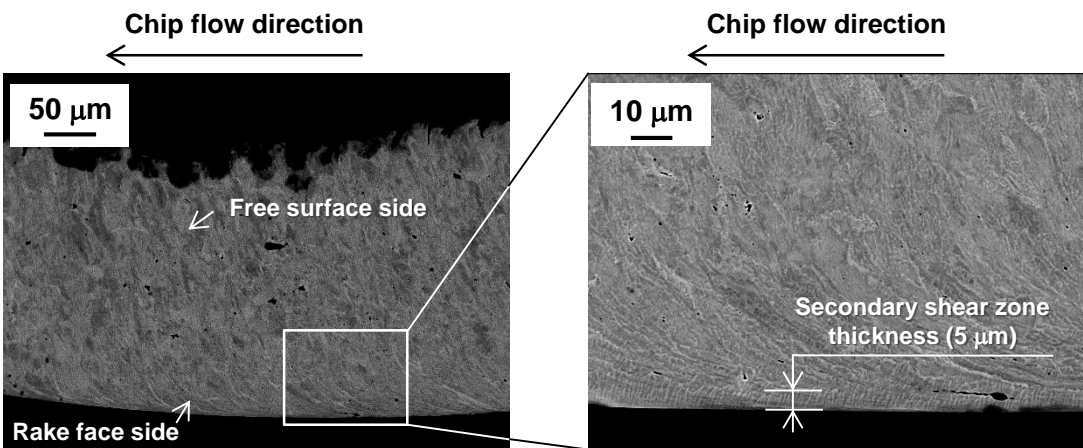
(b) Tapping tool coated with Ni-P/SiC film ($\bar{d} = 1 \mu\text{m}$)

(c) Tapping tool coated with TiCN film

Fig. 5.9 Reflected electron images ($V_r = 10 \text{ m/min}$)



(a) Tapping tool with steam treatment

(b) Tapping tool coated with Ni-P/SiC film ($\bar{d} = 1 \mu\text{m}$)

(c) Tapping tool coated with TiCN film

Fig. 5.10 Reflected electron images ($V_r = 50 \text{ m/min}$)

5.3.4 Effect of stress field in the shear plane on secondary shear zone thickness

Figure 5.11 shows the relation between the normal stress and the local friction coefficient at the sliding zone. The normal stress in the primary shear plane increased with an increase in the local friction coefficient at the sliding zone and varied from 883 MPa to 2120 MPa. For the tapping tool coated with composite film, the normal stress in the shear plane was greater than 1248 MPa under all conditions. Except for the tapping tool coated with TiCN film, the normal stress in the primary shear plane tended to decrease with increasing cutting speed. In contrast, for the tapping tool coated with TiCN film, the normal stress in the shear plane increased with an increase in cutting speed.

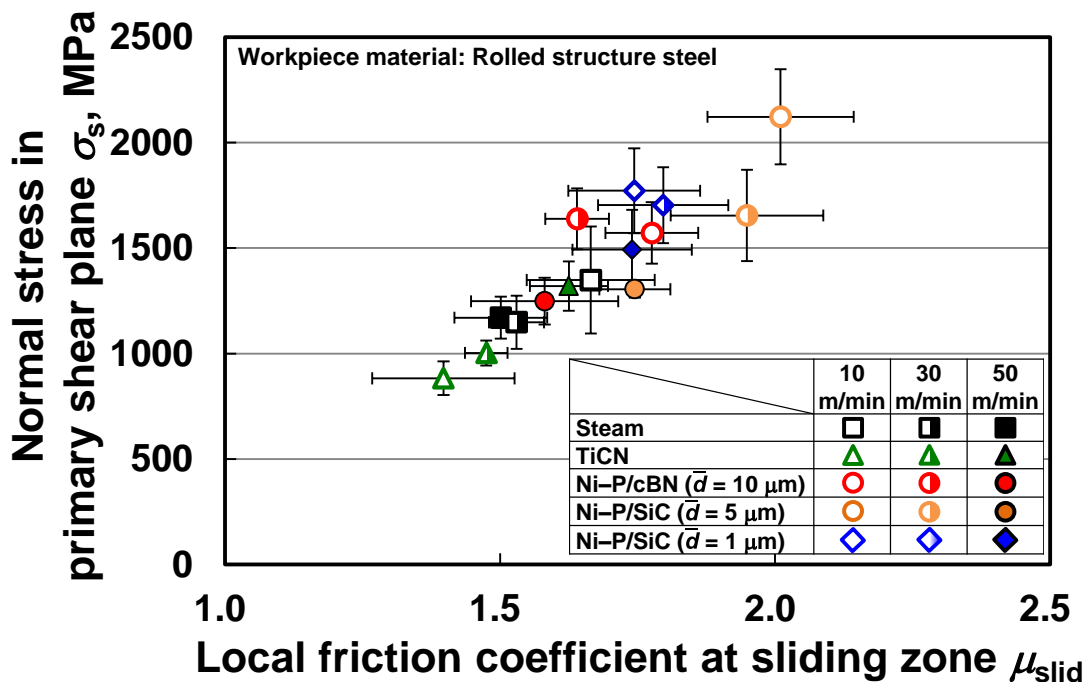


Fig. 5.11 Relation between the local friction coefficient at the sliding zone and normal stress in the primary shear plane

Figure 5.12 shows the relation between shear stress and normal stress in the primary shear plane. As shown in this figure, the shear stress and the normal stress in the primary shear plane exhibit a strong positive correlation. The shear stress in the primary shear plane changed from 709 MPa to 1050 MPa. This change in the shear stress is caused by the high strain, high strain rate, and high temperature of the workpiece material during the cutting process [15]. In particular, deformation resistance increases with an increase in strain and strain rate, and it decreases with increasing temperature. Therefore, for the tapping tools other than the TiCN coated tool, the cutting resistance of the workpiece material decreased with an increase in cutting speed due to its heat-softening [15]. For the tapping tool coated with TiCN film, it is considered that the increasing shear stress as the cutting speed increased was significantly affected by strain hardening and strain rate (as opposed to thermal softening) [16].

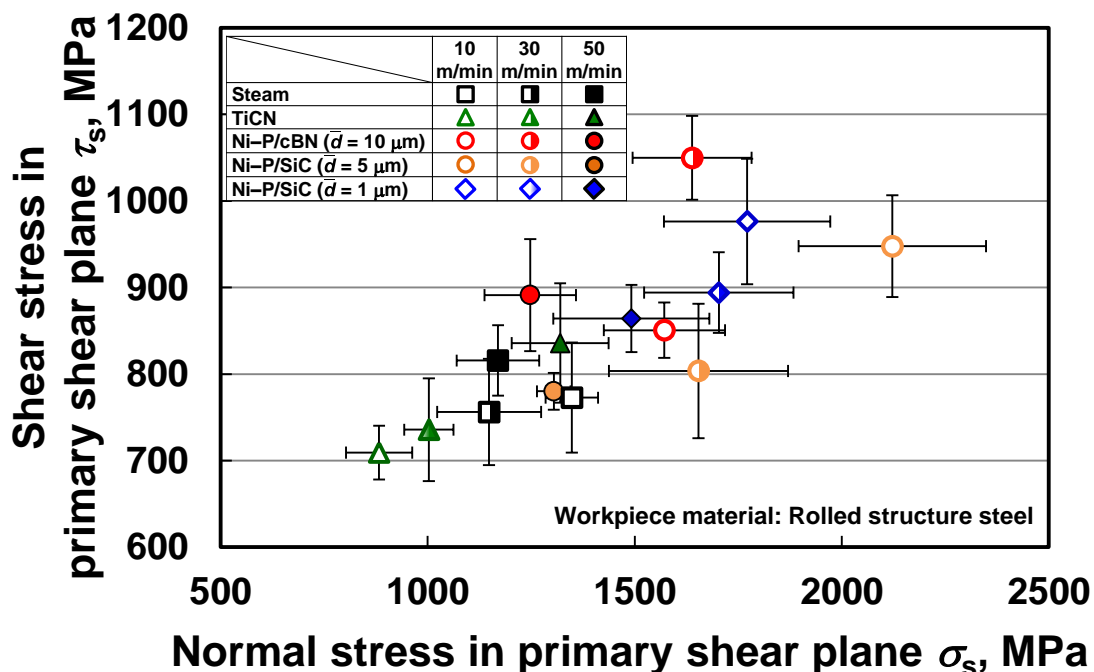


Fig. 5.12 Relation between shear stress and normal stress in the primary shear plane

According to these results, the local friction coefficient at the sliding zone had an impact on the stress fields in the primary shear plane as well as the secondary shear zone. The tapping tools coated with the developed composite films provided higher normal and shear stresses compared with other conventional tapping tools. Therefore, the tapping tools coated with Ni–P/abrasive particle composite films increased the stresses in the primary shear plane and enlarged the secondary shear zone, which resulted in an enhancement of chip curling. Additionally, in this study, the secondary shear zone thickness enlarged the shear angle, as shown in Fig. 5.13. In other words, the tapping tools coated with Ni–P/abrasive particle composite films decreased chip thickness. Since the bending stiffness of a chip was decreased due to reduced thickness, the chip curl for the tapping tools coated with Ni–P/abrasive particle composite films was enhanced. Thus, cutting chips were effectively evacuated and chip snarling was prevented, as shown in Fig. 5.14.

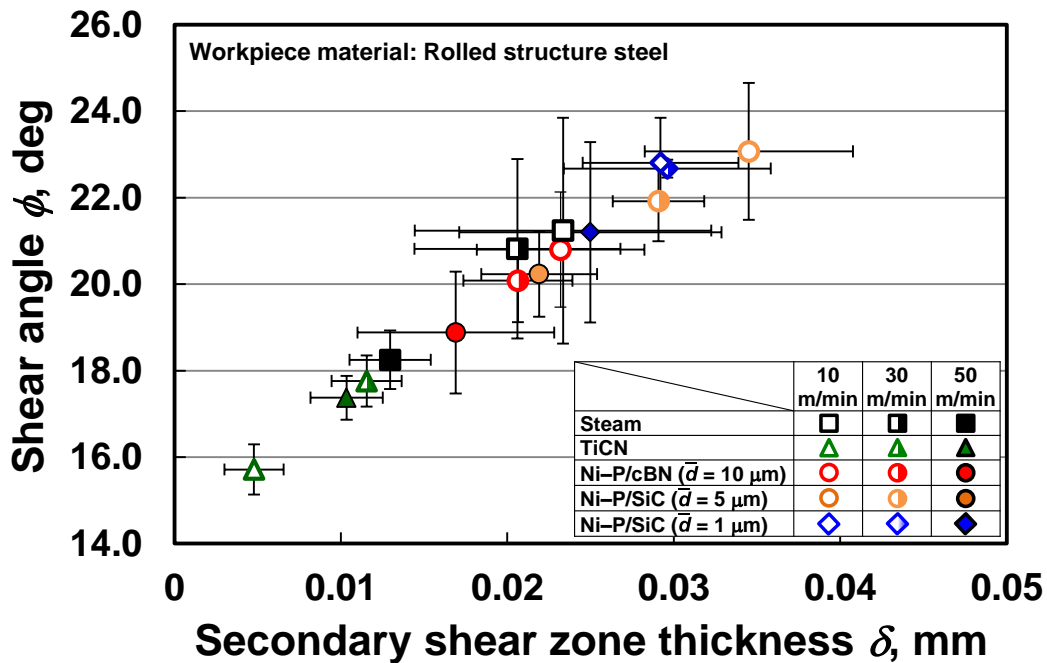


Fig. 5.13 Relation between the secondary shear zone thickness and shear angle

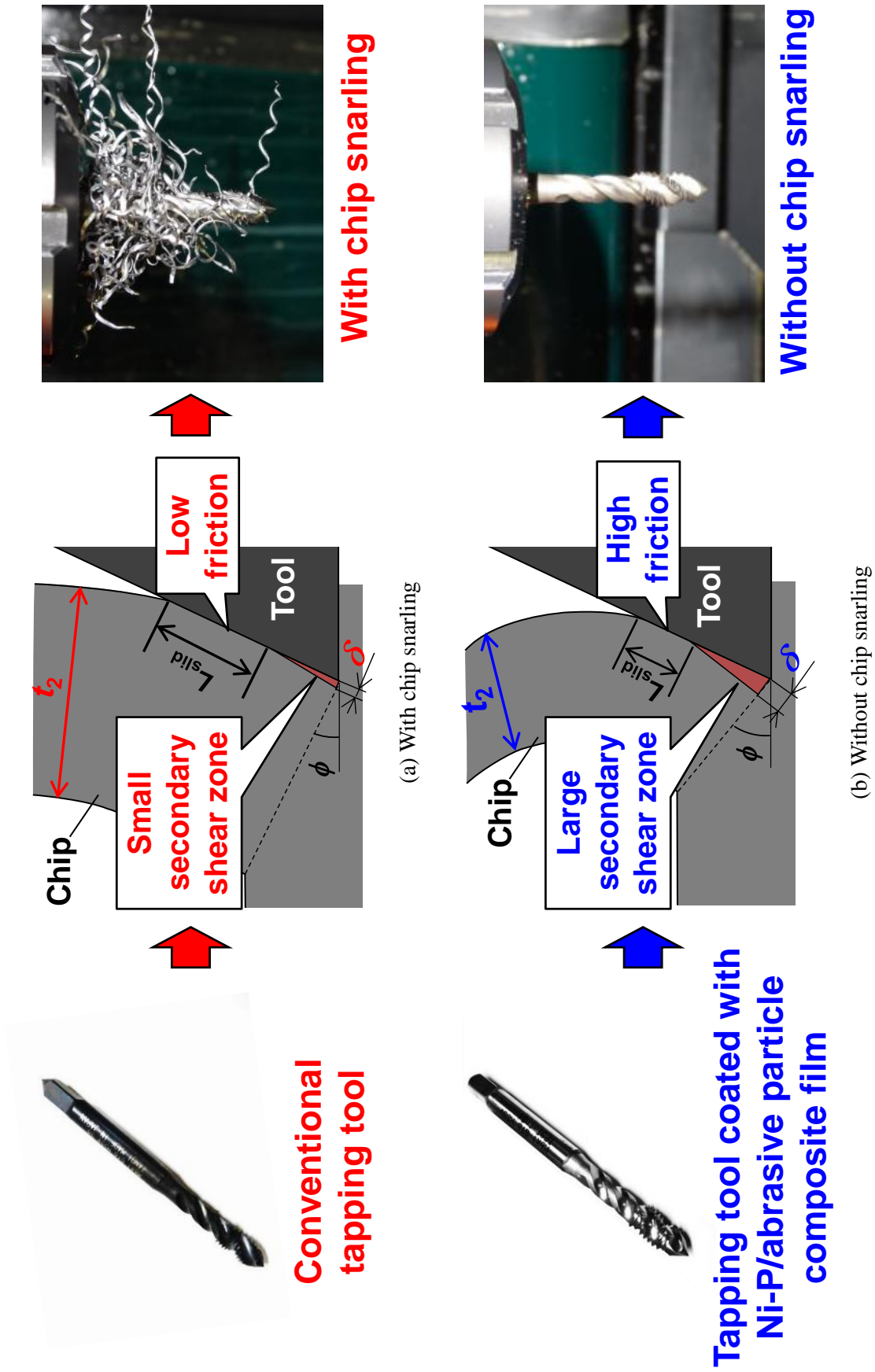


Fig. 5.14 Schematic illustration of the effect of secondary shear zone size and chip curl

5.4 Conclusions

In this chapter, the local friction coefficient at the sliding zone of the chip–tool interface during tapping was estimated based on the sticking–sliding friction model. The effects of the local friction coefficient on chip curl diameter and secondary shear zone thickness were analyzed to investigate the mechanism of chip snarling prevention for tapping tools coated with the composite film.

The conclusions obtained in this chapter are as follows:

- (1) Chip curl diameter decreased with an increase in the local friction coefficient at the sliding zone; the local coefficients of friction for tapping tools coated with composite films (1.58–1.80) were higher than those for tapping tools with conventional surface treatments (1.40–1.65).
- (2) The local friction coefficient at the sliding zone had a significant impact on secondary shear zone thickness; the secondary shear zone thickness increased with an increase in the local friction coefficient at the sliding zone.
- (3) The secondary shear zone was observed for the tapping tool coated with the composite film at 10 and 50 m/min, and the thickness of the secondary shear zone estimated from the observed images was almost equivalent to the calculated values.
- (4) The tapping tools coated with Ni–P/abrasive particle composite films provided a high local friction coefficient at the sliding zone, which increased secondary shear zone thickness and reduced chip curl diameter.

References

- [1] Merchant, E. M., “Mechanics of the Metal Cutting Process. II. Plasticity Conditions in Orthogonal Cutting,” *Journal of Applied Physics*, 16, 1945, 267-275.
- [2] Astakhov, P. V., Shvets, V. S. and Osman, M. O. M., “Chip Structure Classification Based on Mechanics of its Formation,” *Journal of Materials Processing Technology*, 71, 1997, 247-257.
- [3] Okushima, K. and Hitomi, K. “The Mechanism of Chip Curl in Orthogonal Cutting,” *Journal of the Japan Society Precision Engineering*, 25, 1959, 320-327 (in Japanese).
- [4] Okushima, K. and Hitomi, K. “An Analysis of the Mechanism of Orthogonal Cutting and its Application to Discontinuous Chip Formation,” *Journal of Engineering for Industry-Transactions of the ASME*, 83, 1961, 545-555.
- [5] Nakayama, K., Uenoyama, M. and Tamura, K., “Chip Curl in Metal Cutting,” *The Japan Society for Precision Engineering*, 27, 10, 1961, 681-688.
- [6] Cook, N. H., Jhaveri, P. and Nayak, N., “The Mechanism of Chip Curl and its Importance in Metal Cutting,” *Journal of Engineering for Industry*, 85, 4, 1963, 374-380.
- [7] Zhang, Z. Y. and Peklenik, J., “Chip Curl, Chip Breaking and Chip Control of the Difficult-to-Cut Materials,” *CIRP Annals Manufacturing Technology*, 29, 1, 1980, 79-83.
- [8] Usui, E. and H. Takeyama, “A Photoelastic Analysis of Machining Stresses,” *Journal of Engineering for Industry*, 82, 4, 1960, 303-307.
- [9] Shaw, C. M., “A New Mechanism of Plastic Flow,” *International Journal of Mechanical Sciences*, 22, 1980, 673-686.
- [10] Childs, C. H.T., “Friction Modelling in Metal Cutting,” *Wear*, 260, 2006, 310-318.
- [11] Moufki, A., Molinari, A. and Dudzinski, D., “Modelling of Orthogonal Cutting with a Temperature Dependent Friction Law,” *Journal of the Mechanics and Physics of Solids*, 46, 1998, 2103-2138.

- [12] Ozlu, E. and Budak, E., “Experimental Analysis and Modeling of Orthogonal Cutting using Material and Friction Models, in 4th International Conference and Exhibition on Design and Production of MACHINES and DIES/MOLDS,” Cesme, 2007.
- [13] Özel, T. and Zeren, E., “A Methodology to Determine Work Material Flow Stress and Tool-chip Interfacial Friction Properties by using Analysis of Machining,” *Journal of Manufacturing Science and Engineering*, 128, 1, 2005, 119-129.
- [14] Childs, C. H. T., Maegawa, K., Obikawa, T. and Yamane, Y., “Metal Machining: Theory and Applications,” Copublished in North, Central and South America by John Wiley and Sons Inc., New York/Toronto, 2000, 65-68.
- [15] Johnson, R. G. and Cook, H. W., “A Constitutive Model and Data for Metals Subjected to Large Strains, High Strain Rates and High Temperature,” proceeding of the 7th international symposium on ballistics, 1983, 541-547.
- [16] Camuşcu, N., “Effect of Cutting Speed on the Performance of Al₂O₃ based Ceramic Tools in Turning Nodular Cast iron,” *Materials and Design*, 27, 2006, 997-1006.

Chapter 6

Effect of workpiece material on chip snarling for tapping tool coated with Ni–P/abrasive composite film

6.1 Introduction

As noted in Chapter 4, the tapping tool coated with Ni–P/abrasive particle composite film was able to prevent chip snarling in tapping tests on rolled structural steel (JIS SS400) at a cutting speed of 50 m/min, which is five times the standard speed. As discussed in Chapter 5, this was due to the high local coefficient of friction at the sliding zone of the tool–chip interface, which increased the secondary shear-zone thickness and reduced the chip curl diameter. In particular, the tapping tool coated with an Ni–P/SiC particle composite film of $\bar{d} = 1 \mu\text{m}$ prevented chip snarling throughout its full service life, extending the life for the tool to 2.6 times that of the conventional tool. This suggested that a coating of Ni–P/SiC composite film of $\bar{d} = 1 \mu\text{m}$ produces a highly efficient tapping tool. However, so far, these effects were confirmed only for the SS400 workpiece.

Chip curl is influenced by the cutting resistance and deformability of the workpiece material because it is associated with plastic deformation and plastic flow in the shear zone [1]. Yamane and Sekiya [2] suggested that the cutting resistance is influenced by the hardness and tensile strength of the workpiece. The Johnson–Cook material constants [3] give the flow stress $\bar{\sigma}$ as follows:

$$\bar{\sigma} = (A + B \varepsilon^n) \left(1 + C \ln\left(\frac{\dot{\varepsilon}}{\dot{\varepsilon}_0}\right)\right) \left(1 - \left(\frac{T - T_{\text{room}}}{T_m - T_{\text{room}}}\right)^m\right) \quad (6.1)$$

where ε is the plastic strain, $\dot{\varepsilon}$ is the strain rate [s^{-1}], $\dot{\varepsilon}_0$ is the reference plastic strain rate [s^{-1}], T is the temperature of the workpiece material [K], T_m is the melting temperature of the workpiece material [K], T_{room} is the room temperature [K], A is the yield strength [MPa], B is the hardening modulus [MPa], C is the strain rate sensitivity coefficient, n is the hardening coefficient, and m is the

thermal softening coefficient. The flow stress during cutting, which influences the chip curl, is determined by these material properties of the workpiece. As noted above, the addition of a composite film was found to prevent chip snarling at high cutting speeds for the SS400 workpiece. However, it is necessary to confirm that the same effect can be obtained for other workpiece materials.

In this chapter, it was reported that tapping tests conducted on workpieces made from chrome molybdenum steel (JIS SCM440) and carbon steel (JIS S25C and S45C). The tests were conducted to investigate whether the Ni–P/SiC particle composite film ($\bar{d} = 1 \mu\text{m}$) was able to prevent chip snarling for these workpieces.

6.2 Methods

6.2.1 Tapping tests

Table 6.1 summarizes the tapping test conditions. The experimental apparatus and tapping test conditions were the same as those used in the tests presented in Chapter 3 (see Table 6.1). Tapping tools with steam treatment and those coated with TiCN coating were again used for comparison. The evacuated and snarled chips were collected after each thread hole had been cut.

6.2.2 Workpiece materials

When SCM440, S25C, and S45C are subjected to a cutting process, they result in poor chip disposability. Table 6.2 summarizes the material properties of the workpieces. The thermal properties of the three materials were nearly the same. The hardness and the 0.2% proof stress of SCM440 were higher than those of the other materials. The hardness of S25C was same as that of SS400.

Table 6.1 Experimental conditions

Type of tapping tool	Spiral-tap (HSS, M6 × 1)
Surfaae treatment	Ni–P/SiC film ($\bar{d} = 1 \mu\text{m}$)
	Steam treatment
	TiCN film
Workpiece material	Chrome molybdeum steel (JIS SCM440)
	Carbon steel (JIS S25C)
	Carbon steel (JIS S45C)
Cutting speed V_r , m/min	10, 30, 50
Lubricant	Emulsion cutting oil ($\nu = 1.20 \text{ mPa}\cdot\text{s}$ at 21.6°C)
Number of cutting process N , holes	25

Table 6.2 Workpiece material properties [4-10]

	Chrome molybdeum steel (JIS SCM440)	Carbon steel (JIS S25C)	Carbon steel (JIS S45C)	Rolled-structure steel (JIS SS400)
Vickers hardness HV, MPa	1676	1152	1520	1185
0.2% proof stress σ_y , MPa	1123	366	822	245
Density ρ , kg/m^3	7800	7200	7830	7860
Specific heat c , $\text{J}/(\text{kg}\cdot\text{K})$	450	500	480	473
Heat transfer coefficient k , $\text{W}/(\text{m}\cdot\text{K})$	43	40	47	51.3
Melting Temperature T_{melt} , K	1713-1783	1803	1723-1783	1807

6.3 Results and discussion

6.3.1 Chip snarling and chip curl diameter

6.3.1.1 Rate of chip snarling

Figures 6.1–6.3 show the effect of the cutting speed on the rate of chip snarling for each tapping tool. The rate of the tool coated with the Ni–P/SiC film was less than 5% for SCM440, less than 5% for S25C, and less than 10% for S45C. The rate of chip snarling of the tapping tool with steam treatment decreased as the cutting speed increased when used with SCM440 (from 28% to 0%) and S25C (from 24% to 8%); however, it increased when used with S45C (from 0% to 20%). The rate of chip snarling of the tool with TiCN coating was higher at lower cutting speeds (10 and 30 m/min) for all workpiece materials; however, at 50 m/min, it was less than 5%. This suggested that the tool coated with the Ni–P/SiC film was performed better than the other tapping tools in reducing chip snarling when cutting threaded holes in all workpieces.

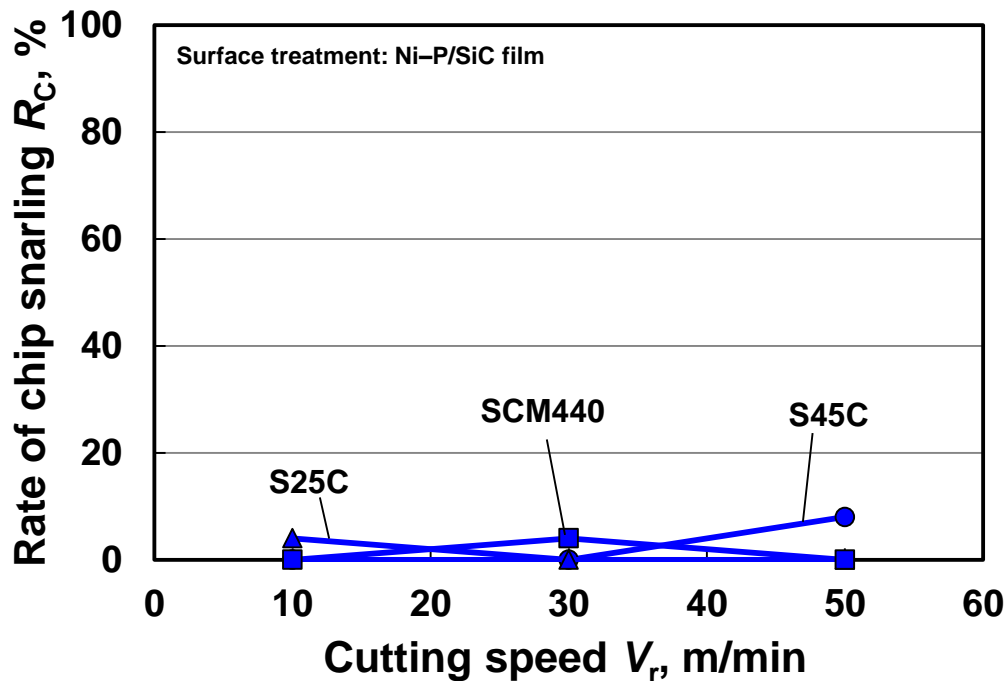


Fig. 6.1 Rate of chip snarling of the tapping tool coated with the Ni–P/SiC film

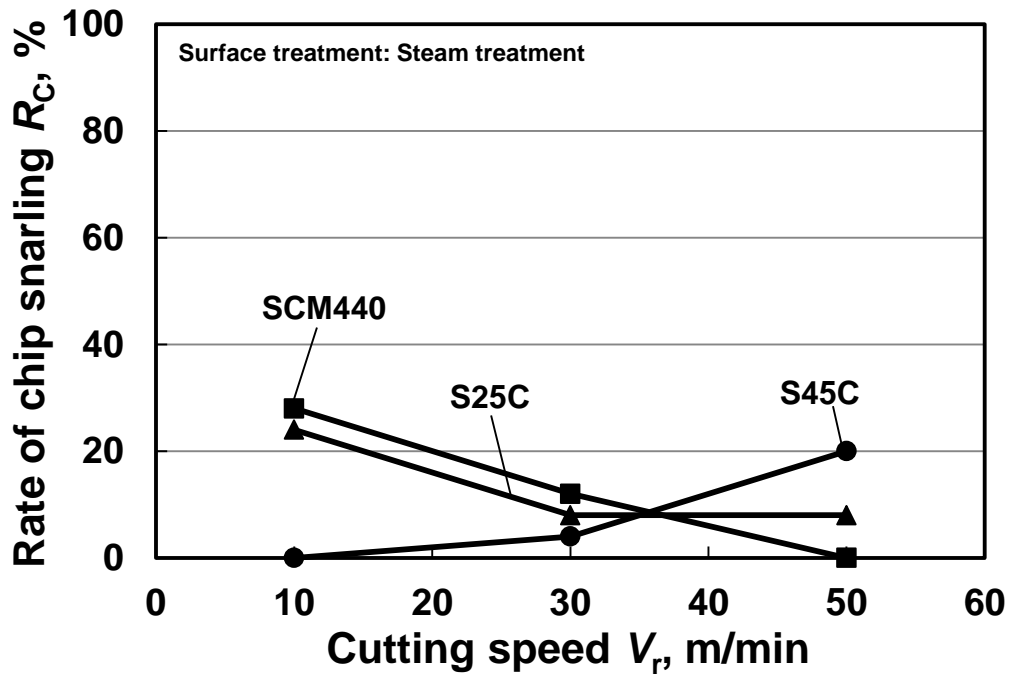


Fig. 6.2 Rate of chip snarling of the tapping tool coated using steam treatment

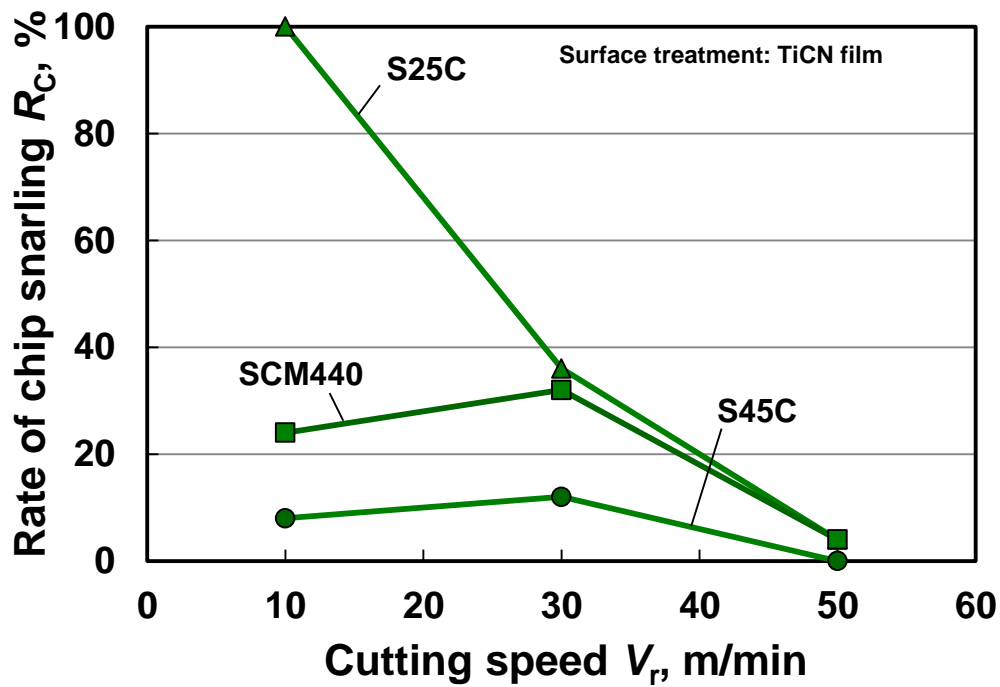


Fig. 6.3 Rate of chip snarling of the tapping tool coated with the TiCN film

6.3.1.2 Chip curl diameter

Figure 6.4 shows the chip curl diameter and the dimensionless chip curl diameter for each tapping tool in tests with SCM440 conducted at 10, 30, and 50 m/min. The chip curl diameter from the tool coated with the Ni–P/SiC film increased in line with the cutting speed. The other tapping tools produced larger diameter chip curls than the composite film-coated tool at 10 and 30 m/min but varied less with speed.

Figure 6.5 shows the chip curl diameter and dimensionless chip curl diameter at 10, 30, and 50 m/min for S25C. The chip curl diameters of the steam-treated and Ni–P/SiC film-coated tools increased in line with the cutting speed, whereas that of the TiCN-coated tool was 3.2 mm at 10 and 30 m/min, decreasing to approximately 2.7 mm at 50 m/min.

Figure 6.6 shows the chip curl diameter and dimensionless chip curl diameter at 10, 30, and 50 m/min for S45C. The chip curl diameters of the steam-treated and Ni–P/SiC film-coated tools increased in line with the cutting speed, whereas that of the TiCN coated tool decreased as the cutting speed increased.

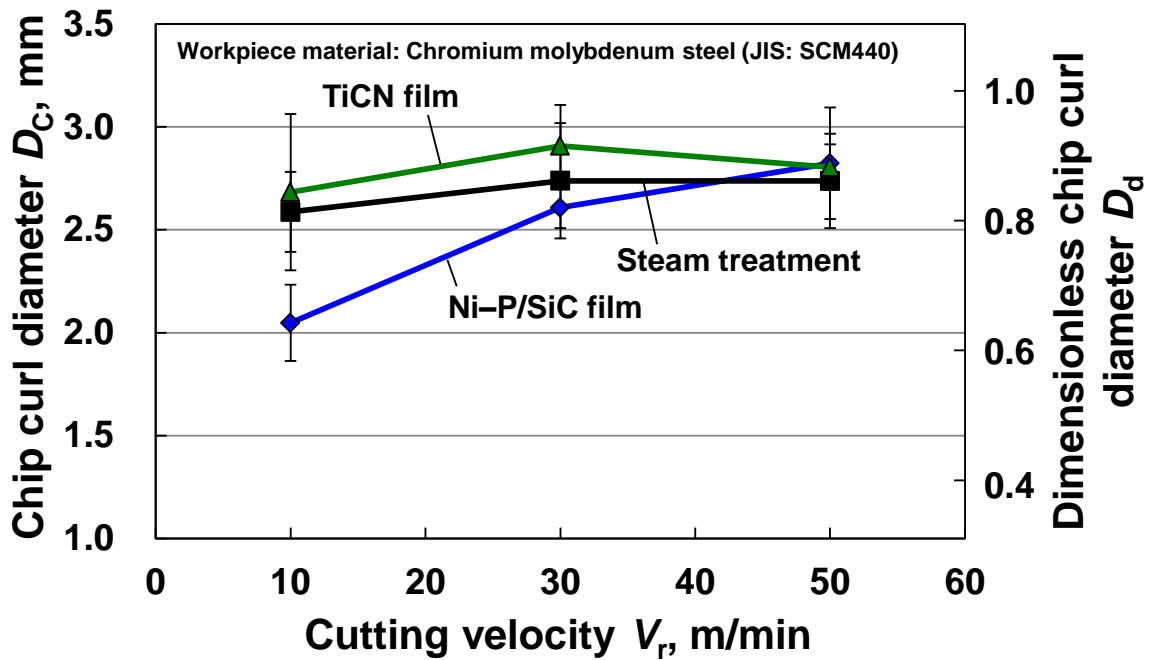


Fig. 6.4 Effect of cutting speed on the chip curl diameter of chromium–molybdenum steel (JIS SCM440)

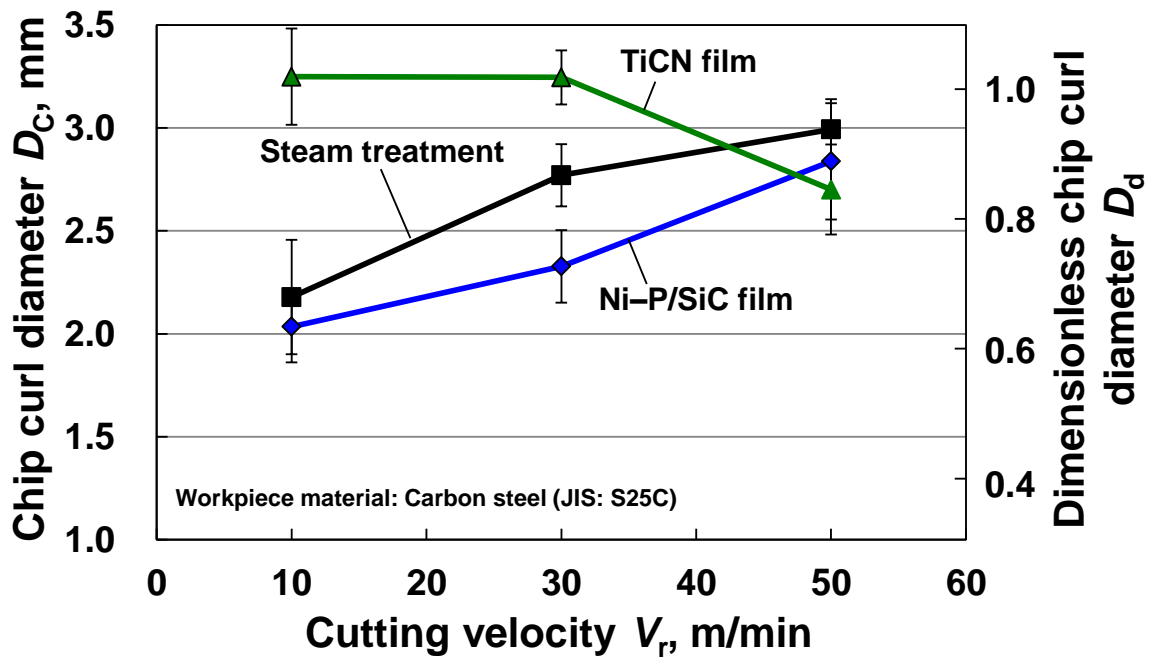


Fig. 6.5 Effect of cutting speed on the chip curl diameter of carbon steel (JIS S25C)

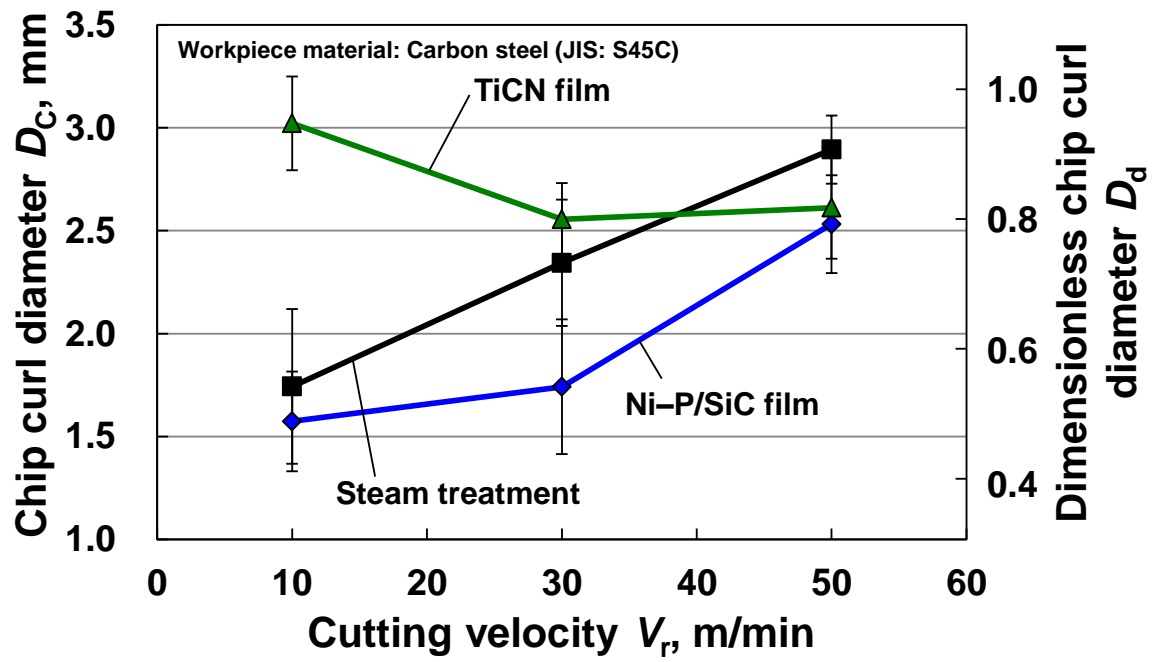


Fig. 6.6 Effect of cutting speed on the chip curl diameter of carbon steel (JIS S45C)

6.3.1.3 Effect of dimensionless chip curl diameter on the rate of chip snarling

Figure 6.7 shows the relation between the rate of chip snarling and the dimensionless chip curl diameter. The figure includes results for SS400 reported in Chapter 4. As shown in Fig. 6.7, the rate of chip snarling increased in line with the dimensionless chip curl diameter, and drastically increased when $D_d \geq 0.9$. For all workpiece materials, the dimensionless chip curl diameter of the Ni-P/SiC film-coated tool was smaller than 0.9 and the rate of chip snarling was less than 10%. This tapping tool produced chips with a curl diameter much shorter than the flute width, achieving good chip discharge and preventing chip snarling.

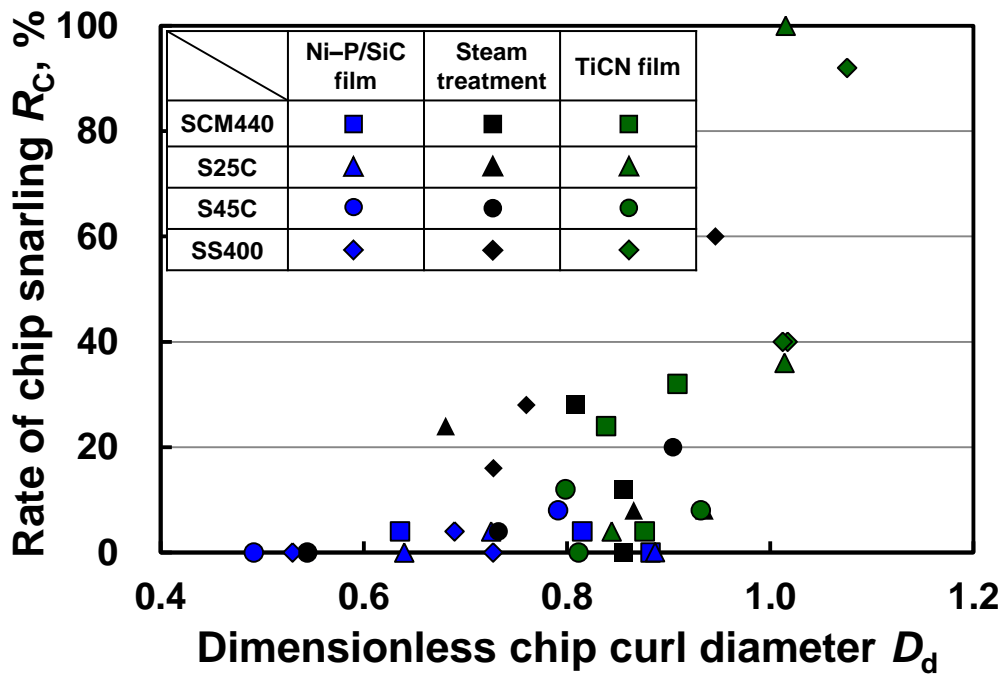


Fig. 6.7 Relation between rate of chip snarling and dimensionless chip curl diameter

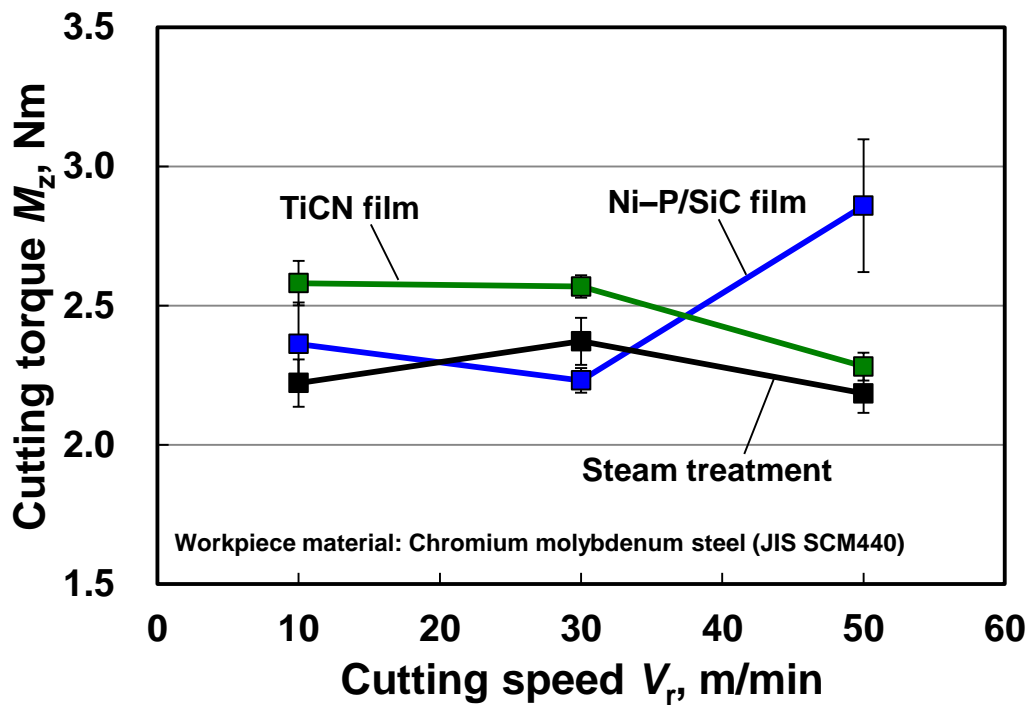
6.3.2 Effect of friction coefficient at the sliding zone on chip curl diameter

6.3.2.1 Cutting torque and thrust force

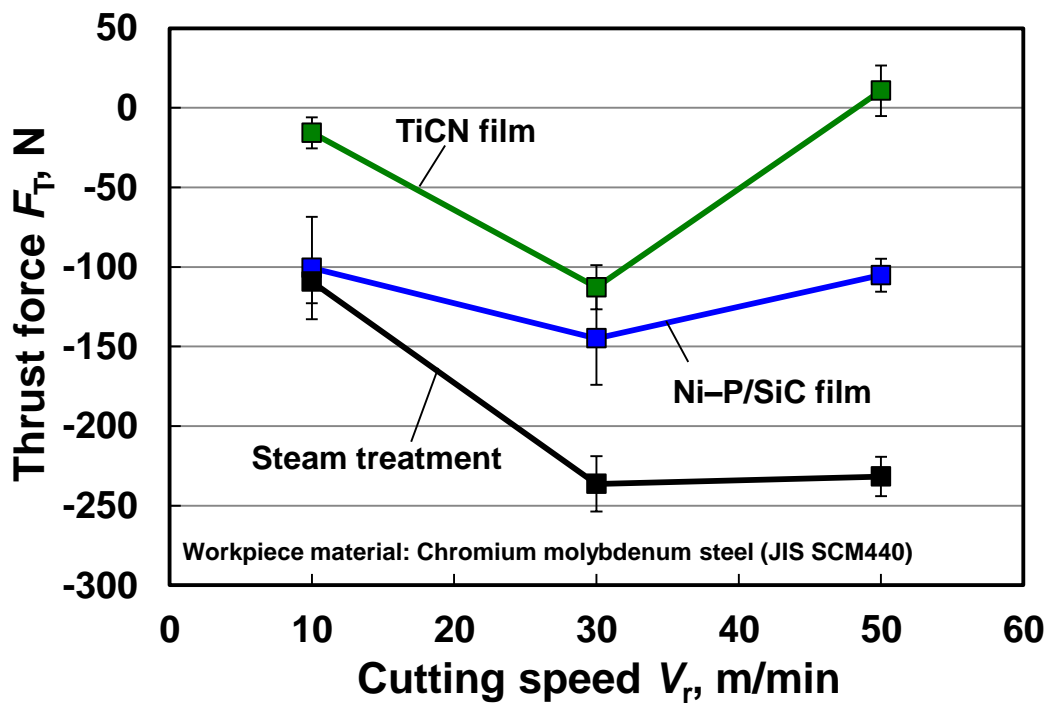
Figure 6.8 shows the effect of cutting speed on cutting torque and thrust force for SCM440. The cutting torque of the steam-treated tool was constant across all cutting speeds at approximately 2.2 Nm. The thrust force of the Ni–P/SiC film-coated tool increased at 50 m/min to approximately 2.8 Nm, while its thrust force at all cutting speeds was greater than –150 N. The thrust force of the steam-treated tool decreased at 30 m/min, and the value of thrust force at 30 and 50 m/min was approximately –240 N. The thrust force of the TiCN-coated tool ranged between 0 and –100 N, and it was higher than that of the other tools at all cutting speeds.

Figure 6.9 shows the effect of the cutting speed on cutting torque and thrust force for S25C. The cutting torque of the steam-treated and Ni–P/SiC film-coated tools at all cutting speeds was approximately 1.9 Nm, whereas that of the TiCN-coated tool ranged between 2.0 and 2.2 Nm, which was higher than that of the other tools at all cutting speeds. The thrust force of the Ni–P/SiC film-coated tool was –150 N at all cutting speeds, whereas that of the steam-treated tool decreased as the cutting speed increased. The thrust force of the tapping tool with TiCN coating was close to –50 N.

Figure 6.10 shows the effect of the cutting speed on cutting torque and thrust force for S45C. The cutting torque of the steam-treated and Ni–P/SiC film-coated tools had a constant value of 2 Nm at all cutting speeds, whereas that of the TiCN-coated tool was higher than the cutting torques of the other tools at all cutting speeds. The thrust force of all tapping tools reached a minimum value at 30 m/min; however, those of the TiCN-coated and Ni–P/SiC film-coated tools were higher than –100 N at all cutting speeds.

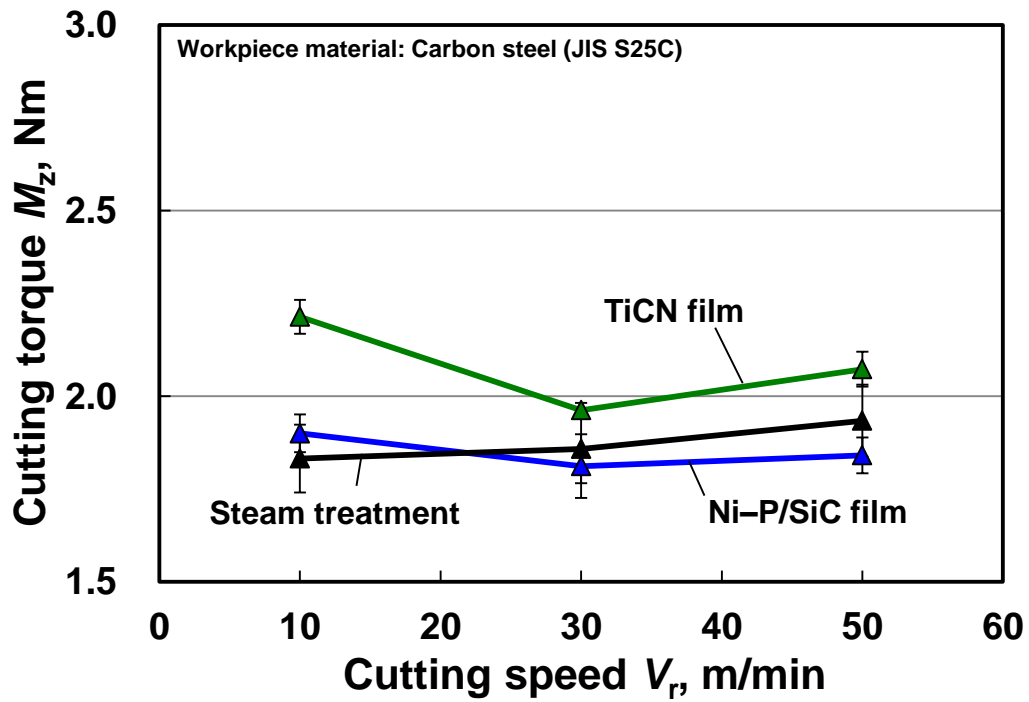


(a) Cutting torque

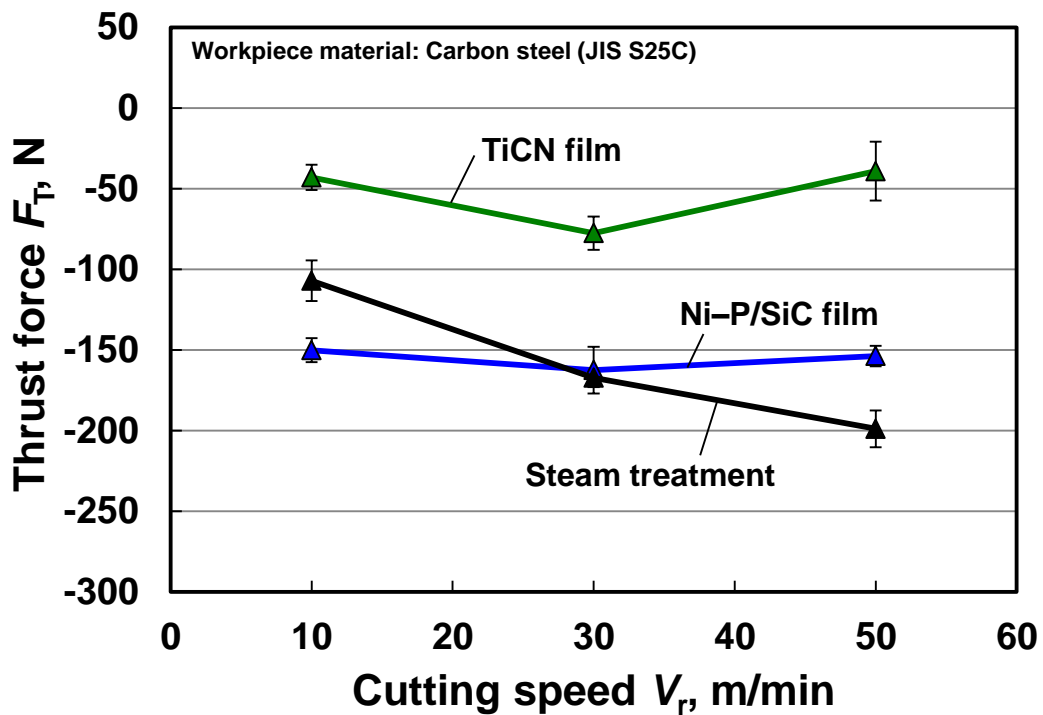


(b) Thrust force

Fig. 6.8 Effect of cutting speed on cutting torque and thrust force for chromium–molybdenum steel (JIS SCM440)

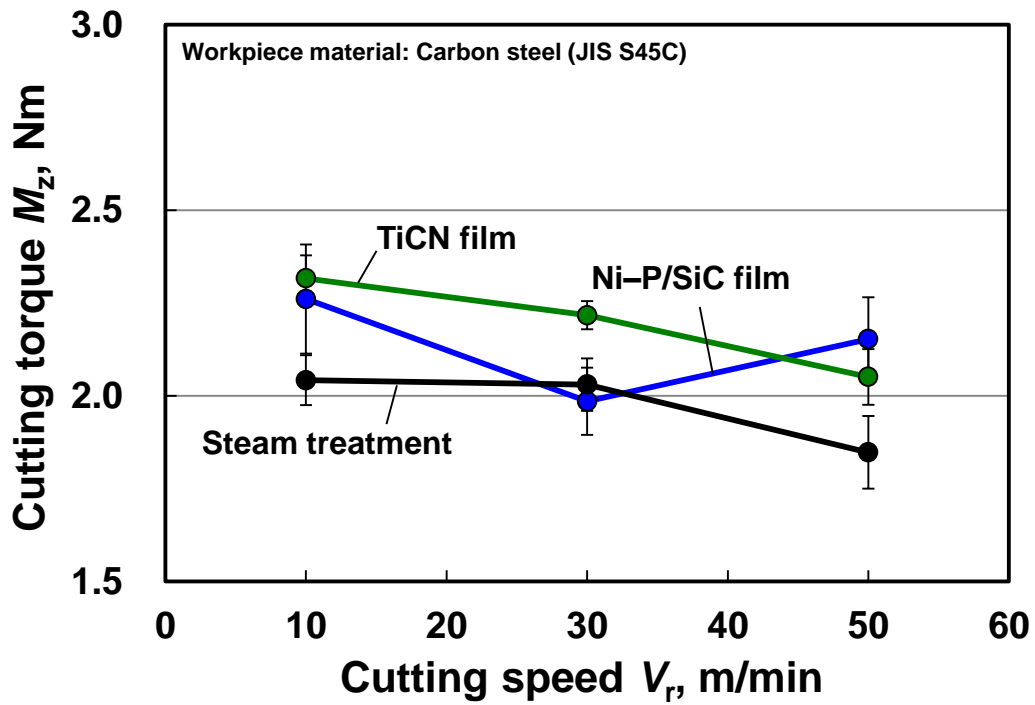


(a) Cutting torque

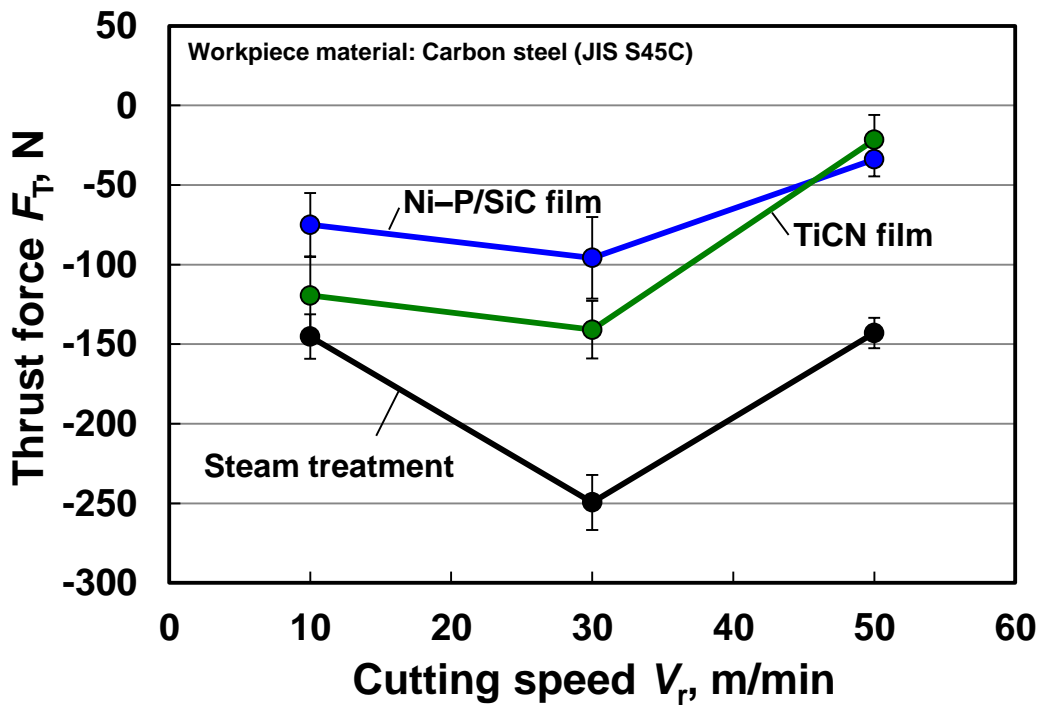


(b) Thrust force

Fig. 6.9 Effect of cutting speed on cutting torque and thrust force for carbon steel (JIS S25C)



(a) Cutting torque



(b) Thrust force

Fig. 6.10 Effect of cutting speed on cutting torque and thrust force for carbon steel (JIS S45C)

6.3.2.2 Local friction coefficient at the sliding zone

The local friction coefficient for each workpiece material was calculated using Eqs. (5.1)–(5.16) from Chapter 5.

Figure 6.11 shows the effect of cutting speed on the local friction coefficient at the sliding zone for SCM440. Regardless of the cutting speed, the coefficients of the TiCN-coated and Ni–P/SiC film-coated tools remained between 1.4 and 1.6. The friction coefficient of the steam-treated tool decreased to 1.1 as the cutting speed increased.

Figure 6.12 shows the effect of cutting speed on the local friction coefficient at the sliding zone for S25C. The local friction coefficient at sliding zone of the tapping tool with TiCN coating ranged between 1.5 and 1.7. The local friction coefficient at sliding zone of the Ni–P/SiC-coated tool ranged between 1.2 and 1.5, and that of the steam-treated tool ranged between 1.1 and 1.4.

Figure 6.13 shows the effect of cutting speed on the local friction coefficient at the sliding zone for S45C. The local friction coefficients at sliding zone of the TiCN-coated and Ni–P/SiC-coated tools increased slightly as the cutting speed increased, whereas that of the steam-treated tool ranged between 1.1 and 1.4.

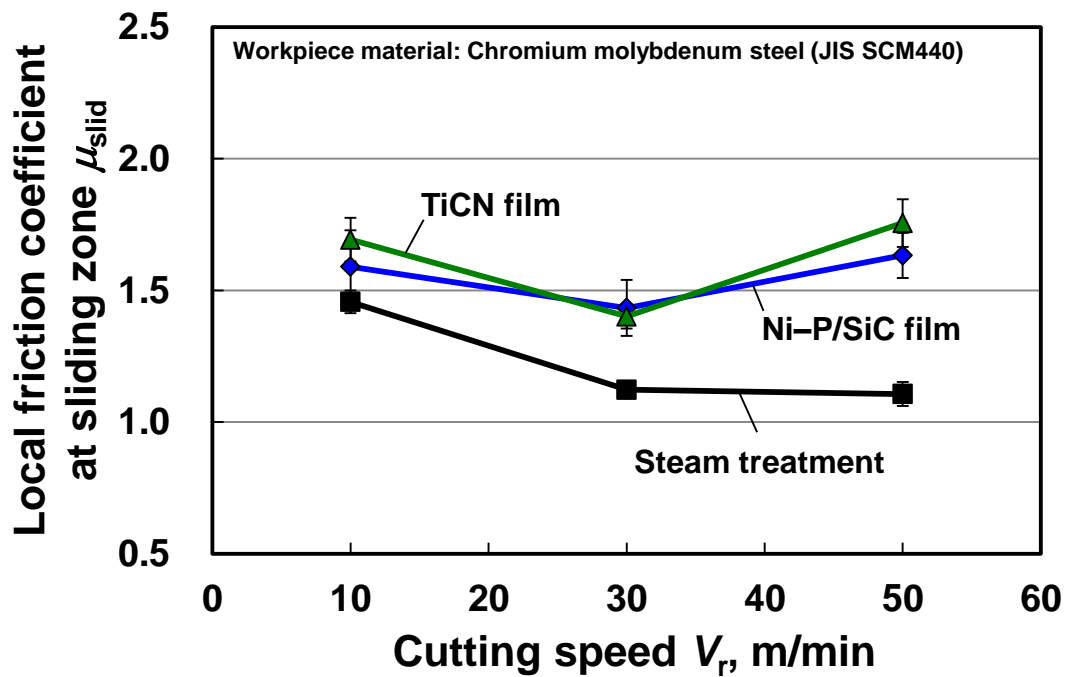


Fig. 6.11 Effect of cutting speed on friction coefficient at sliding zone for chromium–molybdenum steel (JIS SCM440)

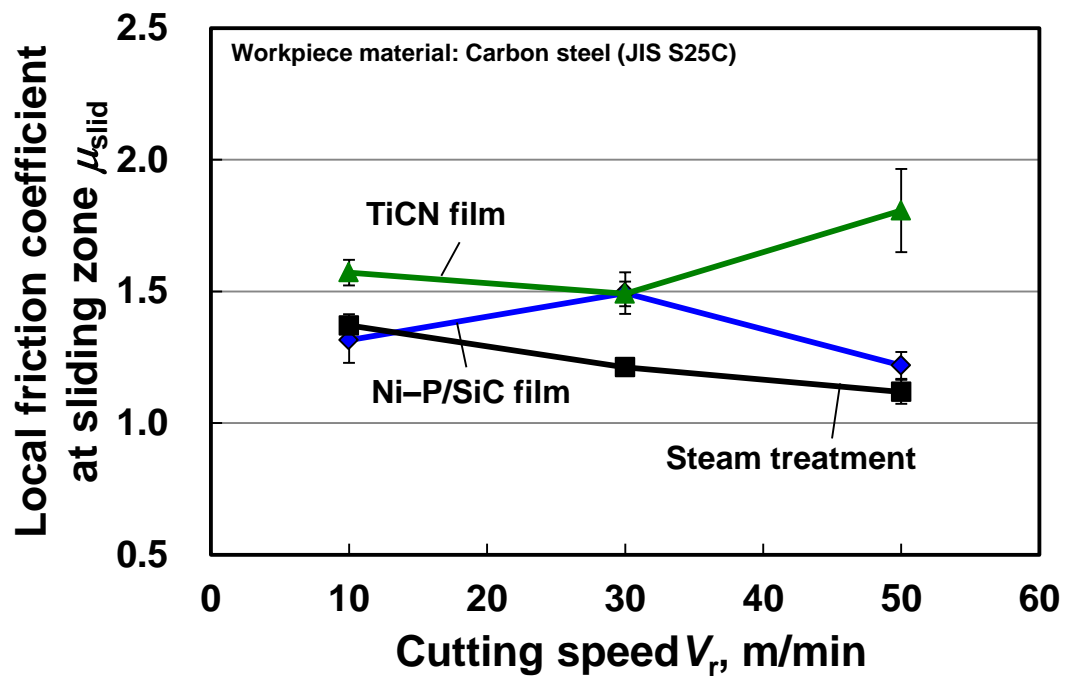


Fig. 6.12 Effect of cutting speed on friction coefficient at sliding zone for carbon steel (JIS S25C)

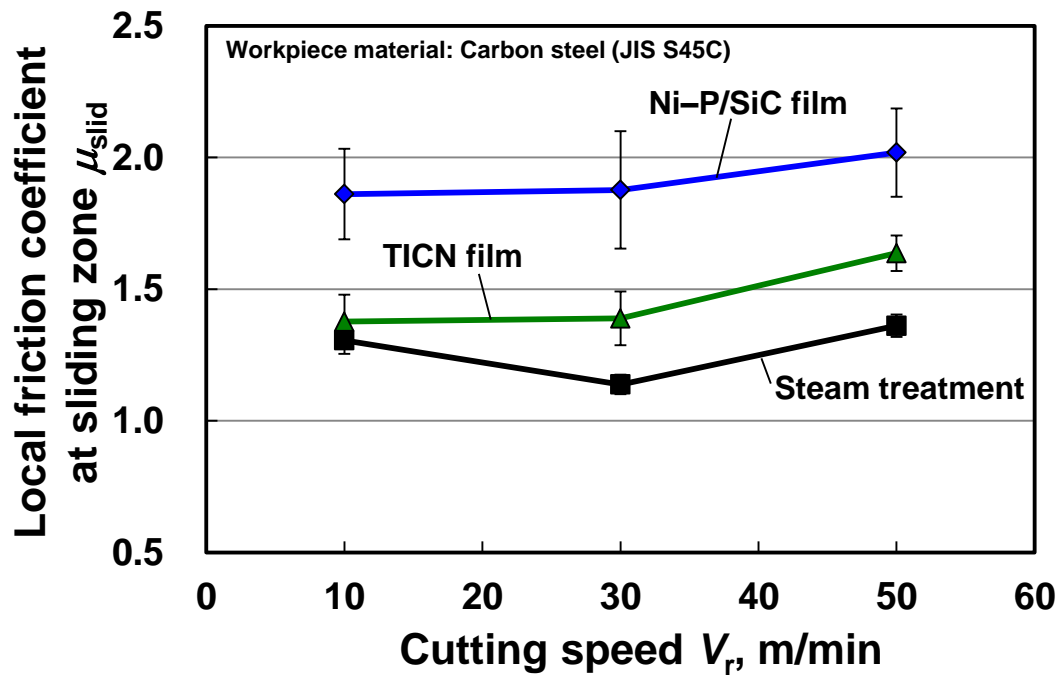


Fig. 6.13 Effect of cutting speed on friction coefficient at sliding zone for carbon steel (JIS S45C)

6.3.2.3 Relation between secondary shear zone thickness and local friction coefficient at the sliding zone

Figure 6.14 shows the relation between the secondary shear zone thickness and the friction coefficient at the sliding zone. The secondary shear zone thickness when cut with the Ni-P/SiC-coated tapping tool increased as the local friction coefficient at the sliding zone increased. The local friction coefficient and the secondary shear zone thickness of this tapping tool were higher than those of the other tools.

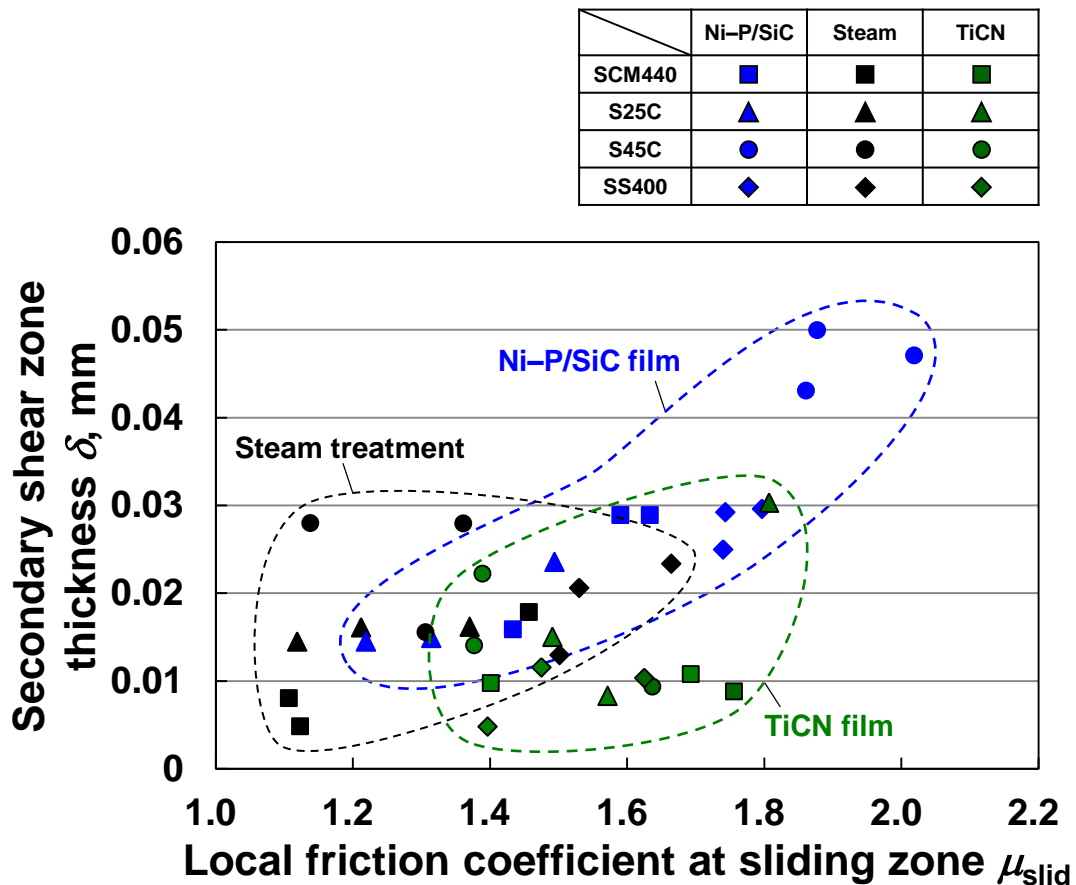
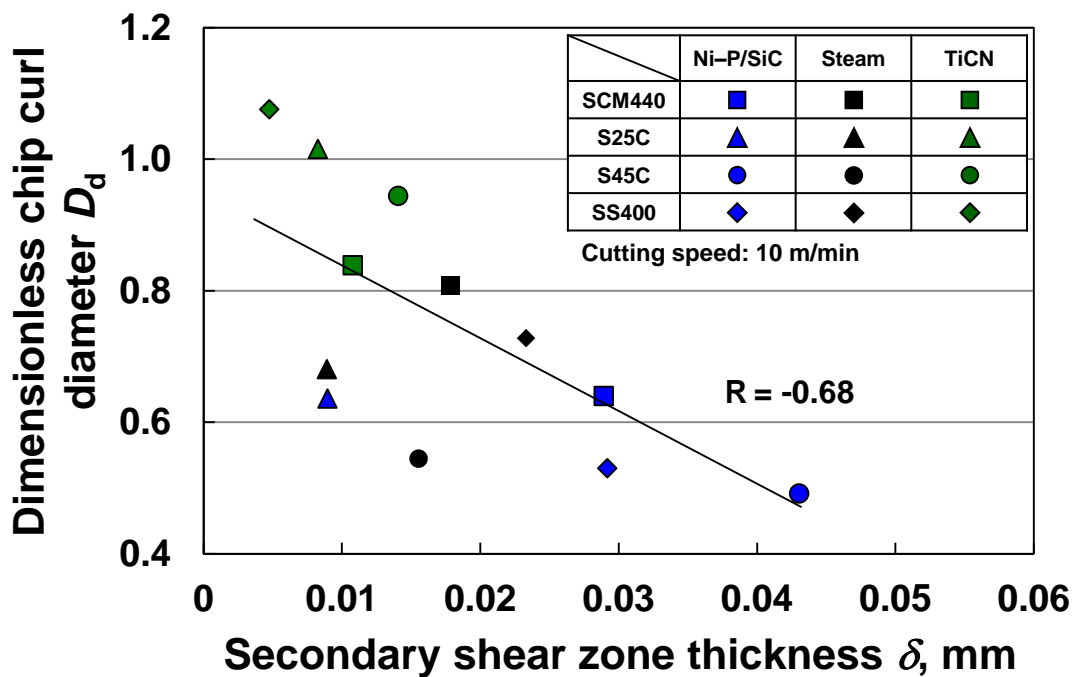


Fig. 6.14 Relation between secondary shear zone thickness and friction coefficient at the sliding zone

6.3.2.4 Relation between dimensionless chip curl diameter and secondary shear zone thickness

Figure 6.15 shows the relation between the dimensionless chip curl diameter and the secondary shear zone thickness. It is evident from the figure that the dimensionless chip curl diameter decreased as the secondary shear zone thickness increased at all cutting speeds. This suggested that increasing the secondary shear zone thickness is an effective way of reducing the dimensionless chip curl diameter. As shown in Fig. 6.7, a dimensionless chip curl diameter of less than 0.9 is required to achieve a rate of chip snarling less than 30%. To bring the D_d values below 0.9, the secondary shear zone thickness at 10, 30, and 50 m/min must be greater than 0.014, 0.015, and 0.027 mm, respectively. A thicker secondary shear zone is therefore required to reduce chip snarling at higher cutting speeds. The temperature at the chip–tool interface increased with the cutting speed, suggesting that the increase in the required secondary shear zone thickness may be related to the temperature at the chip–tool interface.



(a) $V_r = 10$ m/min

Fig. 6.15 Relation between dimensionless chip curl diameter and secondary shear zone thickness

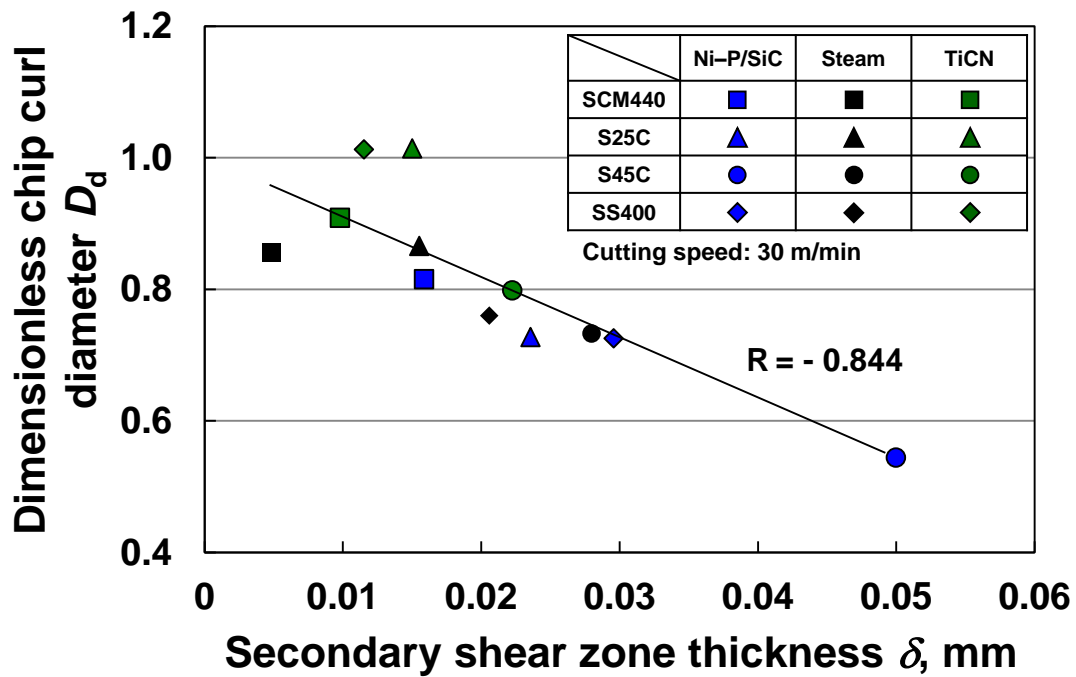
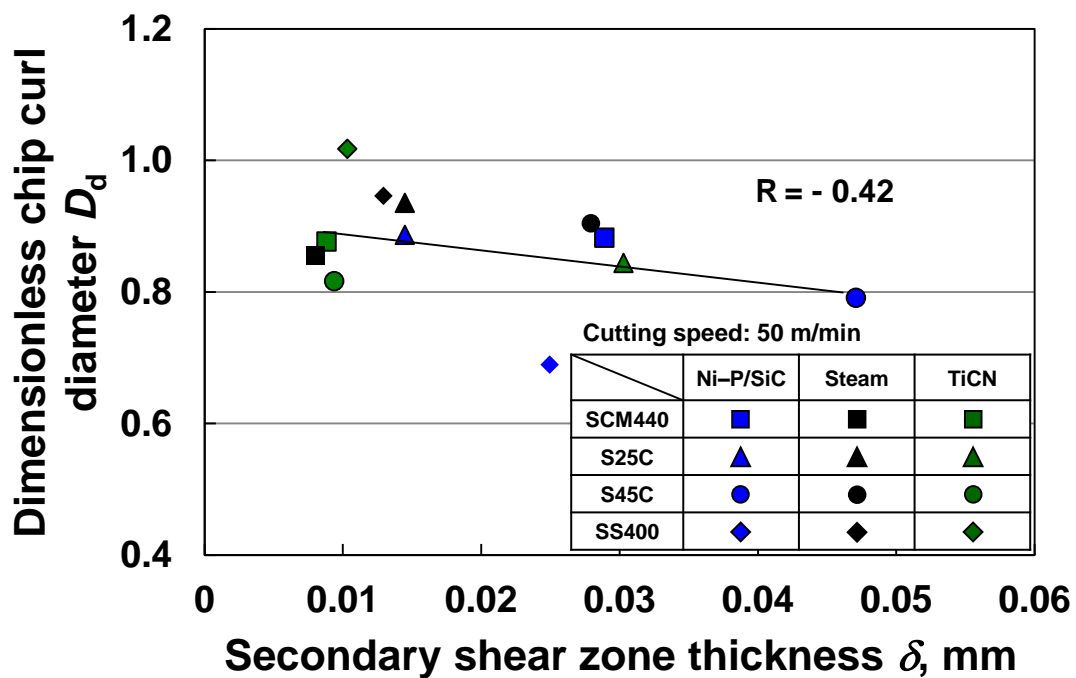
(b) $V_r = 30$ m/min(c) $V_r = 50$ m/min

Fig. 6.15 Relation between dimensionless chip curl diameter and secondary shear zone thickness

6.3.2.5 Effect of secondary shear zone thickness and temperature at the primary shear zone on dimensionless chip curl diameter

In the course of cutting, heat is generated in the primary shear area, the sliding zone at the chip–tool interface, and the flank face at the workpiece–tool interface [11]. In the primary shear zone, the total heat generated per unit of time and area q [$\text{J}/(\text{mm}^2 \cdot \text{s})$] is a function of the shear stress in the primary shear zone τ_s and the shear velocity in the primary shear plane V_s [12], which is expressed as follows:

$$q = \tau_s \times V_s \quad (6.2)$$

$$V_s = \frac{\cos \alpha_e}{\cos(\phi - \alpha_e)} \times V_r \quad (6.3)$$

Where α_e is the effective rake angle [degree], ϕ is the shear angle [degree]. The ratio between the quantity of heat flowing in the chip and the total heat is calculated as the heat volume ratio R [11] using Eqs. (6.4) and (6.5):

$$R = \frac{1}{1 + \frac{0.664\gamma_s}{\sqrt{L}}} \quad (6.4)$$

$$L = \frac{V_s \gamma_s t_1}{4} \cdot \left(\frac{\rho c}{k} \right) \quad (6.5)$$

where γ_s is the shear strain, t_1 is the uncut chip thickness [mm], ρ is the density [kg/m^3], c is the specific heat capacity [$\text{J}/(\text{kg} \cdot \text{K})$], and k is the thermal conductivity [$\text{W}/(\text{m} \cdot \text{K})$]. The mean temperature at the primary shear zone T_{shear} is expressed as follows:

$$T_{\text{shear}} = \frac{Rq}{\rho c} \cdot \left(\frac{t_1 b}{\sin \phi} \right) \cdot \left(\frac{1}{V_s t_1 b} \right) + T_{\text{room}} \quad (6.6)$$

where b is the mean width of the cut chip, which is calculated as $b = (b_t + b_b)/2$, b_t is the width of the free surface of the chip [mm] and b_b is the width of the chip near rake face [mm].

Figure 6.16 shows the distribution of dimensionless chip curl diameter as a function of the temperature at the primary shear zone and the secondary shear zone thickness. The secondary shear

zone thickness decreased as the temperature at the primary shear zone increased. As shown in Fig. 6.16, the dimensionless chip curl diameter exceeded 0.8 when the temperature at the primary shear zone was greater than 614 K or the secondary shear zone thickness was less than 15 μm . In contrast, the dimensionless chip curl diameter was smaller than 0.6, i.e., the rate of chip snarling was zero, when the temperature at the primary shear zone was lower than 495 K and the secondary shear zone thickness was no less than 23 μm .

From Eq. (6.1), an increase in the temperature at the primary shear zone reduced the shear stress in the shear zone. This suggested that the effect of the secondary shear zone thickness on chip curl diameter reduced as the temperature at the primary shear zone increased, as shown in Fig 6.17. The chip curl diameter of the Ni–P/SiC film-coated tool decreased at high cutting speeds because the secondary shear zone was thick and the temperature at the primary shear zone was low. Consequently, the chip curl diameter was smaller than the width of the helical flute, preventing chip snarling on the tapping tool at high cutting speeds.

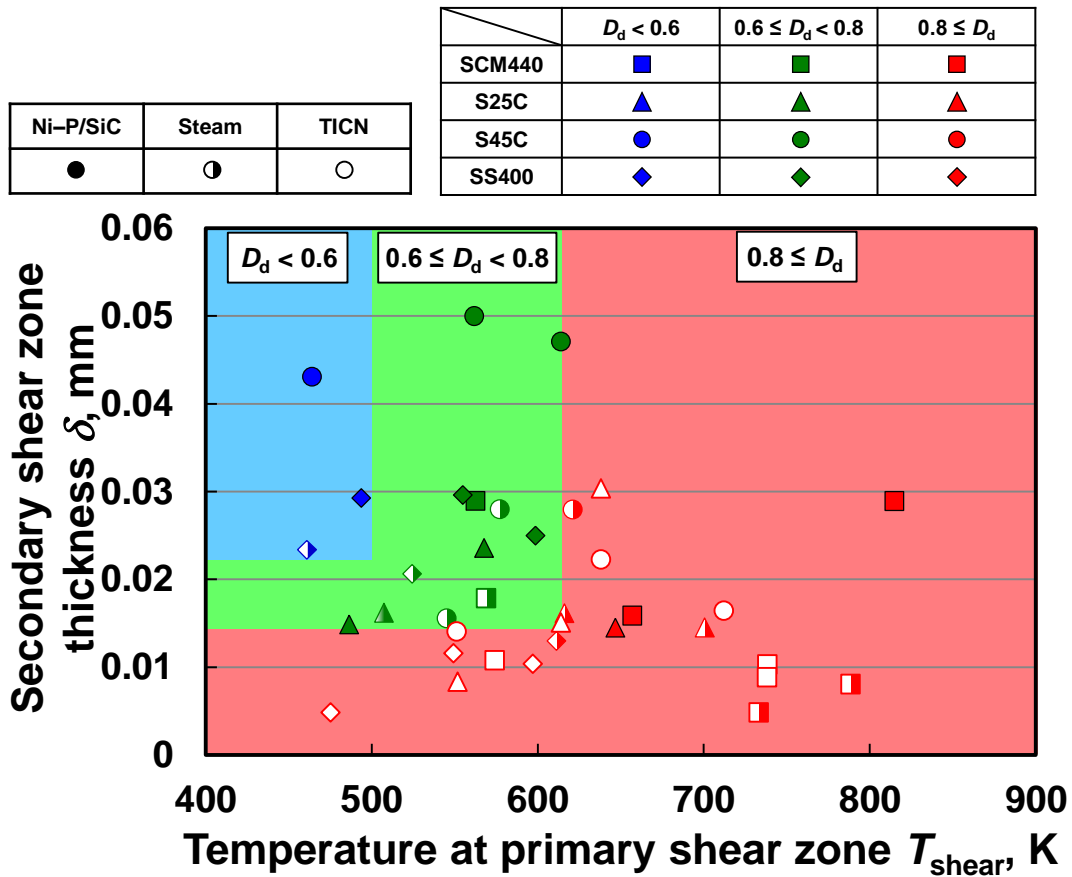


Fig. 6.16 Distribution of dimensionless chip curl diameter as a function of temperature at primary shear zone and secondary shear zone thickness

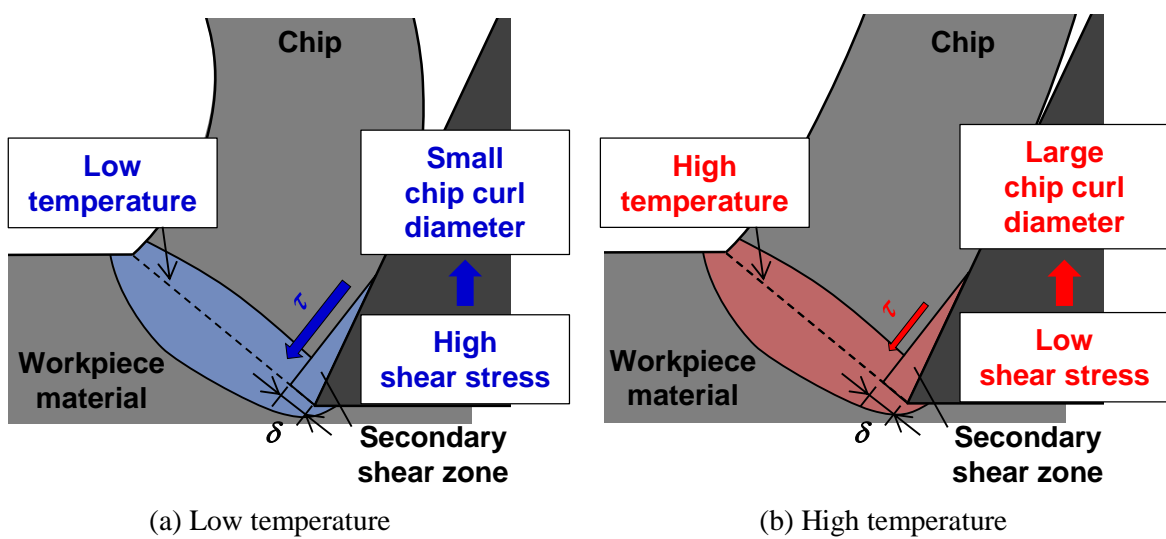


Fig. 6.17 Effect of temperature at primary shear zone on chip curl diameter

6.4 Conclusions

In this chapter, it was reported that tapping tests conducted on workpieces made from SCM440, S25C, and S45C to investigate whether coating the tapping tool with the Ni–P/SiC particle composite film could prevent chip snarling across a wide range of cutting speeds. The relation between workpiece material and chip curl diameter was also investigated.

The conclusions are summarized as follows:

- (1) The rate of chip snarling increased in line with the dimensionless chip curl diameter, particularly when $D_d \geq 0.9$. The dimensionless chip curl diameter of the tapping tool coated with the Ni–P/SiC film ($\bar{d} = 1 \mu\text{m}$) was less than 0.9 for all workpiece materials and the rate of chip snarling was less than 10%.
- (2) When the tapping tool coated with the composite film was used, the secondary shear zone thickness increased as the local friction coefficient at the sliding zone increased. The secondary shear zone thickness was affected by the temperature at the primary shear zone and decreased as this temperature increased.
- (3) The dimensionless chip curl diameter was less than 0.6 when the temperature at the primary shear zone was lower than 495 K and the secondary shear zone thickness was at least 23 μm . This reduced the frequency of chip snarling.
- (4) Coating the tapping tool with the composite film prevented chip snarling when cutting threaded holes in steel workpieces made from JIS SCM440, S25C, S45C, and SS400.

References

- [1] Nakayama, K., Uenoyama, M. and Tamura, K., “Chip Curl in Metal-Cutting Process,” The Japan Society for Precision Engineering, 27, 321, 1961, 681-688 (in Japanese).
- [2] Yamane, Y. and Sekiya, K., “An Evaluation of Difficulty in Machining Difficult-to-Cut Materials by Using Difficult-to-Cut Rating,” The Japan Society for Precision Engineering, 70, 3, 2004, 407-411 (in Japanese).
- [3] Umbrello, D., M’Saoubi, R. and Outerio, C. J., “The Influence of Johnson-Cook Material Constants on Finite Element Simulation of Machining of AISI 316L Steel,” International Journal of Machine Tools and Manufacture, 47, 3-4, 2007, 462-470.
- [4] Huang J. H., Than, T. V., Ngo, T. T. and Wang, C. C., “An Inverse Method for Estimating Heat Sources in a High Speed Spindle,” Applied Thermal Engineering, 105, 25, 2016, 65-76.
- [5] Horikawa, N., Kano, J., Noguchi, T. and Nakamura, T., “Discussion on Calculating Factors in Numerical Analysis of End-Surface Cast-In Insertions,” Journal of Japan Foundry Engineering Society, 75, 2, 2003, 95-101 (in Japanese).
- [6] Mechanical Design Engineer, http://ty-1999.la.coocan.jp/zairyou/zairyou_top.html (accessed 2016-9-12).
- [7] Academy Corner, <http://www.as-1.co.jp/academy/18/18.html> (accessed 2016-9-12).
- [8] Isshiki, Y., Yamaguchi, H., Kawai, G., Ochi, H. and Ogawa, K., “Numerical Analysis of Temperature Distribution in Friction Welding of Two Similar Materials of S25C or SUS304,” Journal of High Temperature Society, 32, 4, 2006, 236-243 (in Japanese).
- [9] Panday, N. P. and Mall, N. R., “Investigation and Optimization of Surface Roughness in Turning of C-45 Alloy Steel by Using Taguchi Method,” ELK Asis Pacific Journals, 2016, 177-180.
- [10] Yamane, S., Tanaka, A., Yamamoto, H., Kaneko, Y. and Oshima, K., “Application of switch back welding to backing less V groove welding on circumference of a circle,” Quarterly journal of the

Japan Welding Society, 25, 1, 2007, 86-94 (in Japanese).

[11] Hirao, M., Terashima, A., Joo, Y. H., Shirase, K. and Yasui, T., “Behavior of Cutting Heat in High Speed Cutting,” The Japan Society for Precision Engineering, 64, 7, 1998, 1067-1071 (in Japanese).

[12] Show, C. M., “Metal Cutting Principles,” Oxford Series on Advanced Manufacturing, 2005, 220.

Chapter 7

Conclusions

In this study, in order to prevent chip snarling and extend tool service life at high cutting velocities, the tapping tool coated with Ni–P/abrasive particle composite film was developed. It was investigated whether the tapping tool prevents chip snarling and increases tool service life even at high cutting velocity conditions. Furthermore, the friction coefficient at sliding zone on cutting edge of tapping tool was estimated and the mechanism of chip snarling prevention was investigated.

The main results and conclusions of the chapter 2 through 6 are as follows:

In Chapter 2, Ni–P/abrasive particle composite films were formed on high-speed steel (HSS) disks using electroless plating. The hardness, adhesion strength, and friction coefficients of the composite-film coated, stream-treated, and TiCN-coated disk specimens were compared. The conclusions of this chapter are as follows:

- (1) Ni–P/abrasive particle composite films were deposited on an HSS disk specimen using cBN particulates with a mean diameter of 10 μm or SiC particulates with mean diameters of 5.0 μm or 1.0 μm . The surface roughness of the composite films was higher than that of the other specimens.
- (2) The hardness of the Ni–P plating film was ~ 11 GPa, which suggests that the composite film, which included the hard particles, was harder than the Ni–P plated film.
- (3) No film separation was observed in the composite films in the scratch tests, which exhibited a peeling resistance greater than that of the other surface-treated specimens.
- (4) The composite films showed friction coefficients greater than 0.15 at sliding velocities under emulsion-oil lubrication (0.05–0.25 m/s), which were higher than those of the other specimens.

The Ni–P/abrasive particle composite films exhibited excellent adhesion strength, wear resistance, and high friction coefficients under emulsion oil lubrication. This suggests that such composite films can be used as coating materials for tapping tools and may increase their service life without inducing chip snarling.

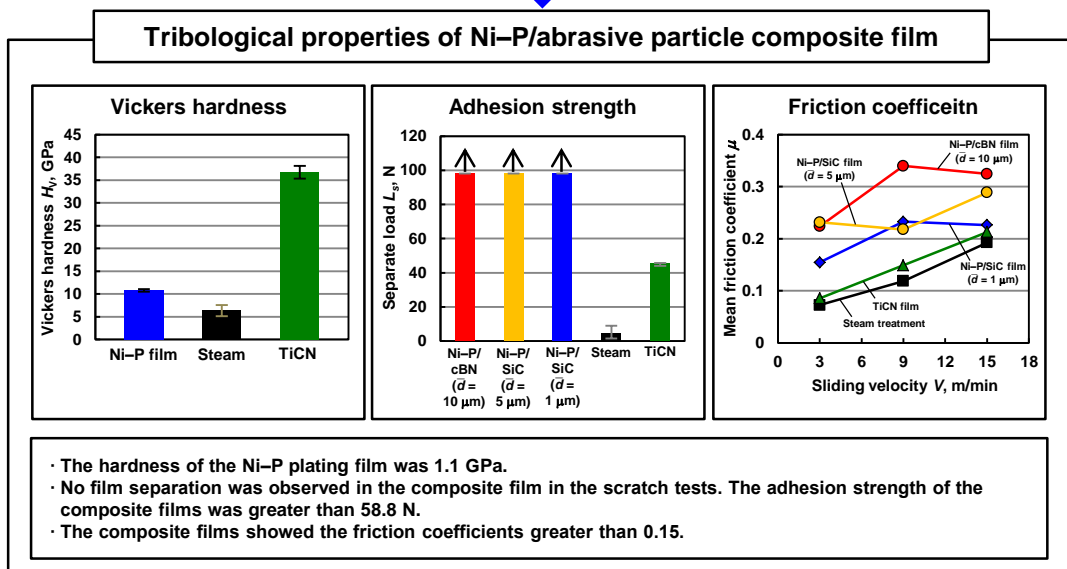
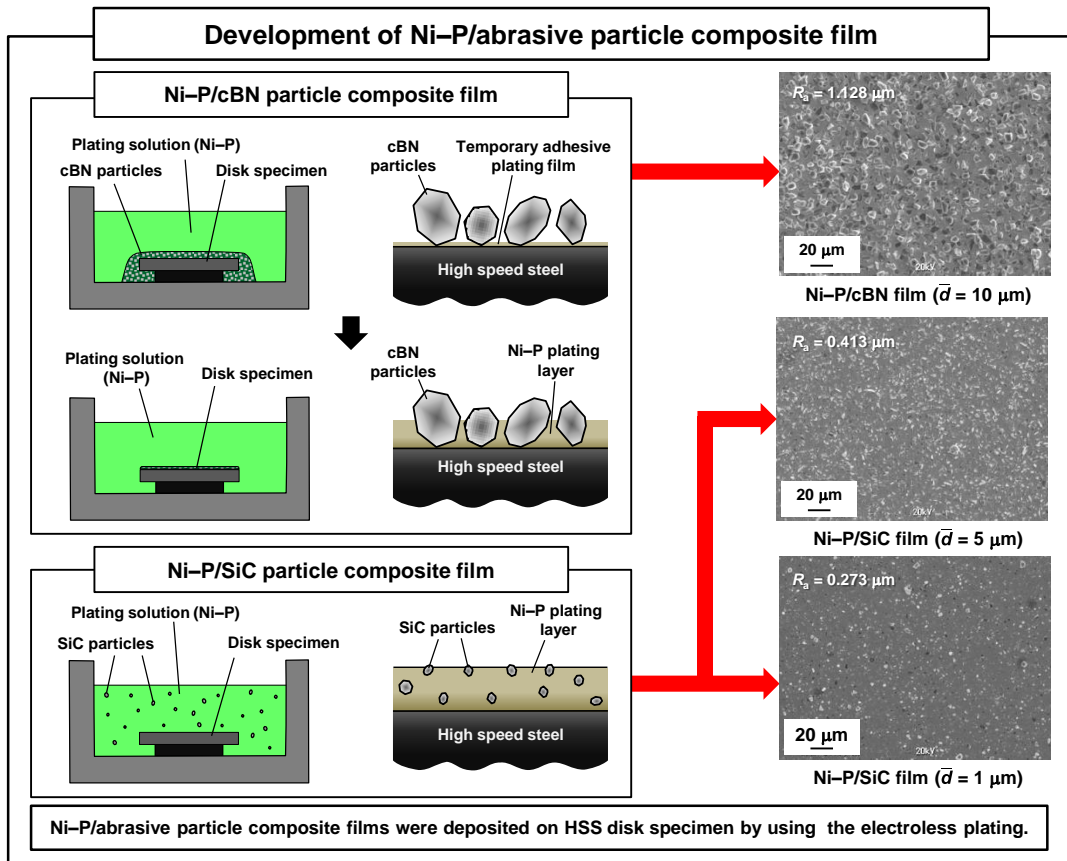
Figure 7.1 illustrates summarized results for Chapter 2.

In Chapter 3, a tapping tool coated with the Ni–P/abrasive particle composite film was developed. The dimensional accuracy of the thread holes and the cutting resistance (i.e., cutting torque and thrust force) were experimentally investigated via tapping tests. The conclusions of this chapter are as follows:

- (1) Tapping tools coated with the Ni–P/cBN ($\bar{d} = 10 \mu\text{m}$), Ni–P/SiC ($\bar{d} = 5 \mu\text{m}$), and Ni–P/SiC ($\bar{d} = 1 \mu\text{m}$) films were developed.
- (2) The thread holes produced by the tools coated with the Ni–P/cBN ($\bar{d} = 10 \mu\text{m}$), Ni–P/SiC ($\bar{d} = 5 \mu\text{m}$), and Ni–P/SiC ($\bar{d} = 1 \mu\text{m}$) films satisfied the relevant standard for thread gauge. However, the surface of the thread holes machined by the tapping tool coated with the Ni–P/cBN particle composite film ($\bar{d} = 10 \mu\text{m}$) was rougher at all cutting velocities.
- (3) The tapping tool coated with the Ni–P/cBN particle composite film ($\bar{d} = 10 \mu\text{m}$) produced the highest cutting torque and thrust force.

The tensile force produced by the tool coated with the Ni–P/abrasive particle composite film was less than 50 N at 50 m/min.

Figure 7.2 illustrates summarized results for Chapter 3.



The results suggested that the Ni-P/abrasive particle composite films can be used as coating materials for tapping tools and may increase their tool service life without inducing chip snarling.

Fig. 7.1 Diagram of summarized results for Chapter 2

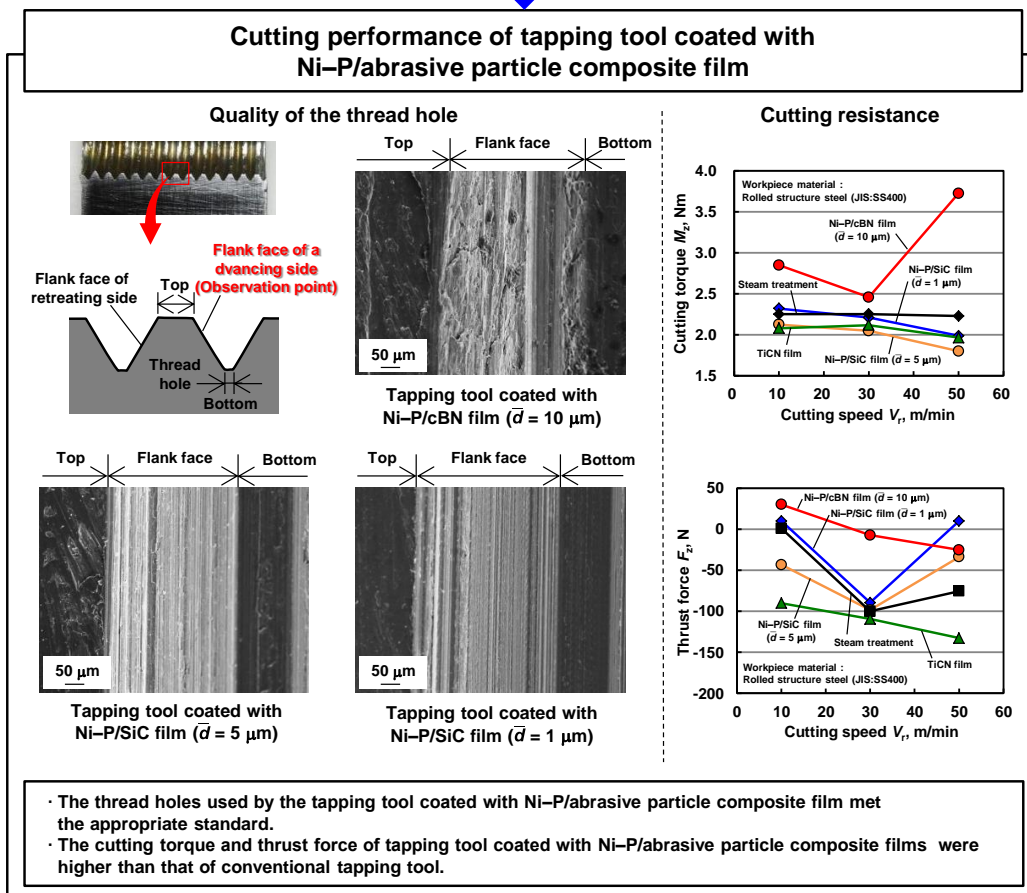
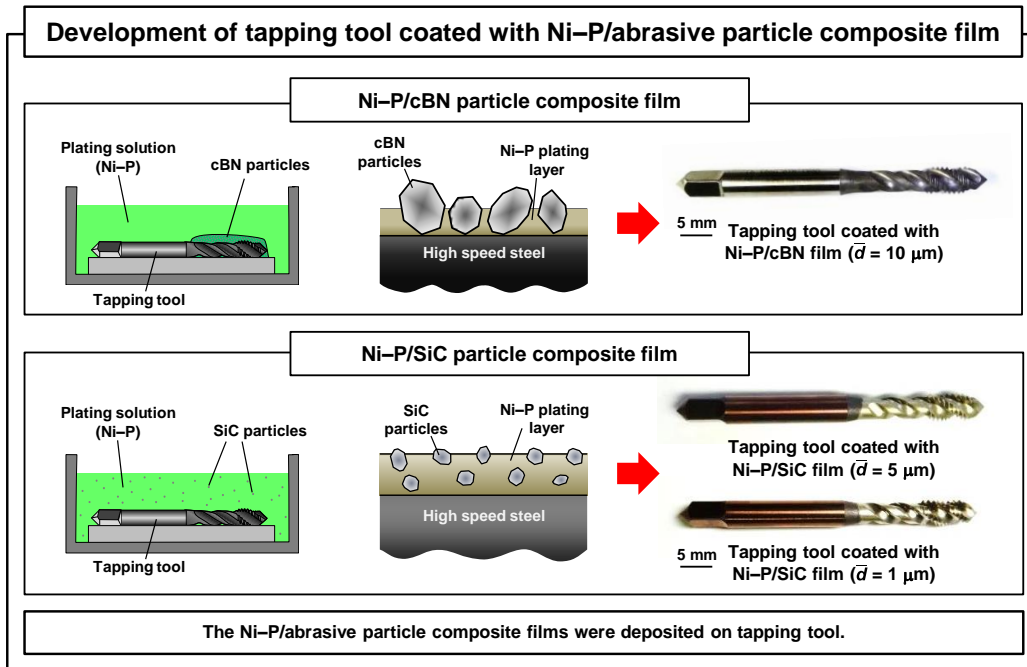


Fig. 7.2 Diagram of summarized results for Chapter 3

In Chapter 4, tapping tests were performed to investigate whether the tapping tools coated with the Ni–P/abrasive particle composite film were able to prevent chip snarling and increase the tool service life at high cutting speeds. The friction coefficient at the tool–workpiece rake face interface was estimated using the measured thrust force and cutting torque, and the effect of the friction coefficient on chip snarling was investigated. The conclusions of this chapter are summarized as follows:

- (1) The tools coated with composite film had lower rates of chip snarling. This was particularly true for the Ni–P/SiC film ($\bar{d} = 1 \mu\text{m}$), which had a chip snarling rate of less than 5%.
- (2) The rate of chip snarling increased in line with the chip curl diameter. The tapping tools coated with composite film were able to prevent snarling by maintaining the chip curl diameter below the width of the helical flute of the tapping tool (3.2 mm) at high cutting speeds. The rate of chip snarling exceeded 40% at a dimensionless chip curl diameter of approximately 1.0.
- (3) The tapping tools coated with composite films had the highest cutting torque under all cutting conditions. The tools coated with the Ni–P/SiC film ($\bar{d} = 5.0 \text{ mm}$) and those coated with the Ni–P/SiC film ($\bar{d} = 1.0 \text{ mm}$) had thrust forces greater than 1.8 Nm, exceeding that of the conventional tapping tool at all cutting speeds. The tool with the Ni–P/cBN film ($\bar{d} = 10 \text{ mm}$) had a thrust force smaller than that of the conventional tool at 30 and 50 m/min.
- (4) The mean friction coefficient between the chip and tool rake face was derived from a coordinate transformation of the measured cutting torques and thrust forces. The mean friction coefficient of the tapping tools coated with the Ni–P/SiC ($\bar{d} = 5 \mu\text{m}$) and Ni–P/SiC ($\bar{d} = 1 \mu\text{m}$) films were higher than that of the conventional tapping tool at all cutting speeds. The chip curl diameter decreased as the mean friction coefficient increased.
- (5) At high cutting speeds ($V_f = 50 \text{ m/min}$), the service life of the tapping tool coated with the Ni–P/SiC film ($\bar{d} = 1 \mu\text{m}$) was 2.6 times as high as that of the conventional steam treatment tool.

Figure 7.3 illustrates summarized results for Chapter 4.

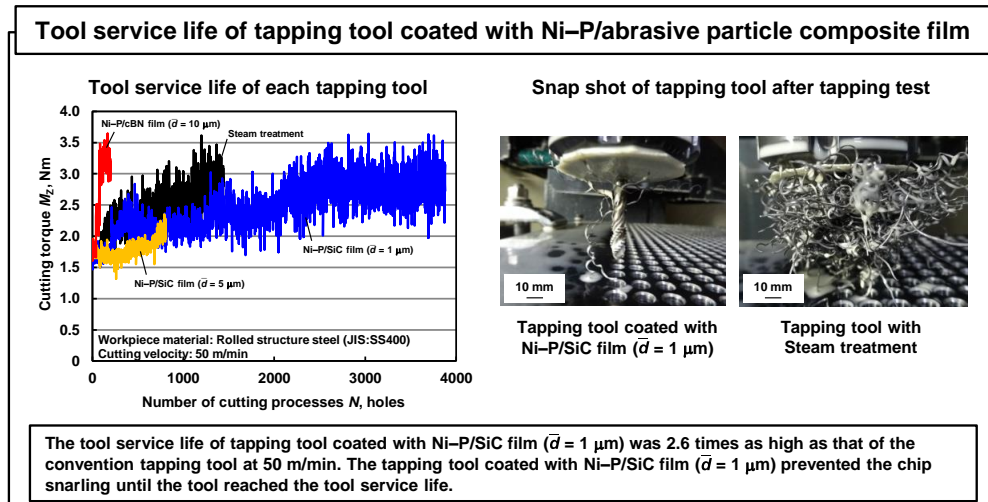
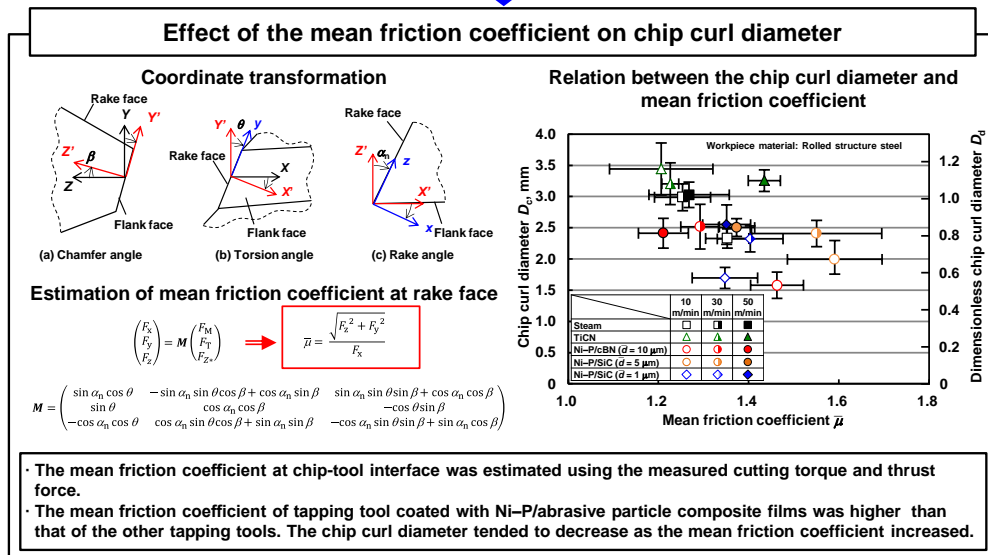
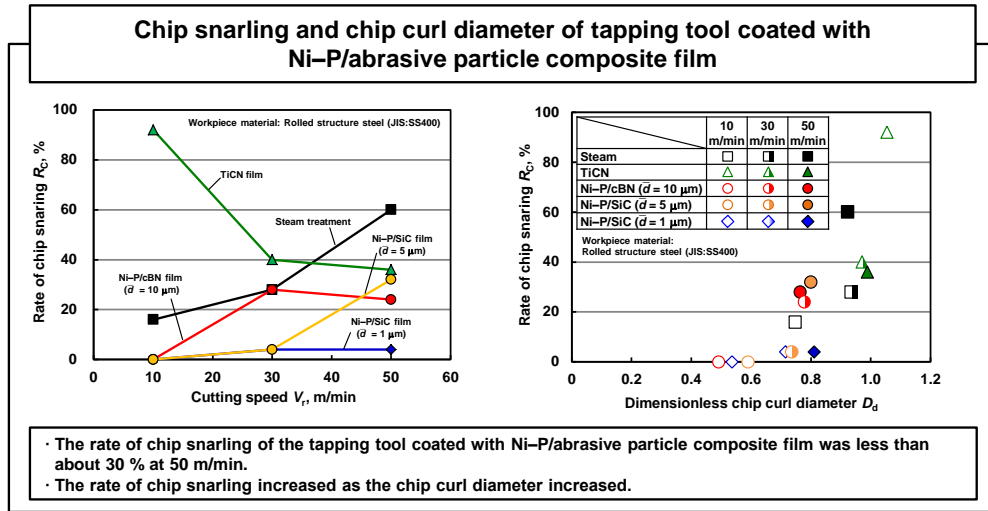


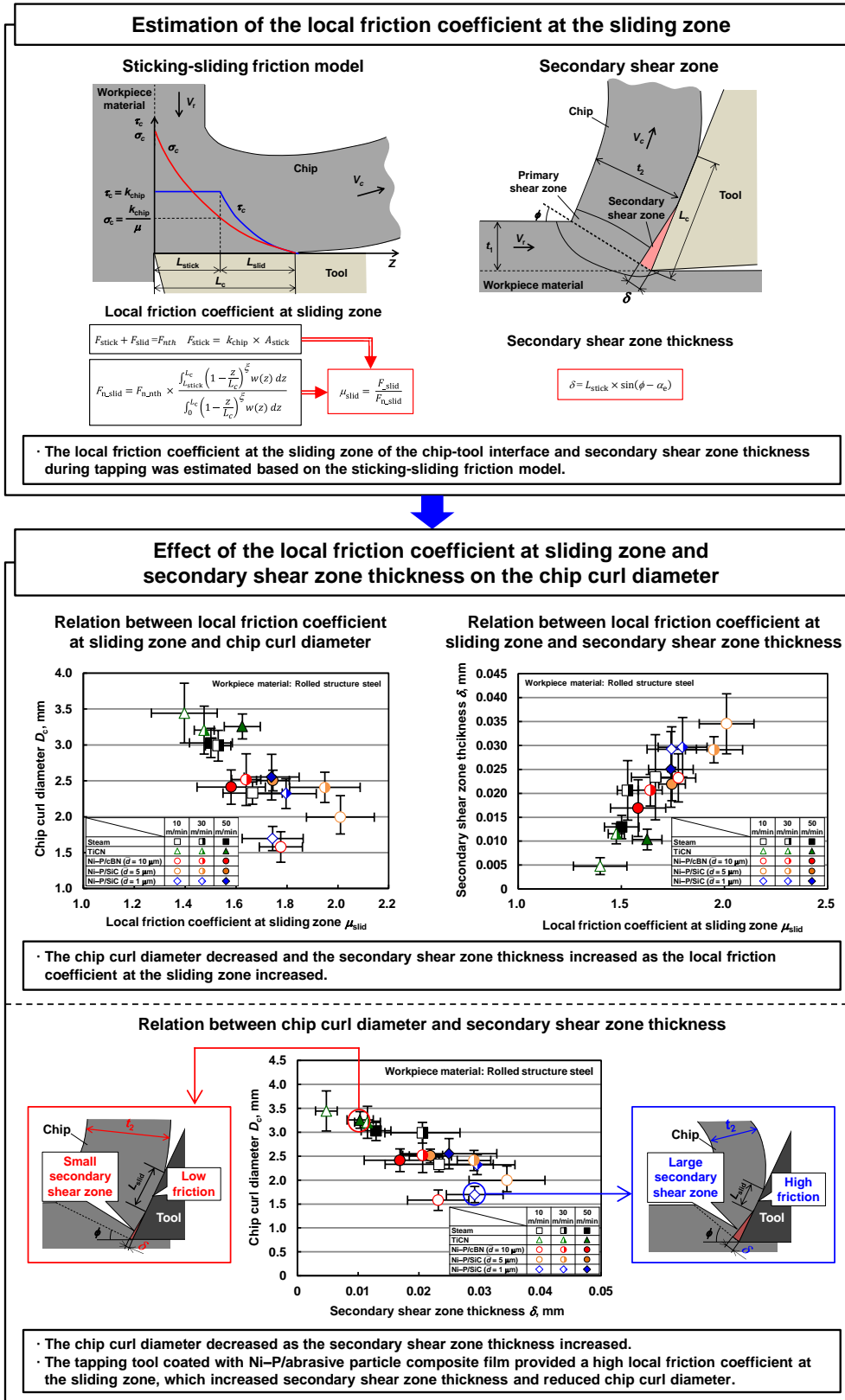
Fig. 7.3 Diagram of summarized results for Chapter 4

In chapter 5, the local friction coefficient at the sliding zone of the chip–tool interface during tapping was estimated based on the sticking–sliding friction model. The effects of the local friction coefficient on chip curl diameter and secondary shear zone thickness were analyzed to investigate the mechanism of chip snarling prevention for tapping tools coated with the composite film.

The conclusions obtained in this chapter are as follows:

- (1) Chip curl diameter decreased with an increase in the local friction coefficient at the sliding zone; the local coefficients of friction for tapping tools coated with composite films (1.58–1.80) were higher than those for tapping tools with conventional surface treatments (1.40–1.65).
- (2) The local friction coefficient at the sliding zone had a significant impact on secondary shear zone thickness; the secondary shear zone thickness increased with an increase in the local friction coefficient at the sliding zone.
- (3) The secondary shear zone was observed for the tapping tool coated with the composite film at 10 and 50 m/min, and the thickness of the secondary shear zone estimated from the observed images was almost equivalent to the calculated values.
- (4) The tapping tools coated with Ni–P/abrasive particle composite films provided a high local friction coefficient at the sliding zone, which increased secondary shear zone thickness and reduced chip curl diameter.

Figure 7.4 illustrates summarized results for Chapter 5.



In Chapter 6, tapping tests were conducted on workpieces made from SCM440, S25C, and S45C to investigate whether coating the tapping tool with the Ni-P/SiC particle composite film could prevent chip snarling across a wide range of cutting speeds. The relation between workpiece material and chip curl diameter was also investigated.

The conclusions of this chapter are summarized as follows:

- (1) The rate of chip snarling increased in line with the dimensionless chip curl diameter, particularly when $D_d \geq 0.9$. The dimensionless chip curl diameter of the tapping tool coated with the Ni-P/SiC film ($\bar{d} = 1 \mu\text{m}$) was less than 0.9 for all workpiece materials and the rate of chip snarling was less than 10%.
- (2) When the tapping tool coated with the composite film was used, the secondary shear zone thickness increased as the local friction coefficient at the sliding zone increased. The secondary shear zone thickness was affected by the temperature at the primary shear zone and decreased as this temperature increased.
- (3) The dimensionless chip curl diameter was less than 0.6 when the temperature at the primary shear zone was lower than 495 K and the secondary shear zone thickness was at least 23 μm . This reduced the frequency of chip snarling.
- (4) Coating the tapping tool with the composite film prevented chip snarling when cutting threaded holes in steel workpieces made from JIS SCM440, S25C, S45C, and SS400.

Figure 7.5 illustrates summarized results for Chapter 6.

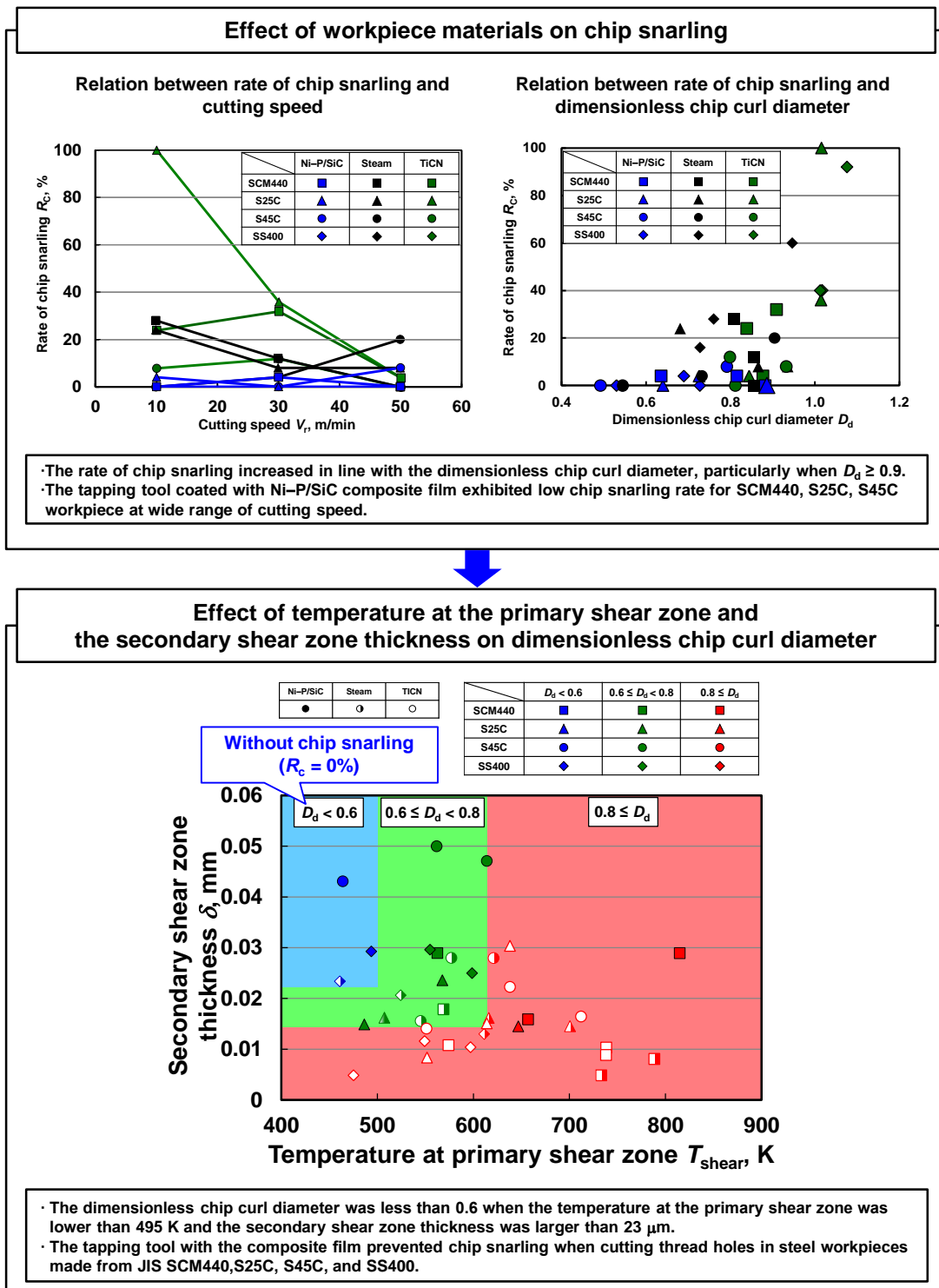


Fig. 7.5 Diagram of summarized results for Chapter 6

Appendix

Fig. A1 shows the geometry of the 4th cutting edge. As shown in this figure, the origin of the coordinate axes located at the point O, which is the nose of the front cutting edge. Thus, the cutting edge width $w(z)$ is given by follows:

(i) $0 \leq z < z_1$

$$w(z) = \left(\frac{1}{\tan \theta'} + \frac{1}{\tan \theta''} \right) \times \frac{z \cos \alpha_e}{\cos \theta} \quad (\text{A1})$$

(ii) $z_1 \leq z < z_2$

$$w(z) = \left(w_1 + \frac{z \cos \alpha_e}{\tan \theta''} \right) \times \frac{1}{\cos \theta} \quad (\text{A2})$$

(iii) $z_2 \leq z \leq L_c$

$$w(z) = (w_1 + w_2) \times \frac{1}{\cos \theta} \quad (\text{A3})$$

where the distance z_1 , z_2 and the width w_1 , w_2 are obtained by following equations.

$$z_1 = t_1 \times \frac{\sin \theta'}{\cos(\frac{\pi}{2} - \theta' - \theta'')} \quad (\text{A4})$$

$$z_2 = \overline{OB} \times \sin \theta'' \quad (\text{A5})$$

$$w_1 = t_1 \times \frac{\cos \theta'}{\cos(\frac{\pi}{2} - \theta' - \theta'')} \quad (\text{A6})$$

$$w_2 = \overline{OB} \times \cos \theta'' \quad (\text{A7})$$

where θ is the torsion angle, θ' is the half angle of thread of screw, θ'' is the angle between \overline{OB} and Y axis, \overline{OB} is the length of the front cutting edge.

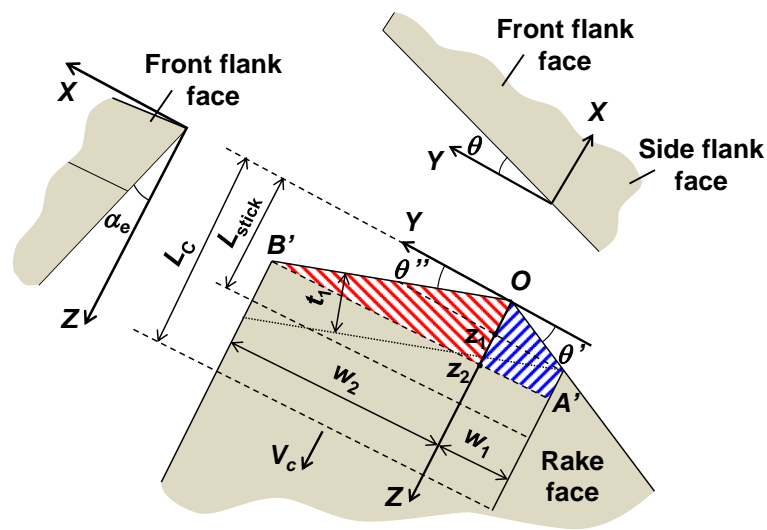


Fig. A1 Calculation of width of the fourth cutting edge.

Acknowledgements

I would like to express my sincere appreciation to my academic advisor, Prof. Kazuo Hokkirigawa, for his incredible kindness, excellent guidance and constant encouragement throughout this work.

I would also like to thank Prof. Tsunemoto Kuriyagawa and Prof. Kazuhiro Ogawa for their careful review, valuable suggestions and participation in this research work as members of the examination committee.

I would like to gratefully acknowledge the enthusiastic supervision of Associate Prof. Takeshi Yamaguchi during this work as well as all his help.

I would also like to specially thank Assistant Prof. Kei Shibata, for the constant help and tremendous assistance with my research work as well as his non-stop willingness to help me.

This research was supported partly by the Center for Revitalization Promotion, Japan Science and Technology Agency. I would also like to thank Dr. Junichi Isoe for careful review and advice.

I am grateful to each member of our laboratory with whom I have had the pleasure to study together for their kind assistance. Mr. Ryo Itagaki and Mr. Syoki Takigushi are specially thanked for their assistance in researching and experimental preparations.

I would like to specially thank Mr. Takeshi Kubo, Mr. Wataru Watanabe, and Mr. Satoru Oyama (MIYAGITANOI MFG. CO., LTD.) for their help with manufacturing the tool specimens used in this work, providing the machining center and each specialized advice.

I would like to thank Tohoku University Creative Engineering Center for providing the scanning electron microscope and processing machine.

I would like to thank Technical Division, School of Engineering Tohoku University for providing the processing machine and Dr. Kosei Kobayashi for assistance in observation of the specimen.

Finally, I am grateful to my parents for support, understanding, endless patience and encouragement.